Microscopic structure of high-spin vibrational excitations in superdeformed ^{190,192,194}Hg

Takashi Nakatsukasa[*]

Atomic Energy of Canada Limited, Chalk River Laboratories, Chalk River, Ontario K0J 1J0, Canada

Kenichi Matsuyanagi

Department of Physics, Kyoto University, Kyoto 606–01, Japan

Shoujirou Mizutori

Department of Mathematical Physics, Lund Institute of Technology, Box 118, S-22100, Lund, Sweden

Yoshifumi R. Shimizu

Department of Physics, Kyushu University, Fukuoka 812, Japan

Microscopic calculations based on the cranked shell model extended by the random-phase-approximation are performed to investigate the quadrupole and octupole correlations for excited superdeformed bands in ^{190}Hg, ^{192}Hg, and ^{194}Hg. The $K=2$ octupole vibrations are predicted to be the lowest excitation modes at zero rotational frequency. At finite frequency, however, the interplay between rotation and vibrations produces different effects depending on neutron number: The lowest octupole phonon is rotationally aligned in ^{190}Hg, is crossed by the aligned two-quasiparticle bands in ^{192}Hg, and retains the $K=2$ octupole vibrational character up to the highest frequency in ^{194}Hg. The γ vibrations are predicted to be higher in energy and less collective than the octupole vibrations. From a comparison with the experimental dynamic moments of inertia, a new interpretation of the observed excited bands invoking the $K=2$ octupole vibrations is proposed, which suggests those octupole vibrations may be prevalent in superdeformed Hg nuclei. [S0556-2813(96)05705-6]

PACS number(s): 21.10.Re, 21.60.Jz, 27.80.+w

I. INTRODUCTION

Theoretical and experimental studies of collective vibrational states built on the superdeformed (SD) yrast band are open topics of interest in the field of high-spin nuclear structure. Since the large deformation and rapid rotation of SD bands may produce a novel shell structure, we expect that surface vibrations will exhibit quite different features from those found in spherical and normal-deformed nuclei. According to our previous work [1–5], low-lying octupole vibrations are more important than quadrupole vibrations when the nuclear shape is superdeformed. Strong octupole correlations in SD states have been also suggested theoretically in Refs. [6–13]. Experimentally, octupole correlations in SD states have been suggested for ^{152}Dy [14], ^{193}Hg [15], and ^{190}Hg [16,17]. We have reported theoretical calculations corresponding to these data for ^{193}Hg [3] and ^{152}Dy [5]. In this paper, we discuss the quadrupole and octupole correlations for ^{190}Hg (which have been partially reported in Refs. [17–19]) and for the neighboring SD nuclei ^{192,194}Hg.

We have predicted the low-lying $K=2$ octupole vibrations for SD Hg isotopes ^{190,192,194}Hg ($E_x \sim 1$ MeV) [3,4]. These predictions differ from the results of generator-coordinate-method (GCM) calculations [13] in which the $K=0$ octupole state is predicted to be the lowest in SD ^{192}Hg and the excitation energies are significantly higher ($E_x \sim 2$ MeV) than in our predictions. Experimentally [17], the Routhians of the lowest octupole state decrease with the

rotational frequency, for example, from $E_x' \approx 0.7$ to 0.3 MeV as $\hbar \omega_{rot}$ goes from 0.25 to 0.35 MeV; therefore to compare the theoretical Routhians directly with the experimental ones, we need to calculate them at finite rotational frequency. For this purpose, the cranked shell model extended by the random-phase approximation (RPA) provides us with a powerful tool to investigate collective excitations at high angular momentum.

A great advantage of this model is its ability to take into account effects of the Coriolis coupling on the collective vibrational motions in a rapidly rotating system. Since in the normal-deformed nuclei it is known that Coriolis coupling effects are important even for the 3^- octupole states [20], one may expect strong Coriolis mixing for high-spin octupole states built on the SD yrast band. On the other hand, our previous calculations suggested weak Coriolis mixing for the lowest octupole state in ^{192}Hg [3] and ^{152}Dy [5]. This may be because the angular momentum of the octupole phonon is strongly coupled to the symmetry axis due to the large deformation of the SD shape. Generally speaking, Coriolis mixing is expected to occur more easily in nuclei with smaller deformation. However, this expectation may not hold for octupole bands in all SD nuclei because Coriolis mixing depends on the shell structure. In this paper we find a significant difference in the Coriolis mixing between an octupole band in ^{190}Hg and the other bands.

Another advantage of this model is that it gives us a unified microscopic description of collective states, weakly collective states, and noncollective two-quasiparticle excitations. A transition of the octupole vibrations into aligned two-quasiparticle bands at high spin in normal-deformed nu-

---

*Electronic address: nakatsukasat@cr1.aecl.ca

clei has been predicted by Vogel [21]. In Ref. [19], this transition is discussed in the context of experimental data on rare-earth and actinide nuclei, and a damping of octupole collectivity at high spin was suggested. Since similar phenomena may happen to octupole vibrations in SD states, it is important that our model describe the interplay between collective and noncollective excitations.

Recent experimental studies reveal a number of interesting features of excited SD bands in even-even Hg isotopes. In ^{190}Hg, almost constant dynamic moments of inertia, $\mathscr{J}^{(2)}$, have been observed by Crowell *et al.* [16]. Reference [17] has established the relative excitation energy of this band and confirmed the dipole character of the decay transitions into the yrast SD band. This band has been interpreted as an octupole vibrational band. Two more excited bands in ^{190}Hg have been observed recently by Wilson *et al.* [18], one of which shows a sharp rise of $\mathscr{J}^{(2)}$ at low frequency. In ^{192}Hg, Fallon *et al.* [22] have reported two excited bands which exhibit peaks in $\mathscr{J}^{(2)}$ at high frequency. In contrast with these atypical $\mathscr{J}^{(2)}$ behaviors, two excited bands in ^{194}Hg originally observed by Riley *et al.* [23] and extended by Cederwall *et al.* [24] show a smooth increase with rotational frequency. We show in this paper that this $\mathscr{J}^{(2)}$ behavior can be explained with a single theoretical model which microscopically takes into account shape vibrations and the Coriolis force.

The purpose of this paper is to present the RPA method based on the cranked shell model and its ability to describe a variety of nuclear properties including shape vibrations at large deformation and high spin. We propose a plausible interpretation for the microscopic structure of excited SD bands in ^{190,192,194}Hg, and show that octupole bands may be more prevalent than expected in these SD nuclei. Section II presents a description of the model, in which we stress our improvements to the cranked Nilsson potential and to the coupled RPA method in a rotating system. Section III presents details of the calculation in which the pairing and effective interactions are discussed. The results for the excited SD ^{190}Hg, ^{192}Hg, and ^{194}Hg are presented in Sec. IV, and compared with the experimental data in Sec. V. The conclusions are summarized in Sec. VI.

II. THEORETICAL FRAMEWORK

The theory of the cranked shell model extended by the random-phase approximation (RPA) was first developed by Marshalek [25] and has been applied to high-spin β and γ vibrational bands [26–28] and to octupole bands [29,1–5]. Since this theory is suitable for describing the collective vibrations built on deformed high-spin states, it is very useful for investigating vibrational motion built on the SD yrast band.

A. Cranked Nilsson potential with the local Galilean invariance

We start with a rotating mean field with a rotational frequency ω_{rot} described by

$$h_{\mathrm{s.p.}} = h_{\mathrm{Nilsson}} + \Gamma_{\mathrm{pair}} - \omega_{\mathrm{rot}} J_x + h_{\mathrm{add}}, \quad (2.1)$$

where h_{Nilsson} is a standard Nilsson potential defined in single-stretched coordinates $r_i' = (\omega_i/\omega_0)^{1/2} r_i$ and $p_i' = (\omega_0/\omega_i)^{1/2} p_i$ $(i = x, y, z)$,

$$h_{\mathrm{Nilsson}} = \sum_{i=x,y,z} \left(\frac{\omega_i}{\omega_0}\right)\left(\frac{p_i'^2}{2M} + \frac{M\omega_0^2}{2}r_i'^2\right) + v_{ll}(l'^2 - \langle l'^2\rangle_N)$$
$$+ v_{ls}l' \cdot \mathbf{s}, \quad (2.2)$$

where $l' = \mathbf{r}' \times \mathbf{p}'$. The pairing field Γ_{pair} is defined by

$$\Gamma_{\mathrm{pair}} = -\sum_{\tau=n,p} \Delta_\tau(P_\tau^\dagger + P_\tau) - \sum_{\tau=n,p} \lambda_\tau N_\tau, \quad (2.3)$$

where $P_\tau = \sum_{k \in \tau, k>0} c_{\bar{k}} c_k$ and $N_\tau = \sum_{k \in \tau} c_k^\dagger c_k$ are the monopole-pairing and number operators, respectively. In Sec. III A, we discuss the details of the pairing field used in the calculations.

A standard cranked Nilsson potential has the disadvantage that it overestimates the moments of inertia compared to a Woods-Saxon potential. This problem comes from the spurious velocity dependence associated with the l^2 term in the Nilsson potential which is absent for Woods-Saxon potential. If the mean-field potential is velocity independent, the local velocity distribution in the rotating nucleus remains isotropic in velocity space, which means that the flow pattern becomes the same as for a rigid-body rotation [30]. However, in the cranked Nilsson potential, this isotropy of the velocity distribution is significantly broken due to the l^2 term. Thus the Coriolis force introduces a spurious flow in the rotating coordinate system, proportional to the rotational frequency. This spurious effect can be compensated by an additional term that restores the local Galilean invariance. This additional term is obtained by substituting (the local Galilean transformation)

$$\mathbf{p} \rightarrow \mathbf{p} - M(\boldsymbol{\omega}_{\mathrm{rot}} \times \mathbf{r}), \quad (2.4)$$

in the ls and l^2 terms of the Nilsson potential. This prescription was suggested by Bohr and Mottelson [30], and developed by Kinouchi [31]. For a momentum-dependent potential $V(\mathbf{r},\mathbf{p})$,

$$V(\mathbf{r},\mathbf{p}) + h_{\mathrm{add}} = V(\mathbf{r}, \mathbf{p} - M(\boldsymbol{\omega}_{\mathrm{rot}} \times \mathbf{r})) \quad (2.5)$$

$$\approx V(\mathbf{r},\mathbf{p}) - \omega_{\mathrm{rot}} M\left(y\frac{\partial}{\partial p_z} - z\frac{\partial}{\partial p_y}\right) V(\mathbf{r},\mathbf{p}) \quad (2.6)$$

$$= V(\mathbf{r},\mathbf{p}) + \frac{i}{\hbar}\omega_{\mathrm{rot}} M(y[z,V] - z[y,V]), \quad (2.7)$$

where we assume uniform rotation around the x axis, $\boldsymbol{\omega}_{\mathrm{rot}} = (\omega_{\mathrm{rot}},0,0)$. Following this prescription, the additional term h_{add} in Eq. (2.1) is obtained for the Nilsson potential (2.2),
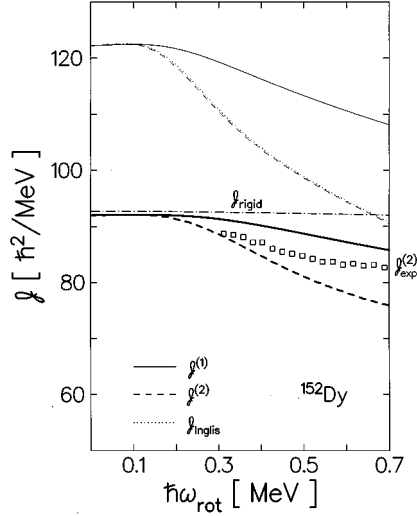
FIG. 1. Kinematic (solid lines) and dynamic (dashed lines) moments of inertia for SD ^{152}Dy calculated in the cranked Nilsson Hamiltonian with (thick lines) and without (thin lines) the additional term h_{add} in Eq. (2.8). The rigid-body and the Inglis moments of inertia are shown by dash-dotted and dotted lines, respectively. The parameters used in the calculation are the same as those used in Ref. [5] and pairing correlations are neglected. Symbols are experimental $\mathscr{I}^{(2)}$ taken from Ref. [14].

$$h_{add} = -\frac{\omega_{rot}}{\sqrt{\omega_y \omega_z}} \left\{ v_{ll} \left[2M\omega_0 \mathbf{r}'^2 - \hbar \left(N_{osc} + \frac{3}{2} \right) \right] l'_x \right.$$

$$\left. + v_{ls} M\omega_0 [\mathbf{r}'^2 s_x - r'_x (\mathbf{r}' \cdot \mathbf{s})] \right\}. \quad (2.8)$$

Note that the term proportional to $(N_{osc} + 3/2)$ in Eq. (2.8) comes from the velocity dependence of $\langle l'^2 \rangle_N$ in Eq. (2.2). This result, Eq. (2.8), has been applied to the SD bands in ^{152}Dy [5] where the single-particle Routhians were found to be very similar to those obtained by using the Woods-Saxon potential. In Fig. 1, moments of inertia for SD ^{152}Dy calculated with and without the additional term (2.8) are displayed. Since the effects of the mixing among the major oscillator shells N_{osc} are neglected in calculating our Routhians, kinematic ($\mathscr{I}^{(1)}$) and dynamic ($\mathscr{I}^{(2)}$) moments of inertia are obtained by adding the contributions of the N_{osc}-mixing effects to the values calculated without them:

$$\mathscr{I}^{(1)} = \frac{\langle J_x \rangle}{\omega_{rot}} + \frac{1}{\omega_{rot}} \int_0^{\omega_{rot}} \Delta\mathscr{I}_{Inglis}(\omega)d\omega$$

$$\approx \frac{\langle J_x \rangle}{\omega_{rot}} + \Delta\mathscr{I}_{Inglis}, \quad (2.9)$$

$$\mathscr{I}^{(2)} = \frac{d\langle J_x \rangle}{d\omega_{rot}} + \Delta\mathscr{I}_{Inglis}, \quad (2.10)$$

$$\Delta\mathscr{I}_{Inglis} = \mathscr{I}_{Inglis} - \mathscr{I}_{Inglis}^{\Delta N=0}$$

$$= 2 \sum_{n(\Delta N=2)} \frac{|\langle n|J_x|0\rangle|^2}{E_n - E_0}, \quad (2.11)$$

where $\Delta\mathscr{I}_{Inglis}$ is difference between the Inglis moments of inertia with and without the $\Delta N_{osc} = 2$ contributions [32]. $\Delta\mathscr{I}_{Inglis}(\omega)$ turned out to be approximately constant against frequency ω and this was used in the last step of Eq. (2.9). The $\mathscr{I}^{(1)}$ and $\mathscr{I}^{(2)}$ values calculated with the additional term are very close to the rigid-body value at low frequency, which means that the spurious effects of the l^2 term have been removed. Note that the abscissa of Fig. 1 corresponds to the "bare" rotational frequency without renormalization. The drastic reduction of $\mathscr{I}^{(1)}$ and $\mathscr{I}^{(2)}$ at high frequency is corrected by the additional term, and this is seen to be important in reproducing the experimental $\mathscr{I}^{(2)}$ behavior of the yrast SD band.

B. RPA in the rotating frame

The residual interactions are assumed to be in a separable form

$$H_{int} = -\frac{1}{2} \sum_{\rho, \alpha} \chi_\rho R_\rho^\alpha R_\rho^\alpha, \quad (2.12)$$

where R_ρ^α are one-body Hermitian operators, and χ_ρ are coupling strengths. The indices α indicate the signature quantum numbers ($\alpha = 0,1$) and ρ specifies other modes. In this paper, we take as R_ρ^α the monopole pairing and the quadrupole operators for positive-parity states, and the octupole and the isovector dipole operators for negative-parity states [see Eq. (3.5)]. Since the K quantum number is not conserved at finite rotational frequency, it is more convenient to make the multipole operators have good signature quantum numbers. In general, the Hermitian multipole (spin-independent) operators with good signature quantum numbers are constructed by

$$Q_{\lambda K}^\alpha = \frac{i^{\lambda + \alpha + K}}{\sqrt{2(1 + \delta_{K0})}} [r^\lambda Y_{\lambda K} + (-)^{\lambda + \alpha} r^\lambda Y_{\lambda - K}], \quad (2.13)$$

with $K \geq 0$, where the spherical-harmonic functions $Y_{\lambda K}$ are defined with respect to the symmetry (z) axis. All multipole operators are defined in doubly stretched coordinates $[r''_i = (\omega_i/\omega_0)r_i]$, which can be regarded as an improved version of the conventional multipole interaction. Sakamoto and Kishimoto [33] have shown that at the limit of the harmonic-oscillator potential (at $\omega_{rot} = 0$), it guarantees nuclear self-consistency [30], restoration of the symmetry broken in the mean field, and separation of the spurious solutions. The coupling strengths χ_ρ should be determined by the self-consistency condition between the density distribution and the single-particle potential (see Sec. III B for details).

To describe vibrational excitations in the RPA theory, we must define the *quasiparticle vacuum* on which the vibrations are built. The observed moments of inertia, $\mathscr{I}^{(2)}$, of the yrast SD bands smoothly increase in the $A = 190$ region, which suggests that the internal structure also smoothly changes as a function of the frequency ω_{rot}. Therefore the *adiabatic representation*, in which the quasiparticle operators are always defined with respect to the yrast state $|\omega_{rot}\rangle$, is considered to be appropriate in this work.

In terms of quasiparticles, the Hamiltonian of Eq. (2.1) can be diagonalized (by the general Bogoliubov transformation) as

$$h_{\text{s.p.}} = \text{const} + \sum_{\mu} (E_{\mu} a_{\mu}^{\dagger} a_{\mu}) + \sum_{\bar{\mu}} (E_{\bar{\mu}} a_{\bar{\mu}}^{\dagger} a_{\bar{\mu}}), \quad (2.14)$$

with

$$a_{\mu}|\omega_{\text{rot}}\rangle = a_{\bar{\mu}}|\omega_{\text{rot}}\rangle = 0, \quad (2.15)$$

where $(a_{\mu}^{\dagger}, a_{\bar{\mu}}^{\dagger})$ represent the quasiparticles with signature $\alpha = (1/2, -1/2)$, respectively. The excitation operators of the RPA normal modes $X_n^{\alpha\dagger}$ ($\alpha = 0,1$) are defined by

$$X_n^{0\dagger} = \sum_{\mu\bar{\nu}} \{\psi_n^0(\mu\bar{\nu}) a_{\mu}^{\dagger} a_{\bar{\nu}}^{\dagger} + \varphi_n^0(\mu\bar{\nu}) a_{\bar{\nu}} a_{\mu}\}, \quad (2.16)$$

$$X_n^{1\dagger} = \sum_{\mu<\nu} \{\psi_n^1(\mu\nu) a_{\mu}^{\dagger} a_{\nu}^{\dagger} + \varphi_n^1(\mu\nu) a_{\nu} a_{\mu}\}$$

$$+ \sum_{\bar{\mu}<\bar{\nu}} \{\psi_n^1(\bar{\mu}\bar{\nu}) a_{\bar{\mu}}^{\dagger} a_{\bar{\nu}}^{\dagger} + \varphi_n^1(\bar{\mu}\bar{\nu}) a_{\bar{\nu}} a_{\bar{\mu}}\}, \quad (2.17)$$

where indices n specify excited states and $\psi_n^{\alpha}(\mu\nu)$ $[\varphi_n^{\alpha}(\mu\nu)]$ are the RPA forward [backward] amplitudes. Quasiparticle-scattering terms such as $a_{\mu}^{\dagger} a_{\nu}$ are regarded as higher-order terms in the boson-expansion theory and are neglected in the RPA.[1]

The equation of motion and the normalization condition in the RPA theory,

$$[h_{\text{s.p.}} + H_{\text{int}}, X_n^{\alpha\dagger}]_{\text{RPA}} = \hbar\Omega_n^{\alpha} X_n^{\alpha\dagger}, \quad (2.18)$$

$$[X_n^{\alpha}, X_{n'}^{\alpha\,\dagger}]_{\text{RPA}} = \delta_{nn'}, \quad (2.19)$$

are solved with the following multidimensional response functions:

$$S_{\rho\rho'}^{\alpha}(\Omega) = \sum_{\gamma\delta} \left\{ \frac{R_{\rho}^{\alpha}(\gamma\delta)^* R_{\rho'}^{\alpha}(\gamma\delta)}{E_{\gamma} + E_{\delta} - \hbar\Omega} + \frac{R_{\rho}^{\alpha}(\gamma\delta) R_{\rho'}^{\alpha}(\gamma\delta)^*}{E_{\gamma} + E_{\delta} + \hbar\Omega} \right\}, \quad (2.20)$$

where $(\gamma\delta) = (\mu\bar{\nu})$ for $\alpha = 0$ states, and $(\gamma\delta) = (\mu<\nu),(\bar{\mu}<\bar{\nu})$ for $\alpha = 1$ states. The two-quasiparticle matrix elements $R_{\rho}^{\alpha}(\gamma\delta)$ are defined by $R_{\rho}^{\alpha}(\gamma\delta) \equiv \langle\omega_{\text{rot}}|a_{\delta} a_{\gamma} R_{\rho}^{\alpha}|\omega_{\text{rot}}\rangle$. Let us denote the transition matrix elements between the RPA excited states $|n\rangle$ and the yrast state as

$$t_{\rho}^{\alpha}(n) \equiv t_n[R_{\rho}^{\alpha}] \equiv \langle\omega_{\text{rot}}|R_{\rho}^{\alpha}|n\rangle$$

$$= \langle\omega_{\text{rot}}|[R_{\rho}^{\alpha}, X_n^{\alpha\dagger}]|\omega_{\text{rot}}\rangle$$

$$= [R_{\rho}^{\alpha}, X_n^{\alpha\dagger}]_{\text{RPA}}. \quad (2.21)$$

Then, the equation of motion (2.18) is equivalent to

$$t_{\rho}^{\alpha}(n) = \sum_{\rho'} \chi_{\rho}^{\alpha} S_{\rho\rho'}^{\alpha}(\Omega) t_{\rho'}^{\alpha}(n). \quad (2.22)$$

RPA solutions (eigenenergies) $\hbar\Omega_n$ are obtained by solving the equation

$$\det\left(S_{\rho\rho'}^{\alpha}(\Omega) - \frac{1}{\chi_{\rho}}\delta_{\rho\rho'} \right) = 0, \quad (2.23)$$

which corresponds to the condition that Eq. (2.22) have a nontrivial solution $[t_{\rho}^{\alpha}(n) \neq 0]$. Each RPA eigenstate is characterized by the corresponding forward and backward amplitudes which are calculated as

$$\psi_n^{\alpha}(\gamma\delta) = \frac{\Sigma_{\rho}\chi_{\rho}^{\alpha} t_{\rho}^{\alpha}(n) R_{\rho}^{\alpha}(\gamma\delta)}{E_{\gamma} + E_{\delta} - \hbar\Omega_n}, \quad (2.24)$$

$$\varphi_n^{\alpha}(\gamma\delta) = \frac{-\Sigma_{\rho}\chi_{\rho}^{\alpha} t_{\rho}^{\alpha}(n) R_{\rho}^{\alpha}(\gamma\delta)^*}{E_{\gamma} + E_{\delta} + \hbar\Omega_n}, \quad (2.25)$$

and satisfies the normalization condition (2.19). The transition matrix elements $\langle\omega_{\text{rot}}|Q|n\rangle$ of any one-body operator Q can be expressed in terms of these amplitudes ψ_n and φ_n:

$$t_n[Q] \equiv \langle\omega_{\text{rot}}|Q|n\rangle$$

$$= \sum_{\gamma\delta} \{Q(\gamma\delta)^* \psi_n(\gamma\delta) - Q(\gamma\delta)\varphi_n(\gamma\delta)\}. \quad (2.26)$$

The phase relation between the matrix elements $Q(\gamma\delta)$ and the amplitudes $(\psi_n(\gamma\delta), \varphi_n(\gamma\delta))$ is very important, because it determines whether the transition matrix element $t_n[Q]$ is coherently enhanced or canceled out after the summation in Eq. (2.26). For instance, a collective quadrupole vibrational state has a favorable phase relation for the quadrupole operators. Therefore, it gives large matrix elements for the $E2$ operators, while for the $M1$ operators, the contributions are normally canceled out after the summation.

Finally we obtain a diagonal form of the total Hamiltonian in the rotating frame by means of the RPA theory,

$$H' = h_{\text{s.p.}} + H_{\text{int}} \approx E_0' + \sum_{n,\alpha} \hbar\Omega_n^{\alpha} X_n^{\alpha\dagger} X_n^{\alpha}, \quad (2.27)$$

where E_0' corresponds to the Routhians for the yrast configuration. Since we are interested in the relative excitation energy between excited states and the yrast state, E_0' need not be explicitly calculated. It is worth noting that since the effect of the cranking term on the quasiparticles depends on rotational frequency, the effects of Coriolis coupling on the RPA eigenstates are automatically taken into account.

III. DETAILS OF CALCULATIONS

A. Mean-field parameters and the improved quasiparticle Routhians

We adopt standard values for the parameters v_{ll} and v_{ls} [34] and use different values of the oscillator frequency ω_0

---

[1] In the following, the notation $[A,B]_{\text{RPA}}$ means that we neglect these higher-order terms in calculating the commutator between A and B.

for neutrons and protons in the Nilsson potential (2.2) in order to ensure equal root-mean-square radii [35]:

$$\omega_0 \rightarrow \begin{cases} \left(\dfrac{2N}{A}\right)^{1/3} \omega_0 & \text{for neutrons,} \\[2ex] \left(\dfrac{2Z}{A}\right)^{1/3} \omega_0 & \text{for protons,} \end{cases} \qquad (3.1)$$

where $\hbar\omega_0 = 41 A^{-1/3}$ MeV.

The quadrupole deformation ϵ is determined by minimizing the total Routhian surface (TRS), and the strength for the monopole pairing interaction G is taken from the prescription of Ref. [36] with the average pairing gap $\widetilde{\Delta} = 12 A^{-1/2}$ MeV and the cutoff parameter of the pairing model space $\Lambda = 1.2\hbar\omega_0$. In principle the pairing gaps (Δ_n, Δ_p) and the chemical potentials (λ_n, λ_p) should be calculated self-consistently satisfying the usual BCS conditions at each rotational frequency:

$$G_\tau \langle \omega_{\rm rot} | P_\tau | \omega_{\rm rot} \rangle = \Delta_\tau, \qquad (3.2)$$

$$\langle \omega_{\rm rot} | N_\tau | \omega_{\rm rot} \rangle = N(Z), \qquad (3.3)$$

with $\tau = (n,p)$. However, the mean-field treatment of the pairing interaction predicts a sudden collapse of the proton pairing gap at $\hbar\omega_{\rm rot} \approx 0.3$ MeV and of the neutron gap at $\hbar\omega_{\rm rot} \approx 0.5$ MeV. This transition causes a singular behavior in the moments of inertia which is inconsistent with experimental observations. It arises from the poor treatment of number conservation, and such sudden transitions should not occur in a finite system like the nucleus. In this paper we have therefore adopted the following phenomenological prescription for the pairing correlations at finite frequency [37]:

$$\Delta_\tau(\omega) = \begin{cases} \Delta_\tau(0)\left[1 - \dfrac{1}{2}\left(\dfrac{\omega}{\omega_c}\right)^2 \right] & \text{for } \omega < \omega_c, \\[2ex] \dfrac{1}{2}\Delta_\tau(0)\left(\dfrac{\omega_c}{\omega}\right)^2 & \text{for } \omega > \omega_c. \end{cases} \qquad (3.4)$$

The chemical potentials are calculated with Eq. (3.3) at each rotational frequency. The parameters $\Delta(0) = 0.8$ (0.6) MeV and $\hbar\omega_c = 0.5$ (0.3) MeV for neutrons (protons) are used in common for ^{190,192,194}Hg.

The quadrupole deformation $\epsilon = 0.44$ is used in the calculations. For simplicity, we assume the deformation to be constant with rotational frequency, and neglect hexadecapole deformation.[2] The equilibrium deformation and pairing gaps have been determined at $\omega_{\rm rot} = 0$, with the truncated pairing model space $\Lambda = 1.2\hbar\omega_0$. Then, the pairing force strengths G_τ are adjusted so as to reproduce the pairing gap of Eq. (3.4) in the whole model space.

The experiments [16,17] have reported a sharp rise of $\mathscr{J}^{(2)}$ moments of inertia for the yrast SD band in ^{190}Hg at $\hbar\omega_{\rm rot} \approx 0.4$ MeV. This rise was reproduced in the cranked

---

[2]Possible errors caused by this simplification will not affect our conclusion because the property of collective RPA solutions under consideration may be insensitive to such details (see also discussions in Sec. IV A).
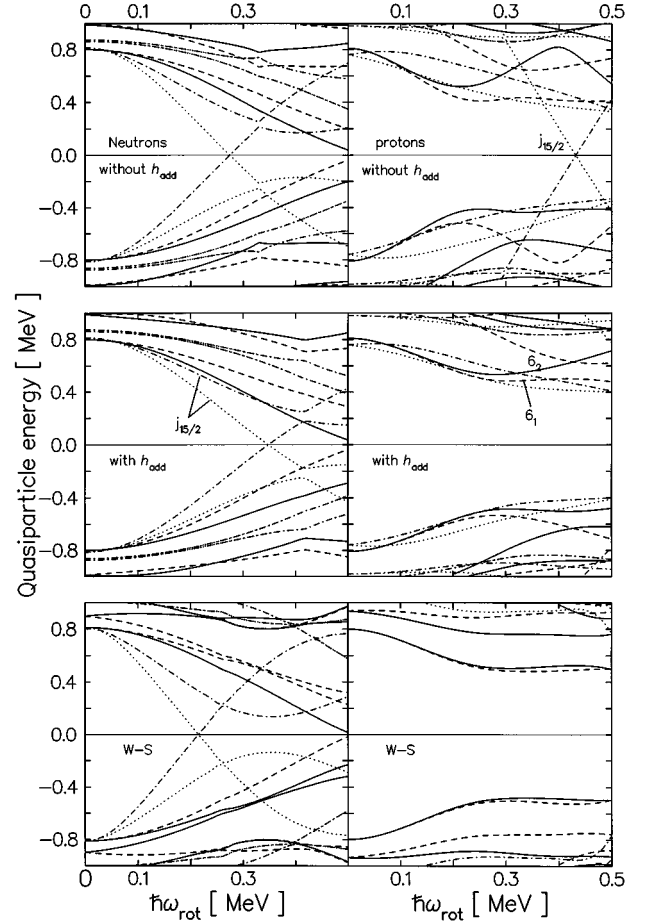

FIG. 2. Quasiparticle Routhians for neutrons (left) and protons (right) in ^{190}Hg. The top parts show the Routhians in the Nilsson potential without the additional term $h_{\rm add}$, the middle for those with $h_{\rm add}$, and the bottom for those in the Woods-Saxon potential with the "universal" parameters. Solid, dashed, dotted, and dash-dotted lines correspond to quasiparticles with $(\pi,\alpha) = (+,-1/2)$, $(+,1/2)$, $(-,-1/2)$, and $(-,1/2)$, respectively. See text for details.

Woods-Saxon calculations [38] and results from a crossing between the yrast band and the aligned $\nu(j_{15/2})^2$ band; however, the predicted crossing frequency was lower ($\hbar\omega_{\rm rot} \approx 0.3$ MeV) than in the experiment. Our Nilsson potential without the additional term (2.8) indicates the same disagreement. In order to demonstrate the effects of the term $h_{\rm add}$ on the Routhians, we present in Fig. 2 the quasiparticle Routhians for ^{190}Hg with $h_{\rm add}$, without $h_{\rm add}$, and for the standard Woods-Saxon potential ($\beta_2 = 0.465$, $\beta_4 = 0.055$). By including $h_{\rm add}$, the correct frequency is reproduced. This term affects the proton Routhians: For example, the alignment of the intruder $\pi j_{15/2}(\alpha = -1/2)$ orbit is predicted to be $i \approx 6.5\hbar$ without $h_{\rm add}$ and this orbit becomes the lowest at $\hbar\omega_{\rm rot} \geq 0.37$ MeV. The alignment is significantly reduced ($i \approx 4\hbar$) with $h_{\rm add}$. The behavior of high-N intruder orbits in the proton Routhians is similar to that in the Woods-Saxon potential. It is worth noting that the conventional renormalization in the Nilsson potential scales the rotational frequency for all orbits, while Eq. (2.8) renormalizes alignment in a different way depending on the spurious effect on each orbit.

B. Residual interactions and the RPA

We adopt the following operators as R_ρ^α in the residual interactions (2.12):

$$P_+ \quad P_- \quad Q_{20}^0 \quad Q_{21}^\alpha \quad Q_{22}^\alpha \quad \text{for } \pi=+ ,$$

$$Q_{30}^1 \quad Q_{31}^\alpha \quad Q_{32}^\alpha \quad Q_{33}^\alpha \quad \widetilde{\tau}_3 Q_{10}^1 \quad \widetilde{\tau}_3 Q_{11}^\alpha \quad \text{for } \pi=- ,$$
(3.5)

where $\widetilde{\tau}_3 = \tau_3 - (N-Z)/A$ which is needed to guarantee the translational invariance. Here, the operators $Q_{\lambda K}^\alpha$ are defined by Eq. (2.13) in the doubly stretched coordinates, and $P_\pm$ are defined by

$$P_+ = \frac{1}{\sqrt{2}}(\widetilde{P}+\widetilde{P}^\dagger),$$
(3.6)

$$P_- = \frac{i}{\sqrt{2}}(\widetilde{P}-\widetilde{P}^\dagger),$$
(3.7)

where $\widetilde{P} = P - \langle \omega_{\rm rot}|P|\omega_{\rm rot}\rangle$. Note that the $K=0$ quadrupole (octupole) operator Q_{20} (Q_{30}) has a unique signature $\alpha=0$ ($\alpha=1$), which corresponds to the fact that $K=0$ bands have no signature partners.

Since we use the different oscillator frequency ω_0 for neutrons and protons in the Nilsson potential [see Eq. (3.1)], we use the following modified doubly stretched multipole operators for the isoscalar channels:

$$Q_{\lambda K}^\alpha \rightarrow \begin{cases} \left(\dfrac{2N}{A}\right)^{2/3} Q_{\lambda K}^\alpha & \text{for neutrons,} \\[2ex] \left(\dfrac{2Z}{A}\right)^{2/3} Q_{\lambda K}^\alpha & \text{for protons.} \end{cases}$$
(3.8)

This was originally proposed by Baranger and Kumar [35] for quadrupole operators. Recently Sakamoto [39] has generalized it for an arbitrary multipole operator and proved that by means of this scaling the translational symmetry is restored in the limit of the harmonic-oscillator potential. In addition, for the collective RPA solutions this treatment makes the transition amplitudes of the electric operators approximately Z/A of those of the mass operators, in the same way as in the case of the static quadrupole moments [28].

We use the pairing force strengths G_τ reproducing the pairing gaps of Eq. (3.4). For the isovector dipole coupling strengths, we adopt the standard values in Ref. [30],

$$\chi_{1K} = -\frac{\pi V_1}{A\langle(r^2)''\rangle_0},$$
(3.9)

with $A\langle(r^2)''\rangle_0 = \langle\Sigma_k^A(r_k^2)''\rangle_0$ and $V_1=130$ MeV. The self-consistent values for the coupling strengths $\chi_{\lambda K}$ of the isoscalar quadrupole and octupole interactions can be obtained for the case of the anisotropic harmonic-oscillator potential [33,39]:

$$\chi_{2K}^{\rm HO} = \frac{4\pi M\omega_0^2}{5A\langle(r^2)''\rangle},$$
(3.10)

$$\chi_{3K}^{\rm HO} = \frac{4\pi}{7}M\omega_0^2\{A\langle(r^4)''\rangle + \tfrac{2}{7}(4-K^2)A\langle(r^4P_2)''\rangle$$
$$+ \tfrac{1}{84}[K^2(7K^2-67)+72]A\langle(r^4P_4)''\rangle\}^{-1},$$
(3.11)

with

$$A\langle(r^nP_l)\rangle \equiv \left(\frac{2N}{A}\right)^{2/3}\left\langle\sum_k^N (r_k)^nP_l\right\rangle_0$$
$$+ \left(\frac{2Z}{A}\right)^{2/3}\left\langle\sum_k^Z (r_k)^nP_l\right\rangle_0.$$
(3.12)

A large model space has been used for solving the coupled RPA equations, including seven major shells with $N_{\rm osc}=3-9$ (2–8) for neutrons (protons) in the calculations of positive-parity states, and nine major shells with $N_{\rm osc}=2-10$ (1–9) for the negative-parity states. The mesh of the rotational frequency for the calculations has been chosen as $\Delta\hbar\omega_{\rm rot}=0.01$ MeV which is enough to discuss the properties of band crossing and Coriolis couplings.

Since our mean-field potential is not the simple harmonic oscillator, we use scaling factors f_λ as

$$\chi_{\lambda K} = f_\lambda\chi_{\lambda K}^{\rm HO},$$
(3.13)

for the isoscalar interactions with $\lambda=2$ and 3. These factors are determined by the theoretical and experimental requirements: As for the octupole interactions, we have the experimental Routhians for the lowest octupole vibrational state in SD ^{190}Hg [17]. We assume the common factor f_3 for all K values and fix it so as to reproduce these experimental data. In this case $f_3=1$ can nicely reproduce the experimental Routhians,[3] and we use the same value for ^{192}Hg and ^{194}Hg. For the quadrupole interactions, we determine it so as to reproduce the zero-frequency (Nambu-Goldstone) mode for $K=1$ at $\omega_{\rm rot}=0$ and use the same value for $K=0$ and 2. $f_2=1.007$, 1.005, and 1.005 are obtained for ^{190}Hg, ^{192}Hg, and ^{194}Hg, respectively, by using the adopted model space. The fact that these values of f_λ are close to unity indicates that the size of the adopted model space is large enough.

According to systematic RPA calculations for the low-frequency β, γ, and octupole states in medium-heavy deformed nuclei, we have found that the values of f_λ reproducing the experimental data are very close to unity for the Nambu-Goldstone mode, the γ and octupole vibrational states. On the other hand, those values are quite different from unity for the β vibrational states. This may be associated with the simplicity of the monopole pairing interaction.

---

[3] This value depends on the treatment of the pairing gaps at finite frequency. If we use constant pairing gaps against $\omega_{\rm rot}$, we get the best value $f_3=1.05$.
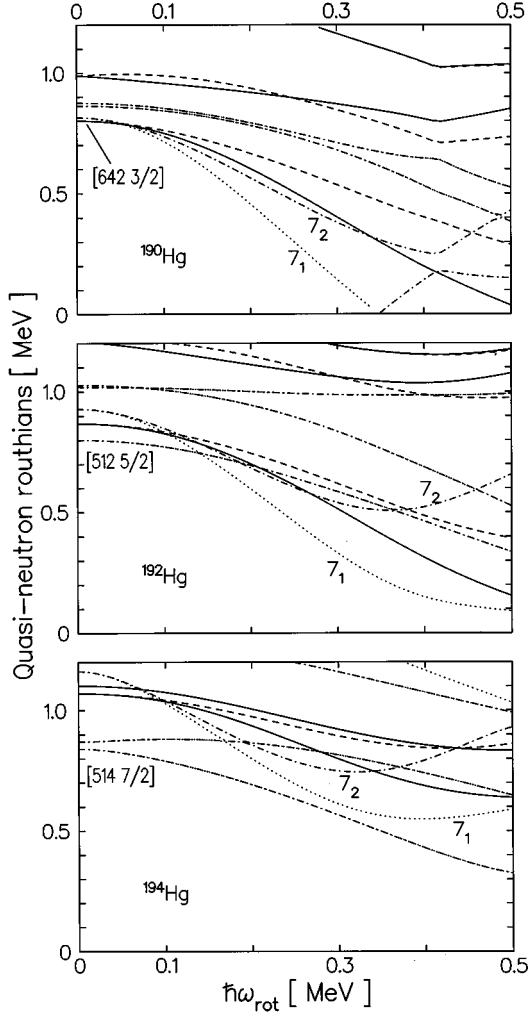
FIG. 3. Neutron quasiparticle Routhians in the Nilsson potential with h_{add} for SD ^{190,192,194}Hg. See text and caption to Fig. 2 for details.

Since we cannot find the realistic force strength χ_{20} for SD states, we do not discuss the property of the β vibrations in this paper.

IV. RESULTS OF NUMERICAL CALCULATIONS

A. Quasiparticle Routhians

In this section we present calculated quasiparticle Routhians in the improved cranked Nilsson potential and discuss their characteristic feature. In Fig. 3 we compare the neutron quasiparticle Routhians for ^{190,192,194}Hg. The proton Routhians of ^{190}Hg are shown above in Fig. 2 and are almost identical for ^{192}Hg and ^{194}Hg.

The calculations show the strong interaction strength between the $\pi([642\ 5/2])^2$ configuration (for simplicity we denote these orbits by $\pi 6_1$ and $\pi 6_2$ in the following) and the yrast configuration which may contribute to the smooth increase of the yrast $\mathscr{J}^{(2)}$ moments of inertia. On the other hand, the interaction of $\nu\ [761\ 3/2]$ orbits ($\nu 7_1$ and $\nu 7_2$ in the following) strongly depends on the chemical potential (neutron number): The interaction is strongest in ^{194}Hg, and weakest in ^{190}Hg. This is qualitatively consistent with the experimental observation of the yrast $\mathscr{J}^{(2)}$ moments of inertia and the experimental quasiparticle Routhians in ^{191,193}Hg [40,41].

The characteristic features of the high-N intruder orbits are similar to those of the Woods-Saxon potential, except the alignments of $\nu 7_1$ and $\nu 7_2$ orbits which are, respectively, $i \approx 3\hbar$ and $2\hbar$ in ours while $i \approx 4\hbar$ and $3\hbar$ in the Woods-Saxon potential. This results in the different crossing frequency between the ground band and the $\nu(j_{15/2})^2$ band, as discussed in Sec. III A. The observed crossing in ^{190}Hg and the quasiparticle Routhians in ^{191,193}Hg seem to favor our results. There are some other minor differences concerning the position of each orbit in the Nilsson and in the Woods-Saxon potential. However, these differences do not seriously affect our main conclusions because the collective RPA solutions are not sensitive to the details of each orbit.

B. Octupole vibrations

Here, we discuss the negative-parity excitations in SD ^{190,192,194}Hg. We have solved the RPA dispersion equation (2.23) and have obtained all low-lying solutions ($E'_x \lesssim 2$ MeV). The excitation energies and the $B(E3)$ values calculated at $\omega_{\text{rot}} = 0$ are listed in Table I. This result shows that $K = 2$ octupole states are the lowest for these Hg isotopes, which is consistent with our previous results [3,4]. The $B(E3;0^+ \rightarrow 3^-,K)$ are calculated by using the strong coupling scheme [30] neglecting effects of the Coriolis force. Absolute values of $B(E3)$'s cannot be taken seriously because they depend on the adopted model space and are very sensitive to the octupole coupling strengths χ_{3K}: For instance, if we use $f_3 = 1.05$ instead of $f_3 = 1$ in Eq. (3.13), the $B(E3)$ increase by about factor of 2 while the reduction of their excitation energy is about 15%. In addition, the effects of the Coriolis coupling tend to concentrate the $B(E3)$ strengths onto the lowest octupole states [20].

At $\omega_{\text{rot}} = 0$, the lowest $K = 2$ octupole states exhibit almost identical properties in ^{190,192,194}Hg. However, they show different behavior as functions of ω_{rot} as shown in Figs. 4, 5, and 6, respectively. All RPA solutions, including noncollective solutions as well as collective vibrational ones, are presented in these figures. The size of the circle on the plot indicates the magnitude of the $E3$ transition amplitudes be-

TABLE I. Calculated excitation energies of octupole vibrations and $B(E3;0^+ \rightarrow 3^-,K)$ values estimated using the strong coupling scheme for SD ^{190,192,194}Hg.

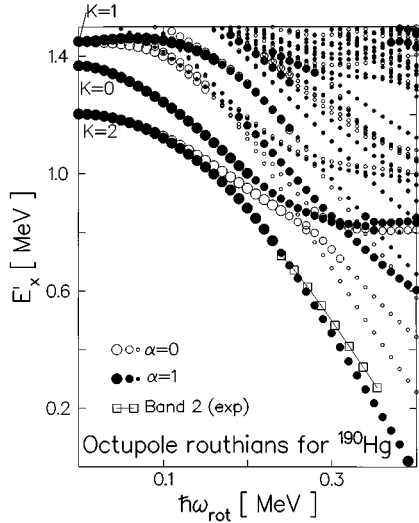| | ^{190}Hg | | | | ^{192}Hg | | | | ^{194}Hg | | | |
	$K=0$	$K=1$	$K=2$	$K=3$	$K=0$	$K=1$	$K=2$	$K=3$	$K=0$	$K=1$	$K=2$	$K=3$
E [MeV]	1.37	1.45	1.20	1.52	1.55	1.58	1.18	1.53	1.83	1.62	1.14	1.53
$B(E3)/B(E3)_{\text{s.p.}}$	6.6	11.9	10.0	1.0	7.6	10.1	10.1	0.8	11.5	11.2	10.2	0.7

FIG. 4. Calculated RPA eigenenergies of negative-parity states for SD ^{190}Hg, plotted as functions of rotational frequency. Open (solid) circles indicate states with signature $\alpha=0$ ($\alpha=1$). Large, medium, and small circles indicate RPA solutions with $E3$ transition amplitudes $(\Sigma_K |\langle n|Q^e_{3K}|\omega_{rot}\rangle|^2)^{1/2}$ larger than $200e$ fm^3, larger than $100e$ fm^3, and less than $100e$ fm^3, respectively. Note that Routhians for the yrast SD band correspond to the horizontal axis ($E'_x=0$). The observed Routhians for band 2 [17] are shown by open squares.

tween a RPA solution and the yrast state.

The $(K,\alpha)=(2,1)$ octupole state in ^{190}Hg has significant Coriolis mixing and the octupole phonon is aligned along the rotational axis at higher frequency. This is caused by the relatively close energy spacing between the $K=2$ and the $K=0,1$ octupole states in this nucleus. These low-K members of the octupole multiplet are calculated to lie much higher in ^{192}Hg and ^{194}Hg, which reduces the Coriolis mixing in these nuclei. As a result of these phonon alignments, the experimental Routhians for band 2 in ^{190}Hg are nicely reproduced by the lowest $\alpha=1$ octupole state. It should be emphasized that although the excitation energy at one frequency point can be obtained by adjusting the octupole-force
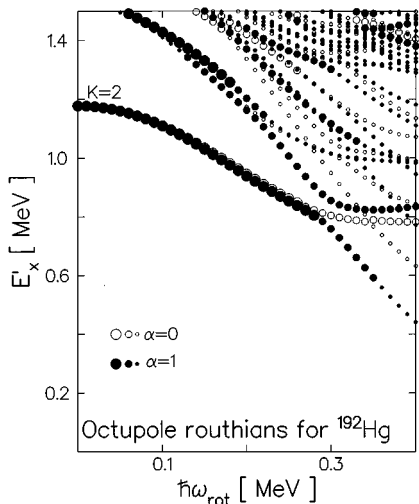

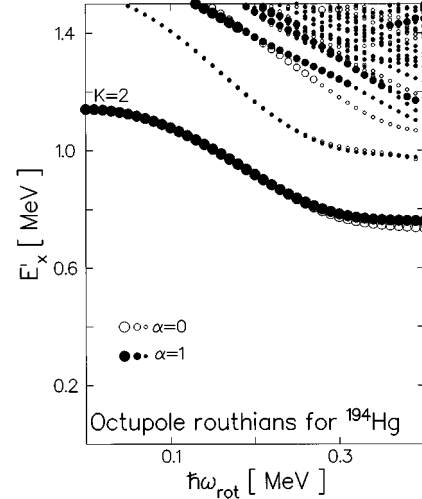FIG. 5. The same as Fig. 4, but for ^{192}Hg.

FIG. 6. The same as Fig. 4, but for ^{194}Hg.

strengths, the agreement over the whole frequency region is not trivial.

Since there is no $K=0$ octupole state in the signature $\alpha=0$ sector, the Coriolis mixing is much weaker for the lowest $(K,\alpha)=(2,0)$ octupole state. The calculation predicts that this state is crossed by the negative-parity two-quasiparticle band $\nu(7_1\otimes[642\ 3/2])_{\alpha=0}$ at $\hbar\omega_{rot}\approx0.27$ MeV.

In ^{192}Hg, the same kind of crossing is seen for both signature partners of the $K=2$ octupole bands. We can clearly see, for the lowest excited state in each signature sector, the transition of the internal structure from collective octupole states (large circles in Fig. 5) to noncollective two-quasineutron states (small circles). The two-quasineutron configurations which cross the octupole vibrational bands are $7_1\otimes[642\ 3/2](\alpha=-1/2)$ for $\alpha=1$ and $7_1\otimes[642\ 3/2](\alpha=1/2)$ for $\alpha=0$. The crossing frequency is lower for the $\alpha=1$ band due to signature splitting of the $\nu[642\ 3/2]$ orbits.

In contrast to ^{190,192}Hg, the $K=2$ octupole bands in ^{194}Hg indicate neither the signature splitting nor the crossings. The Routhians are very smooth up to the highest frequency. This is because the neutron orbits 7_1 and 7_2 have a "hole" character and their interaction strengths with the negative-energy orbits become larger with increasing neutron numbers (see Fig. 3). Therefore these orbits go to higher energy and the energies of the two-quasiparticle bands $\nu(7_1\otimes[642\ 3/2])$ never become lower than the $K=2$ octupole bands even at the highest frequency.

These properties of the $K=2$ octupole vibrations come from the effects of the Coriolis force and from the chemical-potential dependence of the aligned two-quasiparticle bands. In order to reproduce these rich properties of the collective vibrations at finite frequency, a microscopic model, which can describe the interplay between the Coriolis force and the correlations of shape fluctuations, is needed.

C. γ vibrations

In this section we present results for the γ-vibrational states built on the SD yrast band. As mentioned in Sec. III B, we do not discuss the property of the β band since it is

TABLE II. Calculated excitation energies of γ vibrations and $B(E2;0^+\rightarrow 2^+,K=2)$ values estimated using the strong coupling scheme for SD ^{190,192,194}Hg.

	^{190}Hg	^{192}Hg	^{194}Hg
E [MeV]	1.39	1.50	1.45
$B(E2)/B(E2)_{\text{s.p.}}$	2.7	3.0	3.8

difficult to determine a reliable value of the coupling strength χ_{20} for the $K=0$ channel of the quadrupole interaction.

The properties of γ bands at $\omega_{\text{rot}}=0$ are listed in Table II. The excitation energies of γ vibrations are predicted to be higher than the $K=2$ octupole vibrations by 200–350 keV. It is known that calculations using the full model space considerably overestimate the $B(E2)$ values. In Ref. [28], it has been shown that the three-N_{osc}-shell calculation reproduces the experimental values very well. If we use the model space $N_{\text{osc}}=5-7$ (4–6) for neutrons (protons), then the $B(E2)$ values in the table decrease by about factor of 1/3. The collectivity of the γ vibrations turns out to be very weak in these SD nuclei.

Figures 7, 8, and 9 illustrate the excitation energy of γ vibrations as functions of the rotational frequency for ^{190}Hg, ^{192}Hg, and ^{194}Hg, respectively. The unperturbed two-quasiparticle Routhians are also depicted by solid (neutrons) and dashed (protons) lines. Since the K quantum number is not a conserved quantity at finite rotational frequency, we have defined the solutions with the large $K=2$ $E2$ transition amplitude as the γ vibrations. As seen in the figure, they lose
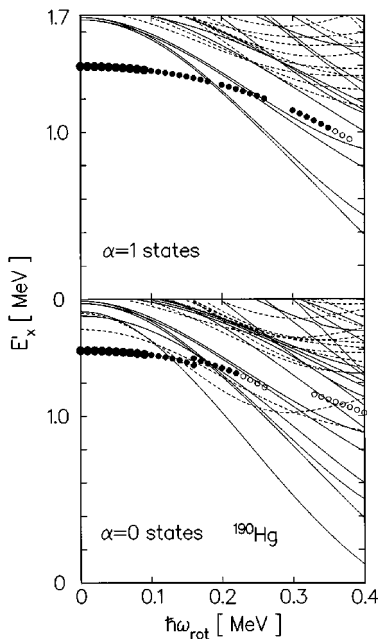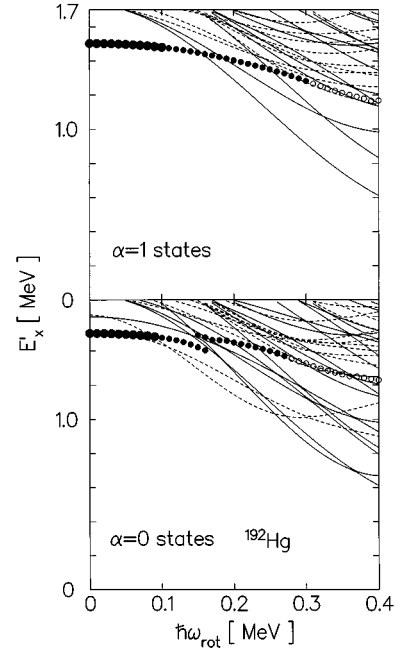

FIG. 8. The same as Fig. 7, but for ^{192}Hg.

their vibrational character by successive crossings with many two-quasiparticle bands and become the dominant two-quasiparticle states at high frequency. The reduction of collectivity is more rapid for the $\alpha=0$ γ vibrations, because the two-quasiparticle states come down more quickly in the $\alpha=0$ sector. Similar crossings occur for the $K=2$ octupole bands in ^{192}Hg (see Fig. 5); however, the crossing frequency is much higher than that of the γ bands. This is because the excitation energies of the octupole bands are relatively lower than those of the γ bands. The predicted properties of γ vibrations are different from those in Ref. [42].

In the frequency region ($0.15\leq\hbar\omega_{\text{rot}}\leq0.4$ MeV) where the excited SD bands are observed in experiments, the γ

FIG. 7. Calculated RPA eigenenergies for γ vibrational states for SD ^{190}Hg, plotted as functions of rotational frequency. The lower part is for the signature $\alpha=0$ Routhians and the upper for the $\alpha=1$. Large solid, small solid, and small open circles indicate the γ vibrational states whose $K=2$ $E2$ amplitudes $|\langle n|Q^e_{22}|\omega_{\text{rot}}\rangle|$ are larger than $20e$ fm^2, larger than $10e$ fm^2, and less than $10e$ fm^2, respectively. The unperturbed two-quasineutron (two-quasiproton) Routhians are also shown by solid (dashed) lines.
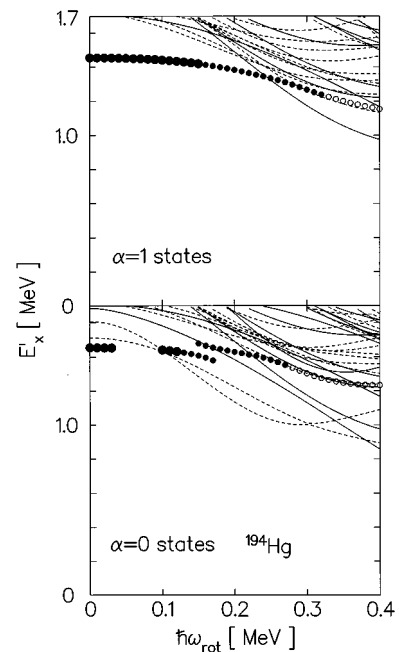

FIG. 9. The same as Fig. 7, but for ^{194}Hg.

TABLE III. The lowest and the second lowest configurations at $\hbar\omega_{\rm rot}=0.4$ MeV in each parity sector. The proposed assignments of the observed excited SD bands are also shown. The excitation energies of the negative-parity two-quasineutron states, 256 keV for ^{190}Hg and 441 and 632 keV for ^{192}Hg, contain very weak octupole correlations. The corresponding unperturbed two-quasineutron energies are 261, 460, and 635 keV, respectively.

		$\pi=+$		$\pi=-$	
		Lowest	Second	Lowest	Second
^{190}Hg	E_x' [keV]	113	389	≈ 0	256
	Config.	$\nu(7_1\otimes 7_2)_{\alpha=0}$	$\nu(7_1\otimes[505\ 11/2])_{\alpha=0,1}$	(oct. vib.)$_{\alpha=1}$	$\nu(7_1\otimes[642\ 3/2])_{\alpha=0}$
	Expt.	Band 3		Band 2	Band 4
^{192}Hg	E_x' [keV]	611	611	441	632
	Config.	$\nu(7_1\otimes[512\ 5/2])_{\alpha=1}$	$\nu(7_1\otimes[512\ 5/2])_{\alpha=0}$	$\nu(7_1\otimes[642\ 3/2])_{\alpha=1}$	$\nu(7_1\otimes[642\ 3/2])_{\alpha=0}$
	Expt.			Band 2	Band 3
^{194}Hg	E_x' [keV]	857	892	738	759
	Config.	$\nu([514\ 7/2])^2_{\alpha=0}$	$\pi([530\ 1/2])^2_{\alpha=0}$	(oct. vib.)$_{\alpha=0}$	(oct. vib.)$_{\alpha=1}$
	Expt.			Band 2	Band 3

bands are predicted to be higher than both the $K=2$ octupole bands and the lowest two-quasiparticle states. Therefore experimental observation of the γ vibrations is expected to be more difficult than that of the octupole bands.

V. COMPARISON WITH EXPERIMENTAL DATA

In this section, we compare the results obtained in the previous section with the available experimental data for the excited SD bands in ^{190,192,194}Hg. The Routhians relative to the yrast SD band have been observed only for band 2 in ^{190}Hg and the comparison with our calculated Routhians has been done in the Sec. IV B. The excitation energies of the other bands are not known. Therefore, in order to compare our theory with experimental data, we have calculated the dynamic moments of inertia, $\mathscr{J}^{(2)}$.

It is known that the effects of $N_{\rm osc}$ mixing, pairing fluctuations, and higher-multipole pairing are important in reproducing absolute magnitude of the moments of inertia. On the other hand, our model aims at describing relative quantities (excitation energy, alignment, etc.) between the excited and yrast bands. Thus, instead of directly calculating $\mathscr{J}^{(2)}$ in terms of Eq. (2.10), we decompose the $\mathscr{J}^{(2)}$ of the excited bands as

$$\mathscr{J}^{(2)}(\omega)=\mathscr{J}_0^{(2)}(\omega)+\frac{di}{d\omega}=\mathscr{J}_0^{(2)}(\omega)-\frac{d^2E_x'}{d\omega^2}, \quad (5.1)$$

where $\mathscr{J}_0^{(2)}$ denotes the dynamic moments of inertia for the yrast SD bands (RPA vacuum), and i and E_x' are the calculated alignments and Routhians relative to the yrast band, respectively. The $\mathscr{J}_0^{(2)}$ values of the yrast SD bands are taken from the experiments and approximated by the Harris expansion,

$$\mathscr{J}_0^{(2)}(\omega)=J_0+3J_1\omega^2+5J_2\omega^4. \quad (5.2)$$

The expression (5.1) phenomenologically takes account of the effects mentioned above. Those effects are included in the experimental $\mathscr{J}_0^{(2)}$ of Eq. (5.2).

The lower the excitation energy of an excited band relative to the yrast SD band, the more strongly will it be populated. In experiments, the SD bands are populated at high frequency; thus, it is the excitation energy in the feeding region at high frequency that is relevant in this problem. We list in Table III the calculated excitation energies of the low-lying positive- and negative-parity states at $\hbar\omega_{\rm rot}=0.4$ MeV.

In ^{190}Hg three excited SD bands (bands 2, 3, and 4) have been observed [16–18]. Band 2 has been assigned as the lowest octupole band [16,17] because of its strong decays into the yrast SD band. According to our calculations, in addition to this octupole band ($\alpha=1$), the aligned two-quasineutron bands come down at high frequency. We assign band 4 at high frequency as the $\nu(7_1\otimes[642\ 3/2])_{\alpha=0}$ because this negative-parity two-quasineutron state is crossed by the $\alpha=0$ octupole band at $\hbar\omega_{\rm rot}\approx0.26$ MeV which may correspond to the observed sharp rise of $\mathscr{J}^{(2)}$ at $\hbar\omega_{\rm rot}\approx0.23$ MeV (Fig. 4). The positive-parity $\nu(7_1\otimes7_2)_{\alpha=0}$ state is also relatively low lying at high frequency. Since this band does not show any crossing at $\hbar\omega_{\rm rot}>0.12$ MeV in the calculations, this may be a good candidate for band 3 (Fig. 7).

In ^{192}Hg, two excited SD bands (bands 2 and 3) have been observed [22] and both bands exhibit a bump in $\mathscr{J}^{(2)}$ at $\hbar\omega_{\rm rot}\approx0.3$ MeV (band 2) and 0.33 MeV (band 3). We assume these bands correspond to $\nu(7_1\otimes[642\ 3/2])_{\alpha=0,1}$ at high frequency. This two-quasineutron configuration for band 2 is the same as that suggested in Ref. [22]. However, our theory predicts a different scenario at low spin: This band is crossed by the octupole band ($\alpha=1$) at $\hbar\omega_{\rm rot}\approx0.3$ MeV. Thus, band 2 is interpreted as an $\alpha=1$ octupole vibrational band in the low-frequency region ($\hbar\omega_{\rm rot}<0.3$ MeV). In the same way, the bump in $\mathscr{J}^{(2)}$ in band 3 is interpreted as a crossing between $\nu(7_1\otimes[642\ 3/2])_{\alpha=0}$ and the $\alpha=0$ octupole vibrational band (Fig. 5).

For high frequencies, the positive-parity $\nu(7_1\otimes[512\ 5/2])$ state is calculated to lie almost at the same energy as the lowest $\alpha=0$ negative-parity state. However, no crossing is predicted for the $\alpha=1$ state at
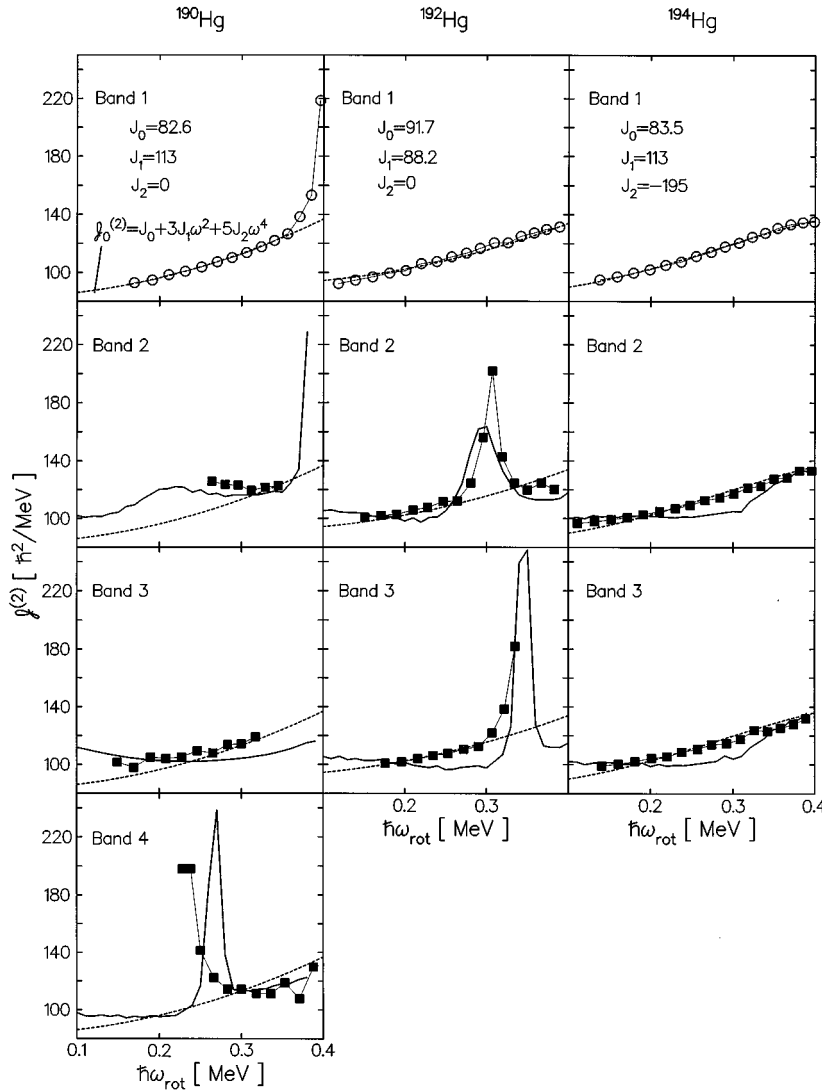
FIG. 10. Calculated (solid lines) and experimental (symbols) dynamic moments of inertia for excited SD bands in ^{190}Hg (left), ^{192}Hg (middle), and ^{194}Hg (right). $\mathcal{J}^{(2)}$ for the yrast SD bands are also displayed at the top. Dotted lines indicate the yrast $\mathcal{J}^{(2)}$, which are approximated by the Harris formula (5.2). The parameters J_0, J_1, and J_2 used in the formula are shown in units of $\hbar^2$ MeV^{-1}, $\hbar^4$ MeV^{-3}, and $\hbar^6$ MeV^{-5}, respectively.

$\hbar\omega_{\rm rot} > 0.15$ MeV but many crossings are predicted for the $\alpha = 0$ state (Fig. 8). Both properties are incompatible with the observed features.

In ^{194}Hg, two excited SD bands (bands 2 and 3) have been observed [23,24]. In contrast to ^{192}Hg, the observed dynamic moments of inertia, $\mathcal{J}^{(2)}$, do not show any singular behavior and are more or less similar to those of the yrast band. Bands 2 and 3 have been interpreted as signature partners because the γ-ray energies of band 3 are observed to lie midway between those of band 2 and furthermore the bands have similar intensity [23]. From these observations and the excitation energies listed in Table III, we assume that both bands correspond to $K = 2$ octupole vibrations ($\alpha = 0$, 1), which are calculated to be the lowest excited states (Fig. 6). Any other assignment faces serious difficulties: (i) The positive-parity two-quasiparticle configurations listed in Table III have no signature partners. (ii) The other low-lying two-quasiparticle states occupy $\nu 7_1$ or $\pi 6_1$ orbits. Now the increase in $\mathcal{J}^{(2)}$ for the yrast SD band is partially attributed to the alignment of these high-j intruder orbits and, since the blocking effect of the quasiparticles prevents any alignment due to band crossings involving these orbits, the lack of alignment should produce an $\mathcal{J}^{(2)}$ curve quite different from

those of the yrast SD band. (iii) The configuration $\nu([512\ 5/2]\otimes[624\ 9/2])$ suggested in Ref. [23] has a problem with its magnetic property, which has been recently pointed out in Ref. [43]. If this configuration is the $K^\pi = 7^-$, then strong $M1$ transitions between the signature partners should have been observed. The energy of the $K^\pi = 2^-$ configuration is certainly lowered by octupole correlations. In our calculations, however, this configuration accounts for only 20% of all components constituting the octupole vibration (iv). The γ vibrations are calculated to be much higher and crossed by several two-quasiparticle bands (Fig. 9). Therefore, we believe the octupole vibration is the best candidate.[4]

Assuming the above configurations, the dynamic moments of inertia, $\mathcal{J}^{(2)}$, are calculated with Eq. (5.1), and compared with the experimental data (Fig. 10). In ^{190}Hg, the characteristic features are well reproduced for bands 2 and 4; the constant $\mathcal{J}^{(2)}$ of band 2 (the $\alpha = 1$ octupole vibration) and the bump of band 4 (the crossing between the $\alpha = 0$

---

[4]The signature for bands 2 and 3 is determined by following the spin assignment in Ref. [23].

octupole vibration and the aligned two-quasineutron band) are reproduced although the crossing frequency is smaller in the experiment. For band 3, the high $\mathscr{J}^{(2)}$ values at low spin are well accounted for by the alignment gain of the two-quasineutron state. However, the calculation predicts the lack of alignment due to the blocking of $N=7$ orbits at $\hbar\omega_{rot}>0.25$ MeV, which makes the $\mathscr{J}^{(2)}$ smaller than those of the yrast band.

In ^{192}Hg, the bumps of $\mathscr{J}^{(2)}$ are nicely reproduced in the calculations, which correspond to the crossings between $K=2$ octupole vibrations and the aligned two-quasineutron bands in each signature partner. The alignment gain Δi before and after crossing for band 2 is $\Delta i \approx 2\hbar$ which is comparable to the experimental value $\Delta i_{expt} \approx 2.6\hbar$ [22].

The agreement is less satisfactory in ^{194}Hg. The calculated $\mathscr{J}^{(2)}$ are lower than the experimental data for $0.2 \lesssim \hbar\omega_{rot} \lesssim 0.35$ MeV (similar disagreement can be seen for band 3 in ^{192}Hg). This effect comes from the blocking effect mentioned above, associated with the $\nu 7_1$, $\nu 7_2$, $\pi 6_1$, and $\pi 6_2$ orbits. In the RPA (Tamm-Dancoff) theory (neglecting the backward amplitudes), the octupole vibrations are described by superposition of two-quasiparticle excitations,

$$|\text{oct vib}\rangle = \sum_{\gamma\delta} \psi(\gamma\delta)|\gamma\delta\rangle, \qquad (5.3)$$

where $|\gamma\delta\rangle = a_\gamma^\dagger a_\delta^\dagger |\omega_{rot}\rangle$. Some of these components $|\gamma\delta\rangle$ associated with the particular orbits ($\nu 7_1$, $\nu 7_2$, $\pi 6_1$, and $\pi 6_2$) show significant lack of alignment. However, if the octupole vibrations are collective enough, the amplitudes $\psi(\gamma\delta)$ are distributed over many two-quasiparticle excitations $|\gamma\delta\rangle$. Thus, each amplitude becomes small and blocking effects may be canceled.

In order to demonstrate this ''smearing'' effect of collective states, we use a slightly stronger octupole force, $f_3=1.05$ in Eq. (3.13), and carry out the same calculations for ^{194}Hg. The results are shown in Fig. 11. The higher coupling strengths make the octupole vibrations more collective and the experimental data are better reproduced. Perhaps the
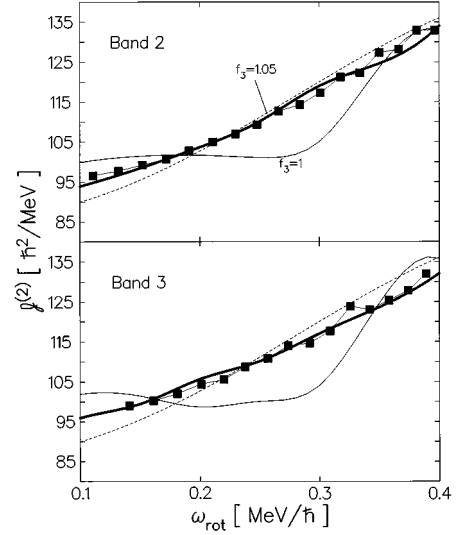

FIG. 11. Calculated (solid lines) and experimental (symbols) dynamic moments of inertia for excited SD bands in ^{194}Hg. Thin solid lines are the same as in Fig. 10, while thick lines indicate the results obtained by using the slightly stronger coupling strengths ($f_3=1.05$) for the octupole interactions. Dotted lines indicate the $\mathscr{J}^{(2)}$ for the yrast SD band (see caption to Fig. 10).

collectivity of these octupole vibrations was underestimated in the calculations with $f_3=1$.

Finally we should mention the decays from the octupole bands to the yrast SD band. We have assigned all observed excited SD bands (except band 3 in ^{190}Hg) as octupole vibrational bands (at least in the low-spin region). However, strong dipole decays into the yrast band have been observed only for band 2 in ^{190}Hg. Although this seems to contradict our proposals, in fact our calculations provide us with a qualitative answer.

Let us discuss the relative $B(E1;\text{oct}\rightarrow\text{yrast})$ values. Using the $E1$ recoil charge ($-Ze/A$ for neutrons and Ne/A for protons), then the $B(E1)$ values at $\hbar\omega_{rot}=0.25$ MeV are calculated to be small for all the $K=2$ octupole bands except

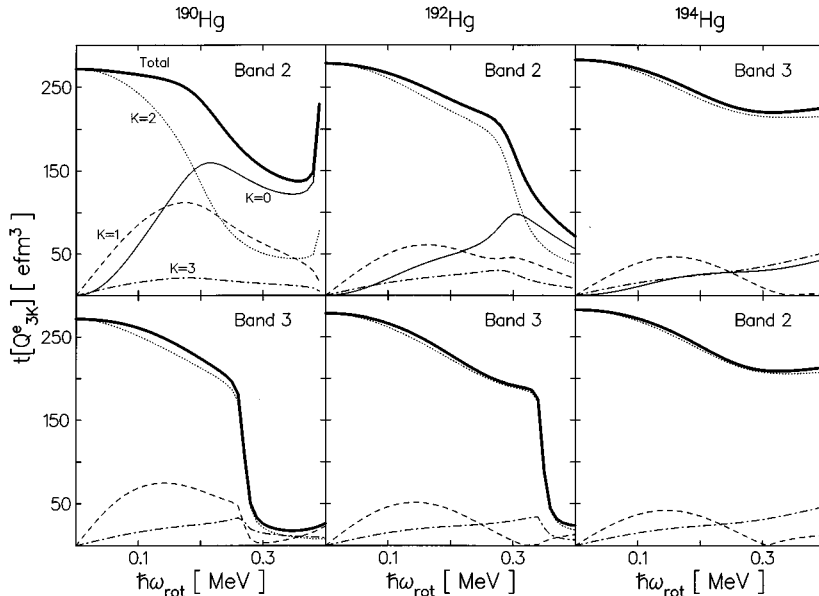FIG. 12. Electric $E3$ transition amplitudes, $|t[1/2(1+\tau_3)Q_{3K}^\alpha]| = |\langle\omega_{rot}|Q_{3K}^e|n\rangle|$, for the lowest RPA solutions with the signature $\alpha=0$ (lower) and the $\alpha=1$ (upper) for ^{190}Hg (left), ^{192}Hg (middle), and ^{194}Hg (right). $K=0$, 1, 2, and 3 components are denoted by solid, dashed, dotted, and dash-dotted lines, respectively. Total values (thick solid lines) are defined by $(\Sigma_K|\langle\omega_{rot}|Q_{3K}^e|n\rangle|^2)^{1/2}$.

for the $\alpha=1$ (band 2) in ^{190}Hg: With the scaling factors $f_3=1\sim1.08$ in Eq. (3.13), the calculation suggests $B(E1)\approx10^{-7}$ Weisskopf units (W.u.) for the $(K,\alpha)=(2,0)$ octupole bands, and $B(E1)\approx10^{-8}$–10^{-6} W.u. for the $(K,\alpha)=(2,1)$ bands. The $B(E1)$ for band 2 in ^{190}Hg is predicted to be larger than these values by one to two orders of magnitude, $B(E1)\approx10^{-6}$–10^{-4} W.u. Although the absolute values are very sensitive to the parameters used in the calculation, the $E1$ strengths of band 2 in ^{190}Hg are always much larger than those for the other bands.

To clarify the reason for this $E1$ enhancement in this particular band, we display the $E3$ amplitudes ($K=0$, 1, 2, and 3) of these octupole states as functions of frequency in Fig. 12. As mentioned in Sec. IV B, the Coriolis mixing is completely different between band 2 in ^{190}Hg and the others: The former has significant Coriolis mixing at finite frequency while the latter retains the dominant $K=2$ character up to very high spin. Since the $K=2$ octupole components cannot carry any $E1$ strength, the strong $E1$ transition amplitudes come from Coriolis coupling, namely, the mixing of the $K=0$ and 1 octupole components. Therefore, the observed decay property does not contradict our interpretation.

VI. CONCLUSIONS

The microscopic structure of the γ and the octupole vibrations built on the SD yrast bands in ^{190,192,194}Hg were investigated with the RPA based on the cranked shell model. The $K=2$ octupole vibrations are predicted to lie lowest. To reproduce the characteristic features of the experimental data it was essential to include octupole correlations and the effect of rapid rotation explicitly. From the calculations, we assigned the following configurations to the observed excited bands:

^{190}Hg Band 2: The rotationally aligned $\alpha=1$ octupole vibration.

  Band 3: the two-quasineutron band $\nu(7_1\otimes7_2)$.

  Band 4: the $(K,\alpha)=(2,0)$ octupole vibration at low spin, the two-quasineutron band $\nu(7_1\otimes[642\ 3/2])_{\alpha=0}$ at high spin.

^{192}Hg Band 2: the $(K,\alpha)=(2,1)$ octupole vibration at low spin, the two-quasineutron band $\nu(7_1\otimes[642\ 3/2])_{\alpha=1}$ at high spin.

  Band 3: the $(K,\alpha)=(2,0)$ octupole vibration at low spin, the two-quasineutron band $\nu(7_1\otimes[642\ 3/2])_{\alpha=0}$ at high spin.

^{194}Hg Band 2: the $(K,\alpha)=(2,0)$ octupole vibration.

  Band 3: the $(K,\alpha)=(2,1)$ octupole vibration.

With these assignments, most of the experimentally observed features were well accounted for in our theoretical calculations.

The Coriolis force makes the lowest octupole state in ^{190}Hg align along the rotational axis, while this effect is predicted to be very weak for other octupole states. This is due to the relatively low excitation energy of the $K=0$ ($\alpha=1$) octupole state in ^{190}Hg, in which the close spacing in energy of the octupole multiplet makes the Coriolis mixing easier. This aligned octupole phonon in ^{190}Hg reproduces the observed behavior for band 2.

Our interpretation for the excited SD bands in ^{192}Hg solves a puzzle mentioned in Ref. [22] in which band 2 was assigned as the two-quasineutron excitation $\nu(7_3\otimes[642\ 3/2])$. The bump in the $\mathscr{J}^{(2)}$ curve was considered to be associated with a crossing between the $\nu7_1$ and $\nu[512\ 5/2]$ orbits. According to this assignment, we expect similar properties for the observed crossing in ^{192}Hg and ^{193}Hg, and the difference of crossing frequencies and alignment gains was a puzzle. This is no longer a puzzle in our interpretation because the microscopic structure of band 2 is the octupole vibration (before the crossing). Because of the correlation-energy gains, the excitation energies of the octupole vibrations should be lower than the unperturbed two-quasiparticle states. Therefore it is natural that the observed crossing frequency is larger than the one predicted by the quasiparticle Routhians without the octupole correlations.

Our interpretation also solves some difficulties in ^{194}Hg: The smooth $\mathscr{J}^{(2)}$ behavior of bands 2 and 3 can be explained by the ''smearing'' effect of the collective states. The nonobservation of the expected strong $M1$ transitions between bands 2 and 3 [43] is solved by substituting the $K=2$ octupole vibrations for the two-quasineutron states $\nu([512\ 5/2]\otimes[624\ 9/2])$, because the octupole correlations lower the $K=2$ configurations and the summation of many two-quasiparticle ($M1$) matrix elements may be destructive [see discussion below Eq. (2.26)].

Enhanced $E1$ transitions from the octupole states to the yrast SD band are expected only for band 2 in ^{190}Hg. This comes about because the other octupole states do not have strong Coriolis mixing and keep their $K=2$ character even at high frequency. This agrees with experimental observations.

Although most of the observed properties are explained by our calculations, there remain some unsolved problems in ^{190}Hg and ^{192}Hg. For ^{190}Hg, according to the calculations with constant pairing gaps reported in Ref. [19], it is suggested that band 4 may correspond to the $(K,\alpha)=(1,0)$ octupole band which is predicted to be crossed by the two-quasineutron band $\nu(7_1\otimes[642\ 3/2])_{\alpha=0}$ at $\hbar\omega_{\rm rot}\approx0.21$ MeV. Because of the phenomenological treatment for the pairing gaps at finite frequency, it is difficult to deny this possibility. The experimental intensity of band 3 raises another ambiguity: Since it is much weaker than bands 2 and 4, it might be associated with a higher-lying configurations [18]. For ^{192}Hg, our calculations predict no signature splitting for the lowest octupole bands at $\hbar\omega_{\rm rot}\lesssim0.25$ MeV. Therefore one may expect γ-ray energies typical of the signature-partner pair for bands 2 and 3 similar to that in ^{194}Hg, which is different from what is observed [22]. Improvement of the pairing interactions (fluctuations, quadrupole pairing) might solve these problems as well as enable us to perform reliable RPA calculations for β vibrations.

Theoretical study of octupole vibrations carrying large $E1$ strengths would be of great interest, because this could offer direct experimental evidence. An improved version of

calculations for $E1$ strengths of high-spin octupole bands is in progress, taking into account the restoration of translational and Galilean invariance. The $K=0$ octupole vibration in ^{152}Dy has been predicted in Ref. [5] and its decay into the yrast band has been suggested [14]. Strong $E1$ transition probabilities have been suggested by Skalski [44] for $K=0$ octupole states in the $A=190$ region. Therefore, the search for low-lying low-K octupole vibrations is an important subject for the future.

[1] S. Mizutori, Y.R. Shimizu, and K. Matsuyanagi, Prog. Theor. Phys. **83**, 666 (1990); **85**, 559 (1991); **86**, 131 (1991).

[2] T. Nakatsukasa, S. Mizutori, and K. Matsuyanagi, Prog. Theor. Phys. **87**, 607 (1992).

[3] T. Nakatsukasa, S. Mizutori, and K. Matsuyanagi, Prog. Theor. Phys. **89**, 847 (1993).

[4] S. Mizutori, T. Nakatsukasa, K. Arita, Y.R. Shimizu, and K. Matsuyanagi, Nucl. Phys. **A557**, 125c (1993).

[5] T. Nakatsukasa, K. Matsuyanagi, S. Mizutori, and W. Nazarewicz, Phys. Lett. B **343**, 19 (1995).

[6] J. Dudek, T.R. Werner, and Z. Szymański, Phys. Lett. B **248**, 235 (1990).

[7] S. Åberg, Nucl. Phys. **A520**, 35c (1990).

[8] J. Höller and S. Åberg, Z. Phys. A **336**, 363 (1990).

[9] P. Bonche, S.J. Krieger, M.S. Weiss, J. Dobaczewski, H. Flocard, and P.-H. Heenen, Phys. Rev. Lett. **66**, 876 (1991).

[10] Xunjun Li, J. Dudek, and P. Romain, Phys. Lett. B **271**, 281 (1991).

[11] W. Nazarewicz and J. Dobaczewski, Phys. Rev. Lett. **68**, 154 (1992).

[12] J. Skalski, Phys. Lett. B **274**, 1 (1992).

[13] J. Skalski, P.-H. Heenen, P. Bonche, H. Flocard, and J. Meyer, Nucl. Phys. **A551**, 109 (1993).

[14] P.J. Dagnall et al., Phys. Lett. B **335**, 313 (1995).

[15] D.M. Cullen et al., Phys. Rev. Lett. **65**, 1547 (1990).

[16] B. Crowell et al., Phys. Lett. B **333**, 320 (1994).

[17] B. Crowell et al., Phys. Rev. C **51**, R1599 (1995).

[18] A.N. Wilson et al., in *Low Energy Nuclear Dynamics (LEND'95)*, Proceedings of European Physical Society XV Nuclear Physics Divisional Conference, St Petersburg, Russia, 1995 (World Scientific, Singapore, 1995), p. 545.

[19] T. Nakatsukasa, Act. Phys. Pol. B **27**, 59 (1996).

[20] K. Neergård and P. Vogel, Nucl. Phys. **A145**, 33 (1970); **A149**, 209 (1970); **A149**, 217 (1970).

[21] P. Vogel, Phys. Lett. **66B**, 431 (1976).

[22] P. Fallon et al., Phys. Rev. C **51**, R1609 (1995).

[23] M.A. Riley et al., Nucl. Phys. **A512**, 178 (1990).

[24] B. Cederwall et al., Phys. Rev. Lett. **72**, 3150 (1995).

[25] E.R. Marshalek, Phys. Rev. C **11**, 1426 (1975); Nucl. Phys. **A266**, 317 (1976).

[26] J.L. Egido, H.J. Mang, and P. Ring, Nucl. Phys. **A339**, 390 (1980).

[27] Y.R. Shimizu and K. Matsuyanagi, Prog. Theor. Phys. **79**, 144 (1983); **72**, 799 (1984).

[28] Y.R. Shimizu and K. Matsuzaki, Nucl. Phys. **A588**, 559 (1995).

[29] I.M. Robledo, J.L. Egido, and P. Ring, Nucl. Phys. **A449**, 201 (1986).

[30] A. Bohr and B.R. Mottelson, *Nuclear Structure* (Benjamin, New York, 1975), Vol. 2.

[31] S. Kinouchi, Ph.D. thesis, University of Tsukuba, 1988.

[32] Y.R. Shimizu, E. Vigezzi, and R.A. Broglia, Nucl. Phys. **A509**, 80 (1990).

[33] H. Sakamoto and T. Kishimoto, Nucl. Phys. **A501**, 205 (1989).

[34] T. Bengtsson and I. Ragnarsson, Nucl. Phys. **A436**, 14 (1985).

[35] M. Baranger and K. Kumar, Nucl. Phys. **A110**, 490 (1968).

[36] M. Brack, J. Damgaard, A.S. Jensen, H.C. Pauli, V.M. Strutinsky, and C.Y. Wong, Rev. Mod. Phys. **44**, 320 (1972).

[37] R. Wyss, W. Satula, W. Nazarewicz, and A. Johnson, Nucl. Phys. **A511**, 324 (1990).

[38] M.W. Drigert et al., Nucl. Phys. **A530**, 452 (1991).

[39] H. Sakamoto, Nucl. Phys. **A557**, 583c (1993).

[40] M.J. Joyce et al., Phys. Lett. B **340**, 150 (1994).

[41] M.P. Carpenter et al., Phys. Rev. C **51**, 2400 (1995).

[42] M. Girod, J.P. Delaroche, J. Libert, and I. Deloncle, Phys. Rev. C **45**, R1420 (1992).

[43] P.B. Semmes, I. Ragnarsson, and S. Åberg, Phys. Lett. B **345**, 185 (1995).

[44] J. Skalski, Phys. Rev. C **49**, 2011 (1994).

Periodic-Orbit Bifurcation and Shell Structure in Reflection-Asymmetric Deformed Cavity

Ayumu SUGITA, Ken-ichiro ARITA* and Kenichi MATSUYANAGI

Department of Physics, Graduate School of Science, Kyoto University
Kyoto 606-8502, Japan
*Department of Physics, Nagoya Institute of Technology, Nagoya 466-8555, Japan

Shell structure of the single-particle spectrum for a reflection-asymmetric deformed cavity is investigated. Clear shell structure emerges for certain combinations of quadrupole and octupole deformations. Semiclassical periodic-orbit analysis indicates that simultaneous bifurcations of short periodic orbits in the equatorial plane play predominant roles in the formation of this new shell structure.

§1. Introduction

Theoretical and experimental exploration of reflection-asymmetric deformed shapes is one of the current topics of interest in finite many-fermion systems like atomic nuclei and metallic clusters.[1]-[6] In theoretical calculations, various approaches such as Hartree-Fock-Bogoliubov methods, microscopic-macroscopic methods and semiclassical methods have been used for this purpose (see Ref. 1) for a review). Each method possesses merits and demerits, so that it would be desirable to explore the subject using various approaches.

A basic motive of the semiclassical periodic-orbit approach[7]-[10] is to understand the origin of shell-structure formation that plays a decisive role in bringing about symmetry-breaking in the average potential of finite quantum systems. Understanding this origin, it would become possible to predict qualitatively where we can expect a particular deformation to appear in the multi-dimensional space spanned by various deformation-parameters.

In the conventional wisdom, the shell-structure would be weakened if a reflection-asymmetric deformation is added to the spheroidal shape. This is because the system becomes non-integrable when an octupole deformation is added, and the degeneracy of the periodic-orbits is reduced. Contrary to this expectation, a clear shell structure was found in Refs. 11) and 12) to emerge for certain combinations of quadrupole and octupole deformations in the reflection-asymmetric deformed oscillator model. It was pointed out that this shell-structure is associated with the bifurcation of periodic orbits.

In this paper, we investigate a three-dimensional cavity as a simple model of single-particle motion in atomic nuclei and in metallic clusters, and we attempt to find the correspondence between quantum shell structure and classical periodic-orbits. We expect that, if we find clear shell structures at certain deformations, they are related to the stabilities of certain periodic orbits and their bifurcations. Our

major purpose is then to identify which kind of bifurcation is responsible for the formation of the shell structure in the cavity model.

A part of this work was previously reported in conference proceedings. [13]

§2. Reflection-asymmetric deformed cavity

To explore whether or not clear shell structure emerges in the single-particle spectra for non-integrable Hamiltonian, we have carried out an analysis of single-particle motion in a reflection-asymmetric, axially-symmetric deformed cavity by parameterizing the surface as

$$R(\theta) = R_0 \left(\frac{1}{\sqrt{(\frac{\cos\theta}{a})^2 + (\frac{\sin\theta}{b})^2}} + a_3 Y_{30}(\theta) \right), \qquad (2 \cdot 1)$$

where a and b are related with the familiar quadrupole deformation parameter δ (equivalent to $\delta_{\rm osc}$ in Ref. 14)) by $a = ((3+\delta)/(3-2\delta))^{2/3}$ and $b = ((3-2\delta)/(3+\delta))^{1/3}$. This shape reduces to a spheroid (integrable cavity) in the limit that the octupole
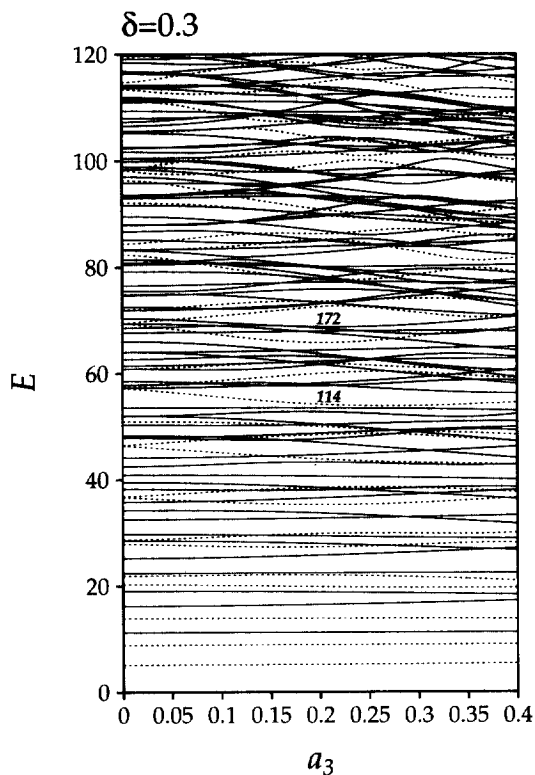

Fig. 1. Single-particle energy spectra of the deformed cavity plotted as a function of the octupole deformation parameter a_3. Dotted and solid lines denote the $K = 0$ and the doubly-degenerate $K \neq 0$ levels, respectively. The quadrupole deformation parameter is fixed at $\delta = 0.3$. The energy is measured in units of $\hbar^2/MR_0^2$, M being the mass.
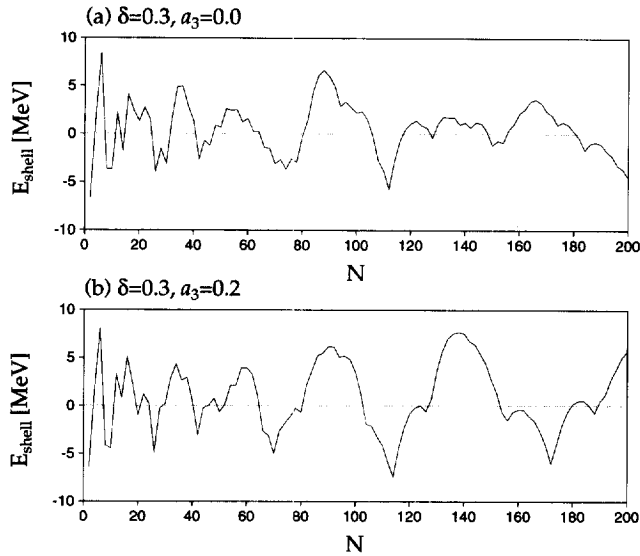
Fig. 2. Shell structure energies of the deformed cavities with $\delta = 0.3$ and $a_3 = 0.0$ (a), 0.2 (b), evaluated with the conventional Strutinsky method and plotted as functions of the particle number N. The energy is evaluated by setting $R_0 = 1.2(2N)^{1/3}$ fm and $Mc^2 = 938$ MeV for nuclei.

deformation parameter a_3 vanishes.

We solve the Schrödinger equation under Dirichlet boundary conditions and evaluate the shell energy by means of the Strutinsky method.[15] To efficiently obtain a large number of eigenvalues as a function of deformation parameters, we have examined four numerical recipes; the plane-wave decomposition (PWD),[16] the spherical-wave decomposition (SWD),[17] the boundary integral method (BIM),[18]-[20] and the coordinate-transformation method (DIAG).[21],[22] The DIAG is the most effective method for near-spherical shapes, but it is not good for strongly deformed shapes. In SWD, PWD and BIM, the eigenvalue problem is converted to a search for the zeros of real functions, minima of positive functions and zeros of complex functions, respectively, and we have found that SWD is the most convenient for the present purpose. Thus we mainly use this method, sometimes cross-checking the results with other methods.

As a typical example, we discuss here the case of $\delta = 0.3$. A more systematic presentation of this work including other cases will be reported elsewhere.[23] Figure 1 displays single-particle spectra calculated as functions of the octupole-deformation parameter a_3. It is seen that a new shell structure emerges at about $a_3 = 0.2$. The deformed magic numbers associated with this shell structure are 26, 42, 70, 114, 172,$\cdots$, taking the spin degeneracy factor into account. Note that these numbers appear at intermediate values between the magic numbers 20, 58, 92, 138, 186,$\cdots$ of the spherical cavity. This indicates that, due to the reflection-symmetry breaking of the cavity, strong $\Delta l = 3$ mixing takes place among levels with large orbital angular momenta l in spherical major shells.

Figure 2 displays shell-structure energies evaluated with the standard Strutinsky procedure and plotted as functions of the particle number N. As expected from Fig. 1, we confirm here that minima develop in association with the formation of the new shell structure at about $a_3 = 0.2$. These shell-energy gains are so large that this shell structure will remain either as minima or valleys with respect to the octupole shape degree of freedom of the total deformation energy surface, even when the liquid-drop deformation energies are added to them.

§3. Fourier transform

To understand the physical reason why such a clear shell structure emerges for a certain combination of the octupole and quadrupole deformations, and to identify the classical periodic orbits responsible for this shell structure formation, we analyze the Fourier transform of the quantum spectrum.

The single-particle equations of motion for the cavity are invariant with respect to the scaling transformation $(\vec{x}, \vec{p}, t) \to (\vec{x}, \alpha\vec{p}, \alpha^{-1}t)$. The action integral S_γ for the periodic orbit γ corresponds to its length L_γ:

$$S_\gamma(E = p^2/2M) = \oint_\gamma \vec{p} \cdot d\vec{q} = pL_\gamma, \tag{3·1}$$

and the trace formula is written as

$$\rho(E) \simeq \bar{\rho}(E) + \sum_\gamma A_\gamma k^{(d_\gamma - 2)/2} \cos(kL_\gamma - \pi\mu_\gamma/2), \tag{3·2}$$

where $\bar{\rho}(E)$ denotes the contributions of orbits of 'zero-length', d_γ the degeneracy and μ_γ the Maslov phase of the periodic orbit γ. This scaling property enables us to make use of the Fourier transformation of the level density with respect to the wave number k. The Fourier transform $F(L)$ of the level density $\rho(E)$ is written as

$$\begin{aligned} F(L) &= \int dk\, k^{-(d-2)/2} e^{-ikL} \rho(E = \hbar^2 k^2/2M) \\ &\simeq \bar{F}(L) + \sum_\gamma A'_\gamma \delta(L - L_\gamma). \end{aligned} \tag{3·3}$$

This may be regarded as the 'length spectrum' exhibiting peaks at the lengths of individual periodic orbits. [8] In numerical calculation, the spectrum is smoothly truncated by a Gaussian with a cutoff wave number $k_c = 1/\Delta L$ as

$$\begin{aligned} F_{\Delta L}(L) &\equiv \int dk\, k^{-(d-2)/2} e^{-ikL} e^{-\frac{1}{2}(k/k_c)^2} \rho(E = \hbar^2 k^2/2M) \\ &= \frac{M}{\hbar^2} \sum_n k_n^{-d/2} e^{-ik_n L} e^{-\frac{1}{2}(k_n/k_c)^2} \end{aligned} \tag{3·4}$$

$$\simeq \bar{F}_{\Delta L}(L) + \sum_\gamma A''_\gamma \exp\left[-\frac{1}{2}\left(\frac{L - L_\gamma}{\Delta L}\right)^2 \right]. \tag{3·5}$$

The amplitude A_γ (or A''_γ) is proportional to the stability factor $1/\sqrt{|2 - \mathrm{Tr}\, M_\gamma|}$ (in
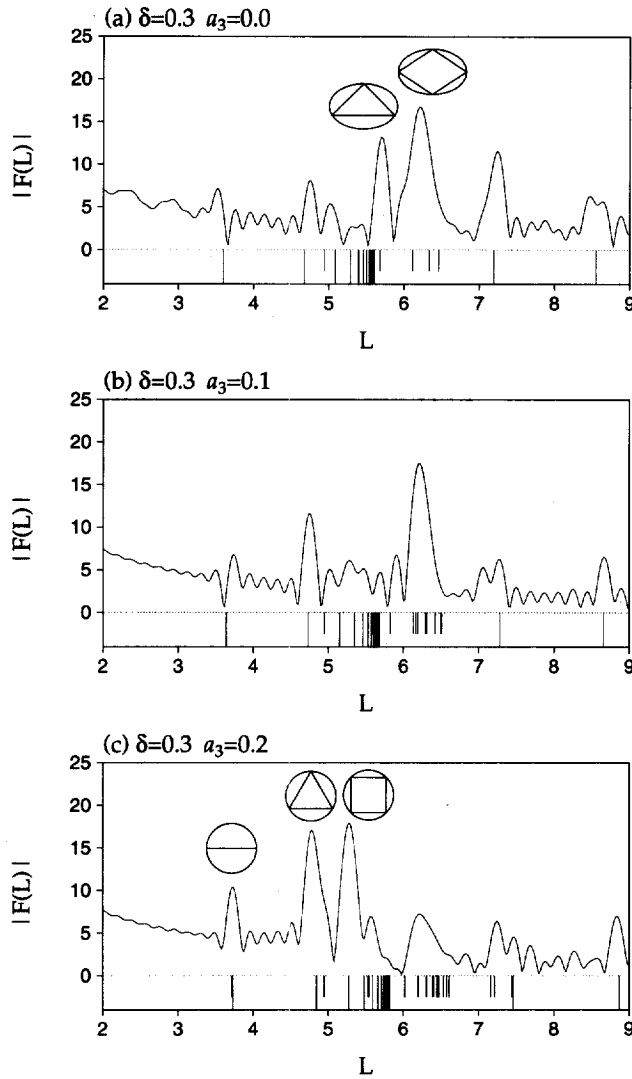
Fig. 3. Fourier transforms of the quantum level densities for deformed cavities with $\delta = 0.3$ and $a_3 = 0.0$ (a), 0.1 (b), 0.2 (c). The degeneracy index $d = 1$ (valid for generic periodic orbits) and Gaussian cutoff wave number $k_c = \sqrt{300}$ are used in (3·4). In each panel, the lengths of classical periodic orbits in the axis-of-symmetry (equatorial) plane are indicated by short (long) vertical lines. The lengths are measured in units of the radius R_0. The classical periodic orbits are calculated by means of the surface-of-section method,[24] which enables us to obtain all periodic orbits whose lengths are less than a certain value.

the stationary-phase approximation), where M_γ is the monodromy matrix of orbit γ. It is expected to be enhanced in the vicinity of the bifurcation point where $\mathrm{Tr}\, M_\gamma = 2$ (see Ref. 12)).

Let us investigate how these peaks change when the shape parameters of the cavity are varied. Figure 3 displays, as an example, how the pattern of the Fourier

transform (3·4) changes as a function of a_3, fixing the quadrupole deformation parameter at $\delta = 0.3$. The highest peaks at the spheroidal limit ($a_3 = 0$) are associated with triangular and quadrilateral orbits in the axis-of-symmetry plane, whose degeneracies are two. It is clearly seen that the heights of peaks decline with increasing a_3. This is because the octupole deformation breaks the spheroidal symmetry and the degeneracy reduces to one corresponding to rotation about the symmetry axis. On the other hand, we can clearly see that the heights of other peaks rise with increasing a_3. These peaks are found to be associated with the diameter, triangular and square orbits in the equatorial plane[*] at the center of the larger cluster of the pear-shaped cavity.

§4. Periodic-orbit bifurcation

The key to understanding the reason that short periodic orbits in the equatorial plane start to play increasingly important roles at finite octupole deformation may lie in the following point: The stability of these orbits is crucially dependent on the curvature of the boundary. The curvature radius in the longitudinal direction changes as the octupole deformation parameter a_3 varies, and at certain combinations of δ and a_3, it matches with the equatorial radius, as illustrated in the top-leftmost figure in Fig. 4. At this point, periodic orbits in the equatorial plane acquire *local spherical symmetry*,[**] and form a locally continuous set of periodic orbits leaving from the equatorial plane. This continuous set makes a coherent contribution to the trace integral and significantly enhances the amplitudes associated with these orbits. This is just the bifurcation point of orbits in the equatorial plane, and new periodic orbits bifurcate from the above locally continuous set. We present in Fig. 5 some periodic orbits born out of the above-mentioned bifurcation.

This kind of bifurcation can be regarded as a special example of the phenomena that Balian and Bloch called 'accidental degeneracy': According to Ref. 8), bifurcations occur when the condition

$$\frac{R_2}{R_1} = \frac{\sin(\pi t/p)^2}{\sin(\pi q/p)^2} \tag{4·1}$$

is met, where R_1 and R_2 denote the main curvature radii for the longitudinal and equatorial directions, respectively, and the integers $(p,\ t,\ q)$ correspond respectively to the number of vertices, the number of turns about the symmetry axis, and the number of vibrations in direction of the symmetry axis. Note that, for $R_1 = R_2$, all orbits ($p = 2, 3, 4, \cdots$) in the equatorial plane simultaneously satisfy the above bifurcation condition with $t = q = 1$. This type of bifurcation is quite peculiar in that the local degeneracy changes by two at the bifurcation point.

---

[*] For convenience, we call the plane where the radius of the circular section assumes its maximum value 'the equatorial plane', although it does not go through the center of the cavity.

[**] Namely, the curvature of the boundary in the vicinity of the equatorial plane locally coincides with that of a sphere.
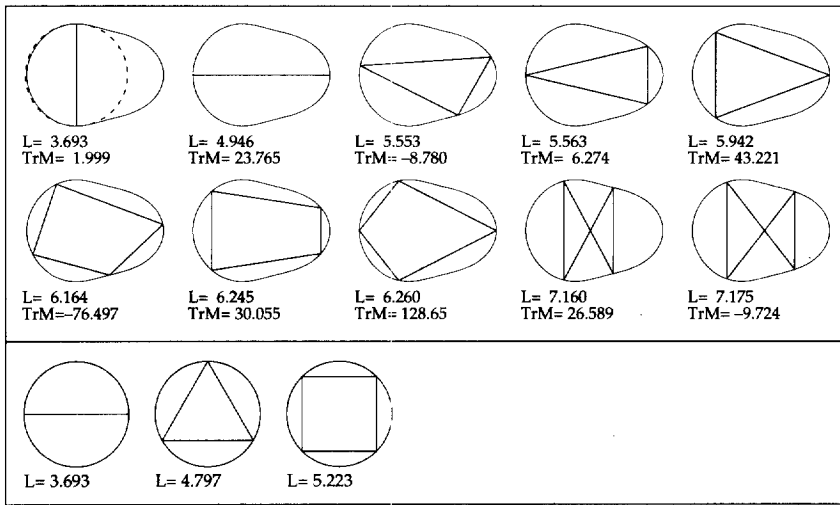
Fig. 4. Periodic orbits in the deformed cavity with $\delta = 0.3$ and $a_3 \simeq 0.16$ (at bifurcation). For each periodic orbit, the length L and the trace of the monodromy matrix, $\mathrm{Tr}\,M$, are indicated. Those in the axis-of-symmetry plane are displayed in the upper panel and those in the equatorial plane in the lower panel. Only linear, triangular and quadrilateral orbits are displayed. In the top left-most figure, a sphere tangent to the boundary at equatorial plane is indicated by a broken line.

Fig. 5. Some short periodic orbits bifurcated from the equatorial-plane orbits. The deformation parameters are $\delta = 0.3$ and $a_3 = 0.2$.

Fig. 6. Bifurcation line of the equatorial-plane periodic orbits in the quadrupole-octupole deformation parameter space. For $\delta = 0.3$, bifurcation occurs at $a_3 \simeq 0.16$.

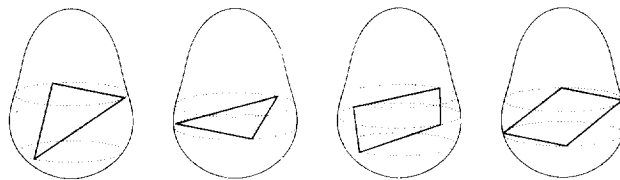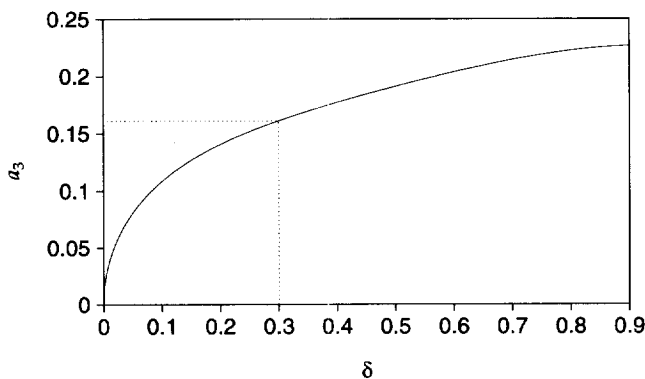Figure 6 displays a bifurcation line of this kind in the quadrupole-octupole deformation parameter space. The bifurcation occurs at $a_3 \simeq 0.16$ for the case of $\delta = 0.3$. In general, clear shell structures will appear along the bifurcation line. Due to these shell structures, large shell energy gains are expected for certain nuclei with such octupole deformations.

§5. Conclusion

We have investigated the shell structure of the single-particle spectrum in a reflection-asymmetric deformed cavity. It may be found that clear shell structure emerges for certain combinations of quadrupole and octupole deformations. The Fourier transform of the quantum spectra clearly indicates that simultaneous bifurcations of the diameter, triangular and square orbits in the equatorial plane play predominant roles in the formation of this new shell structure.

It will be very interesting to investigate whether or not this mechanism of shell enhancement provides a semiclassical interpretation of the reflection-asymmetric shapes of some metallic clusters recently found in the realistic calculations by Frauendorf and Pashkevich.[5] Also, the origin of mass-asymmetry in nuclear fission may be studied in a similar manner (cf. a recent paper by Brack et al.[25]).

It remains as a challenge for the future to develop a semiclassical trace formula which can quantitatively treat the type of bifurcation discussed in this paper.

Acknowledgements

References

1) S. Åberg, H. Flocard and W. Nazarewicz, Ann. Rev. Nucl. Part. Sci. **40** (1990), 439.
2) P. A. Butler and W. Nazarewicz, Rev. Mod. Phys. **68** (1996), 349.
3) M. Brack and R. K. Bhaduri, *Semiclassical Physics* (Addison-Wesley, Reading, 1997).
4) I. Hamamoto, B. Mottelson, H. Xie and X. Z. Zhang, Z. Phys. **D21** (1991), 163.
5) S. Frauendorf and V. V. Pashkevich, Ann. der Phys. **5** (1996), 34.
6) W. D. Heiss, R. G. Nazmitdinov and S. Radu, Phys. Rev. **B51** (1995-I), 1874.
7) M. C. Gutzwiller, J. Math. Phys. **12** (1971), 343.
8) R. Balian and C. Bloch, Ann. of Phys. **69** (1972), 76.
9) V. M. Strutinsky, A. G. Magner, S. R. Ofengenden and T. Døssing, Z. Phys. **A283** (1977), 269.
10) H. Frisk, Nucl. Phys. **A511** (1990), 309.
11) K. Arita, Phys. Lett. **B336** (1994), 279.
12) K. Arita and K. Matsuyanagi, Nucl. Phys. **A592** (1995), 9.
13) K. Arita, A. Sugita and K. Matsuyanagi, *Proc. Int. Symp. on Similarities and Differences between Nuclei and Clusters*, Tsukuba, July 1 – 4, 1997, AIP Conference Proceedings 416, ed. Y. Abe, I. Arai, S. M. Lee and K. Yabana, p. 393.

Proc. Int. Symp. on Atomic Nuclei and Metallic Clusters: Finite Many-Fermion Systems, Prague, Sep. 1 – 5, 1997, Czech. J. of Phys. **48** (1998), 821.
Proc. Int. Conf. on Nuclear Structure and Related Topics, Dubna, Sep. 9 – 13, 1997, ed. S. N. Ershov, R. V. Jolos and V. V. Voronov, p. 198.

14) A. Bohr and B. R. Mottelson, *Nuclear Structure* (Benjamin, 1975), Vol. 2.

15) M. Brack, J. Damgaard, A. S. Jensen, H. C. Pauli, V. M. Strutinsky and C. Y. Wong, Rev. Mod. Phys. **44** (1972), 320.

16) E. J. Heller, in *Chaos and quantum systems, Proc. NATO ASI Les Houches Summer School, 1991*, ed. M. J. Giannoni, A. Voros and J. Zinn-Justin (North-Holland), p. 547.

17) T. Mukhopadhyay and S. Pal, Nucl. Phys. **A592** (1995), 291.

18) M. V. Berry and M. Robnik, J. of Phys. **A19** (1986), 649.

19) M. V. Berry and M. Wilkinson, Proc. R. Soc. London **A392** (1984), 15.

20) B. Li and M. Robnik, J. of Phys. **A27** (1994), 5509.

21) S. A. Moszkowski, Phys. Rev. **99** (1955), 803.

22) J. Blocki, J. Skalski and W. J. Swiatecki, Nucl. Phys. **A594** (1995), 137.

23) A. Sugita, K. Arita and K. Matsuyanagi, in preparation.

24) D. Provost, Phys. Rev. **E51** (1995), 5396.

25) M. Brack, S. Reimann and M. Sieber, Phys. Rev. Lett. **79** (1997), 1817.

Semiclassical Origin of Superdeformed Shell Structure in the Spheroidal Cavity Model

Ken-ichiro ARITA, Ayumu SUGITA* and Kenichi MATSUYANAGI*

Department of Physics, Nagoya Institute of Technology, Nagoya 466-8555, Japan
*Department of Physics, Graduate School of Science, Kyoto University
Kyoto 606-8502, Japan

Classical periodic orbits responsible for emergence of the superdeformed shell structures of single-particle motion in spheroidal cavities are identified and their relative contributions to the shell structures are evaluated. Both prolate and oblate superdeformations (axis ratio approximately 2:1) as well as prolate hyperdeformation (axis ratio approximately 3:1) are investigated. Fourier transforms of quantum spectra clearly show that three-dimensional periodic orbits born out of bifurcations of planar orbits in the equatorial plane become predominant at large prolate deformations, while butterfly-shaped planar orbits bifurcated from linear orbits along the minor axis are important at large oblate deformations.

§1. Introduction

In the last decade, superdeformed spectroscopy, i.e., the study of nuclear structure with large prolate deformations (axis ratio approximately 2:1), has developed enormously, and further significant progress is expected. [1]-[3] It is well known that the superdeformation is the result of shell effect at large deformation, and in fact realistic calculations of both the Strutinsky-Nilsson type and Hartree-Fock type work well for describing shell structures observed in experiments at such large deformations. [4] The purpose of this paper, however, is not to make some realistic calculations in relation to recent experimental findings. Rather, we address here the fundamental question of why a nucleus is superdeformed and investigate the semiclassical origin of emergence of the superdeformed shell structure in a simple model, a spheroidal cavity model.

In the periodic-orbit theory, [5]-[8] based on the semiclassical approximation of the path integral, oscillating parts of single-particle level densities are determined by periodic orbits in the classical counterpart of the single-particle Hamiltonian. We are particularly interested in shell structure, i.e., level densities coarse-grained to a certain energy resolution, which are related with short periodic orbits. As is well known, a nucleus favors such shapes at which prominent shell structures are formed and its Fermi surface lies in a valley of oscillating level density, increasing its binding energy in this way.

With a semiclassical approach, Strutinsky et al. [9] studied the shell structure associated with the spheroidal cavity model and found that planar orbits in the meridian plane are responsible for the shell structure at normal prolate deformations. In addition, they pointed out that some three-dimensional (3D) periodic orbits ap-

pearing at large deformations lead to the shell structure responsible for the fission isomers whose existence has been known since the 1970s, which have superdeformed shapes. As emphasized in Ref. 9), shell structures obtained for the spheroidal cavity model contain basic features, apart from shifts of deformed magic numbers due to the spin-orbit potential, similar to those obtained by the Woods-Saxon potential for heavy nuclei and metallic clusters, and thus this model can be used as a simple model to understand the semiclassical origin of the emergence of regular oscillating patterns in the coarse-grained quantum spectra at large deformations.

Remarkably, however, two decades after the publication of Ref. 9), to the best of our knowledge, little exploration of this idea has been undertaken and the qualitative argument given in that paper has not been fully examined by other researchers, although the spheroidal cavity model has been used for various purposes. [10]-[12] A paper most relevant to the present paper is that of Frisk, [13] who used the periodic-orbit theory and the same cavity model mainly to clarify the origin of the prolate-oblate asymmetry at normal deformations. Although he also briefly discussed the case of large deformations, the importance of 3D orbits was not mentioned.

In this paper, we identify the most important periodic orbits that determine the major pattern of the oscillating level density at large deformations, including prolate superdeformations, prolate hyperdeformations and oblate superdeformations. For this purpose we make full use of the Fourier transformation method. As briefly reviewed in the text, by virtue of the scaling property of the cavity model, Fourier transforms of quantum spectra exhibit peaks at lengths of classical periodic orbits, enabling us to precisely identify important periodic orbits contributing to the shell structure. This method has been well known, [6],[8] but it has not been used for the present subject.

Classical periodic orbits in a spheroidal cavity and their bifurcations with the variation of the axis ratio have been thoroughly studied by Nishioka et al. [14],[15] This paper may be regarded as a continuation of their work in the sense that we investigate quantum manifestations of these periodic orbits and of their bifurcations. (Actually, this was the intention also of the work by Nishioka et al. [14],[15])

We present in §2 the oscillating parts of smoothed level densities as functions of the deformation parameter of the cavity. The Fourier transformation method is recapitulated in §3. Periodic orbits and their bifurcations in a spheroidal cavity are briefly reviewed in §4. The results of the semiclassical analysis of shell structures are presented in §§6–8 for prolate superdeformations, prolate hyperdeformations and oblate superdeformations, respectively, and conclusions are given in §9.

A part of this work was previously reported in conference proceedings. [16]

§2. Oscillating level density

We solve the Schrödinger equation for single-particle motion in a spheroidal cavity under Dirichlet boundary conditions. As is well known, a spheroidal cavity model is integrable and separable by the spheroidal coordinate system, so that these coordinates are frequently used for solving the Schrödinger equation. We have, however, adopted a spherical-wave decomposition method [17] for this purpose. The
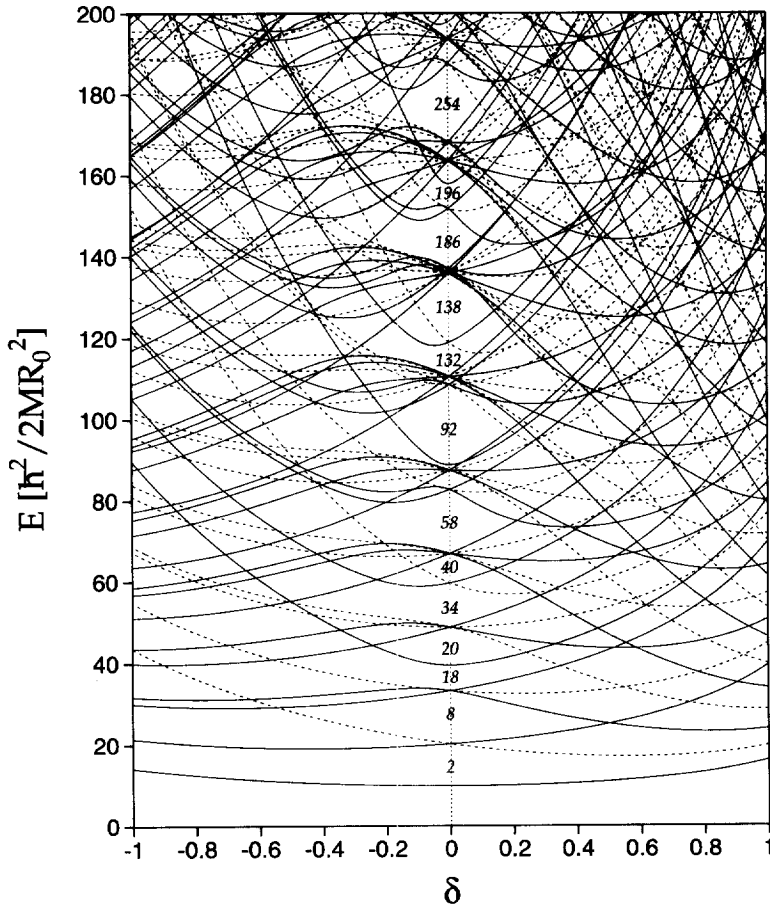
Fig. 1. Single-particle energy diagram for a spheroidal cavity, plotted as a function of the deformation parameter δ. Solid and broken lines represent even- and odd-parity levels. The energy is measured in units of $\hbar^2/2MR_0^2$, where M and R_0 are the mass of the particle and the radius in the spherical limit, respectively. The spin degeneracy factor 2 is taken into account in magic numbers in the spherical limit.

reason is merely that we wrote a computer program based on the latter method for the purpose of efficiently calculating a large number of eigenvalues as function of deformation parameters for cavities of general axially symmetric shapes.[18] With this method, wave functions are expanded in terms of spherical Bessel functions (for the radial coordinate) and associated Legendre functions (for the polar angle coordinate), and expansion coefficients are determined so as to fulfill the boundary conditions (see Refs. 18) and 17) for technical details).

The single-particle energy diagram (as function of deformation parameter δ) obtained in this way is shown in Fig. 1. The deformation parameter δ is related to the axis ratio $\eta \equiv a/b$ by $\delta = 3(\eta - 1)/(2\eta + 1)$ in the prolate case and by $\delta = -3(\eta - 1)/(\eta + 2)$ in the oblate case, where a and b denote the lengths of the major and the minor axes, respectively. The volume-conservation condition is
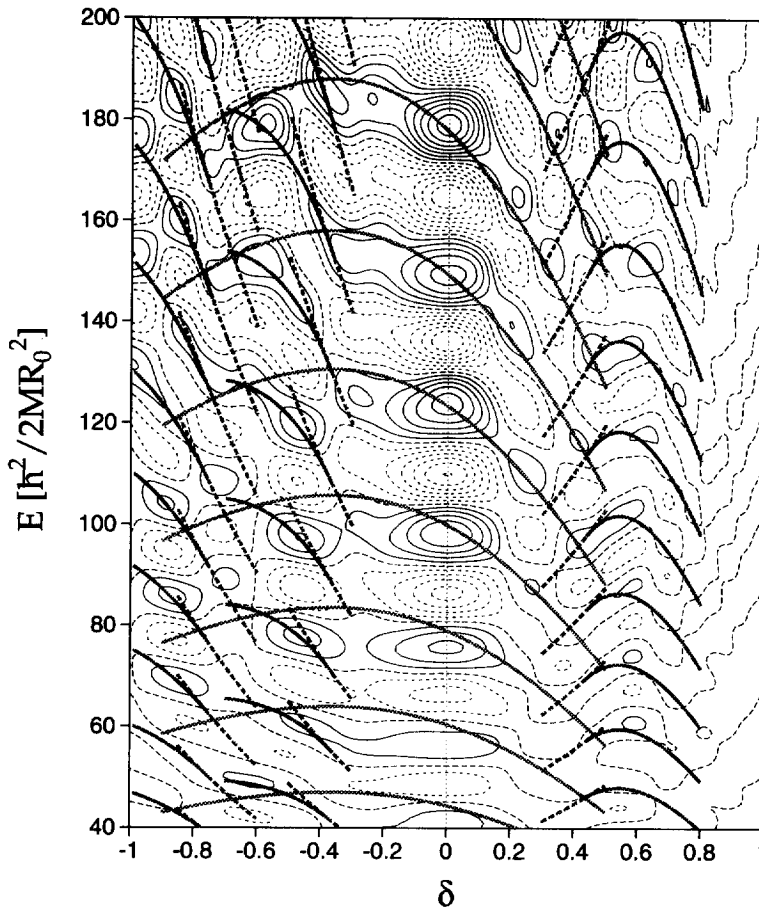
Fig. 2. Oscillating part of the smoothed level density displayed as a function of the energy and deformation parameter δ. Solid, dashed and dotted contour curves correspond to negative, zero and positive values, respectively. The units of energy are the same as in Fig. 1. Strutinsky smoothing is used, with the smoothing width parameter $\Delta k = 0.5$. Constant-action lines for important periodic orbits are indicated: Thick solid lines running through the spherical closed shells are those for tetragonal orbits in the meridian plane. Thick broken and solid lines in the region $\delta = 0.3 \sim 0.8$ are those for five-point star-shaped orbits in the equatorial plane and for 3D orbits (5:2:1) bifurcated from them, respectively. Broken and solid lines in the region $\delta = -0.3 \sim -0.7$ are those for double repetitions of linear orbits along the minor axis and for butterfly-shaped planar orbits (4:1:1) bifurcated from them, respectively. Similarly, broken and solid lines in the region $\delta = -0.6 \sim -1$ are those for triple repetitions of linear orbits along the minor axis and for planar orbits (6:1:1) bifurcated from them, respectively.

imposed so that $ab^2 = R_0^3$ in the prolate case and $a^2b = R_0^3$ in the oblate case, where R_0 is the radius in the spherical limit.

Figures 2 and 3 display the oscillating part of the smoothed level density in the form of a contour map with respect to the energy and deformation parameter, which is coarse-grained with the Strutinsky smoothing parameter $\Delta k = 0.5$. We clearly see regular patterns consisting of several valley and ridge structures. Thick solid and
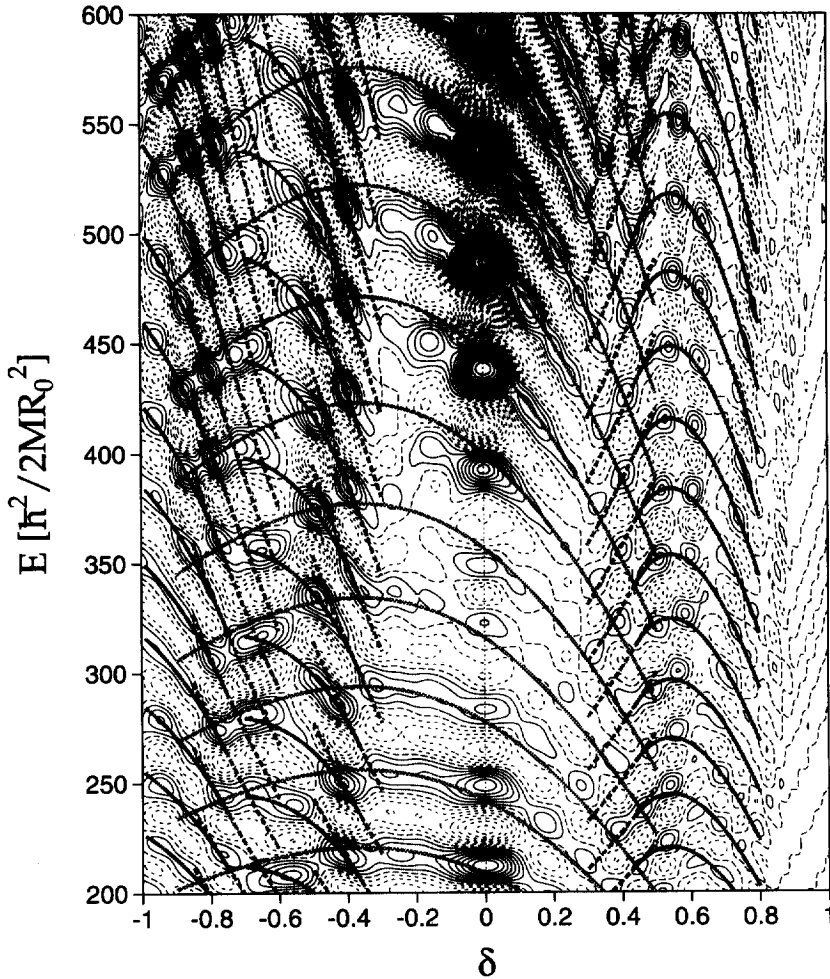
Fig. 3. Same as Fig. 2 but for a higher energy region. The correspondence between valley structures and constant-action curves becomes much clearer in the higher energy region.

broken lines indicate the valley lines predicted by the periodic orbit theory (see §5 and §§6–8 for details).

§3. Fourier transform

Single-particle equations of motion for the cavity are invariant with respect to the scaling transformation $(x, p, t) \rightarrow (x, \alpha p, \alpha^{-1}t)$ and the action integral S_r for a periodic orbit r is proportional to its length L_r:

$$S_r(E = p^2/2M) = \oint_r \boldsymbol{p} \cdot d\boldsymbol{q} = pL_r = \hbar k L_r. \tag{3.1}$$

Thus the semiclassical trace formula for the level density [5] is written as

$$g(E) = \sum_n \delta(E - E_n) = \frac{M}{\hbar^2 k} \sum_n \delta(k - k_n)$$

$$\simeq \bar{g}(E) + \sum_r A_r(k) \cos(kL_r - \pi\mu_r/2), \tag{3.2}$$

where $\bar{g}(E)$ denotes the smooth part corresponding to the contribution of the *zero-length* orbit, and μ_r is the Maslov phase of the periodic orbit r. This scaling property enables us to make use of the Fourier transformation of the level density with respect to the wave number k. The Fourier transform $F(L)$ of the level density $g(E)$ is written as

$$F(L) = \int dk \, e^{-ikL} g(E = \hbar^2 k^2/2M)$$

$$\simeq \bar{F}(L) + \pi \sum_r e^{-i\pi\mu_r/2} A_r(i\partial_L) \, \delta(L - L_r), \tag{3.3}$$

which may be regarded as the 'length spectrum' exhibiting peaks at lengths of individual periodic orbits. [6] In numerical calculations, the spectrum is cut off by a Gaussian with cutoff wave number $k_c = 1/\Delta L$ as

$$F_{\Delta L}(L) \equiv \frac{1}{\sqrt{2\pi}\Delta L} \int dL' \, e^{-\frac{1}{2}(\frac{L-L'}{\Delta L})^2} \, F(L')$$

$$= \frac{M}{\hbar^2} \sum_n \frac{1}{k_n} \, e^{-\frac{1}{2}(k_n/k_c)^2} \, e^{-ik_n L}, \tag{3.4}$$

$$\simeq \bar{F}_{\Delta L}(L) + \pi \sum_r e^{-i\pi\mu_r/2} A_r(i\partial_L) \frac{1}{\sqrt{2\pi}\Delta L} e^{-\frac{1}{2}(\frac{L-L_r}{\Delta L})^2}. \tag{3.5}$$

§4. Periodic-orbit bifurcations

In this section, we recapitulate the theory of classical periodic orbits in the spheroidal cavity following Nishioka et al. [14],[15] and Strutinsky et al. [9] We focus our attention on those orbits having short periods.

As is well known, only linear and planar orbits exist in a spherical cavity. When spheroidal deformations appear, the linear (diameter) orbits bifurcate into those along the major axis and along the minor axis. Likewise, the planar orbits bifurcate into orbits in the meridian plane and those in the equatorial plane. Since the spheroidal cavity model is integrable, all classical orbits lie on a 3D torus, and, in the case of a prolate spheroid, periodic orbits are characterized by three positive integers $(p{:}t{:}q)$, which represent numbers of vibrations or rotations with respect to three spheroidal coordinates. They are denoted as $(n_\epsilon, n_\phi, n_\xi)$ in Refs. 14) and 15), and (n_v, n_ϕ, n_u) in Ref. 9). When the axis ratio η of the prolate spheroid increases, hyperbolic orbits in the meridian plane and three-dimensional orbits successively appear through bifurcations of linear and planar orbits in the equatorial plane. Bifurcations occur when the condition

$$\eta \equiv \frac{a}{b} = \frac{\sin(\pi t/p)}{\sin(\pi q/p)} \tag{4.1}$$

is satisfied.

As we see in succeeding sections, the most important orbits for superdeformed shapes (axis ratio approximately 2:1) are 3D orbits $(p{:}t{:}q) = (p{:}2{:}1)$ with $p = 5, 6, 7, \cdots$. They bifurcate from planar orbits that turn twice $(t = 2)$ about the symmetry axis. Likewise, planar orbits (4:2:1) bifurcate from linear orbits that repeat twice along the minor axis. These new-born orbits resemble the Lissajous figures of the superdeformed harmonic oscillator with frequency ratio $\omega_\perp{:}\omega_z = 2{:}1$. Every bifurcated orbit forms a continuous family of degeneracy two, which implies that we need two parameters to specify a single orbit among a continuous set of orbits belonging to a family having a common value of the action integral (or equivalently, the length).

For prolate hyperdeformed shapes (axis ratio approximately 3:1), bifurcations from linear and planar orbits that turn three times $(t = 3)$ about the symmetry axis are important. The new-born orbits are hyperbolic orbits in the meridian plane (6:3:1) and 3D orbits $(p{:}3{:}1)$ with $p = 7, 8, 9, \cdots$.

In the case of oblate spheroidal cavities, periodic orbits are classified in Ref. 15) into two modes, the whispering-gallery (W) mode and bouncing-ball (B) mode. The systematics of periodic-orbit bifurcations for the W-mode are similar to those for the prolate case and can be treated by just exchanging the roles of t and q. On the other hand, B-mode orbits are successively created through bifurcations of multiple repetitions of linear orbits along the minor axis when the condition

$$\eta \equiv \frac{a}{b} = \frac{1}{\sin(\pi t/p)} \qquad (4\cdot2)$$

is satisfied. Bifurcations of this kind do not depend on q, so that, for instance, planar orbits (4:1:1) are created simultaneously with two families of 3D orbits (4:1:3/2) and (4:1:2). (For B-mode orbits, half integer values of q are allowed as well as integers, due to different definitions of the integration range for the action integral related to q; see Ref. 15).)

Bifurcation points and variations of lengths with deformation are displayed for some short periodic orbits in Table I and Fig. 4.

Table I. Bifurcation points of periodic orbits specified by $(p{:}t{:}q)$ in the spheroidal cavity. Only those for short orbits to be discussed in §§6–8 are displayed.

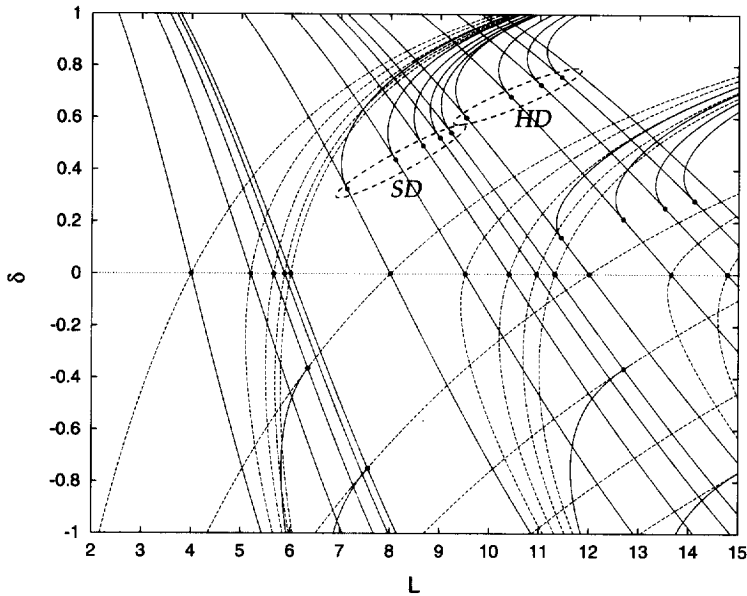| orbit $(p{:}t{:}q)$	axis ratio (a/b)	deformation δ	orbit length in R_0
(4:2:1)	1.414	0.325	7.127
(5:2:1)	1.618	0.438	8.101
(6:2:1)	1.732	0.492	8.654
(7:2:1)	1.802	0.523	8.995
(8:2:1)	1.848	0.542	9.220
(6:3:1)	2.0	0.6	9.524
(7:3:1)	2.247	0.681	10.421
(8:3:1)	2.414	0.728	11.011
(9:3:1)	2.532	0.758	11.437
(4:1:1)	1.414	−0.364	6.350
(6:1:1)	2.0	−0.75	7.560

Fig. 4. Variations of lengths of periodic orbits in a spheroidal cavity with respect to the deformation parameter δ. Only those for short orbits discussed in §§6–8 are displayed. For a more complete diagram, see Nishioka et al. [14), 15)]

§5. Shell structure and constant-action line

Using the trace formula, we can extract information about classical periodic orbits from the Fourier transforms of the level density. In this section we discuss another method of using the trace formula, the constant-action line analysis. [9)] As stated in §3 (see Eq. (3·2)), the quantum level density can be represented as the summation over periodic orbits. If a few orbits having nearly the same action integral dominate in the sum, it is expected that valleys in the contour map of the oscillating part of the smoothed level density versus energy E and deformation δ will be characterized by constant-action lines $S(E, \delta) = $ const for those dominant orbits. The equation for such lines is $kL_r(\delta) - \pi\mu_r/2 = (2n + 1)\pi$, thus,

$$E(\delta) = \frac{1}{2M} \left(\frac{2\pi\hbar(n + 1/2 + \mu_r/4)}{L_r(\delta)} \right)^2 . \quad (n = 0, 1, 2, \cdots) \qquad (5\cdot1)$$

As an example, let us examine the shell structure at normal deformations $|\delta| \lesssim 0.3$. In this region, triangular and tetragonal orbits in the meridian plane give dominant contributions to the level density. This fact was first pointed out by Strutinsky et al. [9)] (Although the triangular orbits were overlooked there, actions of the two families of orbits scale in the same way as functions of deformation parameter so that their argument was correct in essence.) The Fourier amplitudes at lengths of some meridian-plane orbits are plotted in Fig. 5 as functions of the deformation parameter δ. We see that the meridian-plane orbits are important for small δ and that their contributions decline with increasing $|\delta|$. In Figs. 2 and 3, constant-
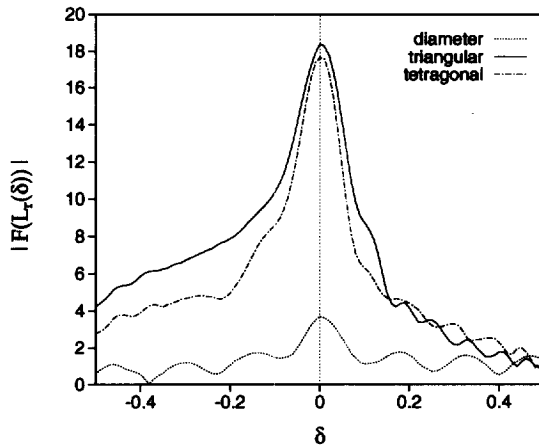
Fig. 5. Absolute values of the Fourier amplitudes defined in Eq. (3·4), at lengths $L = L_r$ of some short meridian-plane orbits, plotted as functions of the deformation parameter δ.

action lines (5·1) for the tetragonal orbits in the meridian plane are indicated. The period of the shell oscillation is mainly determined by the tetragonal orbits, and the valley structure of the level density at normal deformation is nicely explained by their constant-action lines. We also note that the shell effect at spherical shape is weakened at $E \sim 300$, and the phase of valley is shifted from that of the constant-action lines for $E \simeq 250$–350. This is due to the supershell effect associated with the interference of the triangular and tetragonal orbits. [6], [19]

In this way, we can analyze the properties of the shell structure through classical periodic orbits. In the following sections, we utilize these techniques in order to identify dominant classical periodic orbits that characterize the shell structures in superdeformed shapes.

§6. Prolate superdeformations

Figure 6 displays Fourier transforms of quantum spectra for prolate spheroidal cavities with deformation parameter values $\delta = 0.1 \sim 0.6$. At normal deformations with $\delta = 0.1$, as mentioned in the previous section, we notice peaks associated with triangular and tetragonal orbits in the meridian plane. With increasing deformation, bifurcations of linear and planar orbits in the equatorial plane successively take place. Thus, the highest peak at $L \simeq 7$ of the Fourier transform for $\delta = 0.4$ is associated with butterfly-shaped planar orbits $(p{:}t{:}q) = (4{:}2{:}1)$ that bifurcate at $\delta \simeq 0.32$ from double repetitions of linear orbits along the minor axis. For $\delta = 0.5$, the prominent peaks at $L \simeq 8$ and 8.6 correspond to 3D orbits $(5{:}2{:}1)$ and $(6{:}2{:}1)$ bifurcated respectively from five-point star-shaped orbits and double traversals of triangular orbits in the equatorial plane. With further increase in δ, the same kind of 3D orbits successively bifurcate from equatorial-plane orbits. For $\delta = 0.6$ (axis ratio $\eta = 2$), peaks around $L \simeq 9$ are associated with 3D orbits $(7{:}2{:}1)$ and $(8{:}2{:}1)$ that are bifurcated from 7-point star-shaped orbits and double traversals of rectangular orbits in the equatorial
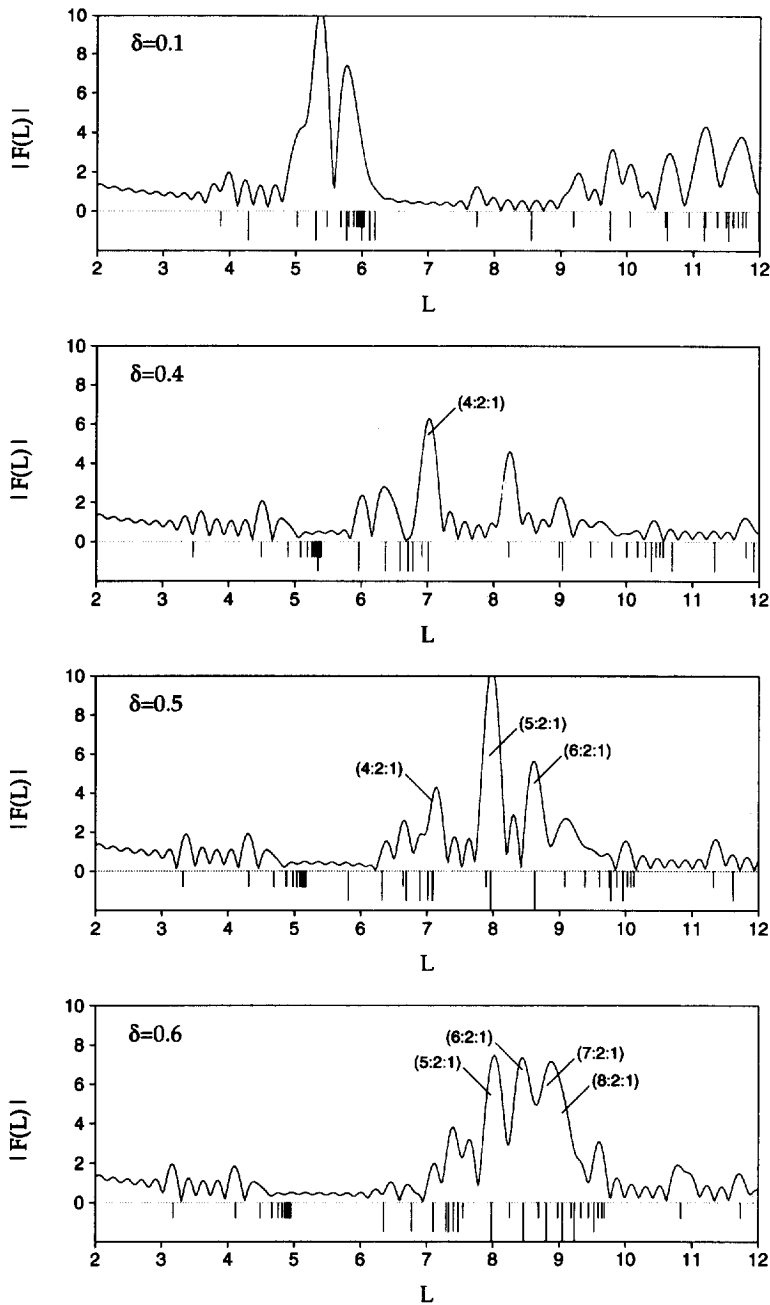
Fig. 6. Length spectra (Fourier transforms of quantum level densities) for spheroidal cavities with deformation parameter $\delta = 0.1, 0.4, 0.5$ and 0.6. The cutoff wave number $k_c = \sqrt{600}$ is used in Eq. (3·4). At the bottom of each figure, the lengths of classical periodic orbits are indicated by vertical lines. Long, middle and short vertical lines are used for 3D orbits, planar orbits in the meridian, and planer orbits in the equatorial planes, respectively.
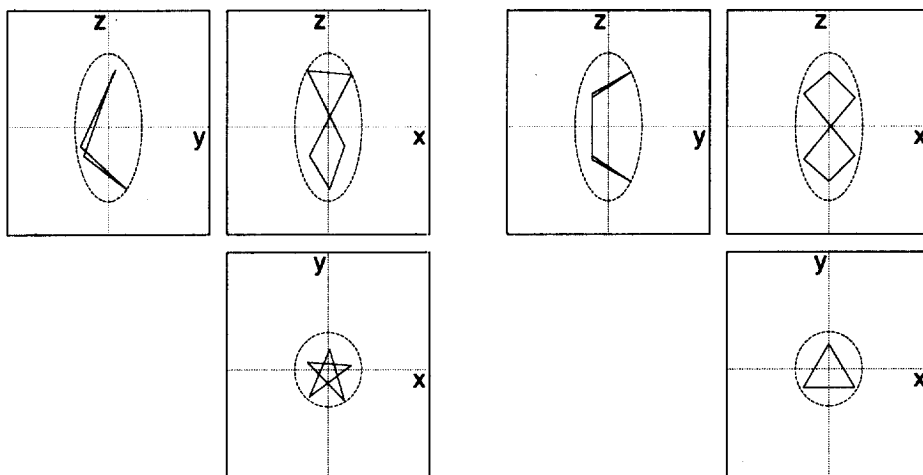
Fig. 7. Three-dimensional orbits (5:2:1) and (6:2:1) in the superdeformed prolate cavity with deformation $\delta = 0.6$ (axis ratio $\eta = 2$). Their projections on the (x, y), (y, z) and (z, x) planes are displayed.

plane.

In Figs. 2 and 3, constant-action lines for the 3D orbits (5:2:1) are indicated. Good correspondence is found between these lines and the valley structure seen in the superdeformed region with δ around 0.6. Thus we can conclude that the bifurcations of equatorial orbits play essential roles in the formation of the superdeformed shell structure, and this shell structure is characterized by the 3D orbits (p:2:1).

Some of these 3D orbits are displayed in Fig. 7. They possess similarities with the figure-eight shaped orbits in the superdeformed harmonic oscillator with frequency ratio $\omega_\perp : \omega_z = 2:1$. An important difference between the cavity model under consideration and the harmonic oscillator model should be noted, however: In the former, such periodic orbits exist for all deformation parameters δ larger than the bifurcation points, whereas in the latter, such orbits appear only for special deformations corresponding to rational ratios of the major and minor axes.

On the other hand, the magnitudes of contributions of individual orbits are found to exhibit a remarkable deformation dependence. Namely, Fourier peak heights associated with new orbits created by bifurcations quickly increase with increasing deformation and reach maximal values. Then, they start to decline. This behavior is seen in Fig. 6. Figure 8 displays the deformation dependence of the Fourier amplitudes $|F(L)|$ defined in Eq. (3·4) at lengths $L = L_r$ for some classical periodic orbits, which confirms the behavior noted above. This behavior has not been pointed out in the previous papers. It should be emphasized that the relative magnitudes and the deformation dependence of contributions of individual periodic orbits found here are significantly different from those roughly estimated in Ref. 9).

To get a deeper understanding of the mechanism of the enhancements associated with the bifurcations noted above, a semiclassical approximation that goes beyond the stationary phase approximation used in deriving the trace formula (3·2) may
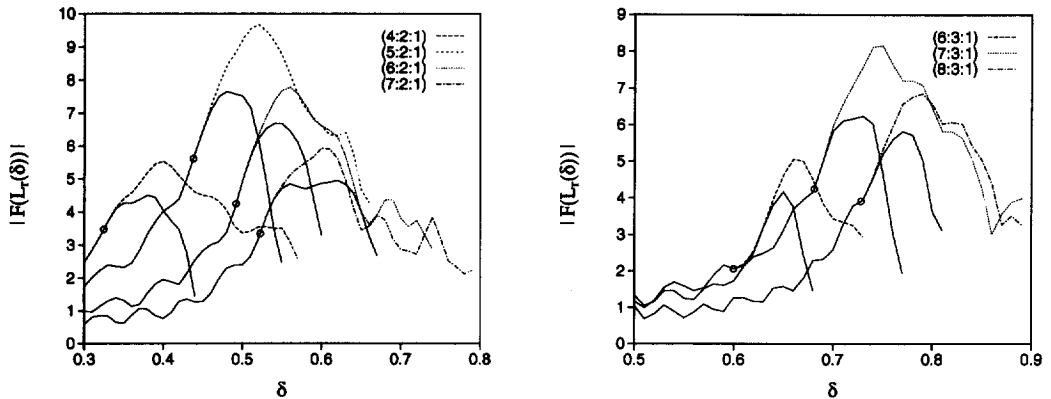
Fig. 8. Same as Fig. 5 but for meridian-plane hyperbolic orbits and 3D orbits (p:2:1) (left-hand side) and (p:3:1) (right-hand side). Solid curves correspond to those for equatorial-plane orbits from which these orbits are bifurcated.

be required. Such a semiclassical theory applicable for three dimensional deformed cavities is not available at present and remains a challenging subject for future study.

§7. Prolate hyperdeformations

Figure 9 displays Fourier transforms for $\delta = 0.7$ and 0.8. For $\delta \simeq 0.7$, the
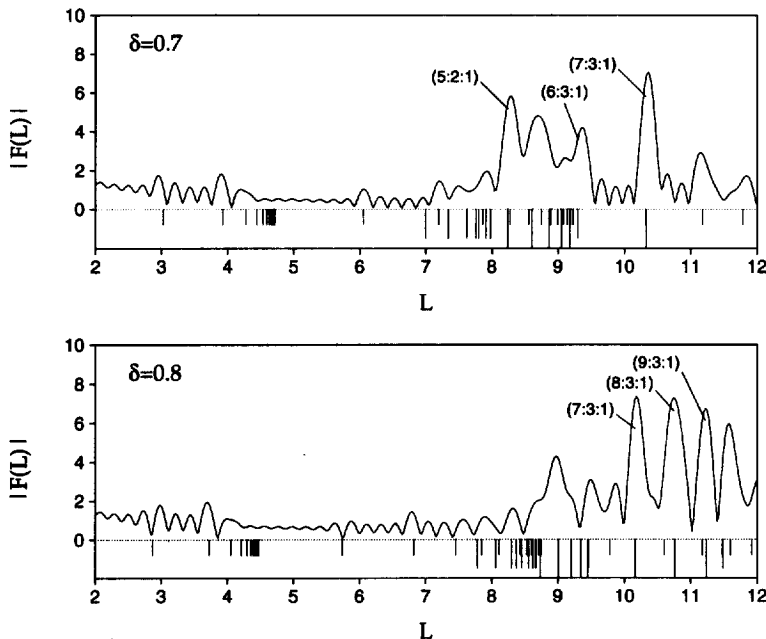
Fig. 9. Same as Fig. 6 but for $\delta = 0.7$ and 0.8 (axis ratio $\eta \simeq 2.3$ and 2.7).
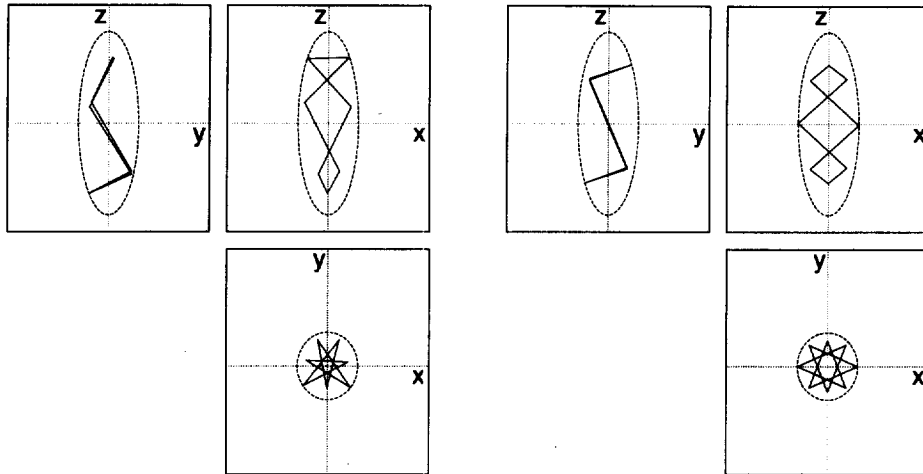
Fig. 10. Same as Fig. 7 but for 3D orbits (7:3:1) and (8:3:1) in the hyperdeformed prolate cavity
with deformation $\delta = 0.8$.

peak at $L \simeq 10.3$ is associated with 3D orbits (7:3:1) bifurcated from 7-point star-shaped orbits in the equatorial plane. For $\delta = 0.80$, we see a rise of the peak at $L \simeq 10.8$, which is associated with 3D orbits (8:3:1) bifurcated from 8-point star-shaped orbits in the equatorial plane. They are displayed in Fig. 10. These 3D orbits resemble the Lissajous figures of the hyperdeformed harmonic oscillator with frequency ratio $\omega_\perp{:}\omega_z = 3{:}1$. In the same manner as for the 3D orbits responsible for superdeformations, Fourier peak heights associated with these newly appearing orbits rapidly increase after the bifurcations, reach the maxima and then decline with increasing deformation (see Fig. 8). Thus, also in this case, bifurcations of equatorial orbits (but of different types (p:3:1)) play the major role in the formation of this shell structure.

§8. Oblate superdeformations

Finally let us consider oblate deformations. Figure 11 displays Fourier transforms of quantum spectra for oblate spheroidal cavities with $\delta = -0.3 \sim -0.85$. For $\delta = -0.3$, the two dominant peaks are associated with triangular and tetragonal orbits in the meridian plane. For $\delta = -0.4$, we see a dominant peak at $L \simeq 6.3$ in addition to the peaks associated with the meridian-plane orbits. This new peak is associated with the butterfly-shaped planar orbits (4:1:1) bifurcated from double repetitions of linear orbits along the minor axis.

At $\delta = -0.75$ (axis ratio $\eta = 2$), the other peak at $L \simeq 7.5$ becomes important. This peak is associated with the triple traversals of linear orbits along the minor axis, which bifurcate just at this shape to planer hyperbolic orbits (6:1:1). They make a predominant contribution for $\delta = -0.85$ (peak at $L \simeq 7.1$).

Constant-action lines for these bifurcated orbits (4:1:1) and (6:1:1) are indicated in Figs. 2 and 3. We see clear correspondence between the shapes of these lines and

Fig. 11. Same as Fig. 6 but for oblate cavities with $\delta = -0.3 \sim -0.85$.

the shape of valleys in the oscillating level density. Combining this good correspondence with the behavior of the Fourier peaks mentioned above, it is evident that these periodic orbits are responsible for the shell structure at oblate superdeformations with an axis ratio of approximately 2:1. According to the classification given

in § 4, these are W-mode orbits.

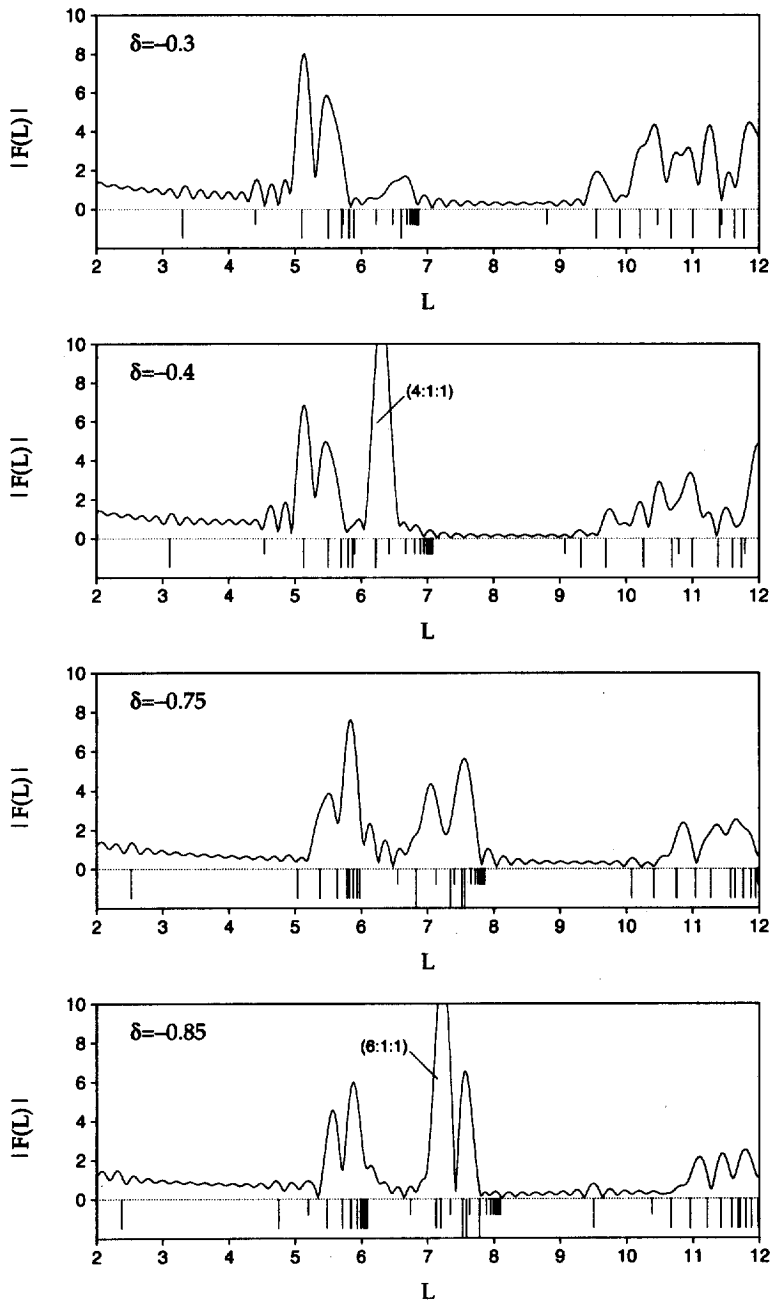In contrast to W-mode orbits, B-mode 3D orbits do not seem very important, although those with $(p{:}t{:}q) = (5{:}1{:}2), (6{:}1{:}2), \cdots$ etc. are already bifurcated from equatorial-plane orbits in the superdeformed region. This is an important difference between the prolate and the oblate superdeformations in the spheroidal cavity model.

§9. Conclusions

Classical periodic orbits responsible for the emergence of the superdeformed shell structure for single-particle motion in spheroidal cavities were identified and their relative contributions to the shell structures were evaluated. Both prolate and oblate superdeformations as well as prolate hyperdeformations were investigated.

Fourier transforms of quantum spectra clearly show that 3D periodic orbits born out of bifurcations of planar orbits in the equatorial plane become predominant at large prolate deformations, while butterfly-shaped planar orbits bifurcated from linear orbits along the minor axis are important at large oblate deformations.

Good correspondence between constant-action lines for these periodic orbits and valley structures in the oscillating part of the smoothed level density confirms the above conclusions.

After writing this paper, we learned that Magner et al. [20] carried out an extensive semiclassical analysis of shell structure in large prolate cavities. In their work, a rather large coarse-graining parameter γ for the level density was used, so that the equatorial-orbit bifurcations discussed in this paper were not clearly seen. It remains a challenge for future study to develop a semiclassical theory capable of treating equatorial-orbit bifurcations, and the phase-space trace formula proposed in Ref. 20) seems to provide a general framework for this aim.

Acknowledgements

References

1) P. J. Nolan and P. J. Twin, Ann. Rev. Nucl. Part. Sci. **38** (1988), 533.
2) R. V. F. Janssens and T. L. Khoo, Ann. Rev. Nucl. Part. Sci. **41** (1991), 321.
3) *Proceedings of the Workshop on Gammasphere Physics*, ed. M. A. Deleplanque, I. Y. Lee and A. O. Macchiavelli (World Scientific, 1996).
4) S. Åberg, H. Flocard and W. Nazarewicz, Ann. Rev. Nucl. Part. Sci. **40** (1990), 439.
5) M. C. Gutzwiller, J. Math. Phys. **12** (1971), 343.
6) R. Balian and C. Bloch, Ann. of Phys. **69** (1972), 76.
7) M. V. Berry and M. Tabor, Proc. R. Soc. London **A349** (1976), 101.
8) M. Brack and R. K. Bhaduri, *Semiclassical Physics* (Addison-Wesley, Reading, 1997).
9) V. M. Strutinsky, A. G. Magner, S. R. Ofengenden and T. Døssing, Z. Phys. **A283** (1977), 269.
10) R. Arvieu, F. Brut, J. Carbonell and J. Touchard, Phys. Rev. **A35** (1987), 2389.
11) Y. Ayant and R. Arvieu, J. of Phys. **A20** (1987), 397.
12) R. Arvieu and Y. Ayant, J. of Phys. **A20** (1987), 1115.
13) H. Frisk, Nucl. Phys. **A511** (1990), 309.

14) H. Nishioka, M. Ohta and S. Okai, Mem. Konan Univ. Sci. Ser. **38**(2) (1991), 1.

15) H. Nishioka, N. Nitanda, M. Ohta and S. Okai, Mem. Konan Univ. Sci. Ser. **39**(2) (1992), 67.

16) K. Arita, A. Sugita and K. Matsuyanagi, *Proc. Int. Symp. on Similarities and Differences between Nuclei and Clusters*, Tsukuba, July 1–4, 1997, AIP Conference Proceedings 416, ed. Y. Abe, I. Arai, S. M. Lee and K. Yabana, p. 393.
   Proc. Int. Symp. on Atomic Nuclei and Metallic Clusters: Finite Many-Fermion Systems, Prague, Sep. 1–5, 1997, Czech. J. of Phys. **48** (1998), 821.
   Proc. Int. Conf. on Nuclear Structure and Related Topics, Dubna, Sep. 9–13, 1997 (Joint Institute for Nuclear Research, 1997), ed. S. N. Ershov, R. V. Jolos and V. V. Voronov, p. 198.

17) T. Mukhopadhyay and S. Pal, Nucl. Phys. **A592** (1995), 291.

18) A. Sugita, K. Arita and K. Matsuyanagi, Prog. Theor. Phys. **100** (1998), 597.

19) H. Nishioka, Klavs Hansen and B. R. Mottelson, Phys. Rev. **B42** (1990), 9377.

20) A. G. Magner, S. N. Fedotkin, F. A. Ivanyuk, P. Meier, M. Brack, S. M. Reimann and H. Koizumi, Ann. der Phys. **6** (1997), 555.
   See also A. G. Magner, S. N. Fedotkin, F. A. Ivanyuk, P. Meier and M. Brack, *Proc. Int. Conf. on Atomic Nuclei and Metallic Clusters: Finite Many-Fermion Systems*, Prague, Sep. 1–5, 1997, Czech. J. of Phys. **48** (1998), 845.

Symmetry Breaking and Bifurcations
in the Periodic Orbit Theory. I

—— Elliptic Billiard ——

Alexander G. Magner,[1,2,3] Sergey N. Fedotkin,[1,2]
Ken-ichiro Arita,[4] Toshiyuki Misu,[5] Kenichi Matsuyanagi,[3]
Thomas Schachner[2] and Matthias Brack[2]

[1]*Institute for Nuclear Research, 252028 Prospekt Nauki 47, Kiev–28, Ukraine*
[2]*Institute for Theoretical Physics, University of Regensburg*
D-93040 Regensburg, Germany
[3]*Department of Physics, Graduate School of Science, Kyoto University*
Kyoto 606-8502, Japan
[4]*Department of Physics, Nagoya Institute of Technology*
Nagoya 466-8555, Japan
[5]*Cyclotron Radio-isotope Center, Tohoku University, Sendai 980-8578, Japan*

We derive an analytical trace formula for the level density of two-dimensional elliptic billiards using an improved stationary phase method. The result is a continuous function of the deformation parameter (eccentricity) through all bifurcation points of the short diameter orbit and its repetitions, and possesses the correct limit of circular billiard at zero eccentricity. Away from the circular limit and the bifurcations, it reduces to the usual (extended) Gutzwiller trace formula, which for the leading-order families of periodic orbits is identical to the result of Berry and Tabor. We show that the circular disk limit of the diameter-orbit contribution is also reached through contributions from closed (periodic and non-periodic) orbits of the hyperbolic type with an even number of reflections from the boundary. We obtain the Maslov indices depending on deformation and energy in terms of the phases of the complex error and Airy functions. We find enhancement of the amplitudes near the common bifurcation points of short-diameter and hyperbolic orbits. The calculated semiclassical level densities and shell energies are in good agreement with the quantum mechanical ones.

§1. Introduction

The periodic orbit theory (POT), developed by Gutzwiller [1,2] for chaotic systems, by Balian and Bloch [3] for cavities, and by Berry and Tabor [4,5] for integrable systems, has proved to be an important semiclassical tool not only for an approximate quantization but also for the description of gross-shell effects in finite fermion systems. [6,7] Gutzwiller's approach has been extended to take into account continuous symmetries [6,8]‑[12] and is therefore applicable to systems with mixed classical dynamics, including the integrable and hard-chaos limits.

An important role is played by the classical degeneracy of the periodic orbits in systems with continuous spatial or dynamical symmetries: the orbits are then not isolated in phase space (as assumed in Gutzwiller's original trace formula, and as is the case in chaotic systems), but occur in degenerate families with identical actions.

The degree of degeneracy $\mathcal{K}$ is defined as the number of independent parameters that are necessary to uniquely specify an orbit within each family. For example, the orbit families with the highest degeneracy in spherical systems with spatial $SO(3)$ symmetry have $\mathcal{K} = 3$, corresponding to the three Euler angles that specify the orientation of an orbit within the plane of motion and the orientation of the plane itself, the orbit families in two-dimensional systems with $U(1)$ rotational symmetry have $\mathcal{K} = 1$, and the isotropic harmonic oscillator in two dimensions has $SU(2)$ symmetry and hence orbit families with $\mathcal{K} = 2$. Orbits with different degeneracies $\mathcal{K}$ may also occur in a single system, such as the spherical cavity discussed by Balian and Bloch[3] where the diameter orbit has $\mathcal{K} = 2$ and all other orbits have $\mathcal{K} = 3$, the spheroidal cavity[13] where $\mathcal{K} = 2$, 1 and 0 occur (the latter corresponding to isolated orbits), and elliptic billiard with $\mathcal{K} = 1$ and 0, as discussed in the present paper.

However, problems arise for all these trace formulae in connection with the breaking of a continuous symmetry and with the bifurcation of stable periodic orbits when a continuous parameter (energy, deformation, external field) is varied. The reason is that at such critical points the standard stationary phase approximation, used for integrations in the derivation of the trace formula, breaks down and leads to divergences and/or discontinuities of the amplitudes in the trace formula. This happens most frequently in mixed systems, but it occurs also in integrable systems. Typical examples are two-dimensional elliptic billiard and the three-dimensional spheroidal cavity. In the former, all repetitions of the short diameter orbits undergo bifurcations at specific deformations, whereby new families of hyperbolic orbits are created. Similarly, in the latter system, the periodic orbits lying in the equatorial plane perpendicular to the symmetry axis bifurcate also at specific deformations, whereby new three-dimensional orbits appear.[13] In both systems, all bifurcations and the limit to the spherical shape lead to divergent amplitudes in the trace formulae (see Refs. 6), 11) and 14) – 21)). Since for each family with a given value of $\mathcal{K}$, the extended Gutzwiller trace formula[6,8 - 10] has an amplitude proportional to $\hbar^{-(1+\mathcal{K}/2)}$, it is evident that the breaking of a continuous symmetry must be accompanied by a discontinuous change of the amplitudes, which manifests itself in the form of a singularity when one attempts to reach the unbroken symmetry limit. (An exceptional situation occurs in anisotropic harmonic oscillators, when changing from irrational to rational frequency ratios: here the divergences of the different periodic orbit contributions have been shown[23] to cancel identically, such that the trace formulae — which are quantum-mechanically exact here — hold for arbitrary frequency ratios, although their analytical form is different in different limits (see also Ref. 7).))

Since symmetry breaking and orbit bifurcations occur in almost all realistic physical systems, there is a definite need to overcome these singularities. The importance of bifurcation effects in connection with the emergence of the 'superdeformed' shell structure in atomic nuclei is emphasized in Refs. 6), 18) and 20) – 22). In order to improve the POT in these critical situations, various methods have been proposed. As in the treatment of continuous symmetries considered in Refs. 8) – 11), they essentially consist of taking some integrals in the derivation of the trace formula more exactly than in the standard stationary phase method (SPM).

Berry and Tabor suggest in Ref. 4) a quite general method to treat bifurcations in integrable systems. Starting from the trace integral for the level density in action-angle variables, they reduce it to a Poisson-sum trace formula and perform all trace integrations except one with the SPM, extending the integration limits from $-\infty$ to $+\infty$. At bifurcations, this leads to singularities in the amplitudes when the stationary points are close to the limits of the integration range. According to Ref. 4), in this case one has to take the integral within the exact finite range. The integration range need not necessarily include the stationary points (in the case of negative or complex stationary points), but the latter are assumed to be close to the integration limits. For integrable systems, this idea was applied to the periodic-orbit families with the highest degeneracies, for which one can carry out the integrals over the action angles exactly, giving 2π for each degree of freedom. [5] This is the starting point of a uniform approximation that was further developed by various authors. [24] ‑ [26]

Another type of uniform approximation was initiated by Ozorio de Almeida and Hannay [27] (see also Ref. 28)) and developed further by Sieber and Schomerus [29] ‑ [31] for various generic types of bifurcations. Writing the trace integral in a phase-space representation, they expand the action around the bifurcation points into so-called normal forms which usually can be integrated analytically with finite results. The correct asymptotic recovery of the Gutzwiller amplitudes far from the bifurcation points can be obtained by a suitable mapping transformation whereby the amplitude function, together with the Jacobian of the mapping transformation, is expanded up to an order consistent with that of the action in the exponent of the integrand. Near the bifurcation points, there is a common contribution of all participating (real or complex, so-called 'ghost') orbits to the trace formula.

A similar technique, starting from the Berry-Tabor approach for integrable systems and using a 'pendulum mapping', was used by Tomsovic, Grinberg and Ullmo [32], [33] to derive a generic uniform approximation for the breaking of orbit families with a one-dimensional degeneracy, corresponding to $U(1)$ symmetry, into pairs of stable and unstable isolated orbits. Finally, some analytical uniform trace formulae for the breaking of the higher-dimensional $SU(2)$ and $SO(3)$ symmetries in specific two- and three-dimensional systems have been derived very recently. [34] Hereby the trace integral was performed over the de Haar measure of the corresponding symmetry groups, as in the derivation of the unperturbed trace formulae for these continuous symmetries, [10] and the mapping was done onto the forms of the action integrals obtained in perturbation theory. [35], [36]

It should be mentioned that all the uniform approximations mentioned above can be used only for one isolated critical point of symmetry breaking or orbit bifurcation. They fail, in particular, [29] ‑ [31], [33], [34] when two critical points are so close that the actions of the participating orbits at these points differ by less than $\sim \hbar$. To our knowledge, no common uniform treatment of two nearby bifurcations (in the above sense), or of a bifurcation near a symmetry-breaking point, has been reported to this time.

In this paper, we propose an approach to simultaneously overcome the divergences due to symmetry breaking and any number of bifurcations in two-dimensional elliptic billiard and the three-dimensional spheroidal cavity. Although our frame-

work is quite general, we limit its application here to elliptic billiard. The three-dimensional spheroidal cavity will be treated in a succeeding paper, [13] and the extension to non-integrable systems is planned for future research. We start from a phase-space trace formula, [11], [37] which after some transformations becomes identical to that obtained from the mixed phase-space representation of the Green function in Refs. 30) and 38), as explained there and below (see §4.3). Analogous versions of the phase-space trace formulae are suggested in Refs. 5) and 10).

In contrast to previous investigations, [4], [5], [24]-[26] we calculate the integrals over angles, also, using the stationary phase method. Note that we also include orbits with lower degeneracies, such as the isolated diameters in elliptic billiard and the equatorial orbits in the spheroidal cavity, thereby extending the method of Ref. 4). Our main point is that the stationary-phase integrals over both action and angle variables are calculated with expansions of the phase and amplitudes, as in the standard SPM, but within *finite* intervals in all cases in which these integrals would lead to divergences if one or both integration limits were taken to ∞ or $-\infty$. We also discuss the role of non-periodic closed orbits (see §5.4). For the Maslov indices, which for the bifurcating orbits depend on the deformation, and near the critical points also on the energy, we follow the basic ideas of Maslov and Fedoryuk. [39]-[42] We obtain separate contributions to the trace formula from the bifurcating periodic orbits, and we remove the singularity of the isolated long diameter (i.e., the separatrix) near the circular shape of the elliptic billiard in a simpler way than in Ref. 26).

In this way we obtain an analytical trace formula for the elliptic billiard system that gives finite and continuous contributions at all deformations, including the circular disk limit and all bifurcation points of the short diameter orbit. Although its derivation and its explicit form are quite different, our final trace formula is similar to the uniform approximations mentioned above in the sense that it is connected smoothly to the standard (extended) Gutzwiller trace formulae for different orbit types with deformations sufficiently far away from all critical points.

§2. Phase-space trace formula in the closed orbit theory

2.1. *Semiclassical trace formula*

The level density $g(\varepsilon)$ is obtained from the Green function $G(\boldsymbol{r}', \boldsymbol{r}''; \varepsilon)$ by taking the imaginary part of its trace:

$$
\begin{aligned}
g(\varepsilon) &= -\frac{1}{\pi} \operatorname{Im} \int d\boldsymbol{r}'' \int d\boldsymbol{r}' \, G(\boldsymbol{r}', \boldsymbol{r}''; \varepsilon) \delta(\boldsymbol{r}'' - \boldsymbol{r}') \\
&= -\frac{1}{\pi} \operatorname{Im} \int d\boldsymbol{r}'' \int d\boldsymbol{r}' \int d\tilde{\boldsymbol{p}} \, G(\boldsymbol{r}', \boldsymbol{r}''; \varepsilon) \exp\left[-\frac{i}{\hbar} \tilde{\boldsymbol{p}} \cdot (\boldsymbol{r}'' - \boldsymbol{r}')\right]. \quad (2\cdot1)
\end{aligned}
$$

Within the semiclassical Gutzwiller theory, [1], [2] the Green function $G(\boldsymbol{r}', \boldsymbol{r}''; \varepsilon)$ can be represented by the sum over all classical trajectories α connecting two spatial points $\boldsymbol{r}'$ and $\boldsymbol{r}''$ at fixed energy ε. Inserting it into (2·1), we obtain the semiclassical

level density

$$g_{\text{scl}}(\varepsilon) = \frac{2}{(2\pi\hbar)^{(3n+1)/2}} \, \text{Im} \sum_\alpha \int d\boldsymbol{r}'' \int d\tilde{\boldsymbol{p}} \int d\boldsymbol{r}' |\mathcal{J}(\boldsymbol{p}', t_\alpha; \boldsymbol{r}'', \varepsilon)|^{1/2}$$

$$\times \exp\left\{ \frac{i}{\hbar} \left[S_\alpha(\boldsymbol{r}', \boldsymbol{r}'', \varepsilon) - \tilde{\boldsymbol{p}} \cdot (\boldsymbol{r}'' - \boldsymbol{r}') \right] - \frac{i\pi}{2}\mu_\alpha \right\}. \tag{2.2}$$

Here $S_\alpha(\boldsymbol{r}', \boldsymbol{r}'', \varepsilon) = \int_{\boldsymbol{r}'}^{\boldsymbol{r}''} d\boldsymbol{r} \cdot \boldsymbol{p}$ is the action along the trajectory α, n is the spatial dimension, and μ_α is related to the number of *conjugate points* (i.e., turning and caustics points along the trajectory).[42] $\mathcal{J}_\alpha(\boldsymbol{p}', t_\alpha; \boldsymbol{r}'', \varepsilon)$ is the Jacobian for the transformation from initial momentum $\boldsymbol{p}'$ (at the point $\boldsymbol{r}'$) and time interval t_α (for the classical motion along the trajectory from initial to final point) to the final coordinate $\boldsymbol{r}''$ and energy ε.

2.2. *Phase space variables*

Integrating over $\boldsymbol{r}'$ in Eq. (2.2) along the direction transverse to the trajectory α with the stationary phase method (SPM), we are left with the integral over the component of $d\boldsymbol{r}'$ parallel to the trajectory, which gives just an energy conserving delta function $\delta(\varepsilon - H(\boldsymbol{r}', \boldsymbol{p}'))$. We hence arrive at the phase-space trace formula[37]

$$g_{\text{scl}}(\varepsilon) = \frac{1}{(2\pi\hbar)^2} \, \text{Re} \sum_\alpha \int d\boldsymbol{r}'' \int d\boldsymbol{p}' \, \delta(\varepsilon - H(\boldsymbol{r}', \boldsymbol{p}')) \, |\mathcal{J}(\boldsymbol{p}''_\perp, \boldsymbol{p}'_\perp)|^{1/2}$$

$$\times \exp\left\{ \frac{i}{\hbar} \left[S_\alpha(\boldsymbol{p}', \boldsymbol{p}'', t_\alpha) + (\boldsymbol{p}'' - \boldsymbol{p}') \cdot \boldsymbol{r}'' \right] - i\nu_\alpha \right\}. \tag{2.3}$$

Here $\mathcal{J}(\boldsymbol{p}''_\perp, \boldsymbol{p}'_\perp)$ is the Jacobian for the transformation from initial to final momentum components $\boldsymbol{p}'_\perp$ and $\boldsymbol{p}''_\perp$, respectively, perpendicular to the trajectory α. This Jacobian is equal to one of the elements of the stability matrix (see, e.g., Ref. 7)). $S_\alpha(\boldsymbol{p}', \boldsymbol{p}'', t_\alpha)$ is the action in the momentum representation

$$S_\alpha(\boldsymbol{p}', \boldsymbol{p}'', t_\alpha) = -\int_{\boldsymbol{p}'}^{\boldsymbol{p}''} d\boldsymbol{p} \cdot \boldsymbol{r}(\boldsymbol{p}), \tag{2.4}$$

which is related to the usual action in coordinate space

$$S_\alpha(\boldsymbol{r}', \boldsymbol{r}'', \varepsilon) = \int_{\boldsymbol{r}'}^{\boldsymbol{r}''} d\boldsymbol{r} \cdot \boldsymbol{p}(\boldsymbol{r}) \tag{2.5}$$

by the Legendre transformation

$$S_\alpha(\boldsymbol{r}', \boldsymbol{r}'', \varepsilon) - \boldsymbol{p}' \cdot (\boldsymbol{r}'' - \boldsymbol{r}') = S_\alpha(\boldsymbol{p}', \boldsymbol{p}'', t_\alpha) + (\boldsymbol{p}'' - \boldsymbol{p}') \cdot \boldsymbol{r}''. \tag{2.6}$$

The phase ν_α in Eq. (2.3) contains, in addition to $\frac{\pi}{2}\mu_\alpha$ in Eq. (2.2), the phases arising from the integration over $\boldsymbol{r}'$ in the stationary phase approximation.

Note that the integrand in the phase-space trace formula (2.3) (except for the exponent related to the phase part proportional to $\boldsymbol{r}''$) is the semiclassical Green function in the mixed representation that contains explicitly an energy-conserving δ-function in our case, unlike the form discussed in Ref. 10). (Consequently, the

momentum components are not independent, which is important for the following application of the stationary phase method; see more details in the next subsection and in §4.) Due to energy conservation, i.e., $H(\boldsymbol{r}', \boldsymbol{p}') \equiv H(\boldsymbol{r}'', \boldsymbol{p}'')$, the trace formula (2·3) can be rewritten in an alternative form where the integration variables are changed from $(\boldsymbol{r}'', \boldsymbol{p}')$ to $(\boldsymbol{r}', \boldsymbol{p}'')$. The sum in (2·3) runs over all isolated classical trajectories α with starting momentum $\boldsymbol{p}'$ and final point $\boldsymbol{r}''$ (or with starting point $\boldsymbol{r}'$ and final momentum $\boldsymbol{p}''$ in the alternative form), for a fixed time interval t_α of the classical motion along α.

2.3.   *Periodic orbit theory*

The trajectories α in the phase space trace formula (2·3) are not necessarily closed orbits in the usual coordinate space. However, after separation of the extended Thomas-Fermi part (corresponding to the 'zero length orbits') and integration over one of the momentum components exploiting the δ-function, we use further semiclassical approximations. We first write the stationary-phase conditions for the integration variables in (2·3). The stationary conditions for the momentum variable $\boldsymbol{p}'$ are the closing condition for the trajectories α in the usual coordinate space, $\boldsymbol{r}' = \boldsymbol{r}''$, and the Jacobian in Eq. (2·3) is unity due to the Liouville Theorem of phase-space volume conservation (see Ref. 7)). The additional stationary-phase conditions for the integration over spatial variables $\boldsymbol{r}''$ selects the periodic orbits, $\boldsymbol{p}' = \boldsymbol{p}''$, and we obtain the POT and all known trace formulas including the Poisson-sum trace formula. [37] We then integrate over components of the phase-space variables exactly if we have identities for them. Other integrations will be done using an improved stationary phase method (ISPM). 'Improved' here means that we carry out the integrations in *finite* ranges, after expanding the exponent of the integrand around the stationary point up to second order terms, and taking the amplitude at the stationary point (or use a higher-order expansion of amplitude and phase, if necessary). All stationary points that appear outside the physical region of integration over the phase-space variables are also taken into account, even if they are complex. In this way we obtain simple and continuous analytical solutions that remain finite at all critical (bifurcation and symmetry-breaking) points. In contrast to other uniform approximations mentioned in the Introduction, our results appear as explicit sums over separate contributions that correspond to the periodic orbits in the asymptotic regions away from the critical points.

§3.   Classical mechanics

3.1.   *Elliptic billiard as an integrable system*

We consider an elliptic billiard with axes a and b (with $a \leq b$) along the x and y coordinate axes, respectively, and ideally reflecting walls. This is an integrable system which can be separated into the elliptic coordinates (u, v) defined in terms of the Cartesian coordinates (x, y) by

$$x = \zeta \cos u \sinh v, \qquad y = \zeta \sin u \cosh v, \qquad \zeta = \sqrt{b^2 - a^2}, \qquad (3·1)$$

with

$$-\pi \leq u \leq \pi, \qquad 0 \leq v < v_b. \tag{3.2}$$

Hereby $(x, y) = (0, \pm\zeta)$ are the foci of ellipses given by $v = $ const, and $v = v_b$ is the elliptic boundary. It is convenient to introduce the deformation parameter $\eta = b/a \geq 1$ and to keep the area of the ellipse constant by setting $ab = R^2$, so that $b = R\sqrt{\eta}$ and $a = R/\sqrt{\eta}$. The second constant of the motion, in addition to the energy ε, is the product of the angular momenta l_- and l_+ with respect to the two foci. For the following, it is advantageous to use the single-valued quantity σ defined by

$$\sigma = 1 + \frac{l_- l_+}{2m\varepsilon\zeta^2}. \tag{3.3}$$

There are two types of orbits, depending on the relative sign of l_- and l_+: *elliptic orbits* circulating around both foci for $l_- l_+ > 0$ or $\sigma > 1$, and librating *hyperbolic orbits* for $l_- l_+ < 0$ or $\sigma < 1$. The names used here indicate that the former are limited to the area between the elliptic boundary given by $v = v_b$ and a confocal elliptic caustic given by $v = v_c$, whereas the latter are confined to the area between the two branches of a hyperbolic caustic given by $u = \pm u_c$ and the elliptic boundary. The critical values for the boundary and the caustics are given by

$$v_b = \operatorname{arccosh}\left(\eta/\sqrt{\eta^2 - 1}\right), \quad v_c = \operatorname{arccosh}(1/\sqrt{\sigma}), \quad u_c = \arcsin(\sqrt{\sigma}). \tag{3.4}$$

In terms of the above quantities, the single-valued action integrals I_u and I_v become

$$I_u = \oint p_u du = \frac{p\zeta}{\pi} \int_{-u_c}^{u_c} du \sqrt{\sigma - \sin^2 u},$$

$$I_v = \oint p_v dv = \frac{p\zeta}{\pi} \int_{v_c}^{v_b} dv \sqrt{\cosh^2 v - \sigma}, \tag{3.5}$$

where $p = \sqrt{2m\varepsilon} = \hbar k$ is the constant classical momentum of the particle. Since the system is integrable, its Hamiltonian depends only on the actions and not on the variables u and v, i.e., $H(I_u, I_v, u, v) \equiv H(I_u, I_v)$.

3.2. *Periodic orbits*

As shown by Berry and Tabor, [4] the periodic orbits of an integrable system can be found by the condition that the angular frequencies (for angle variables conjugate to the actions) have rational ratios. In the present case, these frequencies are given by $\omega_u = \partial H/\partial I_u$, $\omega_v = \partial H/\partial I_v$, so that the periodic orbits are characterized by pairs of positive integers M_u and M_v as

$$\frac{\omega_u}{\omega_v} \equiv \frac{1}{2}\left[1 - \frac{F(\theta, \kappa)}{F(\frac{\pi}{2}, \kappa)}\right] = \frac{M_u}{M_v}, \qquad (M_u \geq 1, \ M_v \geq 2M_u) \tag{3.6}$$

where

$$\kappa = \sin u_c / \cosh v_c, \quad \theta = \arcsin(\cosh v_c / \cosh v_b), \tag{3.7}$$
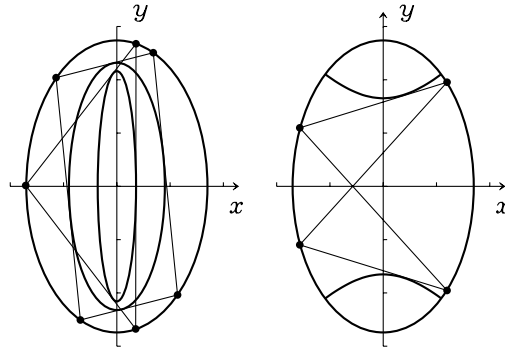
Fig. 1. Some classical periodic orbits in elliptic billiard are represented by thin solid curves. The left-hand side corresponds to elliptic triangular $(1,3)$ and rhomboidal $(1,4)$ orbits, and the right-hand side corresponds to the hyperbolic butterfly orbit $(1,4)$, from Ref. 11).

and $\mathrm{F}(\theta, x)$ is the elliptic integral of the first kind. [47] The greatest common divisor of M_u and M_v corresponds to the repetition number $M = 1, 2, 3, \cdots$ of a primitive periodic orbit (n_u, n_v):

$$(M_u, M_v) = (Mn_u, Mn_v) = M(n_u, n_v). \tag{3·8}$$

The solutions of Eq. (3·6) for κ and θ which correspond to families of degenerate periodic orbits with $\mathcal{K} = 1$ are, labeled accordingly for elliptic and hyperbolic orbits,

$$\left\{ \begin{matrix} \kappa_e = \frac{1}{\sqrt{\sigma}} \\ \kappa_h = \sqrt{\sigma} \end{matrix} \right\}, \quad \left\{ \begin{matrix} \theta_e = \arcsin\left(\sqrt{\sigma(1 - 1/\eta^2)}\right) \\ \theta_h = \arcsin\left(\sqrt{1 - 1/\eta^2}\right) \end{matrix} \right\}. \tag{3·9}$$

Figure 1 shows the shortest periodic orbits of each kind. The degeneracy parameter $\mathcal{K}$ was defined as the number of parameters that specify the orbits within a family with a common action. Due to the separation of variables in elliptic coordinates (3·1) we have two single-valued action integrals I_u and I_v (3·5). They are related through the energy conserving equation $\varepsilon = H(I_u, I_v)$ and can be written in terms of one parameter of the family σ (or l_-l_+); i.e., we have $\mathcal{K} = 1$ (see Refs. 6), 8), 9), 11), 50) for more details).

3.3. *Energy surface*

For the energy surface $\varepsilon = H(I_u, I_v)$ one can get from Eq. (3·5) the parametric equations (A·1) for the elliptic orbits and (A·2) for the hyperbolic orbits. [19] The energy curve (A·1) or (A·2) can also be considered through the single-valued parameter σ or double-valued κ defined within the same range $0 \le \kappa \le 1$ for both kinds of orbits. The solutions σ found from the periodic orbit equations (3·6) for elliptic orbits satisfy the inequality $\sigma > 1$ in the elliptic part (A·1) of the energy curve. On the other hand, $\sigma < 1$ for the hyperbolic part (see Fig. 2(a)). The two regions are separated by the separatrix point $\sigma_s = 1$, corresponding to the long diameter orbit, where the value of the action $I_u = I_u^{(s)}$ is given by

$$I_u^{(s)} = 2p\zeta/\pi. \qquad (\sigma_s = 1) \tag{3·10}$$
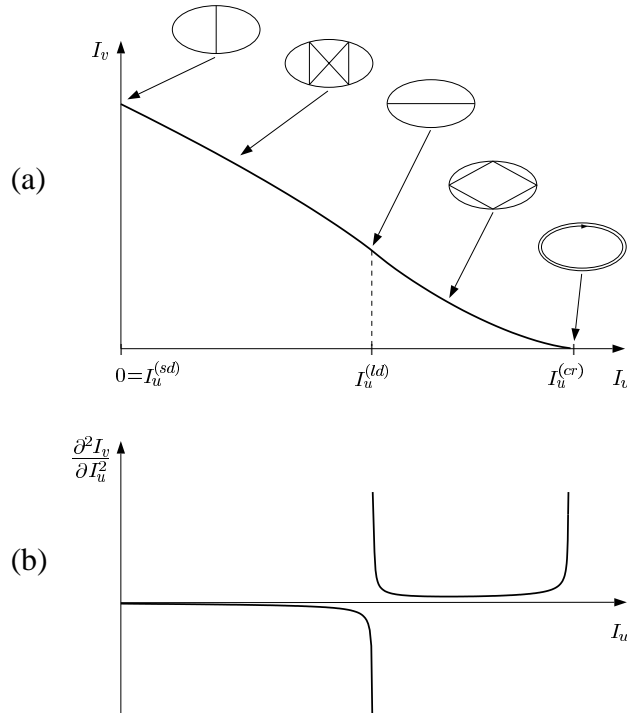
Fig. 2. Energy surface $I_v(I_u)$ and curvature $\partial^2 I_v/\partial I_u^2$ in the upper and lower panels, respectively, from Ref. 19).

Thus, each phase space torus is split into two regions by the separatrix, a hyperbolic region and an elliptic region. In the hyperbolic part $(0 \leq \sigma < 1)$, the action variable I_u changes from 0 to the separatrix value $I_u^{(s)}$. In the elliptic part $(1 < \sigma \leq \sigma_{\text{cr}})$, I_u changes from the separatrix value to the maximum value $I_u^{(\text{cr})}$ that corresponds to a 'creeping' (or 'whispering gallery') orbit and is given by

$$I_u^{(\text{cr})} = \frac{2pR\sqrt{\eta}}{\pi} \, \mathrm{E}\left(\frac{\pi}{2}, \frac{1}{\sqrt{\sigma_{\text{cr}}}}\right) = \frac{2pR\sqrt{\eta}}{\pi} \, \mathrm{E}\left(\frac{\pi}{2}, \frac{\sqrt{\eta^2 - 1}}{\eta}\right),$$
$$\sigma_{\text{cr}} = \cosh^2 v_b = \eta^2/(\eta^2 - 1). \tag{3.11}$$

The short diameter (1,2) and its repetitions $M(1,2)$ correspond to the end point of the hyperbolic region at $\sigma = 0$ $(\kappa = 0)$, which is isolated in phase space $\{\Theta_u, I_u\}$. Equation (3·6) for the periodic orbits at this σ can be solved analytically with respect to θ. Identifying the root $\theta(\eta, n_u/n_v)$ with its definition (3·9) for hyperbolic orbits, we realize that all short diameters $M(1,2)$ bifurcate at the deformations,

$$\eta_{\text{bif}}(M, n) = \frac{1}{\sin(\pi n_u/n_v)} = \frac{1}{\cos(n\pi/2M)}, \quad (n = 1, 2, 3, \cdots, M-1) \tag{3.12}$$

and at each bifurcation a new family of hyperbolic orbits $M(n_u, n_v)$ with Mn_v reflection points is 'born'. The second equation presents the same bifurcation points and

shows explicitly that the bifurcation deformations η_{bif} are also identical to the corresponding divergences of the Gutzwiller amplitudes for short diameters (see Eq. (6.47) of Ref. 7)). Each of the emerging hyperbolic orbits $M_1(M-n, 2M)$ with M_1 repetitions and n from Eq. (3·12) coincides exactly with the corresponding short diameter $M_1 M(1,2)$ repeated $M_1 M$ times at the deformation η_{bif}. For instance, for the triply repeated short diameter $3(1,2)$ $(M_1 = 1, M = 3)$ there are two bifurcation points at the deformations $\eta_{\mathrm{bif}} = 2/\sqrt{3}$ and 2 where the primitive hyperbolic orbits $(2,6)$ $(n = 1)$ and $(1,6)$ $(n = 2)$, respectively, are born (see these orbits in Fig. 3.6 in Ref. 19) and discussion nearby, and also Ref. 14) and Fig. 1a there). However, the short diameters are *isolated* in the phase space of action-angle variables $\{\Theta_u, I_u\}$. They emerge as terms of the periodic orbit sum which are additional to the families of hyperbolic tori (see a more detailed discussion below). The contribution of the primitive short diameter $1(1,2)$ can be calculated by the original Gutzwiller trace formula, except near the circular shape.[7],[19] This formula will be improved near all bifurcation points (3·12) and the circular shape in §5.2.

The long diameter orbits $M(1,2)$ are also characterized by $2M$ reflection points and correspond to a specific *isolated* point in $\{\Theta_u, I_u\}$ space. They are related to the separatrix value $\sigma = 1$ ($\kappa = 1$). Again, their amplitudes can be calculated with the standard Gutzwiller trace formula for isolated orbits, with the same exception near the symmetry-breaking point of the circular shape[7],[19] (see §5.3 for the improved solution in terms of Airy functions near this point).

The limit of a circular disk ($\eta = 1$) may in some sense also be considered as a (one-sided) bifurcation point: Here the family of diameter orbits (with $\mathcal{K} = 1$) break into two isolated diameters with $\mathcal{K} = 0$ and complicated hyperbolic orbit families ($\mathcal{K} = 1$) with $n_u \to \infty$, $n_v \to \infty$, and $n_u : n_v \to 1 : 2$, when the deformation ($\eta > 1$) is turned on. Inversely, the long and short diameters and hyperbolic orbits that have $\mathcal{K} = 0$ and 1 in the ellipse, respectively, merge into the families of diameter orbits with $\mathcal{K} = 1$ as $\eta \to 1$. The discontinuous change of $\mathcal{K}$ at $\eta = 1$ is accompanied by a divergence of the diametric amplitudes in the standard SPM. This is the symmetry-breaking problem discussed in the Introduction and below in §§5.2 and 5.3.

Figure 2(a) shows the energy surface in action space, in the form of the curve $I_v = I_v(\varepsilon, I_u)$ at fixed energy ε. Specific primitive orbits (with $M = 1$) are illustrated, with the arrows pointing to the corresponding stationary points I_u^*: the short diameter (at $I_u^* = 0$ or $\sigma = 0$, with $\Theta_u^* = 0, \pi$), the 'butterfly' (or 'bow-tie') orbit, the long diameter (at $I_u^* = I_u^{(s)}$, with $\sigma = 1$ and $\Theta_u^* = \pm\pi/2$), the rhomboidal orbits with four reflections, and the 'creeping' orbit (at $I_u^* = I_u^{(\mathrm{cr})}$) as the limit of a 'whispering-gallery' mode with a number of reflections $n_v = \infty$ and winding number $n_u = 1$. The limits of the separatrix correspond to infinite values of n_v and n_u for hyperbolic and elliptic orbits with the ratio n_u/n_v going to $1/2$ from either side (see also Ref. 14)). We use the same notation for both short and long diameters in terms of the integers n_u, n_v and M as for the elliptic and hyperbolic one-parametric families, specifying them also by the stationary points in the phase space variables σ (or I_u) for all orbits and Θ_u for the isolated ones, if necessary.

3.4. *Curvature*

A key quantity in the semiclassical theory in terms of the action-angle variables is the curvature K of the energy surface

$$K = \frac{\partial^2 I_v}{\partial I_u^2} = \left(\frac{\partial^2 I_v}{\partial \sigma^2} + \frac{\omega_u}{\omega_v} \frac{\partial^2 I_u}{\partial \sigma^2} \right) \bigg/ \left(\frac{\partial I_u}{\partial \sigma} \right)^2 . \qquad (3\cdot13)$$

The partial derivatives appearing on the right-hand side above are given in Appendix A. Figure 2(b) displays K versus I_u. In the limit $\sigma \to 0$ one finds the curvature for the twice repeated short diameters considered as primitive orbits. [19] For our definition of the (non-repeated) primitive orbits, the curvature K_s is larger by a factor of 2, i.e.,

$$K_s = -\frac{1}{\pi p R \eta^{3/2}}, \qquad (3\cdot14)$$

which is finite and negative for all deformations. K remains negative for the entire hyperbolic part $0 \leq \sigma < 1$ of the curve, whereas it is positive for the elliptic part $1 < \sigma < \sigma_{\mathrm{cr}}$. At the critical points $\sigma = 1$ (separatrix) and at σ_{cr} (creeping point), the curvature diverges. It tends to $-\infty$ as one approaches the separatrix from the hyperbolic side, and to $+\infty$ from the elliptic side. For $\sigma \to \sigma_{\mathrm{cr}}$ it also tends to $+\infty$.

§4. Phase space trace formula in action-angle variables

4.1. *Action-angle variables*

We now transform the phase space trace formula (2·3) from the usual phase space variables $(\boldsymbol{r}, \boldsymbol{p})$ to the angle-action variables $(\boldsymbol{\Theta}, \boldsymbol{I})$. The latter are useful for integrable systems because the Hamiltonian H does not depend on the angle variables $\boldsymbol{\Theta}$, i.e., $H = H(\boldsymbol{I})$. For elliptic billiard one has from (2·3)

$$g_{\mathrm{scl}}(\varepsilon) = \frac{1}{(2\pi\hbar)^2} \mathrm{Re} \sum_\alpha \int d\Theta_u'' \int d\Theta_v'' \int dI_u' \int dI_v' \, \delta(\varepsilon - H(I_u', I_v'))$$

$$\times \exp\left\{ \frac{i}{\hbar} \left[S_\alpha(\boldsymbol{I}', \boldsymbol{I}'', t_\alpha) + (\boldsymbol{I}'' - \boldsymbol{I}') \cdot \boldsymbol{\Theta}'' \right] - i\nu_\alpha \right\}, \qquad (4\cdot1)$$

where $\boldsymbol{\Theta} = \{\Theta_u, \Theta_v\}$ are the angles and $\boldsymbol{I} = \{I_u, I_v\}$ the actions for the elliptic billiard defined in the previous section. For simplicity we omit here and below the Jacobian pre-exponential factor of Eq. (2·3), because this Jacobian taken at the stationary points is always unity when we apply the improved stationary phase method for calculation of the integral over phase space variables, as noted above.

4.2. *Stationary phase method and classical degeneracy*

As noted in the Introduction, we emphasize that *even for integrable systems* the trace integral (4·1) is more general than the Poisson-sum trace formula which is the starting point of Refs. 4) and 5) for the semiclassical derivations. These two trace formulae become identical when we assume that the phase of the exponent also does not depend on the angle variables $\boldsymbol{\Theta}$, like the Hamiltonian. Then, the integral over angles in (4·1) simply gives $(2\pi)^n$, where n is the spatial dimension ($n = 2$ for

the elliptic billiard) (see Ref. 5)). In this case the stationary condition for all angle variables are identities in the 2π interval. This is true for the contribution of the most degenerate classical orbits, like elliptic and hyperbolic orbits, with $\mathcal{K} = 1$ in elliptic billiard. For the case of orbits with smaller degeneracy, like the isolated diameters ($\mathcal{K} = 0$) in elliptic billiard, the exponent phase is strongly dependent on some angles with definite discrete stationary points. We therefore need to integrate over such angles using the standard or improved SPM. Other examples are the equatorial orbits ($\mathcal{K} = 1$) and diameters along the symmetry axis (separatrix with $\mathcal{K} = 0$) in the spheroidal cavity ($n = 3$), the degeneracy parameters of which are smaller than the largest possible value $\mathcal{K} = \mathcal{K}_{\max} = 2$ for the elliptic and hyperbolic orbits in the meridian plane, and for three-dimensional orbits. We have a similar situation also for the diameters with $\mathcal{K} = 2$ in the spherical cavity ($\mathcal{K}_{\max} = 3$), orbits along the symmetry axis for axially-symmetric cavities, and so on. Thus, the stationary conditions with respect to the angle variables for orbits with smaller degeneracies are not identities. Moreover, the stationary points in the cases mentioned above occupy subspaces of the phase space which are isolated in the rational tori that lead to separate contributions to the trace formula, except for the most degenerate orbit families, as we see below for the case of elliptic billiard.

4.3. *Stationary phase conditions*

We first perform the integral over I'_v in Eq. (4·1) exactly. Due to the energy conserving δ-function, we are left with the integrals over the angles Θ''_u and Θ''_v and the action I'_u:

$$g_{\mathrm{scl}}(\varepsilon) = \frac{1}{(2\pi\hbar)^2} \, \mathrm{Re} \sum_\alpha \int d\Theta''_u \int d\Theta''_v \int dI'_u \, \frac{1}{|\omega'_v|}$$
$$\times \exp\left[\frac{i}{\hbar}\left(S_\alpha(\boldsymbol{I'}, \boldsymbol{I''}, t_\alpha) + (\boldsymbol{I''} - \boldsymbol{I'}) \cdot \boldsymbol{\Theta''}\right) - i\nu_\alpha\right], \qquad (4\cdot2)$$

$$S_\alpha(\boldsymbol{I'}, \boldsymbol{I''}, t_\alpha) = -\int_{\boldsymbol{I'}}^{\boldsymbol{I''}} d\boldsymbol{I} \cdot \boldsymbol{\Theta}(\boldsymbol{I}). \qquad (4\cdot3)$$

We first write down the stationary phase equation for I_u:

$$\left(\frac{\partial S_\alpha(\boldsymbol{I'}, \boldsymbol{I''}, t_\alpha)}{\partial I'_u}\right)^* - \Theta''_u \equiv \Theta'_u - \Theta''_u = 2\pi M_u, \qquad (4\cdot4)$$

where M_u is an integer. The star indicates that we take the quantities at the stationary point $I'_u = I^*_u$. We now use the Legendre transformation (2·6), which reads

$$S_\alpha(\boldsymbol{I'}, \boldsymbol{I''}, t_\alpha) + (\boldsymbol{I''} - \boldsymbol{I'}) \cdot \boldsymbol{\Theta''} = S_\alpha(\boldsymbol{\Theta''}, \boldsymbol{\Theta'}, \varepsilon) - \boldsymbol{I'} \cdot (\boldsymbol{\Theta''} - \boldsymbol{\Theta'}), \qquad (4\cdot5)$$

$$S_\alpha(\boldsymbol{\Theta'}, \boldsymbol{\Theta''}, \varepsilon) = \int_{\boldsymbol{\Theta'}}^{\boldsymbol{\Theta''}} d\boldsymbol{\Theta} \cdot \boldsymbol{I}(\boldsymbol{\Theta}).$$

Making use of this transformation, the stationary phase conditions for angles Θ_u and Θ_v are written as

$$\left(\frac{\partial S_\alpha(\boldsymbol{\Theta'}, \boldsymbol{\Theta''}, \varepsilon)}{\partial \boldsymbol{\Theta''}} + \frac{\partial S_\alpha(\boldsymbol{\Theta'}, \boldsymbol{\Theta''}, \varepsilon)}{\partial \boldsymbol{\Theta'}}\right)^* \equiv \boldsymbol{I''} - \boldsymbol{I'} = 0. \qquad (4\cdot6)$$

For the following derivations we have to decide which stationary phase conditions from Eqs. (4·4) and (4·6) are identities for the finite volume of the phase-space tori and which are equations for the isolated stationary points. To do this, we must calculate separately the contributions from the most degenerate (elliptic and hyperbolic) families ($\mathcal{K} = 1$) to the improved trace formula and those from diameters in elliptic billiard. These two contributions are different with respect to the above-mentioned decision concerning the integration over the angles $\boldsymbol{\Theta}$. After the integration over one of the angle variables, say Θ_v, corresponding to the identity in the stationary phase conditions (4·6) due to an invariance of the action along the periodic orbit in Eq. (4·2), one gets Eq. (7) of Ref. 30) derived earlier by Bruno. [38] Thus, we obtain the result of Refs. 30) and 38) within periodic orbit theory. Our phase-space trace formula (2·3) is more general because it can be applied to more exact calculations of the level density, without using the stationary phase conditions like Eqs. (4·6), in terms of closed (periodic and non-periodic) orbits.

Note that we have separate contributions coming from each kind of family and isolated orbits *even near the bifurcation points* (3·12) where we have the end point. Taking the deformation within a small distance from η_{bif}, we are left with two separate close stationary points and then use the Maslov-Fedoryuk theory [39]–[42] as for caustic and turning points. Finally, after the integration using the improved stationary phase method, we look at the limit $\eta \rightarrow \eta_{\text{bif}}$ to the bifurcation point. In particular, this idea of Maslov and Fedoryuk is applied in Appendix B for the calculation of the contribution of the long diameter at the separatrix.

§5. Trace formulas for the elliptic billiard

5.1. *Elliptic and hyperbolic orbit families* ($\mathcal{K} = n - 1 = 1$)

Each family of elliptic or hyperbolic orbits with a common action occupies a two-dimensional finite area in the elliptic billiard. In this case, the stationary conditions (4·6) for the integration over the angle variables Θ_u and Θ_v become identities, since the integrand does not depend on the angle variables, and we have the conservation of the action variable $I'_u = I''_u = I_u$ fulfilled identically along each classical trajectory α. Taking the integrals over $\boldsymbol{\Theta}$ gives a factor of $(2\pi)^2$, and we are left with the Poisson-sum trace formula like in Refs. 4) and 5):

$$
\begin{aligned}
g_{\text{scl}}(\varepsilon) &= \frac{1}{\hbar^2} \operatorname{Re} \sum_{\boldsymbol{M}} \int d\boldsymbol{I} \, \delta(\varepsilon - H(\boldsymbol{I})) \exp\left[\frac{2\pi i}{\hbar} \boldsymbol{M} \cdot \boldsymbol{I} - i\nu_{\boldsymbol{M}}\right] \\
&= \frac{1}{\hbar^2} \operatorname{Re} \sum_{\boldsymbol{M}} \int dI_u \, \frac{1}{|\omega_v|} \exp\left[\frac{2\pi i}{\hbar} \boldsymbol{M} \cdot \boldsymbol{I} - i\nu_{\boldsymbol{M}}\right].
\end{aligned} \tag{5·1}
$$

Here $\boldsymbol{M} = (M_u, M_v)$ are integers which correspond to those in Eq. (3·8). Next we transform the integration variable in the last expression of Eq. (5·1) from I_u to σ defined by (3·3). Thus, the level density component $\delta g_{\text{scl},1}$ related to the one-parameter families can be written as a sum of contributions from the hyperbolic

$(\delta g_{\mathrm{scl},1}^{(h)}(\varepsilon))$ and the elliptic $(\delta g_{\mathrm{scl},1}^{(e)}(\varepsilon))$ parts of the tori. Their sum is

$$\delta g_{\mathrm{scl},1}(\varepsilon) = \frac{1}{\pi \varepsilon_0 p R^2} \,\mathrm{Re} \sum_{\boldsymbol{M}} \frac{1}{n_v} \int_0^{\sigma_{\mathrm{cr}}} d\sigma L_{\boldsymbol{M}} \frac{\partial I_u}{\partial \sigma} \exp\left[\frac{2\pi i}{\hbar} \boldsymbol{M} \cdot \boldsymbol{I}(\sigma) - i\nu_{\boldsymbol{M}}\right], \quad (5\cdot2)$$

where $\varepsilon_0 = \hbar^2/(2mR^2)$, $\boldsymbol{I}(\sigma)$ are the actions defined by Eqs. (3·5), $L_{\boldsymbol{M}}$ are the 'lengths' of the primitive orbits with $M = 1$ given by

$$L_{\boldsymbol{M}} = \frac{2\pi n_v p}{m\omega_v}$$
$$= 2n_v b \,\sin\theta \left[\mathrm{E}(\theta, \kappa) - \frac{\mathrm{F}(\theta, \kappa)}{\mathrm{F}(\frac{\pi}{2}, \kappa)} \,\mathrm{E}(\tfrac{\pi}{2}, \kappa) + \cot\theta \sqrt{1 - \kappa^2 \sin^2\theta}\right], \quad (5\cdot3)$$

and $\theta(\sigma)$ and $\kappa(\sigma)$ are defined by Eq. (3·9). The 'lengths' become the true lengths of the corresponding periodic orbits when they are taken at σ equal to the real positive roots of Eq. (3·6) inside the integration range. For other values of σ, the 'lengths' are nothing else than the functions (5·3) introduced in place of ω_v for convenience. The integration range from the bifurcation point $\sigma = 0$ to the separatrix $\sigma_s = 1$ covers the contributions of all hyperbolic orbits. The remaining part of Eq. (5·2) from $\sigma = 1$ to the creeping value σ_{cr} gives the contributions from the elliptic tori.

As we see below, the choice of σ as the integration variable significantly improves the precision of the SPM. We hence apply the stationary condition (4·4) for the phase in the integrands of Eq. (5·2) with respect to σ rather than to I_u. With Eqs. (3·9), this condition becomes identical to Eq. (3·6) and determines the stationary phase point $\sigma' = \sigma'' = \sigma^*$ related to $I'_u = I''_u = I^*_u$. We have used here the conservation of σ (or the additional integral of motion $l_+ l_-$) along the periodic orbit. We now expand the phase up to second order as

$$S_\alpha(\boldsymbol{I}', \boldsymbol{I}'', t_\alpha) + (\boldsymbol{I}'' - \boldsymbol{I}') \cdot \boldsymbol{\Theta}'' = 2\pi \boldsymbol{M} \cdot \boldsymbol{I} = S_\beta(\varepsilon) + \frac{1}{2} J_\beta^\parallel (\sigma - \sigma^*)^2, \quad (5\cdot4)$$

where S_β is the action along the periodic orbit β determined by Eq. (3·6),

$$S_\beta(\varepsilon) = 2\pi M (n_u I_u(\sigma^*) + n_v I_v(\sigma^*)), \quad (5\cdot5)$$

and $J_\beta^\parallel$ is the Jacobian stability factor with respect to σ along the energy surface:

$$J_\beta^\parallel = \left(\frac{\partial^2 S}{\partial \sigma^2}\right)_{\sigma = \sigma^*, \beta} = 2\pi M \left(n_u \frac{\partial^2 I_u}{\partial \sigma^2} + n_v \frac{\partial^2 I_v}{\partial \sigma^2}\right)_{\sigma = \sigma^*, \beta}. \quad (5\cdot6)$$

It is related to the curvature K_β (3·13) of the energy surface by

$$J_\beta^\parallel = 2\pi M n_v K_\beta \left(\frac{\partial I_u}{\partial \sigma}\right)_{\sigma = \sigma^*, \beta}^2 = 2\pi M n_v \epsilon |K_\beta| \left(\frac{\partial I_u}{\partial \sigma}\right)_{\sigma = \sigma^*, \beta}^2, \quad (5\cdot7)$$

where $\epsilon = +1$ for elliptic orbits and $\epsilon = -1$ for hyperbolic orbits. We now substitute the expansion (5·4) and take the pre-exponential factor off the integral in Eq. (5·2).

For the sake of simplicity, we only consider the lowest order in the expansion of the phase and the pre-exponential factor in Eq. (5·2) in the variable σ, although higher-order expansions can in principle be used to improve the precision of the SPM. Thus, we are left with the integral from $\sigma = 0$ to 1 for the hyperbolic orbits, and from $\sigma = 1$ to σ_{cr} for the elliptic orbits.

When the stationary point σ^* is far from the limits of these intervals, one can extend the integration range from $-\infty$ to ∞ and get the result of the standard POT.[4] Near the bifurcation points (3·12) of the short diameter orbit (where the hyperbolic orbit families appear), however, the stationary point σ^* is close to zero. In this case we cannot extend the lower limit to $-\infty$, but, rather, we must take the integral exactly from $\sigma = 0$. On the other hand, when the stationary point σ^* approaches the integration limit σ_s (3·10) or σ_{cr} (3·11), hyperbolic or elliptic orbits with an increasing number n_v of corners appear. In these cases, too, we cannot extend the integration limits to $\pm\infty$. Taking the integral over σ within the *finite limits*, we obtain a trace formula in terms of complex Fresnel functions or generalized error functions. The contributions of the one-parameter orbit families $\delta g_{\mathrm{scl},1}(\varepsilon)$ are then given in the form

$$\delta g_{\mathrm{scl},1}(\varepsilon) = \mathrm{Re} \sum_\beta A_\beta^{(1)}(\varepsilon) \exp\left[ikL_\beta - i\nu_\beta^{(\mathrm{tot})}\right]. \tag{5·8}$$

Here, the sum is taken over both elliptic and hyperbolic orbit families, $k = \sqrt{2m\varepsilon}/\hbar$. The amplitude $A_\beta^{(1)} = |\mathcal{A}_\beta^{(1)}|$ of the orbit family β is given through

$$\mathcal{A}_\beta^{(1)} = \frac{L_\beta}{2\varepsilon_0 \pi k R^2 \sqrt{-\epsilon i M^3 n_v^3 |\hbar K_\beta|}} \, \mathrm{erf}\left(\mathcal{Z}_{\beta,1}^\parallel, \mathcal{Z}_{\beta,2}^\parallel\right). \tag{5·9}$$

Here L_β is the 'length' of the orbit family (5·3) corresponding to the stationary point σ^* ($M = 1$). We have introduced here the generalized error function $\mathrm{erf}(z_1, z_2)$,

$$\mathrm{erf}(z_1, z_2) = \frac{2}{\sqrt{\pi}} \int_{z_1}^{z_2} dz\, e^{-z^2} = \mathrm{erf}(z_2) - \mathrm{erf}(z_1), \tag{5·10}$$

$\mathrm{erf}(z)$ being the standard error function[47] with (complex) argument z. The complex quantities $\mathcal{Z}_{\beta,1}^\parallel$ and $\mathcal{Z}_{\beta,2}^\parallel$ in (5·9) are given in terms of the Jacobian $J_\beta^\parallel$ (5·6) and the stationary points σ^*:

$$\mathcal{Z}_{\beta,1}^\parallel = \sqrt{\frac{\epsilon i |J_\beta^\parallel|}{2\hbar}}\left(\sigma_{\min}^{(\epsilon)} - \sigma^*\right), \qquad \mathcal{Z}_{\beta,2}^\parallel = \sqrt{\frac{\epsilon i |J_\beta^\parallel|}{2\hbar}}\left(\sigma_{\max}^{(\epsilon)} - \sigma^*\right), \tag{5·11}$$

where $\sigma_{\min}^{(\epsilon)}$ and $\sigma_{\max}^{(\epsilon)}$ are related to the integration limits by

$$\sigma_{\min}^{(\epsilon)} = \left\{\begin{array}{ll} 1, & \epsilon = 1 \\ 0, & \epsilon = -1 \end{array}\right\}, \qquad \sigma_{\max}^{(\epsilon)} = \left\{\begin{array}{ll} \sigma_{\mathrm{cr}}, & \epsilon = 1 \\ 1\,, & \epsilon = -1 \end{array}\right\}. \tag{5·12}$$

The phases $\nu_\beta^{(\mathrm{tot})}$ in (5·8) are related to the Maslov indices. They have a constant part ν_β, which is independent of the deformation η and energy ε. At deformations

that are far enough from bifurcation points, such that the stationary points are far enough from the integration limits, we can determine this asymptotic part ν_β by transforming the error functions to Fresnel functions [47] with real limits and extending the integration limits to $\pm\infty$. We thereby arrive at the amplitude $A_\beta^{(1)}$ of the standard POT, [4), 11), 44)]

$$A_\beta^{(1)} = \frac{L_\beta}{\varepsilon_0 \pi k R^2 \sqrt{M^3 n_v^3 \, |\hbar K_\beta|}}, \tag{5.13}$$

and ν_β is determined by the number of turning and caustic points, as in the theory of Maslov and Fedoryuk. [39) - 42)] In terms of the numbers n_v and n_u and the repetition number M, it is given by

$$\nu_\beta = \frac{3\pi}{2} n_v M \qquad\qquad \text{for } \epsilon = +1,$$
$$\nu_\beta = \frac{\pi}{2}(2n_u + 2n_v)M \qquad \text{for } \epsilon = -1. \tag{5.14}$$

From Eqs. (5.8), (5.9) and (5.14) we determine an extra contribution to the total phase $\nu_\beta^{(\text{tot})}$

$$\nu_\beta^{(\text{tot})} = \nu_\beta^{(\text{tot})}(\eta, kR) = \nu_\beta - \frac{\pi}{4}\epsilon - \arg\left\{\text{erf}\left(\mathcal{Z}_{\beta,1}^\parallel, \mathcal{Z}_{\beta,2}^\parallel\right)\right\}, \tag{5.15}$$

which analytically connects the asymptotic values ν_β and depends on the energy through kR. The final result (5.15) for the total phase depends also on the deformation parameter η.

Note that σ^* is negative for $\eta < \eta_{\text{bif}}$. In the derivation of Eqs. (5.8) and (5.9), we have changed the integration variable from σ to $z = \sqrt{-\epsilon i |J_\beta^\parallel|/(2\hbar)}(\sigma - \sigma^*)$ in order to transfer the kR and η dependence of the integrand to the limits of the complex generalized error functions (5.10). Note also that our energy and deformation dependent phase $\nu_\beta^{(\text{tot})}$ are essentially different from those in Ref. 26) and much simpler in analytical structure. In contrast to Refs. 26) and 29), we have not used any assumption concerning the smoothness of the phase. Our solution is regular at the separatrix and creeping points, at all bifurcation points, and in the circular disk limit. We easily get the correct circular disk limit [46)] and the Berry-Tabor result [4)] for larger deformations far from the bifurcations.

Equations (5.8), (5.9) and (5.15) represent one of our central results concerning the contributions of the degenerate orbit families ($\mathcal{K} = 1$) that simultaneously solves the symmetry-breaking problem for both hyperbolic and elliptic orbits: near $\eta = 1$ and other bifurcation points for all hyperbolic orbits, and near the separatrix σ_s and the 'creeping' point σ_{cr} for all elliptic orbits. The additional contributions of the isolated orbits ($\mathcal{K} = 0$) will be derived in the following two subsections.

Formally, our result (5.8) coincides with the first main term of the Berry-Tabor trace formula (see Eq. (24) of Ref. 4)) using the simplest method for the expansions near the stationary point instead of a more general and more complicated mapping procedure. The next two terms of their formula, being of higher order in $\sqrt{\hbar}$, can be

obtained by taking account of the linear term in the expansion of the pre-exponential factor over $\sigma - \sigma^*$. They were neglected in our approach because we are interested here only in the main term of the SPM expansion, in order to get the simplest possible solution of the bifurcation problem. With the higher-order corrections, we should take into account the fact that the ratio of the contribution of the linear term to that of the zero-order term of the amplitude is of the same order as the relative contribution of the next order (cubic) term in the expansion of the phase. For a consistent treatment of the level density in the semiclassical asymptotic approximation $kR \gg 1$, one would have to collect both corrections.

5.2. *Short diametric orbits* ($\mathcal{K} = 0$)

For the contribution of the isolated ($\mathcal{K} = 0$) diameters, only one of the two stationary phase conditions (4·6) corresponding to the Θ_v variable is an identity. The other one for Θ_u is a nontrivial equation for the discrete number of stationary points that differs by integer multiples of π. Indeed, due to the integrability of motion in the elliptic billiard one has

$$\Theta_u = \omega_u t + \Theta_u^{(0)}, \qquad \Theta_v = \omega_v t + \Theta_v^{(0)}, \qquad (5\cdot16)$$

where $\boldsymbol{\Theta}^{(0)}$ is the initial angle $\boldsymbol{\Theta}$ at $t = 0$. Since the frequency ω_u in Eq. (5·16) is zero for short diameters, for instance, there is no room for an identity in the stationary phase condition for the variable Θ_u in Eq. (4·2). Hence, the Poisson-sum trace formula cannot be applied to get the contribution from the short diameters, unlike in the derivations in Ref. 24). The stationary points for the integration in Eq. (4·2) over the angle Θ_u for short diameters are constants $\Theta_u^* = \pi M$ for $M = 0, \pm 1, \cdots$. Due to the periodicity of the angle variable with the period 2π, we must deal with the two stationary points $\Theta_u^* = 0$ and π in the integration interval from $-\pi$ to π over the angle Θ_u in Eq. (4·2). We can then reduce the initial integration interval for the angle variable Θ_u to the region from $-\pi/2$ to $\pi/2$, taking into account the integration over other angles (related to the motion along the same periodic orbit in the opposite direction) by the factor 2 (due to the time reversal invariance of the Hamiltonian). Within this reduced integration interval, only one stationary point $\Theta_u^* = 0$ must be taken into account in the calculation with the improved stationary phase method.

For the other variable Θ_v, for the short diameters, we have an identity in the corresponding equation from Eq. (4·6). The integrand in (4·2) is independent of the variable Θ_v, and the integral gives simply 2π. Thus, the integrand for the contribution of the short diameters essentially depends only on Θ_u and possesses relevant stationary points. When we take this integral using the SSPM we immediately obtain Gutzwiller's result for short diameters with his stability factor in the denominator. This stability factor is zero at the bifurcation points. Below, we obtain the short diameter term improved at the bifurcation points. For this purpose we first follow the same method in the integration over Θ_u and I_u as we did in the integration over I_u for elliptic and hyperbolic orbits with highest degeneracies. The integration interval over I_u for the contribution of the short diameters is also finite from 0 to the maximal "creeping" value $I_u^{(\mathrm{cr})}$ (3·11), which corresponds to the region of the σ

variable $0 \leq \sigma \leq \sigma_{\mathrm{cr}}$.

Thus, for short diameters, we use the stationary condition for the angle variable Θ_u and expand the phase of the exponent in Eq. (4·2) about the short diameter,

$$S_\alpha = S_{sM}(\varepsilon) + \frac{1}{2} J_{sM}^\perp \Theta_u^2, \qquad (5\cdot17)$$

with $S_{sM}(\varepsilon)$ being the action along the short diameter, $S_{sM}(\varepsilon) = 4\,p(\varepsilon)\,aM$, and $\Theta_u^* = 0$. $J_{sM}^\perp$ is the Jacobian corresponding to the second variation of the action S_α with respect to the angle variable Θ_u,

$$J_{sM}^\perp = \left(\frac{\partial^2 S_\alpha}{\partial \Theta_u'^2} + 2\frac{\partial^2 S_\alpha}{\partial \Theta_u' \partial \Theta_u''} + \frac{\partial^2 S_\alpha}{\partial \Theta_u''^2} \right)_{sM} = \left(-\frac{\partial I_u'}{\partial \Theta_u'} - 2\frac{\partial I_u'}{\partial \Theta_u''} + \frac{\partial I_u''}{\partial \Theta_u''} \right)_{sM},$$
$$(5\cdot18)$$

according to Eq. (4·5). The Jacobian $J_{sM}^\perp$ is expressed in terms of the diametric curvature K_s (3·14) and Gutzwiller's stability factor F_{sM},

$$F_{sM} = -\left(\frac{-\frac{\partial I_u'}{\partial \Theta_u'} - 2\frac{\partial I_u'}{\partial \Theta_u''} + \frac{\partial I_u''}{\partial \Theta_u''}}{\frac{\partial I_u'}{\partial \Theta_u''}} \right)_{sM} = 4\sin^2\left[M \arccos(2\eta^{-2} - 1) \right], \quad (5\cdot19)$$

which is independent of the choice of the phase space variables

$$J_{sM}^\perp = F_{sM} J_{sM}^{(\Theta)} = -\frac{F_{sM}}{4\pi M K_s}, \qquad (5\cdot20)$$

where

$$J_{sM}^{(\Theta)} = -\left(\frac{\partial I_u'}{\partial \Theta_u''} \right)_{sM} \qquad (5\cdot21)$$

and K_s is the short diametric curvature given by Eq. (3·14) ($\epsilon = -1$). In the second equality of Eq. (5·20) we used a simple relation between the Jacobians $J_{sM}^{(\Theta)}$, $J_\beta^{\parallel}$ and K_s. This relation follows directly from their definitions and simple properties of the Jacobians:

$$\frac{J_{sM}^{(\Theta)} J_\beta^{\parallel}}{\left(\frac{\partial I_u}{\partial \sigma} \right)^2} = -1. \qquad (5\cdot22)$$

After the exact integration over Θ_v in Eq. (4·2) which gives 2π as explained above, we substitute the expansion (5·17) of the action S_α and take the amplitude factor at the stationary point $\Theta_u^* = 0$. We take the integral over Θ_u within the finite range from $-\pi/2$ to $\pi/2$. This can be reduced further to the integral from 0 to $\pi/2$ with the factor 2 due to spatial symmetry, in addition to the time reversibility factor 2 mentioned above. Integrating over I_u as in the previous subsection, one finally gets

$$\delta g_{\mathrm{scl},0}^{(s)} = \mathrm{Re} \sum_M \mathcal{A}_{sM}^{(0)} \exp[ikL_{sM} - i\nu_{sM}]. \qquad (5\cdot23)$$

Here, L_{sM} is the length of the diameter orbit, $L_{sM} = 4Ma$,

$$\mathcal{A}_{sM}^{(0)} = \frac{2a}{\varepsilon_0 \pi k R^2} \frac{1}{\sqrt{|F_{sM}|}} \operatorname{erf}\left(\mathcal{Z}_{sM,1}^{\parallel}, \mathcal{Z}_{sM,2}^{\parallel}\right) \operatorname{erf}\left(\mathcal{Z}_{sM,1}^{\perp}, \mathcal{Z}_{sM,2}^{\perp}\right), \qquad (5\cdot24)$$

and $\mathcal{Z}_{sM,1}$ and $\mathcal{Z}_{sM,2}$ are defined by

$$\mathcal{Z}_{sM,1}^{\parallel} = 0, \quad \mathcal{Z}_{sM,2}^{\parallel} = \sqrt{\frac{i\left|J_{sM}^{\parallel}\right|}{2\hbar}}\sigma_{\mathrm{cr}}, \qquad (5\cdot25)$$

$$\mathcal{Z}_{sM,1}^{\perp} = \sqrt{\frac{-i\left|J_{sM}^{\perp}\right|}{2\hbar}}\Theta_u' = 0, \quad \mathcal{Z}_{sM,2}^{\perp} = \sqrt{\frac{-i\left|J_{sM}^{\perp}\right|}{2\hbar}}\Theta_u'' = \frac{\pi}{2}\sqrt{\frac{-i\left|J_{sM}^{\perp}\right|}{2\hbar}}. \quad (5\cdot26)$$

For any finite deformation and sufficiently large kR, Eq. (5·24) is greatly simplified by using asymptotics for the first error function and one obtains

$$\mathcal{A}_{sM}^{(0)} = \frac{2a}{\varepsilon_0 \pi k R^2} \frac{1}{\sqrt{|F_{sM}|}} \operatorname{erf}\left(\mathcal{Z}_{sM,1}^{\perp}, \mathcal{Z}_{sM,2}^{\perp}\right). \qquad (5\cdot27)$$

The constant part ν_{sM} of the Maslov phases in Eq. (5·23) is obtained in the same way as in the previous subsection:

$$\nu_{sM} = 3\pi M - \frac{\pi}{2}. \qquad (5\cdot28)$$

For deformations far from the bifurcation points, the level density $\delta g_{\mathrm{scl},0}^{(s)}$ (5·23) asymptotically reduces to the standard Gutzwiller formula for isolated short diameters,[1),2),7)]

$$\delta g_{\mathrm{scl},0}^{(s)}(\varepsilon) \to \frac{2a}{\varepsilon_0 \pi k R^2} \sum_M \frac{1}{\sqrt{F_{sM}}} \sin(kL_{sM} - \nu_{sM}). \qquad (5\cdot29)$$

The total Maslov phase $\nu_{sM}^{(\mathrm{tot})}$ for the diameter orbits is

$$\nu_{sM}^{(\mathrm{tot})} = \nu_{sM} - \arg\left\{\operatorname{erf}\left(\mathcal{Z}_{1,sM}^{\parallel}, \mathcal{Z}_{2,sM}^{\parallel}\right)\right\} - \arg\left\{\operatorname{erf}\left(\mathcal{Z}_{1,sM}^{\perp}, \mathcal{Z}_{2,sM}^{\perp}\right)\right\}$$
$$\approx \nu_{sM} - \arg\left\{\operatorname{erf}\left(\mathcal{Z}_{1,sM}^{\perp}, \mathcal{Z}_{2,sM}^{\perp}\right)\right\} \qquad (5\cdot30)$$

for large kR.

Near the bifurcation points where $F_{sM} \to 0$, one obtains from Eq. (5·23) the finite limit,

$$\delta g_{\mathrm{scl},0}^{(s)} \to \frac{a}{\pi \varepsilon_0 k R^2} \operatorname{Re} \sum_M \frac{1}{\sqrt{2Mi\hbar\left|K_s\right|}} \operatorname{erf}\left(\mathcal{Z}_{sM,1}^{\parallel}, \mathcal{Z}_{sM,2}^{\parallel}\right) e^{i(kL_{sM} - \nu_{sM})}$$
$$\approx \frac{\eta^{1/4}}{\varepsilon_0 \sqrt{2\pi kR}} \operatorname{Re} \sum_M \frac{1}{\sqrt{M}} e^{i(kL_{sM} - \nu_{sM} - \pi/4)}. \qquad (5\cdot31)$$

Note that the two last terms in Eq. (24) of Ref. 4) are smaller than the above contribution (5·31) at the bifurcation deformations η_{bif} (3·12) by the factor $\sqrt{kR}$.

Therefore, these two terms are the next order semiclassical corrections and can be neglected in comparison with the term (5·31) obtained above. Moreover, the ISPM solution (5·23) is not related to the "diametric" part of the Poisson-sum trace formula (5·2) with $n_u = 1$ and $n_v = 2$, as follows from the derivations in Ref. 24) ($\alpha_1 = 2, \alpha_2 = \lambda = 2$ in the notation of Ref. 24) applied for short diameters in elliptic billiard, $\alpha_1 = 2n_u$) (see below for the more detailed discussion). Thus, our derivation is essentially different from that suggested earlier in Ref. 24) (where the last two terms in Eq. (24) of Ref. 4) are retained without considering the contribution (5·31)).

Taking the limit of Eq. (5·31) for $\eta \to 1$ we obtain the same contribution of the diameters in the circular disk [46] as found from the "diametric" part of the Poisson-sum trace formula,

$$\delta g_{\mathrm{scl},1}^{(d)}(\varepsilon) = \frac{1}{\varepsilon_0 \sqrt{2\pi kR}} \sum_M \frac{1}{\sqrt{M}} \sin(kL_{sM} - \nu_{sM} + \pi/4). \qquad (5\cdot32)$$

The value in this limit is larger by the factor $\sqrt{kR}$ than the standard Gutzwiller result for isolated orbits as at any other bifurcation points.

5.3. *Long diameters and the separatrix*

As shown in §2, the curvature K goes to $+\infty$ from the right side and $-\infty$ from the left side near the separatrix ($\sigma = 1$) with the same modulus (see Eqs. (A·5), (A·6) and Fig. 2(b)). The derivation for short diameters of the previous section with the expansion of the action exponent phase to second order terms cannot be applied in this case. However, we note that the behavior of the curvature near the separatrix in the action I_u (or σ) variable is similar to that for the eigenvalues of the matrix of the second derivatives of the action in the usual coordinate space near the turning points. One can thus apply the Maslov and Fedoryuk idea for the calculation of the Maslov indices (see Refs. 39) – 42)). Following this idea we first expand the phase of the exponent in Eq. (4·1) with respect to the action I_u taking into account up to third order terms (see Eq. (B·1) in Appendix B). Then we use the linear transformation (B·9) to the new variable z to get the standard exponent in the integral representation of the Airy functions. Within this method, we take the small first derivative (small parameter c_1) and the large second derivative (curvature) in the cubic polynomial expansions (B·1) taking σ within a small distance from the separatrix $\sigma = 1$. After some algebraic transformations we obtain Eq. (B·12) in Appendix B in the limit $\sigma \to 1$. Note that an idea similar to that we used here, in which σ is considered *near* the singular separatrix point $\sigma = 1$ and finally, only after the calculation of the integrals, the limit $\sigma \to 1$ is taken, is applied in the derivations of the *separate* contributions of the hyperbolic orbit family and short diameters to the periodic orbit sum, as mentioned above.

For the angle integral in Eq. (B·12), we use the same Maslov-Fedoryuk method [39]–[42] applied for the caustic case. As a result, one obtains (see Appendix B)

$$\delta g_{\mathrm{scl},0}^{(l)}(\varepsilon) = \frac{b}{\varepsilon_0 \pi kR^2} \mathrm{Re} \sum_M e^{i[kL_{lM} + \frac{2}{3}(w_\parallel^{3/2} + w_\perp^{3/2}) - \nu_{lM}]}$$

$$\times \sqrt{\frac{\sqrt{w_{\parallel} w_{\perp}}}{\left| c_2^{\parallel} c_2^{\perp} \right|}} \Big[\mathrm{Ai}(-w_{\parallel}) + i \, \mathrm{Gi}(-w_{\parallel}) \Big]$$

$$\times \Big[\mathrm{Ai}\left(-w_{\perp}, \mathcal{Z}_{lM,1}^{\perp}, \mathcal{Z}_{lM,2}^{\perp}\right) + i \, \mathrm{Gi}\left(-w_{\perp}, \mathcal{Z}_{lM,1}^{\perp}, \mathcal{Z}_{lM,2}^{\perp}\right) \Big]. \tag{5.33}$$

Here, the complete and incomplete Airy (or Gairy) functions with one and three arguments (Eq. (B·14)) are used in line with the definitions in Refs. 47) and 48) (see also Appendix B for the definitions of all other quantities).

For large $kR\sqrt{\eta^2 - 1}$, near the separatrix $\sigma \to 1$, the parameter $w_{\perp}$ is negligible in Eq. (B·17) for the limits $\mathcal{Z}_{1,lM}^{\perp}$ and $\mathcal{Z}_{2,lM}^{\perp}$ and the integration range can be extended from 0 to ∞. The incomplete Airy integrals in Eq. (5·33) approach the complete ones and the asymptotic forms of all Airy functions like $\mathrm{Ai}(-w)$ and $\mathrm{Gi}(-w)$ are now used. [47] Finally, we asymptotically obtain the standard Gutzwiller result for the isolated diameters, [1), 2), 7]

$$\delta g_{\mathrm{scl},0}^{(l)}(\varepsilon) = -\frac{2b}{\varepsilon_0 k R^2} \, \mathrm{Re} \sum_M e^{i[kL_{lM} + \frac{2}{3}(w_{\parallel}^{3/2} + w_{\perp}^{3/2}) - \nu_{lM}]} \sqrt{\frac{\sqrt{w_{\parallel} w_{\perp}}}{|F_{lM}|}}$$

$$\times \Big[\mathrm{Ai}(-w_{\parallel}) + i \, \mathrm{Gi}(-w_{\parallel}) \Big] \Big[\mathrm{Ai}(-w_{\perp}) + i \, \mathrm{Gi}(-w_{\perp}) \Big]$$

$$\to \frac{2b}{\varepsilon_0 \pi k R^2} \sum_M \frac{1}{\sqrt{|F_{lM}|}} \sin(kL_{lM} - \nu_{lM}), \tag{5.34}$$

where F_{lM} is the Gutzwiller stability factor for long diameters,

$$F_{lM} = -4 \sinh^2 \Big[M \, \mathrm{arccosh}(2\eta^2 - 1) \Big], \tag{5.35}$$

$$\nu_{lM} = 3\pi M - \frac{\pi}{2}. \tag{5.36}$$

In the second equation we used the asymptotics of the $\mathrm{Ai}(-w)$ and $\mathrm{Gi}(-w)$ functions. [47] We found also the constant part ν_{lM} of the phase by using the Maslov-Fedoryuk theory. The deformation and energy-dependent Maslov phases are determined by the additional phases in the exponent and the argument of the product of the square brackets in (5·33) through complex combinations of the Airy and Gairy functions and their arguments.

In the circular shape limit, both the upper and the lower limits of the incomplete Airy functions in Eq. (5·33) tend to zero, and the angle integral has the finite limit $\pi/2$ because $c_2^{\parallel}$, $c_3^{\perp}$ and $w_{\perp}$ vanish (see Appendix B). With this, the other factors near the separatrix $\sigma \to 1$ ensure that the amplitudes for long diameters diminish because $w_{\parallel}$ (B·11) vanishes at the separatrix (see also Ref. 47)). Therefore, the long diameter contribution becomes zero in the circular shape limit.

Thus, for deformations far from the bifurcations, the results (5·23) and (5·33) of the ISPM reduce to the standard Gutzwiller formula. In the circular disk limit the improved short diameter density (5·23) continuously approaches the diametric contribution to the circular disk density, while the long diameter (separatrix) contribution diminishes. Note that our ISPM solution (5·33) for the unstable long diameters

is not related to the Poisson-sum trace formula (5·1), in particular, with its "diametric" part because of the existence of the *isolated* stationary points for the *angle* variable Θ_u as for short diameters. Moreover, the uniform approximation Eq. (24) of Ref. 4) is singular at the separatrix because of the divergence of the curvature K_l for $\sigma \to 1$, as noted in Ref. 26). However, instead of using the continuation of the WKB approach to the complex plane as suggested in Ref. 26), we applied the simpler Maslov-Fedoryuk method [39]‑[42] and obtained the analytical dependence of the Maslov phase on the deformation and energy through the exponent phase and complex arguments of the Airy functions as well as their complex summations.

5.4. *Closed orbits and the circular disk limit*

To get a more exact solution for the diameter contribution to the level density and check the precision of the ISPM, we come back to the initial trace formula Eq. (2·2) before application of the ISPM for the calculation of this trace.[*] For this purpose we take exactly the trace integral (2·2) in suitable variables. This is the trace formula in terms of the sum over all closed (periodic and non-periodic) orbits α,

$$\delta g_{\rm scl}(\varepsilon) = 2 \, (2\pi\hbar)^{-3/2} \, \frac{m}{\sqrt{p}} \sum_\alpha \int \frac{dx \, dy}{\sqrt{J_\alpha(x,y)}} \sin(k L_\alpha - \nu_\alpha), \tag{5·37}$$

where $J_\alpha(x,y)$ is the stability factor defined through the Jacobian $\mathcal{J}_\alpha(\boldsymbol{p}'t_\alpha, \boldsymbol{r}''\varepsilon)$ by

$$\mathcal{J}_\alpha(\boldsymbol{p}'t_\alpha, \boldsymbol{r}''\varepsilon) = \frac{m^2}{p} \left(\frac{\partial \theta_p'}{\partial \bar{y}''} \right)_\alpha = \frac{m^2}{p} \frac{1}{J_\alpha(x,y)}. \tag{5·38}$$

Here the deflection $\delta\bar{y}''$ of the final path point in the perpendicular direction of the local Cartesian system $(\bar{x}, \bar{y})$ comes from the angle variation $\delta\theta_p'$ of the initial momentum, [11],[46] (see Fig. 3).

We then simplify the trace formula (5·37), taking the contribution of the main shortest closed orbits α with the two reflection points denoted below by the index "co2" as an example. For an arbitrary point (x, y) inside the elliptic billiard, one can find such orbits "co2" that are triangles with two vertices at the elliptic boundary and one vertex at the point (x, y) (see Fig. 4). There are two kinds of such orbits. For any point (x, y) we can plot the hyperbola and ellipse confocal to the boundary, which are the orbit-length invariant curves. Indeed, moving the initial point (x, y) along such a hyperbola (or an ellipse) we have the one-parametric family of the triangle-like orbits with the same action ($\mathcal{K} = 1$). We refer to them as the hyperbolic and elliptic "co2" orbits, respectively.

For the calculation of the trace integral (5·37) it is convenient to use the elliptic coordinates (u, v), (3·1). After this coordinate transformation, we can take the sine function of the action off the v or u integration for the hyperbolic or elliptic "co2" orbits, respectively, because the action is independent of the corresponding elliptic

---

[*] Equation (2·1) can be obtained also from the phase space trace formula Eq. (2·3) taking the integral over two components of the momentum $\boldsymbol{p}'$ along the energy surface using the stationary phase method.
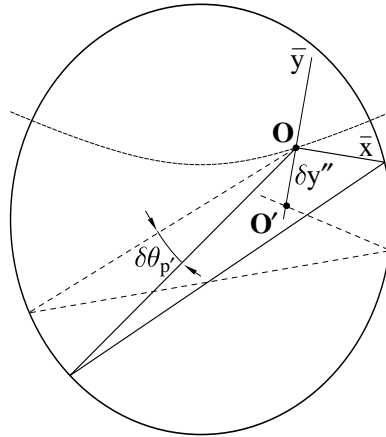
Fig. 3. Illustration of the caustic method for evaluating the stability factor J_α in Eq. (5·38) for the closed two-reflection orbit "co2". The deflection angle $\delta\theta'_p$ at the initial point $O(\boldsymbol{r}')$, variation $\delta\bar{y}''$ of the final point $O'(\boldsymbol{r}'')$ with respect to O, and the coordinate system $(\bar{x}, \bar{y})$ are shown. The thick solid curves and dashed curves represent the hyperbolic orbit "co2" and the perturbed orbit, respectively. The thin solid curve indicates the orbit-length invariant hyperbola confocal to the boundary.
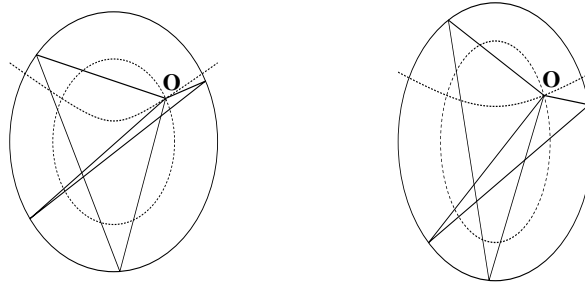

Fig. 4. Closed non-periodic two-reflection orbits with the elliptic and hyperbolic caustics at the initial point $O(x, y)$ are indicated by thin and thick solid curves, respectively, for the deformation $\eta = 1.05$ (left-hand side) and 1.2 (right-hand side). O is the vertex common to both triangular orbits. The dashed curves indicate the orbit-length invariant ellipse and hyperbola crossing the initial point. The hyperbolic orbit is close to the diameter of the circular shape for small deformations.

coordinate. Finally, one obtains from Eq. (5·37)

$$\delta g_{\mathrm{scl},1}^{(\mathrm{hco2})}(\varepsilon) = 2(2\pi\hbar)^{-3/2}\frac{m\zeta^2}{\sqrt{p}}\int\frac{du\sin(kL_{\mathrm{hco2}}(u) - \nu_{\mathrm{hco2}})\,dv(\sinh^2 v + \cos^2 u)}{\sqrt{J_{\mathrm{hco2}}(x(u,v), y(u,v))}}$$

$$(5\cdot39)$$

for the contribution from the hyperbolic "co2" orbits (hco2), and a similar equation for the elliptic "co2" orbits. An explicit expression for the stability factor $J_{\mathrm{co2}}(x, y)$ evaluated using the caustic method [11] is presented in Appendix C.

Note that the hyperbolic "co2" orbits with the initial point (x, y) reduce to the disk diameters crossing the same point in the circular disk limit (see Fig. 4). The
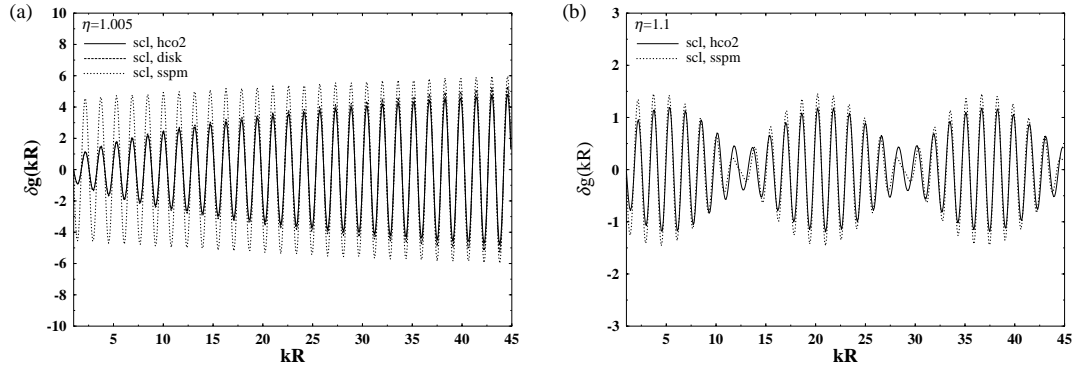
Fig. 5. (a) Convergence to the circular shape limit: The contribution of the closed two-reflection orbits of the hyperbolic type "hco2" (see Fig. 4) to the level density $\delta g(kR)$ is represented by the solid curve for the deformation $\eta = 1.005$, while Gutzwiller's trace formula (SSPM) for isolated diameters and the circular disk trace formula are indicated by dotted and dashed curves, respectively. The dashed curve overlaps with the solid curve, so that it cannot be distinguished from the latter. (b) Convergence to the Gutzwiller trace formula for $\eta = 1.1$. The notation is the same as in (a).

stability factor $J_{\mathrm{hco2}}(x, y)$, (C·1), turns into the analytical circular disk expression of Ref. 46). The circular disk limit of the level density (5·39) coincides with the diameter contribution $\delta g^{(d)}_{\mathrm{scl},1}(\varepsilon)$, (5·32), as shown in Fig. 5(a). The opposite limit of (5·39) far from the bifurcations is the Gutzwiller SPM for the short and long isolated diameters (see Fig. 5(b)). The contribution of the elliptic "co2" is negligibly small everywhere, and it vanishes at the circular disk shape as higher order $\hbar$ corrections.

§6.   Level density, shell energy and averaging

6.1.   *Total level density*

The total semiclassical POT density can be written as the sum over all periodic orbit families considered in the previous section,

$$\delta g_{\mathrm{scl}}(\varepsilon) = \delta g_{\mathrm{scl},1}(\varepsilon) + \delta g^{(s)}_{\mathrm{scl},0}(\varepsilon) + \delta g^{(l)}_{\mathrm{scl},0}(\varepsilon) = \sum_{\beta} \delta g^{(\beta)}_{\mathrm{scl}}(\varepsilon), \qquad (6\cdot1)$$

where the first term is the contribution (5·8) from the elliptic and hyperbolic orbits. The second and third terms are the contributions from the short (5·23) and the long (5·33) diameters, respectively. Near the circular limit, the last two terms for one period ($M = 1$) can be replaced by the contribution of the hyperbolic "co2" orbits (5·39) to obtain a more precise semiclassical result.

6.2.   *Semiclassical shell energy*

The shell-correction energy δE can be expressed in terms of the oscillating part $\delta g^{(\beta)}_{\mathrm{scl}}(\varepsilon)$ of the semiclassical level density as [6), 7), 11)]

$$\delta E = 2 \sum_{\beta} \left(\frac{\hbar}{t_\beta}\right)^2 \delta g_{\text{scl}}^{(\beta)}(\varepsilon_F), \qquad N = 2 \int_0^{\varepsilon_F} d\varepsilon g(\varepsilon). \qquad (6 \cdot 2)$$

Here, t_β is the time of the motion along the periodic orbit β (including its repetitions),

$$t_\beta = M_\beta T_\beta = \frac{2\pi M_\beta}{\Omega_\beta}, \qquad (6 \cdot 3)$$

where T_β is the period of the primitive orbit with the Fermi energy ε_F, M_β the repetition number, Ω_β the frequency, and N the particle number. Note that we have taken into account the spin degeneracy factor 2 in (6·2).

The semiclassical representation of the shell-correction energy (6·2) differs from that of δg only by the factor $(\hbar/t_\beta)^2 = (\hbar^2 k_F/mL_\beta)^2$, which suppresses contributions from longer orbits. Thus short periodic orbits play dominant roles in determining the shell-correction energy.

6.3. *Average level density*

For the purpose of presenting the level density improved at the bifurcation points we need to consider a level density slightly averaged, thus avoiding the convergence problems that usually arise when one is interested in a full semiclassical quantization.

The averaging is done by folding the level density with a Gaussian of width Γ:

$$g_\Gamma(\varepsilon) = \frac{1}{\sqrt{\pi}\Gamma} \int_{-\infty}^{\infty} d\varepsilon' \, g(\varepsilon') \, e^{-\left(\frac{\varepsilon-\varepsilon'}{\Gamma}\right)^2}. \qquad (6 \cdot 4)$$

The choice of the Gaussian form of the averaging function is immaterial and guided only by mathematical simplicity. For cavities it is also convenient to use the level density defined as a function of kR averaged with a Gaussian of width γ:

$$g_\gamma(kR) = \frac{1}{\sqrt{\pi}\gamma} \int_{-\infty}^{\infty} d(k'R) \, g(k'R) \, e^{-\left(\frac{(k-k')R}{\gamma}\right)^2}, \qquad (6 \cdot 5)$$

where

$$g(kR) = \sum_i \delta((k - k_i)R) = 2kR\varepsilon_0 \sum_i \delta(\varepsilon - \varepsilon_i) = 2kR\varepsilon_0 g(\varepsilon), \qquad (6 \cdot 6)$$

$\varepsilon_0 = \hbar^2/2mR^2$ and the dimensionless parameter γ is related to Γ by

$$\Gamma = 2\gamma\sqrt{\varepsilon\varepsilon_0}. \qquad (6 \cdot 7)$$

Applying the averaging procedure defined above to the semiclassical level density (6·1), one obtains [3], [46], [11]

$$\delta g_{\Gamma,scl}(\varepsilon) = \sum_{\beta} \delta g_{\text{scl}}^{(\beta)}(\varepsilon) \, e^{-\left(\frac{\Gamma t_\beta}{2\hbar}\right)^2} = \sum_{\beta} \delta g_{\text{scl}}^{(\beta)}(\varepsilon) \, e^{-\left(\frac{\gamma L_\beta}{2R}\right)^2}. \qquad (6 \cdot 8)$$

The latter equation is written specifically for billiard problems in terms of the orbit length L_β (in units of a typical length scale R) and γ. The averaging yields an exponential decrease of the amplitudes with increasing L_β and/or γ. As shown in Ref. 11), for γ of order unity, all longer paths are strongly damped and only the shortest periodic orbits contribute to the oscillating part of the level density, yielding its gross-shell structure. For a study of the bifurcation phenomenon, however, we need smaller values of γ.

Finally, we should note that the higher the degeneracy of an orbit, the larger the volume occupied by the orbit family in the phase space and also, the shorter its length, the more important its contribution to the average level density.

§7. Quantum elliptic billiard

7.1. *Numerical method for the spectrum calculation*

Single-particle energies ε_i of a particle of mass m moving freely inside the elliptic boundary $v \leq v_b$ can be obtained by a number of numerical methods. Following the procedure employed in previous works [18), 20)] by some of the present authors, one can expand the deformed single-particle wave functions $\Psi(r, \theta)$ into a circular basis with well-defined orbital angular momentum l as

$$\Psi_i^{(++)}(r,\theta) = \sum_{l=0}^{(e)} A_l J_l(k_i r)\cos(l\theta), \quad \Psi_i^{(-+)}(r,\theta) = \sum_{l=1}^{(o)} B_l J_l(k_i r)\sin(l\theta),$$

$$\Psi_i^{(+-)}(r,\theta) = \sum_{l=1}^{(o)} A_l J_l(k_i r)\cos(l\theta), \quad \Psi_i^{(--)}(r,\theta) = \sum_{l=2}^{(e)} B_l J_l(k_i r)\sin(l\theta), \quad (7\cdot1)$$

where $J_l(x)$ are the cylindrical Bessel functions of the first kind, $k_i = \sqrt{2m\varepsilon_i}/\hbar$, the superscripts $(++)$ etc. indicate the parities with respect to reflections about the x and y axes, and the superscripts (e) and (o) indicate the sums with respect to even and odd l, respectively. The expansion coefficients A_l and B_l can be determined by applying Dirichlet boundary conditions.

In the present analysis we employed, in addition to the above circular-wave decomposition method, the numerical procedure based on a rather standard approach, the transformation of the Schrödinger equation into an elliptic coordinate system. [26), 52), 53)] In terms of elliptic coordinates (3·1), the Schrödinger equation can be written as

$$\left[\sqrt{\xi^2 - 1}\frac{\partial}{\partial\xi}\left\{\sqrt{\xi^2 - 1}\frac{\partial}{\partial\xi}\right\} + \sqrt{1 - \phi^2}\frac{\partial}{\partial\phi}\left\{\sqrt{1 - \phi^2}\frac{\partial}{\partial\phi}\right\}\right]\psi(\xi,\phi)$$

$$+ \frac{2m\varepsilon_i\zeta^2(\xi^2 - \phi^2)}{\hbar^2}\psi(\xi,\phi) = 0, \qquad (7\cdot2)$$

where $\xi = \cosh v$ and $\phi = \cos u$. Following Ref. 52), this equation can be separated into two ordinary differential equations by assuming $\psi(\xi,\phi) = R(\xi)S(\phi)$. The
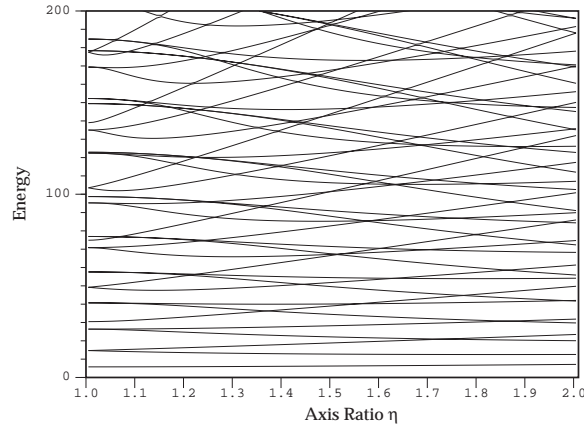
Fig. 6. Single-particle spectra (in units of ε_0) for elliptic billiard plotted as functions of the deformation parameter η.

functions R and S are solutions of the ordinary differential equations

$$(\xi^2 - 1)\frac{d^2 R_l(c, \xi)}{d\xi^2} + \xi \frac{dR_l(c, \xi)}{d\xi} - \left[\lambda_l - c^2\xi^2\right] R_l(c, \xi) = 0,$$

$$(1 - \phi^2)\frac{d^2 S_l(c, \phi)}{d\phi^2} - \phi \frac{dS_l(c, \phi)}{d\phi} + \left[\lambda_l - c^2\phi^2\right] S_l(c, \phi) = 0, \qquad (7 \cdot 3)$$

where λ_l is the separation constant and $c = \zeta\sqrt{2m\varepsilon_i}/\hbar$ for $\xi \leq \xi_b = \cosh v_b$. The internal radial functions $R_l(c, \xi)$ are expanded in terms of Bessel functions of the first kind. The expansion coefficients and the separation constant λ_l can be determined from the three-term recurrence relations found in various references.[47), 52) - 54)]

By imposing usual boundary conditions on the radial wave functions, i.e., $R_l(c, \xi_b) = 0$, one finds the eigenenergies ε_i. All eigenvalues up to $kR \approx 40$ with the coordinate-transformation method can be calculated numerically in matter of minutes without overlooking solutions near level crossings, and hence the procedure is certainly effective for the present model. The results obtained from both numerical procedures were carefully compared and found to exhibit a nice convergence.

In Fig. 6 the deformation dependence of the single-particle energies for the elliptic billiard is presented. In the circular limit, the familiar shell gaps are clearly observed, while different shell gaps start to develop at higher deformations. Below we identify the semiclassical origin of these shell structures at higher deformations.

7.2. *Strutinsky's smoothed level densities and shell energies*

With the aid of the Strutinsky averaging procedure,[57)] clear oscillatory patterns of the coarse-grained level density emerge, as shown in Fig. 7, where (a) and (b) are obtained with the Gaussian smoothing parameter γ (defined by (6·7)) of 0.30 and 0.64, respectively. As clearly seen from these figures, the choice of a Gaussian smoothing parameter γ is crucial for properly identifying the coarse-grained level density, and hence the contribution of classical periodic orbits. In the circular limit $\eta = 1.0$, the two Gaussian-smoothed level densities exhibit similar oscillations,
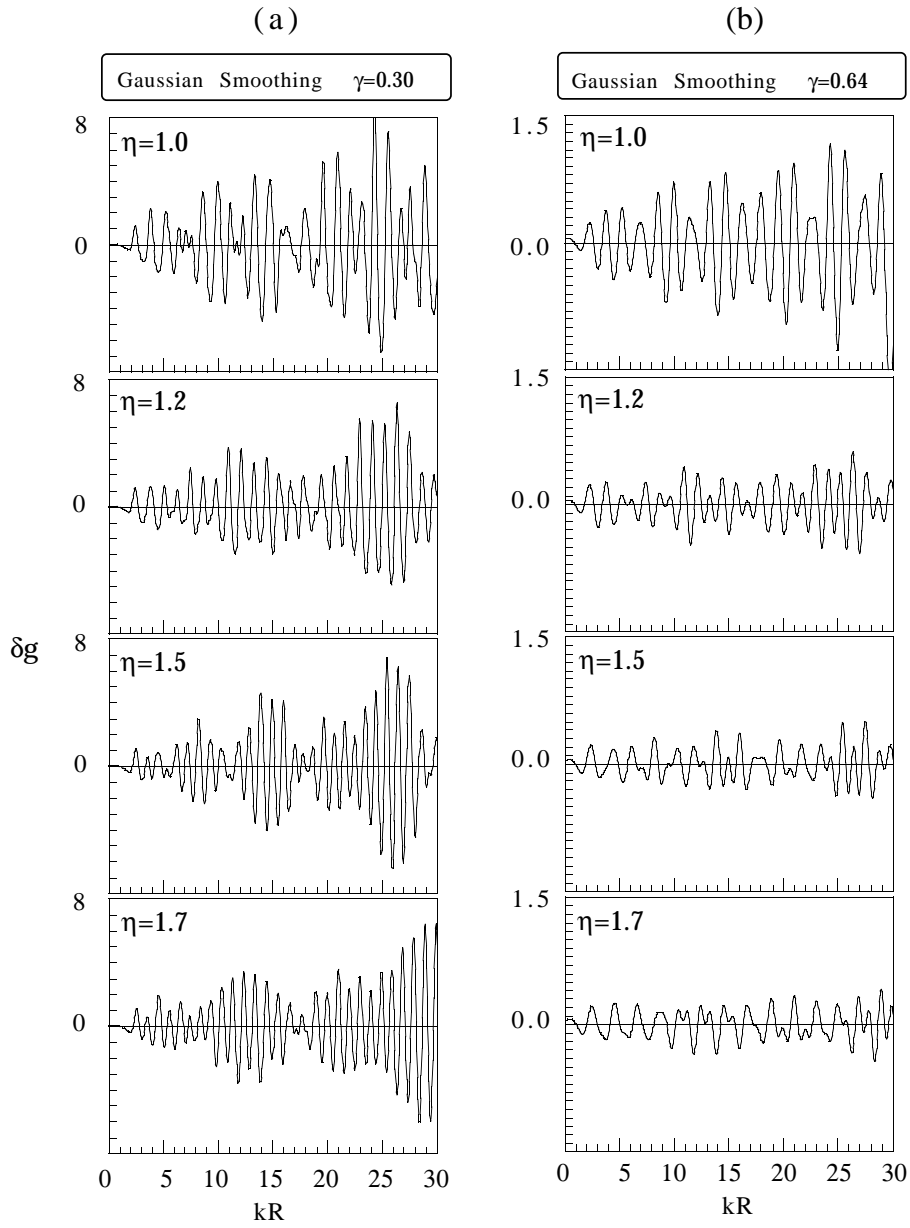
Fig. 7.   Coarse-grained level densities with the Gaussian smoothing parameter $\gamma = 0.3$ (a) and 0.64 (b).

whereas the shell gaps for $\gamma = 0.64$ start to collapse with increasing deformation. In particular for deformations η larger than 1.5, strong shell patterns cease to exist for the case $\gamma = 0.64$, while for $\gamma = 0.3$ appreciable effects still remain and more oscillations appear as the deformation increases.

In the semiclassical picture, for a given value of γ the contributions from only
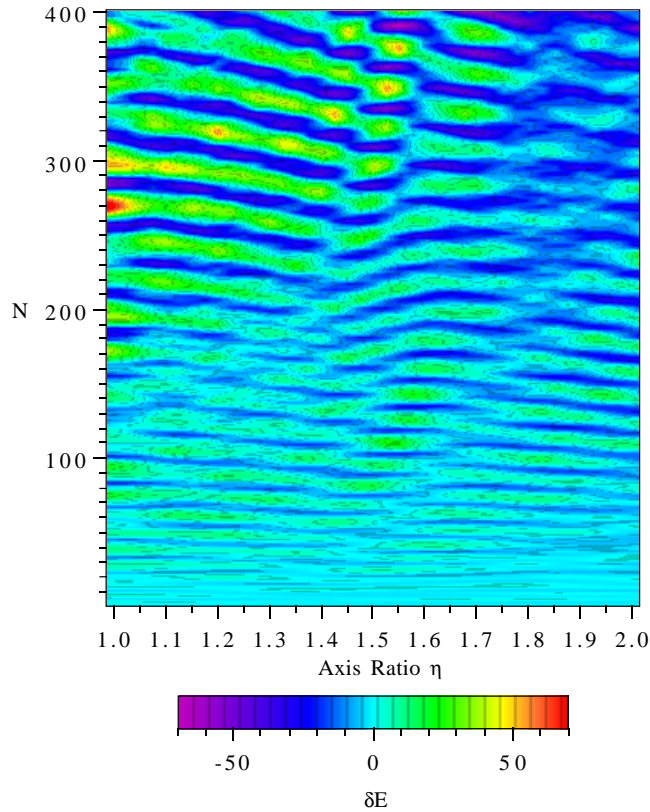
Fig. 8. Shell structure energy δE (in units of ε_0) plotted as a function of both the deformation η and the particle number N.

those periodic orbits of length up to $L_{\max} \approx \pi R/\gamma$ can be considered. In this context, it is important to locate the actual shell-energy minima, irrespective of the choice of a Gaussian smoothing parameter.

In terms of the particle number N, one can also obtain the shell-correction energy δE defined as the difference between the sum of single-particle energies of N lowest levels (taking the spin-degeneracy factor 2 into account) and the Strutinsky averaged energies, i.e.,

$$\delta E = \sum_{i=1}^{N} \varepsilon_i - \tilde{E}, \qquad \tilde{E} = 2 \int_{-\infty}^{\tilde{\varepsilon}_F} d\varepsilon' \, \varepsilon' \, \tilde{g}(\varepsilon'), \qquad (7\cdot4)$$

with the Fermi energy $\tilde{\varepsilon}_F$ satisfying

$$N = 2 \int_{-\infty}^{\tilde{\varepsilon}_F} d\varepsilon' \, \tilde{g}(\varepsilon'). \qquad (7\cdot5)$$

Figure 8 illustrates the oscillating pattern of the shell-correction energy δE as function of both the deformation η and particle number N. It is clear from the figure that the distance between the major shell gaps shrink with increasing deformation. In
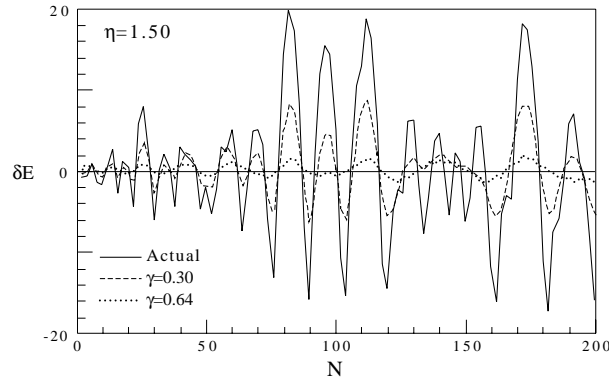
Fig. 9. Smoothed shell-correction energies for $\eta = 1.5$ with Gaussian smoothing parameter $\gamma = 0.3$ (dashed curve) and 0.6 (dotted curve). Those without smoothing are plotted by the solid curve.

the considered range of deformation it is found that the actual magic numbers determined through the above procedure cannot be reproduced with the choice $\gamma = 0.64$, whereas the value $\gamma = 0.3$ is sufficiently small to avoid demolishing but sufficiently large to preserve the actual coarse-grained shell structure. It is explicitly shown in Fig. 9, where the shell-correction energies are now calculated by applying Gaussian smoothing parameters $\gamma = 0.3$ and 0.64, for the case $\eta = 1.5$ as an example. In this case, the actual magic numbers are found to be $\cdots$, 16, 22, 30, 38, 52, $\cdots$, which exactly coincide with those for $\gamma = 0.3$, while those calculated with $\gamma = 0.64$ show larger oscillations where magic numbers $\cdots$, 16, 30, $\cdots$ are missing. The same is true for other deformations considered in this paper. Thus, the coarse-grained shell structure obtained with $\gamma = 0.64$ is too rough and therefore we adopt $\gamma = 0.3$ to improve the precision of its description.

7.3. *Shell structure and Fourier spectra*

Equations of single-particle motion in billiard are invariant with respect to the scaling transformation $(\boldsymbol{r}, \boldsymbol{p}, t) \to (\boldsymbol{r}, \alpha\boldsymbol{p}, \alpha^{-1}t)$. The action integral S_β for a periodic orbit β is proportional to its length L_β:

$$S_\beta(E = p^2/2m) = \oint_\beta d\boldsymbol{r} \cdot \boldsymbol{p} = pL_\beta = \hbar k L_\beta. \qquad (7\cdot6)$$

The semiclassical trace formula for the level density is then written as

$$g_{\mathrm{scl}}(\varepsilon) = \tilde{g}(\varepsilon) + \sum_\beta A_\beta(kR)\cos\left(kL_\beta - \frac{\pi}{2}\mu_\beta\right), \qquad (7\cdot7)$$

where $\tilde{g}(\varepsilon)$ denotes the smooth part corresponding to the contribution of zero-length orbits, $A_\beta = |\mathcal{A}_\beta|$, and μ_β is the Maslov phase (the deformation and energy dependent phase of Eqs. (5·15) and (5·30) in our improved semiclassical approximation). As previously discussed, the stationary phase approximation employed in deriving the Gutzwiller trace formula breaks down at bifurcation points for stable periodic orbits, and consequently it results in the divergence of the amplitudes $A_\beta(kR)$ in
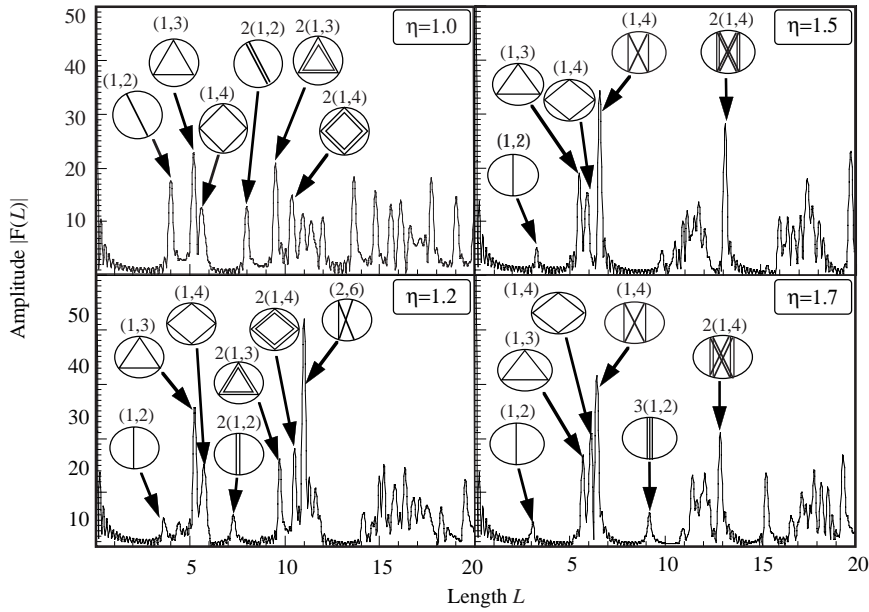
Fig. 10. Fourier transforms of the single-particle level density for elliptic billiards with $\eta = 1.0$ (a),
1.2 (b), 1.5 (c) and 1.7 (d). Some periodic orbits that correspond to peaks are illustrated.

Eq. (7·7), whereas in the present ISP treatment, those amplitudes are smooth func-
tions of both deformation and energy.

   In order to examine the classical-quantum correspondence in shell structure,
one can perform the Fourier transform $F(L)$ of the quantum level density $g(\varepsilon)$ with
respect to the wave number k,

$$F(L) = \int dk \, e^{-ikL} g(\varepsilon) e^{-\frac{1}{2}\left(\frac{k}{k_c}\right)^2} = \frac{1}{2\varepsilon_0 R^2} \sum_i \frac{1}{k_i} e^{-ik_i L} e^{-\frac{1}{2}\left(\frac{k_i}{k_c}\right)^2}, \qquad (7\cdot8)$$

which may be regarded as a 'length spectrum' exhibiting peaks at lengths of indi-
vidual periodic orbits. Here the Gaussian factor is included to smoothly cutoff the
spectrum in the high-energy region. In numerical calculations, we use $k_c = k_{\max}/\sqrt{2}$,
$k_{\max}$ being the maximum wave number included. The above method of taking the
Fourier transform of the quantum level density is known to be a powerful tool to in-
vestigate the role of classical periodic orbits in the appearance of shell fluctuations in
quantum systems, and from such observations one can also extract the semiclassical
contributions of individual periodic orbits.

   Fourier spectra for deformations $\eta = 1.0$, 1.2, 1.5 and 1.7 are presented in
Figs. 10(a)–(d), respectively. At the axis ratio $\eta = 1.0$, the diameter and elliptic
orbits are found to be equally important. The fact that the main contribution to the
gross-shell structure comes from the shorter periodic orbits implies the significance
of three classical periodic orbits in the circular limit, namely the diameter, triangu-
lar, and square shape orbits. As the deformation increases, the Fourier amplitudes
for triangular and rhombic orbits still exhibit fairly strong effects, while those for
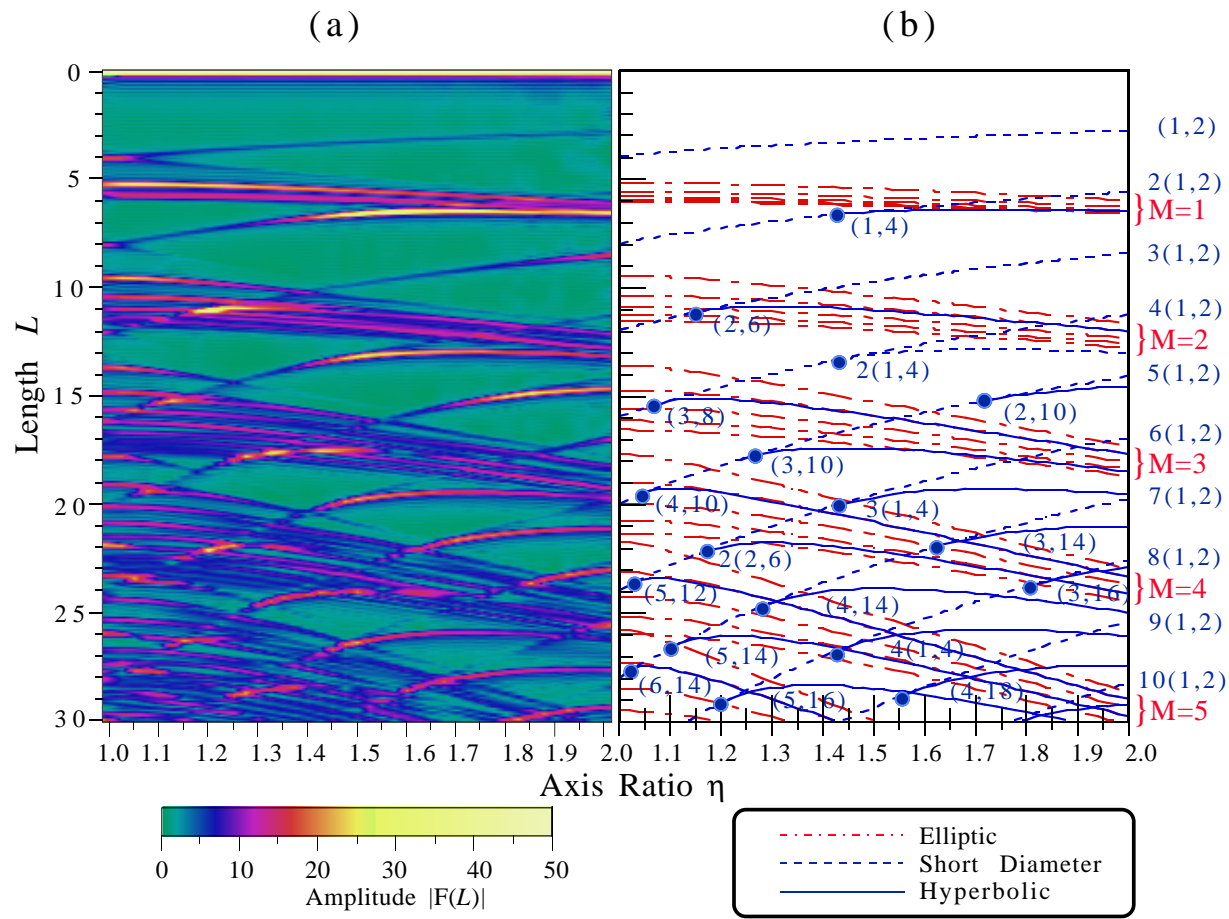
Fig. 11. (a) Modulus of the Fourier amplitudes plotted as functions of both orbit-length L and deformation η. (b) The lengths L of classical periodic orbits calculated as functions of deformation η. Solid, dashed and dash-dotted curves are used for hyperbolic, short-diameter and elliptic orbits, respectively.
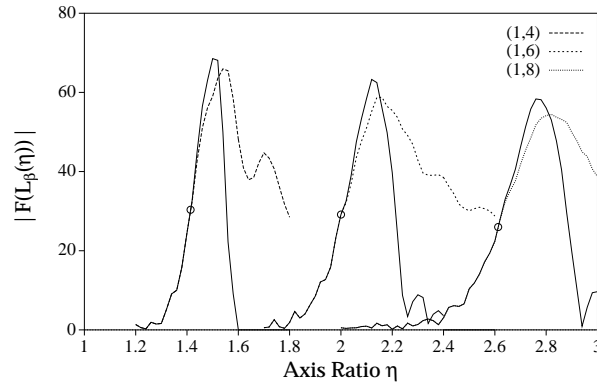
Fig. 12. Deformation dependence of Fourier peak heights for hyperbolic and short diametric orbits 2(1,2), (1,4), 3(1,2), (1,6), 4(1,2) and (1,8). Solid curves are used for multiple traversals along the short diameter, $M(1,2)$ with $M = 1, 2, 3$, while long-dashed, short-dashed and dotted curves are used for hyperbolic $(1,4), (1,6), (1,8)$ orbits, respectively. The open circles indicate the bifurcation points.

diameter orbits start to decline quickly and significant rearrangement can be observed. In particular at deformations $\eta = 1.5$ and 1.7, one can conclude, in addition to triangular and rhombic shape orbits, the gross-shell fluctuations are also governed by the (1,4) hyperbolic orbits bifurcated from the 2(1,2) short diameter orbit at the critical deformation $\eta = \sqrt{2}$.

Figure 11(a) displays the deformation dependence of Fourier amplitudes calculated from the quantum single-particle spectra. Here the enhancement of peaks indicates a larger contribution from the corresponding classical periodic orbits β of length L_β to the shell structure. In the circular limit, the system possesses the highest symmetry, and the breaking of this symmetry due to a small deviation of its shape results in the orbital bifurcation. With increasing deformation, the short diameter orbits with M repetitions $M(1,2)$ also bifurcate and create hyperbolic orbits at the critical deformations $\eta_{\rm bif}$ given by Eq. (3·12). The length of those classical periodic orbits as a function of deformation can be calculated,[14] as shown in Fig. 11(b). It is clearly seen from both figures that the bifurcations of stable periodic orbits give rise to an increase in the Fourier amplitudes. The significant enhancements seen in the figure exactly coincide with the corresponding lengths of the newly created hyperbolic orbits, and hence they stress the importance of the orbital bifurcations.

In this context, similar enhancements for the case of a spheroidal cavity of superdeformed shape were also reported in Ref. 21), where superdeformed shell structure is associated with bifurcations of periodic orbits with two repetitions on the equatorial plane. In the present work, particular attention is paid to investigate such correlations between bifurcations of stable periodic orbits and quantum level-density oscillations.

In Fig. 12, Fourier peak heights for some of the important hyperbolic orbits, namely those bifurcated from the short diameter orbits of 2, 3 and 4 repetitions, 2(1,2), 3(1,2) and 4(1,2), are displayed as functions of the deformation parameter
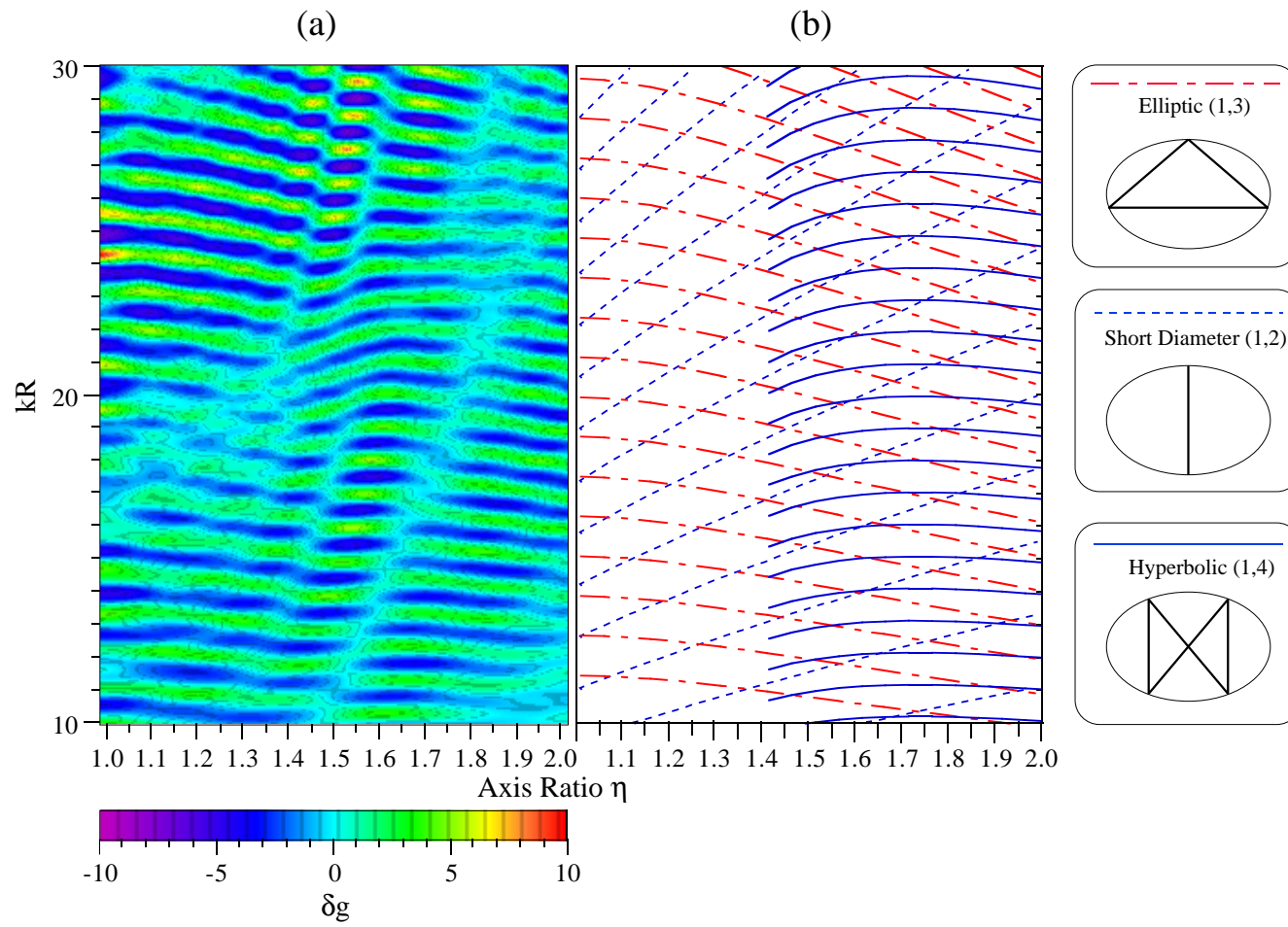
Fig. 13. (a) Smoothed level density plotted in the k-η plane. (b) The constant action lines in the k-η plane for the elliptic $(1,3)$ orbit (dash-dotted curves), the primitive short diameter $1(1,2)$ orbit (short-dashed curves), and the hyperbolic $(1,4)$ orbit (solid curves).

η. Interestingly, the Fourier peaks for these newly created orbits exhibit a universal deformation dependence; that is, their heights reach the maxima shortly after their bifurcation points and quickly decrease with increasing deformation. Such remarkable features were already seen in Fig. 8, where the shell valleys for η approximately larger than 1.5 can be understood to vary along the constant-action lines $S(k,\eta) = $ const of the (1,4) hyperbolic orbits, as explained below.

Suppose some classical periodic orbits β of length L_β are the dominant components in the semiclassical trace formula for the oscillating level density. Then the shell valley maxima/minima follows the constant-action lines $S_\beta(k,\eta) = $ const of those dominating classical periodic trajectories. Referring to Eq. (7·7), such lines are determined by

$$kL_\beta - \frac{\pi}{2}\mu_\beta = (2n+1)\pi, \qquad n = 0, 1, 2, \cdots. \tag{7·9}$$

We demonstrate the above dependence in Fig. 13(a), where the smoothed level densities are plotted in the k-η plane. As indicated in Fig. 13(b), it is interesting to note that the shell valley structures seen in Fig. 13(a) can be described by the constant-action lines of three major periodic orbits: Near the circular limit, the shell valleys vary along those of elliptic (mainly triangular and rhombic) orbits; in the right-half region of Fig. 13(a) the influence of newly created (1,4) hyperbolic orbits is visible; and the contribution of short diameter orbits are less pronounced but certainly non-negligible throughout the considered range of deformation. The equality Eq. (7·9) indicates the inverse proportionality relation between the orbital length L_β and wave number k. As the length of a trajectory β increases, the values of k decrease, and consequently the smoothed level densities exhibit more oscillations. In particular, since the length of the (1,4) hyperbolic orbits gradually increases for $\eta \approx \sqrt{2}$–1.7 and then slowly decreases for $\eta > 1.7$, the corresponding constant-action lines behave in the same manner. Such a tendency was already observed in Fig. 8, where the contribution from the (1,4) hyperbolic orbits to the shell energy δE is apparent in the region $\eta > 1.5$, indicating the essential role of the orbital bifurcations in quantal shell formations.

§8. Comparison between quantum and semiclassical calculations

Figures 14–16 show the modulus of the complex amplitude for a few short orbits. The semiclassical amplitudes for the hyperbolic "butterfly" $M(n_u, n_v) = (1, 4)$ and elliptic triangular (1,3) orbit families calculated using the ISPM are in good agreement with the exact calculation of the Poisson-sum trace integral (4·2) (see Figs. 14 and 15, respectively). All ISPM amplitudes are continuous function of the deformation through the bifurcation point $\eta = \sqrt{2}$. A significant enhancement of the butterfly amplitude is seen at the deformation $\eta = 1.5$–1.6 slightly to the right of the bifurcation point (see Fig. 14).

The ISPM amplitude for the primitive short diameter 1(1,2) quickly approaches the Gutzwiller SSPM result as one goes away from the circular limit and, for larger deformations, its magnitude is relatively small compared with those of the other
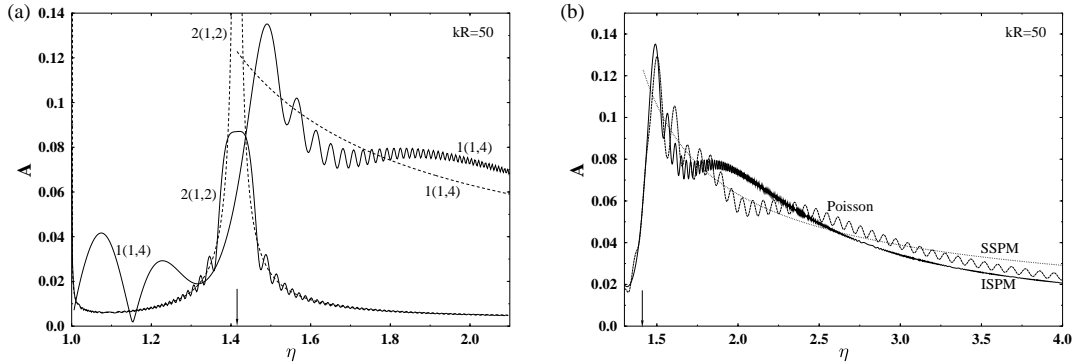
Fig. 14. (a) Amplitude modulus A for bifurcating short diameter $2(1,2)$ and butterfly $1(1,4)$ orbits obtained using ISPM are indicated by solid curves as functions of the deformation parameter η. Standard results of the extended Gutzwiller periodic orbit theory (SSPM) are indicated by short-dashed curves. (b) ISPM amplitudes for the butterfly orbit (solid curve) are compared with the exact calculation of the Poisson-sum trace formula (5·1) (dashed curve marked "Poisson") and SSPM of Berry and Tabor [4] (dotted curve).
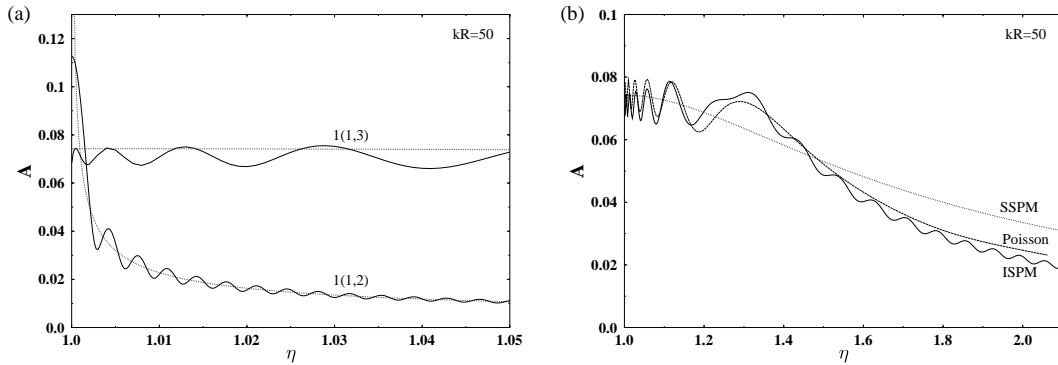

Fig. 15. (a) Same as in Fig. 14(a) but for primitive short diameter $1(1,2)$ and triangle $1(1,3)$ orbits for smaller deformations. (b) Comparison of the amplitudes for $1(1,3)$ with exact calculations and SSPM. (Notation is the same as in Fig. 14(b)).

orbits mentioned above (see Fig. 15).

In Fig. 16 we compare the ISPM result with the modulus of the "diametric" part of the Poisson-sum trace formula corresponding to $n_u = 1$, $n_v = 2$ and $M = 2$, which is regarded in Ref. 24) as representing short and long diameters, as well as the standard Gutzwiller results. The ISPM amplitude for the bifurcating short diameter $2(1,2)$ has the maxima; at the bifurcation deformation $\sqrt{2}$, which is significantly larger than the butterfly and triangular amplitudes, and at the circular shape (see also Figs. 14 and 15). (Similar maxima at the circular shape appear for any short diameter orbit. The maximum for the short diameter $1(1,2)$ is the largest one, in particular, larger than for the triangular orbit (see Fig. 15(a)).) As seen from Fig. 16, there is the same circular shape limit for the ISPM approach and the "diametric" part of the Poisson-sum trace formula, which is identical to the diameter family amplitude in the circular disk.
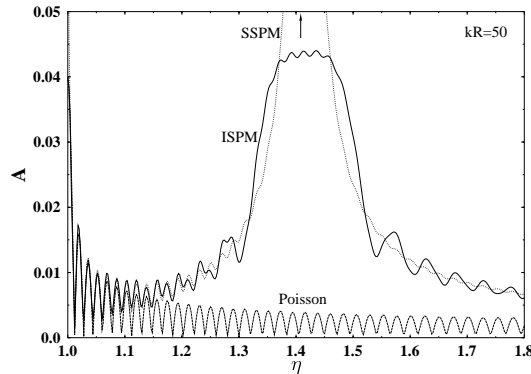
Fig. 16. ISPM amplitude modulus (solid curve) for the sum of short and long diameter $2(1, 2)$ orbits is compared with the $(n_u = 1, n_v = 2, M = 2)$ part of the Poisson-sum trace formula (5·1) (long-dashed curve) and the Gutzwiller SSPM (dotted curve).

Apparently, the behavior of the ISPM amplitude for two repetitions of the short diameter 2(1,2) is essentially different from that of the "diametric" part of the Poisson-sum trace integral, which exhibits no enhancement near the bifurcation point. Thus, the Poisson-sum trace formula (5·1) describes families with maximum degeneracy, like hyperbolic and elliptic orbits, rather than isolated diameters. For isolated orbits with smaller degeneracy, like diameters in elliptic billiard the Poisson-sum trace formula cannot be applied because of the isolated stationary points for the angle Θ_u variable. This is the reason for the agreement of the ISPM and SSPM asymptotics unlike for the "diametric" term of the Poisson-sum trace integral in Eq. (5·1). This implies that the diameters cannot be included in the usual EBK rational torus quantization. However, the diameters could be included in a more general quantization rule in terms of the averaged ISPM level densities (6·1) in a similar way as that pointed out in Refs. 9) and 12).

We note a significant improvement of the ISPM results compared to the SSPM for σ close to the separatrix value 1 and the creeping value σ_{cr} (3·11). These cases might seem to be important only in the limit $\eta \to \infty$ when σ_{cr} tends to unity. However, even for $0 \leq \eta \lesssim 2$ we meet situations in which the stationary points are close to the critical points $\sigma = 1$ and $\sigma = \sigma_{cr}$, so that we must integrate within the finite limits.

We compare in Fig. 17 the semiclassical level densities $\delta g_{scl}(kR)$ calculated using the ISPM with the quantum results for the averaging parameter $\gamma = 0.3$. The results obtained with the ISPM are in good agreement with quantum results even near the bifurcation point $\sqrt{2}$, where the SSPM gives a divergent result due to the zeros of the stability factor F_{sM} for short diameters 2(1,2). For deformations like 1.2 and 1.7 far from the bifurcation, one obtains a fair agreement between the ISPM and the SSPM.

Figure 18 displays the nice convergence of the ISPM results to those using the circular disk trace formula for $\eta \to 1$. This convergence is seen for any small deformation when the semiclassical parameter kR becomes sufficiently large. With the
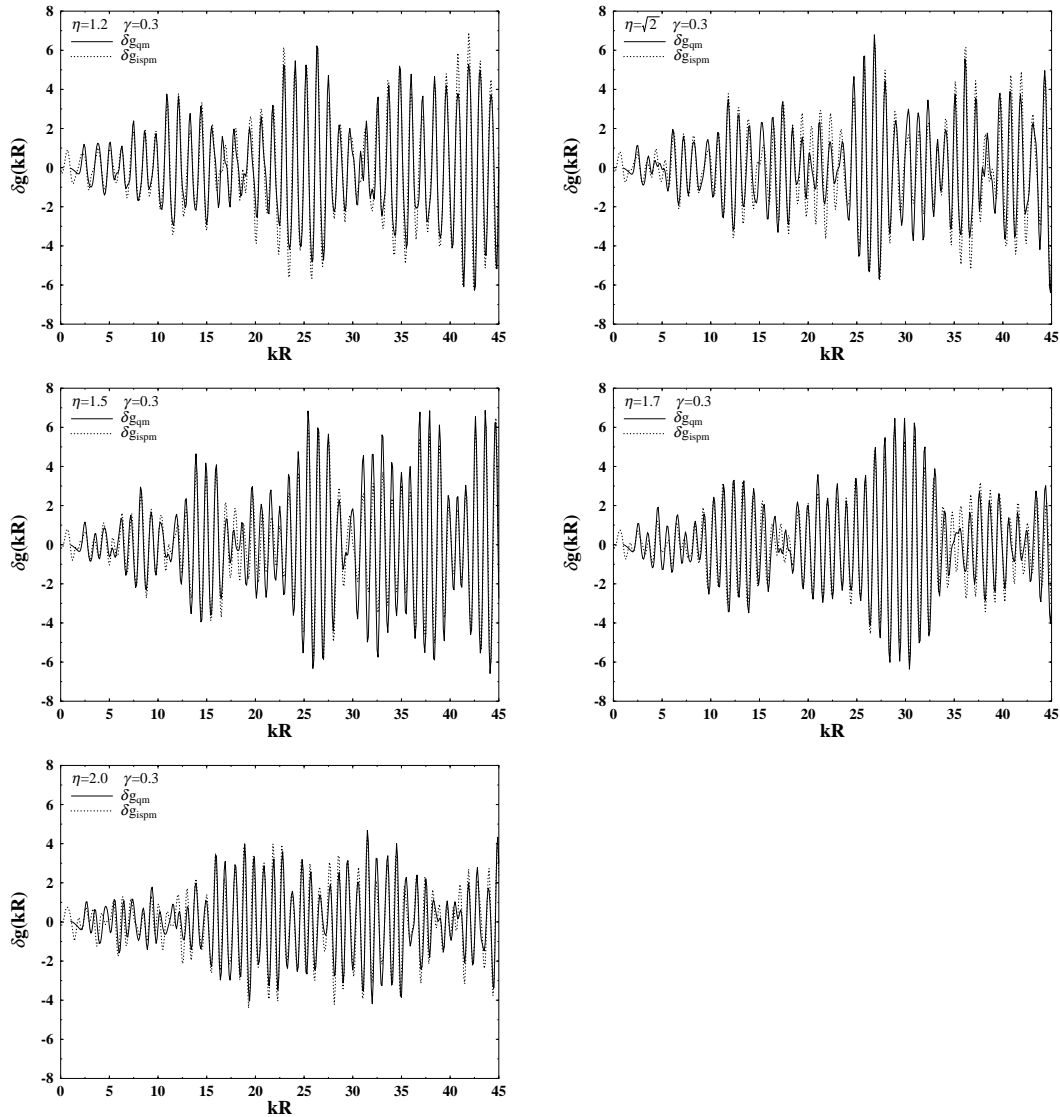
Fig. 17. Quantum and semiclassical (ISPM) oscillating level densities $\delta g(kR)$ versus kR for several deformations. The averaging parameter $\gamma = 0.3$, the parameter of Strutinsky's shell correction method $\tilde{\gamma} = 2.0$, and the correction polynomial degree $2\mathcal{M} = 6$ are used.

inclusion of the closed (periodic and non-periodic) hyperbolic orbit contribution, one gets even better agreement with the quantum densities near the circular disk shape. For deformations far from the circular shape ($\eta \gtrsim 1.1$) and far from other bifurcation points, the contribution of the hyperbolic "co2" orbits approach Gutzwiller's SSPM result for the isolated diameters (see Fig. 5(b)).

For the averaging parameter value $\gamma = 0.64$, we have good convergence of POT sums for the ISPM and SSPM with a few short periodic orbits with $M \leq 1$, $n_u = 1$ and $n_v \leq 10$. This is due to the damping factor in Eq. (6·8) which ensures the
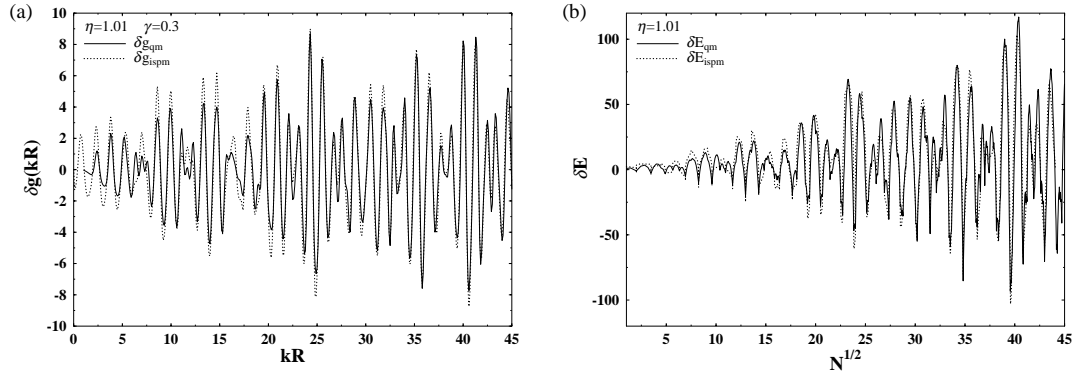
Fig. 18. Oscillating level density $\delta g(kR)$ versus kR (left-hand side) and shell energy δE in units of ε_0 versus $N^{1/2}$ (right-hand side) for the small deformation 1.01. The solid and dotted curves indicate results of quantum and ISPM calculations, respectively. The parameters for the Strutinsky's shell correction method are the same as in Fig. 17.
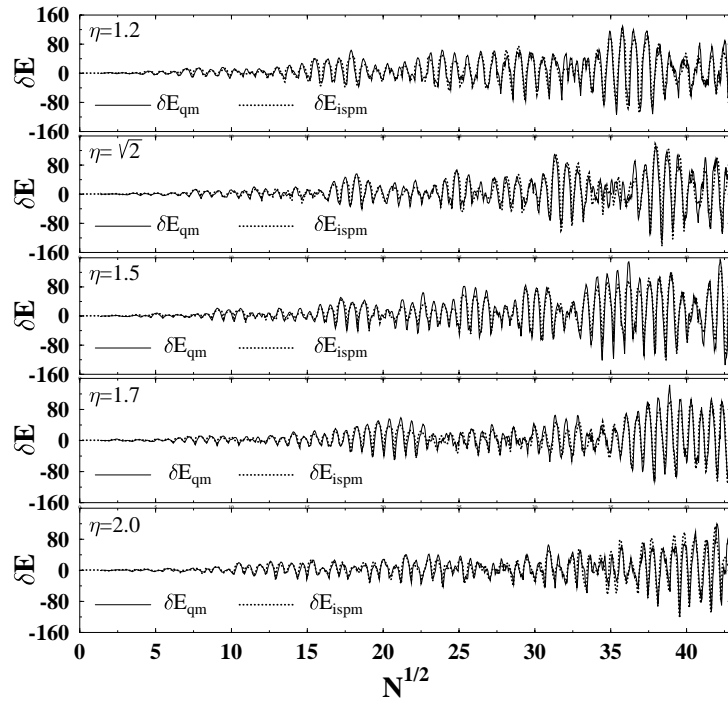
Fig. 19. Quantum and ISPM shell energy δE (in units of ε_0) are plotted by the solid and dotted curves, respectively, as functions of $N^{1/2}$.

convergence of the POT sum. For the smaller value $\gamma = 0.3$ we need more orbits with $M \leq 2$, $n_u \leq 2$ and $n_v \leq 10$. Note that for $\gamma = 0.3$ we have much better agreement of the ISPM results with the quantum mechanical calculations than in the case of SSPM for the deformations near the bifurcations including the transition to the circular shape (see Fig. 7).
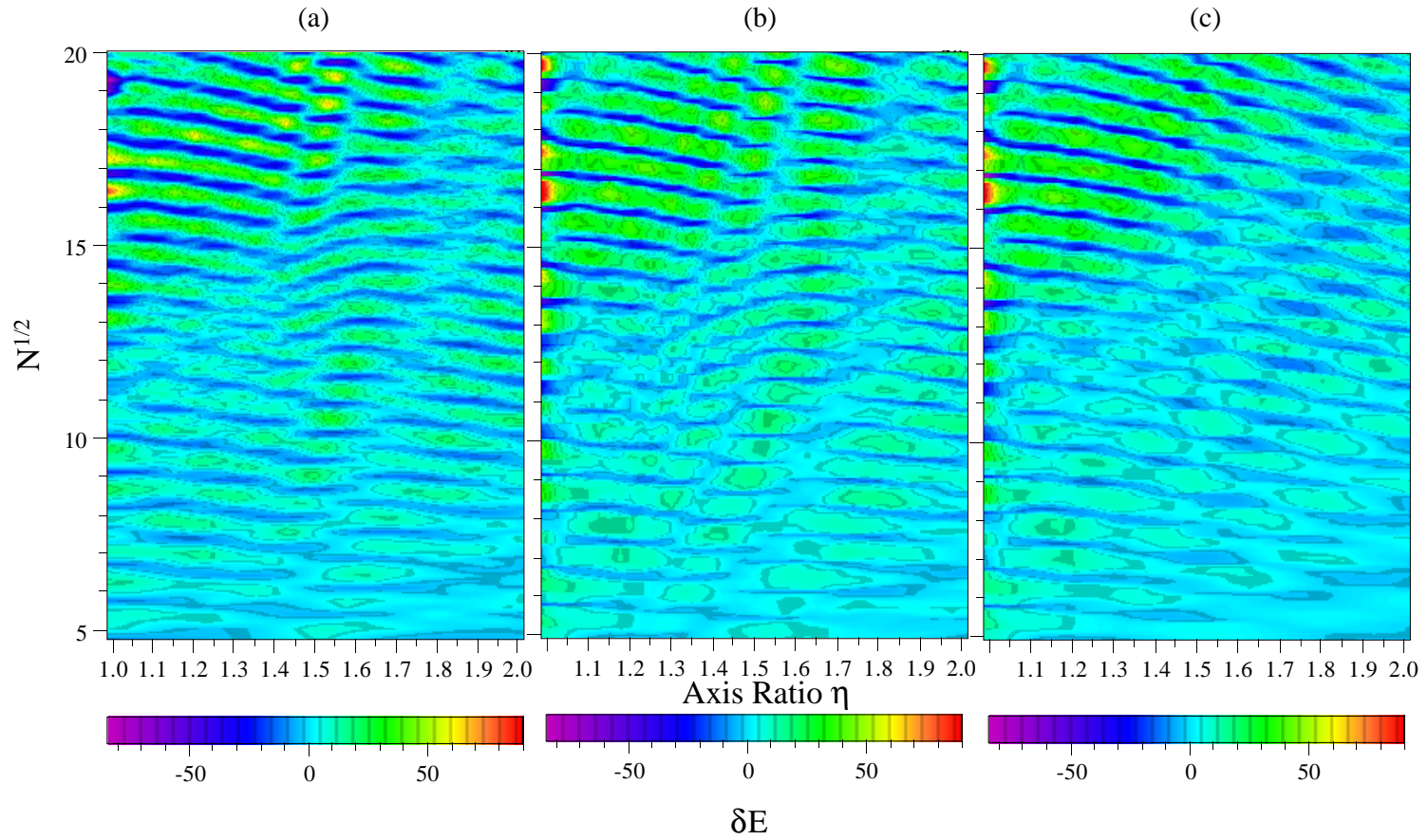
Fig. 20. Shell energy maps δE as functions of $N^{1/2}$ and deformation η. The quantum results as in Figs. 16, 18 and 19 appear on the left-hand side. The semiclassical ISPM results with and without taking account of the bifurcating orbits appear in the middle and on the right-hand side, respectively (see text).

Figures 19 and 20 show nice agreement of the ISPM results for the shell-correction energies with the corresponding quantum results. Note that we can substitute the exact Fermi energy ε_F into the semiclassical shell energy δE (6·2) by using the second equation of (6·2) for the particle number and quantum level density, as in Ref. 11). This is important to get the correct behavior of the shell-correction energy as a function of particle number N, as explained in Ref. 11). It is evident from Fig. 20 that the nice agreement between the ISPM and quantum results in the strongly deformed region of $\eta \geq \sqrt{2}$ cannot be attained without including the contributions from bifurcating 2(1,2) and (1,4) orbits.

In all our calculations we used the semiclassical approximation improved at the bifurcation points which becomes better with increasing kR for all deformation sizes including the bifurcation points.

§9.   Conclusion

The most essential new result of this paper in comparison to the Berry-Tabor theory are the two additional terms (the second and third ones in Eq. (6·1)) in the improved trace formula for elliptic billiard. These two terms represent the contributions from the short and long diameters which are continuous functions through all bifurcation points. For deformations far from the bifurcation points, we asymptotically obtain the standard Gutzwiller result for isolated diameters and the correct trace formula for diameters in spherical limit of circular billiard. Our results for the hyperbolic and elliptic orbits improved near the bifurcation points are simpler than those suggested within the uniform approximation.[4),26)]

Making use of our improved trace formula, we have demonstrated the importance of bifurcations of the repeated short diameter orbit in the emergence of shell structure at large deformations.

Acknowledgements

Appendix A
—— *Curvatures* ——

The actions I_u and I_v given by Eq. (3·5) are expressed explicitly in terms of the elliptic integrals.[47),49)] For elliptic orbits one has

$$
\begin{aligned}
I_u &= \frac{2}{\pi} \zeta \sqrt{2m\varepsilon\sigma}\ \mathrm{E}\left(\frac{\pi}{2}, \frac{1}{\sqrt{\sigma}}\right), \\
I_v &= \frac{1}{\pi} \zeta \sqrt{2m\varepsilon\sigma}\left[\mathrm{E}\left(\theta_e, \frac{1}{\sqrt{\sigma}}\right) - \mathrm{E}\left(\frac{\pi}{2}, \frac{1}{\sqrt{\sigma}}\right) + \frac{\eta^2 - \sigma(\eta^2 - 1)}{\eta\sqrt{\eta^2 - 1}}\right], \quad \text{(A·1)}
\end{aligned}
$$

while for hyperbolic orbits,

$$I_u = \frac{2}{\pi}\zeta\sqrt{2m\varepsilon}\left[\mathrm{E}\left(\frac{\pi}{2},\frac{1}{\sqrt{\sigma}}\right) - (1-\sigma)\,\mathrm{F}\left(\frac{\pi}{2},\frac{1}{\sqrt{\sigma}}\right)\right],$$

$$I_v = \frac{1}{\pi}\zeta\sqrt{2m\varepsilon}\left\{(1-\sigma)\left[\mathrm{F}\left(\frac{\pi}{2},\frac{1}{\sqrt{\sigma}}\right) - \mathrm{F}\left(\theta_h,\frac{1}{\sqrt{\sigma}}\right)\right]\right.$$

$$\left. + \mathrm{E}\left(\theta_h,\frac{1}{\sqrt{\sigma}}\right) - \mathrm{E}\left(\frac{\pi}{2},\frac{1}{\sqrt{\sigma}}\right) + \frac{\eta^2 - \sigma(\eta^2-1)}{\eta\sqrt{\eta^2-1}}\right\}. \qquad \text{(A·2)}$$

Equations (A·1) and (A·2) may be regarded as equations for the energy surface $\varepsilon(I_u, I_v)$ written in terms of the parameter σ for its elliptic and hyperbolic parts, respectively.

The curvature K of the energy curve is obtained by differentiating Eqs. (A·1) and (A·2) with respect to the parameter σ. In this way one gets Eq. (3·13) with the following derivatives for elliptic orbits:

$$\frac{\partial I_u}{\partial\sigma} = \frac{1}{\pi}\frac{\zeta\sqrt{2m\varepsilon}}{\sqrt{\sigma}}\,\mathrm{F}\left(\frac{\pi}{2},\frac{1}{\sqrt{\sigma}}\right),$$

$$\frac{\partial^2 I_u}{\partial\sigma^2} = -\frac{1}{2\pi}\frac{\zeta\sqrt{2m\varepsilon}}{\sqrt{\sigma^3}}\,\Pi\left(\frac{\pi}{2},\frac{1}{\sigma},\frac{1}{\sqrt{\sigma}}\right),$$

$$\frac{\partial I_v}{\partial\sigma} = -\frac{1}{2\pi}\frac{\zeta\sqrt{2m\varepsilon}}{\sqrt{\sigma}}\left[\mathrm{F}\left(\frac{\pi}{2},\frac{1}{\sqrt{\sigma}}\right) - \mathrm{F}\left(\theta_e,\frac{1}{\sqrt{\sigma}}\right)\right],$$

$$\frac{\partial^2 I_v}{\partial\sigma^2} = \frac{1}{4\pi}\frac{\zeta\sqrt{2m\varepsilon}}{\sqrt{\sigma^3}}\left[\Pi\left(\frac{\pi}{2},\frac{1}{\sigma},\frac{1}{\sqrt{\sigma}}\right) - \Pi\left(\theta_e,\frac{1}{\sigma},\frac{1}{\sqrt{\sigma}}\right) + \frac{\eta\sqrt{\eta^2-1}}{\sqrt{1-(1-\sigma^{-1})\eta^2}}\right],$$
$$\text{(A·3)}$$

while for hyperbolic orbits,

$$\frac{\partial I_u}{\partial\sigma} = \frac{1}{\pi}\zeta\sqrt{2m\varepsilon}\,\mathrm{F}\left(\frac{\pi}{2},\sqrt{\sigma}\right),$$

$$\frac{\partial^2 I_u}{\partial\sigma^2} = \frac{1}{2\pi}\frac{\zeta\sqrt{2m\varepsilon}}{\sigma}\left[\Pi\left(\frac{\pi}{2},\sigma,\sqrt{\sigma}\right) - \mathrm{F}\left(\frac{\pi}{2},\sqrt{\sigma}\right)\right],$$

$$\frac{\partial I_v}{\partial\sigma} = \frac{1}{2\pi}\zeta\sqrt{2m\varepsilon}\left[\mathrm{F}\left(\theta_h,\sqrt{\sigma}\right) - \mathrm{F}\left(\frac{\pi}{2},\sqrt{\sigma}\right)\right],$$

$$\frac{\partial^2 I_v}{\partial\sigma^2} = \frac{1}{4\pi}\frac{\zeta\sqrt{2m\varepsilon}}{\sigma}\left[\Pi\left(\theta_h,\sigma,\sqrt{\sigma}\right) - \Pi\left(\frac{\pi}{2},\sigma,\sqrt{\sigma}\right)\right.$$

$$\left. + \mathrm{F}\left(\frac{\pi}{2},\sqrt{\sigma}\right) - \mathrm{F}\left(\theta_h,\sqrt{\sigma}\right)\right]. \qquad \text{(A·4)}$$

With Eq. (A·3) we obtain the curvature K_β (3·13) for elliptic orbits as

$$K_\beta = \frac{\pi}{4p\zeta}\frac{\kappa}{\mathrm{F}^2(\frac{\pi}{2},\kappa)}\left[\frac{\mathrm{F}(\theta,\kappa)}{\mathrm{F}(\frac{\pi}{2},\kappa)}\Pi\left(\frac{\pi}{2},\kappa^2,\kappa\right) - \Pi(\theta,\kappa^2,\kappa) + \frac{\eta\sqrt{\eta^2-1}}{\sqrt{1-(1-\kappa^2)\eta^2}}\right].$$
$$\text{(A·5)}$$

For hyperbolic orbits we have

$$K_\beta = \frac{\pi}{4p\zeta} \frac{1}{\kappa^2 \, \mathrm{F}^2(\frac{\pi}{2}, \kappa)} \left[\Pi(\theta, \kappa^2, \kappa) - \frac{\mathrm{F}(\theta, \kappa)}{\mathrm{F}(\frac{\pi}{2}, \kappa)} \Pi\left(\frac{\pi}{2}, \kappa^2, \kappa \right) \right]. \tag{A·6}$$

Appendix B
—— *Separatrix* ——

As for the case of turning points, [39) - 42)] one writes

$$\frac{1}{\hbar} \left[S_\alpha(\boldsymbol{I}', \boldsymbol{I}'', t_\alpha) - (\boldsymbol{I}'' - \boldsymbol{I}') \cdot \boldsymbol{\Theta}'' \right] = c_0^\| + c_1^\| x + c_2^\| x^2 + c_3^\| x^3 + \dots$$

$$\equiv \tau_0^\| + \tau_1^\| z + \frac{1}{3} z^3. \tag{B·1}$$

Here,

$$x = (I_u' - I_u'^{\,*})/\hbar, \tag{B·2}$$

$$c_0^\| = \frac{1}{\hbar} \left[S_\alpha^*(\boldsymbol{I}', \boldsymbol{I}'', t_\alpha) - (\boldsymbol{I}' - \boldsymbol{I}'')^* \cdot \boldsymbol{\Theta}''^* \right] = \frac{1}{\hbar} S_\alpha^*(\boldsymbol{\Theta}', \boldsymbol{\Theta}'', \varepsilon), \tag{B·3}$$

$$c_1^\| = \left(\frac{\partial S_\alpha}{\partial I_u'} - \Theta_u'' \right)^* = \Theta_u' - \Theta_u'' \to 0, \qquad (\sigma \to 1) \tag{B·4}$$

$$c_2^\| = \frac{\hbar}{2} \left(\frac{\partial^2 S_\alpha}{\partial I_u'^{\,2}} \right)^* = 2\pi M \hbar K^\| \to \infty, \qquad (\sigma \to 1) \tag{B·5}$$

$$c_3^\| = \frac{\hbar^2}{6} \left(\frac{\partial^3 S_\alpha}{\partial I_u'^{\,3}} \right)^* = \frac{2\pi \hbar^2 M}{3} \left(\frac{\partial K^\|}{\partial I_u} \right) < 0, \qquad (\sigma \to 1) \tag{B·6}$$

where the symbol $*$ indicates that $I_u' = I_u'' = I_u^*$. The asymptotic behavior of the constants $c_i^\|$ near the separatrix $\sigma \approx 1$ was found from

$$K^\| \to \frac{\pi \log[(1 + \sin\theta)/(1 - \sin\theta)]}{p\zeta(\sigma - 1) \log^3(\sigma - 1)}, \qquad (\sigma \to 1) \tag{B·7}$$

$\theta \to \theta_h(\eta)$ formally, see (3·9),

$$\frac{\partial K^\|}{\partial I_u} \to -\frac{2\pi^2 \log[(1 + \sin\theta)/(1 - \sin\theta)]}{(p\zeta(\sigma - 1) \log^2(\sigma - 1))^2}. \qquad (\sigma \to 1) \tag{B·8}$$

The second equality in Eq. (B·1) was obtained by a linear transformation with some constants α and β,

$$x = \alpha z + \beta, \qquad \alpha = (3 c_3^\|)^{-1/3}, \qquad \beta = -c_2^\|/(3 c_3^\|), \tag{B·9}$$

$$\tau_0^\| = (c_0 - c_1 c_2/(3 c_3) + 2 c_2^3/(27 c_3^2))^\|, \qquad \tau_1^\| = \alpha[c_1 - c_2^2/(3 c_3)]^\|. \tag{B·10}$$

Near the stationary point for $\sigma \to 1$, one has $c_1^\| \to 0$ and $\tau_1^\| \to -w_\|$ with the positive quantity

$$w_\| = \left(\frac{c_2^2}{(3 c_3)^{4/3}} \right)^\| \to \left| \frac{M \log[(1 + \sin\theta)/(1 - \sin\theta)] p\zeta(\sigma - 1)}{2\hbar \log(\sigma - 1)} \right|^{2/3}. \tag{B·11}$$

Using the expansion (B·1) in Eq. (4·1) and taking the integral over the angle Θ_v'' exactly, i.e. writing 2π instead of this integral, one gets

$$
\begin{aligned}
\delta g_{\mathrm{scl}}^{(lM)} &= -\frac{2}{\hbar} \operatorname{Re} \sum_\alpha \int d\Theta_u'' \frac{1}{|\omega_v^*|} e^{i(\tau_0 - \nu_\alpha)} \sqrt{\frac{\sqrt{w_\parallel}}{c_2^\parallel}} \\
&\quad \times \left[\operatorname{Ai}\left(-w_\parallel, \mathcal{Z}_{lM,1}^\parallel, \mathcal{Z}_{lM,2}^\parallel\right) + i \operatorname{Gi}\left(-w_\parallel, \mathcal{Z}_{lM,1}^\parallel, \mathcal{Z}_{lM,2}^\parallel\right) \right] \\
&\approx -\frac{2}{\hbar} \operatorname{Re} \sum_\alpha \int d\Theta_u'' \frac{1}{|\omega_v^*|} e^{i(\tau_0 - \nu_\alpha)} \sqrt{\frac{\sqrt{w_\parallel}}{c_2^\parallel}} \left[\operatorname{Ai}\left(-w_\parallel\right) + i \operatorname{Gi}\left(-w_\parallel\right) \right],
\end{aligned}
$$

(B·12)

where

$$
\mathcal{Z}_{lM,1}^\parallel = \sqrt{w_\parallel}, \qquad \mathcal{Z}_{lM,2}^\parallel = \sqrt{\frac{c_2^\parallel}{\sqrt{w_\parallel}} \frac{I_u^{(\mathrm{cr})}}{\hbar}} + \sqrt{w_\parallel}.
$$

(B·13)

Here, $\operatorname{Ai}(-w, z_1, z_2)$ and $\operatorname{Gi}(-w, z_1, z_2)$ are incomplete Airy and Gairy functions, [48]

$$
\left\{ \begin{matrix} \operatorname{Ai}(-w, z_1, z_2) \\ \operatorname{Gi}(-w, z_1, z_2) \end{matrix} \right\} = \frac{1}{\pi} \int_{z_1}^{z_2} dz \left\{ \begin{matrix} \cos \\ \sin \end{matrix} \right\} \left(-wz + z^3/3\right),
$$

(B·14)

and $\operatorname{Ai}(-w)$ and $\operatorname{Gi}(-w)$ are the corresponding standard complete functions. [47] Here we used in the second equation of Eq. (B·12) the fact that for any finite deformation η and large kR near the separatrix ($\sigma \to 1$) one gets (see Eq. (B·11))

$$
\mathcal{Z}_{lM,1}^\parallel \to 0, \quad \mathcal{Z}_{lM,2}^\parallel \to 4 \left[\frac{M \log[(1 + \sin\theta)/(1 - \sin\theta)]p\zeta}{2(\sigma - 1)^2 \log^4(\sigma - 1)} \right]^{1/3}
$$

$$
\times \left[\frac{\eta}{\sqrt{\eta^2 - 1}} \operatorname{E}\left(\frac{\pi}{2}, \frac{\sqrt{\eta^2 - 1}}{\eta}\right) - 1 \right] \to \infty. \quad \text{(B·15)}
$$

Using an analogous expansion of the action τ_0 in Eq. (B·12) with respect to the angle Θ_u'' to third order and making a linear transformation like Eq. (B·9), one arrives at Eq. (5·33). We introduced in (5·33) several new quantities, like

$$
w_\perp = \left(\frac{c_2^2}{(3c_3)^{4/3}} \right)^\perp > 0,
$$

(B·16)

$$
\mathcal{Z}_{lM,2}^\perp = \sqrt{w_\perp}, \qquad \mathcal{Z}_{lM,2}^\perp = \frac{\pi}{2} \left(\left|3c_3^\perp\right| \right)^{1/3} + \sqrt{w_\perp},
$$

(B·17)

$$
c_2^\perp = \frac{1}{2\hbar}(J_\alpha^\perp)^* = \frac{1}{2\hbar} \left(\frac{\partial^2 S_\alpha}{\partial \Theta_u'^2} + 2\frac{\partial^2 S_\alpha}{\partial \Theta_u' \partial \Theta_u''} + \frac{\partial^2 S_\alpha}{\partial \Theta_u''^2} \right)_{lM}^* = -\frac{F_{lM}}{8\pi M K^\parallel}, \quad \text{(B·18)}
$$

where F_{lM} is the stability factor for long diameters (see Eq. (5·35)):

$$
\begin{aligned}
c_3^\perp &= \frac{1}{6\hbar} \left[\frac{\partial^3 S_\alpha}{\partial \Theta_u'^3} + 3\frac{\partial^3 S_\alpha}{\partial \Theta_u'^2 \partial \Theta_u''} + 3\frac{\partial^3 S_\alpha}{\partial \Theta_u' \partial \Theta_u''^2} + \frac{\partial^3 S_\alpha}{\partial \Theta_u''^3} \right]^* \\
&= \frac{1}{6\hbar} \left[\frac{\partial J_\alpha^\perp}{\partial \Theta_u'} + \frac{\partial J_\alpha^\perp}{\partial \Theta_u''} \right]^* < 0.
\end{aligned}
$$

(B·19)

Note that, according to Eq. (B·18), the quantity $c_2^\perp$ goes to 0 near the separatrix ($\sigma \to 1$) as in the caustic case. This is the reason that the Maslov-Fedoryuk theory [39] - [42] can be used for the transformation of the integral over the angle Θ_u'' in Eqs. (B·12) into Eq. (5·33).

Appendix C
—— *Jacobians for Closed Orbits with Two Reflection Points* ——

The Jacobian $J_{\text{co2}}^{\parallel}$ defined by the derivative in Eq. (5·38) for closed orbits α like "co2" with two reflection points, $J_{\text{co2}}^{\parallel} = \left(\delta \bar{y}'' / \delta \theta_p' \right)_{\text{co2}}$, can be calculated by means of the caustic method. [11] The main idea of this method is to use a specific property of the trajectories in the billiard system like elliptic cavity. These trajectories consist of straight lines which are tangent to a curve called an elliptic or hyperbolic caustic between turning points. Our trajectory stability problem for the variations $\delta \bar{y}''$ at a given $\delta \theta_p'$ (see Fig. 3) is much simplified by reducing it to the calculation of the caustics semi-axes a_c, b_c and $a_c + \delta a_c, b_c + \delta b_c$ for the closed orbit "co2" and its $\delta \theta_p'$ deflection, respectively. For the case of closed non-periodic orbits "co2", the semi-axes a_c and b_c and their variations are functions of the initial point (x, y), in contrast with the stability problem for the periodic orbits of Ref. 11). The orbit-length invariant curve (confocal-to-boundary ellipse or hyperbola crossing the point (x, y) (see Fig. 4)) and its semi-axis variations play a similar role for the calculation of the "co2" stability factor $J_{\text{co2}}^{\parallel}$ with that of the boundary parameter for the periodic orbits in Ref. 11). In this way this stability factor is obtained in the form

$$J_{\text{co2}}^{\parallel} = \frac{q_0 - q_1}{\sqrt{1 + q_1}} \mathcal{D}, \qquad \mathcal{D} = \frac{x'' - x}{\delta \theta_p'}, \tag{C·1}$$

where x'' is the x-coordinate of the final point O' (see Fig. 3), and q_0 and q_1 are the tangents of the slope angle for the initial and final directions of particle motion along the orbit "co2",

$$q_0 = \pm \frac{x_{c1}}{y_{c1}} \left(\frac{b_c}{a_c} \right)^2, \qquad q_1 = \pm \frac{x_{c2}}{y_{c2}} \left(\frac{b_c}{a_c} \right)^2. \tag{C·2}$$

Here, the upper and lower signs stand for the hyperbolic and elliptic closed orbits, (x_{c1}, y_{c1}) and (x_{c2}, y_{c2}) are the first and last tangent-to-caustics points of the trajectory "co2",

$$x_{c1} = \frac{B_c + \sqrt{B_c^2 - A_c C_c}}{A_c}, \quad y_{c1} = \left\{ \begin{array}{c} 1 \\ (a_c - x)/|a_c - x| \end{array} \right\} b_c \sqrt{1 \pm \left(\frac{x_{c1}}{a_c} \right)^2}, \quad (C·3)$$

$$x_{c2} = \frac{B_c - \sqrt{B_c^2 - A_c C_c}}{A_c}, \quad y_{c2} = \left\{ \begin{array}{c} -A_c/|A_c| \\ 1 \end{array} \right\} b_c \sqrt{1 \pm \left(\frac{x_{c2}}{a_c} \right)^2}, \quad (C·4)$$

respectively, and

$$A_c = b_c^2 x^2 \mp a_c^2 y^2, \qquad B_c = \mp a_c^2 b_c^2 x, \qquad C_c = a_c^4 (b_c^2 - y^2). \tag{C·5}$$

The semi-axes a_c and b_c, as functions of the initial point (x, y) for the hyperbolic and elliptic caustics for the orbit "co2" (see Fig. 4), are given by

$$a_c = a\sqrt{\frac{\mp(b_x - b_c)\mathcal{Z}}{b_x + b_c}}, \qquad b_c = b\sqrt{1 - \mathcal{Z}}, \qquad \text{(C·6)}$$

where a_x and b_x are the semi-axes for the confocal-to-boundary hyperbola and the ellipse crossing any current initial and final point (x, y) of the orbit "co2" inside the elliptic billiard,

$$b_x^2 = \frac{x^2 + y^2 + b^2 - a^2 \mp \sqrt{(x^2 + y^2 + b^2 - a^2)^2 - 4y^2(b^2 - a^2)}}{2},$$
$$a_x^2 = \mp(b_x^2 - b^2 + a^2), \qquad \text{(C·7)}$$

and $\mathcal{Z}$ is the root of the cubic algebraic equation

$$(1 - \eta^2)^2 \mathcal{Z}^3 + \left[(1 + \eta^2)^2 \left(\frac{b_x}{b}\right)^2 + 1 - \eta^4\right]\mathcal{Z}^2$$
$$+ \left[2\eta^2 - 1 - 2(1 + \eta^2)\left(\frac{b_x}{b}\right)^2\right]\mathcal{Z} + \left(\frac{b_x}{b}\right)^2 - 1 = 0. \quad \text{(C·8)}$$

The factor $\mathcal{D}$ in Eq. (C·1) is given by

$$\mathcal{D} = \frac{2a_x \Phi_a G}{A_0}, \qquad \text{(C·9)}$$

where

$$\Phi_a = \eta^2 f_c \left[\frac{\mp 4a_c^2 b^2 + \eta^2(a^2 \pm a_c^2)^2 - b_c^4/\eta^2}{2a_c(b^2 - b_c^2 \pm \eta^2 a_c^2)^2}\right], \qquad \text{(C·10)}$$

$$f_c = 2\left[d_0 x + \frac{q_0(d_0^2 - b^2 + a^2)}{1 + q_0^2}\right], \qquad d_0 = y - q_0 x, \qquad \text{(C·11)}$$

$$G = \frac{2B_0 d_0 q_0 + A_0(b_x^2 \mp a_x^2 - d_0^2) - C_0(1 + q_0^2)}{2\sqrt{B_0^2 - A_0 C_0}} - d_0 q_0$$
$$+ \frac{(1 + q_0^2)(B_0 - \sqrt{B_0^2 - A_0 C_0})}{A_0}, \qquad \text{(C·12)}$$

with

$$A_0 = b_x^2 \mp a_x^2 q_0^2, \qquad B_0 = \mp a_x^2 d_0 q_0, \qquad C_0 = \mp a_x^2(d_0^2 - b_x^2). \qquad \text{(C·13)}$$

Here we have used the invariance of the Jacobian $\mathcal{J}(x, y)$ with respect to time reversal.

References

1) M. C. Gutzwiller, J. Math. Phys. **12** (1971), 343; and earlier references quoted therein.
2) M. C. Gutzwiller, *Chaos in Classical and Quantum Mechanics* (Springer-Verlag, New York, 1990).
3) R. B. Balian and C. Bloch, Ann. of Phys. **69** (1972), 76; and earlier references quoted therein.
4) M. V. Berry and M. Tabor, Proc. Roy. Soc. London **A349** (1976), 101.
5) M. V. Berry and M. Tabor, J. of Phys. **A10** (1977), 371.
6) V. M. Strutinsky, A. G. Magner, S. R. Ofengenden and T. Døssing, Z. Phys. **A283** (1977), 269.
7) M. Brack and R. K. Bhaduri, *Semiclassical Physics* (Addison and Wesley, Reading, 1997).
8) V. M. Strutinsky, Nucleonica **20** (1975), 679.
9) V. M. Strutinsky and A. G. Magner, Sov. Phys. Part. & Nucl. **7** (1977), 138.
10) S. C. Creagh and R. G. Littlejohn, Phys. Rev. **A44** (1990), 836; J. of Phys. **A25** (1992), 1643.
11) A. G. Magner, S. N. Fedotkin, F. A. Ivanyuk, P. Meier, M. Brack, S. M. Reimann and H. Koizumi, Ann. of Phys. **6** (1997), 555.
12) A. G. Magner, S. N. Fedotkin, F. A. Ivanyuk, P. Meier and M. Brack, Czech. J. of Phys. **48** (1998), 845.
13) A. G. Magner et al., to be published.
14) S. Okai, H. Nishioka and M. Ohta, Mem. Konan Univ. Sci. Ser. **37** (1) (1990), 29.
15) H. Nishioka, M. Ohta and S. Okai, Mem. Konan Univ. Sci. Ser. **38** (2) (1991), 1.
16) H. Nishioka, N. Nitanda, M. Ohta and S. Okai, Mem. Konan Univ. Sci. Ser. **39** (2) (1992), 67.
17) H. Nishioka, M. Ohta and S. Okai, Konan Univ. Preprint (unpublished, 1993).
18) K. Arita and K. Matsuyanagi, Nucl. Phys. **A592** (1995), 9.
19) Th. Schachner, Diploma thesis, Regensburg University (unpublished, 1997).
20) A. Sugita, K. Arita and K. Matsuyanagi, Prog. Theor. Phys. **100** (1998), 597.
21) K. Arita, A. Sugita and K. Matsuyanagi, *Proc. Int. Conf. on "Atomic Nuclei and Metallic Clusters," Praha, 1997*, Czech. J. of Phys. **48** (1998), 821.
22) K. Arita, A. Sugita and K. Matsuyanagi, Prog. Theor. Phys. **100** (1998), 1223.
23) M. Brack and S. R. Jain, Phys. Rev. **A51** (1995), 3462.
24) P. J. Richens, J. of Phys. **A15** (1982), 2110.
25) M. Sieber, J. of Phys. **A30** (1997), 4563.
26) H. Waalkens, J. Wiersig and H. Dullin, Ann. of Phys. **260** (1997), 50.
27) A. M. Ozorio de Almeida and J. H. Hannay, J. of Phys. **A20** (1987), 5873.
28) A. M. Ozorio de Almeida: *Hamiltonian Systems: Chaos and Quantization* (Cambridge University Press, Cambridge, 1988).
29) M. Sieber, J. of Phys. **A29** (1996), 4716.
30) M. Sieber, J. of Phys. **A30** (1997), 4563.
31) H. Schomerus and M. Sieber, J. of Phys. **A30** (1997), 4537.
32) S. Tomsovic, M. Grinberg and D. Ullmo, Phys. Rev. Lett **75** (1995), 4346.
33) D. Ullmo, M. Grinberg and S. Tomsovic, Phys. Rev. **E54** (1996), 135.
34) M. Brack, P. Meier and K. Tanaka, J. of Phys. **A32** (1999), 331.
35) S. C. Creagh, Ann. of Phys. **248** (1997), 60.
36) M. Brack, S. C. Creagh and J. Law, Phys. Rev. **A57** (1998), 788.
37) A. G. Magner, M. Brack, S. N. Fedotkin and K. Matsuyanagi, manuscript in preparation.
38) A. D. Bruno, Preprint Inst. Prikl. Mat. Akad. Nauk SSSR Moskva (in Russian, 1970), p. 44 (quoted in Ref. 30)).
39) M. V. Fedoryuk, Sov. J. Comp. Math. and Math. Phys. **4** (1964), 671; **10** (1970), 286.
40) V. P. Maslov, Theor. and Math. Phys. **2** (1970), 30.
41) M. V. Fedoryuk, *Saddle-Point Method*, in Russian (Nauka, Moscow 1977).
42) M. V. Fedoryuk, *Asymptotics: Integrals and sums*, in Russian (Nauka, Moscow 1987).
43) H. Nishioka, K. Hansen and B. R. Mottelson, Phys. Rev. **B42** (1990), 9377.
44) H. Frisk, Nucl. Phys. **A511** (1990), 309.
45) V. M. Strutinsky, Nucl. Phys. **A122** (1968), 1; and earlier references quoted therein.
46) S. Reimann, M. Brack, A. G. Magner, J. Blaschke and M. V. N. Murthy, Phys. Rev. **A53** (1996), 39.

47) M. Abramowitz and I. A. Stegun, *Handbook of mathematical functions* (Dover, New York, 1964).
48) W. E. Frahn, *Heavy-ion, high-spin states and nuclear structure*, v. I, p.192 (IAEA, Vienna, 1975).
49) P. F. Byrd and M. D. Friedman: *Handbook of Elliptic Integrals for Engineers and Scientists* (Springer-Verlag, New York, 1971).
50) L. D. Landau and E. M. Lifshits, *Theoretical Physics, Vol. 1: Classical mechanics*, in Russian (Nauka, Moscow 1973).
51) M. Brack, S. M. Reimann and M. Sieber, Phys. Rev. Lett. **79** (1997), 1817.
52) P. H. Morse and H. Feshbach, *Methods of theoretical physics* (McGraw-Hill, New York, 1953).
53) T. Misu, W. Nazarewicz and S. Åberg, Nucl. Phys. **A614** (1997), 44.
54) A. C. Merchant and W. D. M. Rae, Nucl. Phys. **A571** (1994), 43.
55) S. A. Moszkowski, Phys. Rev. **99** (1955), 803.
56) G. S. Ezra, J. Chem. Phys. **104** (1996), 1.
57) V. M. Strutinsky and F. A. Ivanyuk, Nucl. Phys. **A255** (1975), 405.

High-spin yrast structure of ^{32}S suggested by symmetry-unrestricted, cranked Hartree–Fock calculations

Masayuki Yamagami, Kenichi Matsuyanagi

Department of Physics, Graduate School of Science, Kyoto University, Kitashirakawa, Kyoto 606-8502, Japan

Abstract

The high-spin yrast structure of ^{32}S is investigated by means of the cranked Skyrme–Hartree–Fock method in the three-dimensional Cartesian-mesh representation without imposing restrictions on spatial symmetries. The result suggests that (1) a crossover from the superdeformed to the hyperdeformed-like configurations takes place on the yrast line at angular momentum $I \simeq 24$, which corresponds to the "band termination" point in the cranked harmonic-oscillator model, and (2) non-axial octupole deformations of the Y_{31} type play an important role in the yrast states in the range $5 \leqslant I \leqslant 13$. © 2000 Elsevier Science B.V. All rights reserved.

1. Introduction

Since the discovery of the superdeformed (SD) rotational band in ^{152}Dy, about two hundreds SD bands have been found in various mass ($A = 60, 80, 130, 150, 190$) regions [1–6]. It turned out that every regions of superdeformation have their own characteristics and offer a number of interesting questions; investigations of them have been significantly enlarging and deepening our understanding of nuclear structure. Yet, the doubly magic SD band in ^{32}S, which has been expected for quite a long time [7–10], remains unexplored, and will become a great challenge in the coming years [6]. Exploration of the SD band in ^{32}S will certainly give a strong impact toward understanding the possible connection between the SD structure and the molecular resonance phenomena associated with the ^{16}O + ^{16}O configurations (see, e.g., [11,12] for reviews). More generally speaking, the nucleus ^{32}S seems to be situated in a key position in the investigation of possible relationships (such as discussed in [13–15]) between the SD states systematically observed in heavy nuclei and

the cluster structures widely observed in light nuclei (see, e.g., [16] for a review). Thus, excited states in ^{32}S have been theoretically studied by Nilsson–Strutinsky approaches [7–10], selfconsistent mean-field approaches [17,18], spherical shell-models [19,20], and cluster-structure and molecular-resonance points of view [21–25].

The aim of this paper is to study the high-spin yrast structure of ^{32}S from the point of view of exploring exotic shapes in nuclear high-spin states by means of the cranked Hartree–Fock (HF) method with the use of the Skyrme forces [26,27], which is called "the cranked SHF method". One of the recent advances in nuclear structure theory is that it has become possible to carry out the HF calculation in the three-dimensional (3D) Cartesian-mesh representation [28–30,32]. This approach has been extended [18,33,34] to a rotating frame by introducing the cranking term and applied to the high-spin yrast states of ^{32}S in Ref. [18] with the use of the BKN interaction [31]. In these cranked HF calculations, however, parity and signature symmetries are assumed for the intrinsic wave functions in order to simplify the calculation. We refer an excellent review by Åberg, Flocard and Nazarewicz [2] for an overview of studies on nuclear shapes in terms of various kinds of mean-field theory, especially other than the cranked SHF approach.

Recently, we constructed a new computer code for the cranked SHF calculation based on the 3D Cartesian-mesh representation, which provides a powerful tool for exploring exotic shapes (breaking both axial and reflection symmetries in the intrinsic states) at high spin in unstable nuclei as well as in stable nuclei. As a first application of this new code, we investigated the high-spin yrast structure of ^{32}S, and found [35] that (1) a drastic structure change may occur above angular momentum $I \simeq 24$ in the yrast line, and (2) non-axial octupole deformations of the Y_{31} type arise in the yrast line in the range $5 \leqslant I \leqslant 13$. The present paper is intended to give a more detailed account of this work. Quite recently, Molique, Dobaczewski and Dudek [36] investigated several SD configurations in ^{32}S (not restricted to the yrast states) as well as in neighboring odd-A nuclei by means of the cranked SHF method with the SLy4 force [37] in the harmonic oscillator basis. On the other hand, they did not discuss the yrast states above $I \simeq 24$ as well as non-axial octupole deformations, which are the major subjects of this paper.

After a brief account of the cranked SHF calculational method in Section 2, an overview of the obtained yrast line for ^{32}S is given in Section 3. In Section 4, we discuss properties of the high-spin limit of the SD band, paying special attention to a band-crossing phenomenon associated with the level crossing with the rotation-aligned $[440]\frac{1}{2}$ level. The result of the cranked SHF calculation is compared in Section 5 with that of the cranked harmonic oscillator (CHO) model calculation. In Section 6, effects of the rotation-induced, time-odd components in the selfconsistent mean field on the properties of the SD band are briefly discussed. In Section 7, we discuss about the Y_{31} deformed solutions of the cranked SHF equations, which constitute the yrast line in the range $5 \leqslant I \leqslant 13$. Although, at the present time, experimental data directly comparable with our theoretical calculations seem to be unavailable, we briefly remark in Section 8 on some recent experimental references. Conclusions are given in Section 9.

2. Cranked SHF calculation

The cranked HF equation for a system uniformly rotating about the x-axis is given by

$$\delta \langle H - \omega_{\text{rot}} J_x \rangle = 0, \tag{1}$$

where ω_{rot} and J_x mean the rotational frequency and the x-component of angular momentum, and the bracket denotes the expectation value with respect to a Slater determinantal state. We solve the cranked HF equation for a Hamiltonian of the Skyrme type by means of the imaginary-time evolution technique [28] in the 3D Cartesian-mesh representation. We adopt the standard algorithm [28–30,34] in the numerical calculation, but completely remove various restrictions on spatial symmetries. Namely, we basically use the procedure developed and applied to the yrast line of ^{24}Mg by Bonche, Flocard and Heenen [34], except that the parity and the signature symmetries are not imposed on the individual wave functions. In this connection, we mention that a similar HF code (with parity projection but without the cranking term) was constructed by Takami et al. [38] and successfully applied to the description of cluster structures in light nuclei, ^{8}Be, ^{12}C, ^{16}O and ^{20}Ne. The same code (but without parity projection) was recently used to explore exotic shapes in proton-rich $N \simeq Z$ nuclei in the ^{80}Zr region [39,40], and tetrahedral and triangular shapes are suggested to appear near the ground states of some nuclei in this region. In Refs. [34,39,40], the pairing correlations were taken into account in the BCS approximation. In the present calculation, we neglect the pairing, since they are not expected to play an important role at high-spin states in ^{32}S.

When we allow for the simultaneous breaking of both reflection and axial symmetries, it is crucial to accurately fulfill the center-of-mass condition

$$\left\langle \sum_{i=1}^{A} x_i \right\rangle = \left\langle \sum_{i=1}^{A} y_i \right\rangle = \left\langle \sum_{i=1}^{A} z_i \right\rangle = 0, \tag{2}$$

and the principal-axis condition

$$\left\langle \sum_{i=1}^{A} x_i y_i \right\rangle = \left\langle \sum_{i=1}^{A} y_i z_i \right\rangle = \left\langle \sum_{i=1}^{A} z_i x_i \right\rangle = 0. \tag{3}$$

For this purpose we examined several techniques [41] and confirmed that the constrained HF procedure with quadrupole constraints [42] works well. Thus, we replace the "Routhian" $R = H - \omega_{\text{rot}} J_x$ in Eq. (1) with

$$R' = R - \sum_{k=1}^{3} \mu_k \left\langle \sum_{i=1}^{A} (x_k)_i \right\rangle^2 - \sum_{k<k'}^{3} \mu_{k,k'} \left\langle \sum_{i=1}^{A} (x_k x_{k'})_i \right\rangle^2. \tag{4}$$

In numerical calculations, we confirmed that the constraints (2) and (3) are fulfilled to the order O(10^{-15}) with values of the parameters $\mu_k \sim$ O(10^2) and $\mu_{k,k'} \sim$ O(1). We solved these equations inside the sphere with radius $R = 8$ [fm] and mesh size $h = 1$ [fm], starting with various initial configurations. The 11-point formula was used as the difference formula for the Laplacian operator. As usual, the angular momentum is evaluated as $I\hbar = \langle J_x \rangle$.

In this paper, we use the standard SIII and SkM* forces. With the use of the SIII force [26], Tajima et al. [30] carried out a systematic SHF + BCS calculation for the ground-state quadrupole deformations of nuclei in a wide area of nuclear chart. They have carefully examined the possible error due to the use of the mesh size $h = 1$ [fm] and found that the deformation energies obtained with this mesh size are quite accurate. On the other hand, the SkM* force [27] was designed to accurately describe properties at large deformations like fission barriers, so that it may be suited for the description of superdeformations [32]. In recent years, several newer versions of the Skyrme forces have been proposed (see, e.g., Ref. [43]) in order to improve isospin properties of the Skyrme forces. Although the major purpose of them is to better describing neutron-rich unstable nuclei, it will also be interesting to employ such versions to examine the dependence of the results reported in this paper on the effective interactions adopted. We defer such a more extensive calculation to the future.

3. Structure of the yrast line

The calculated yrast line is displayed in Fig. 1, and angular momenta and deformations of the yrast states are drawn as functions of rotational frequency in Figs. 2 and 3. In these and succeeding figures, the calculation were done in step of $\Delta\omega_{\rm rot} = 0.2$ MeV/$\hbar$, and the calculated points (indicated by symbols) are smoothly interpolated by lines. The quadrupole deformation parameters β_2 and γ are defined as
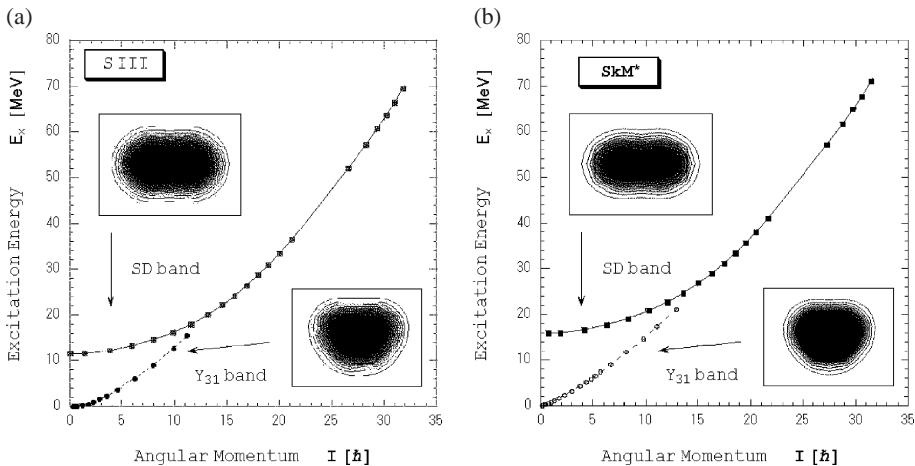
Fig. 1. (a) Excitation energy vs. angular-momentum plot for the yrast structure of ^{32}S, calculated with the SIII force. Density distributions on the plane *perpendicular* to the rotation axis are shown, as insets, for the SD band (solid line) and the Y_{31} band (dashed line). The calculation was done in step of $\Delta\omega_{\rm rot} = 0.2$ MeV/$\hbar$, and the calculated points (indicated by symbols) are smoothly interpolated by lines. (b) Same as (a), but with the SkM* force.
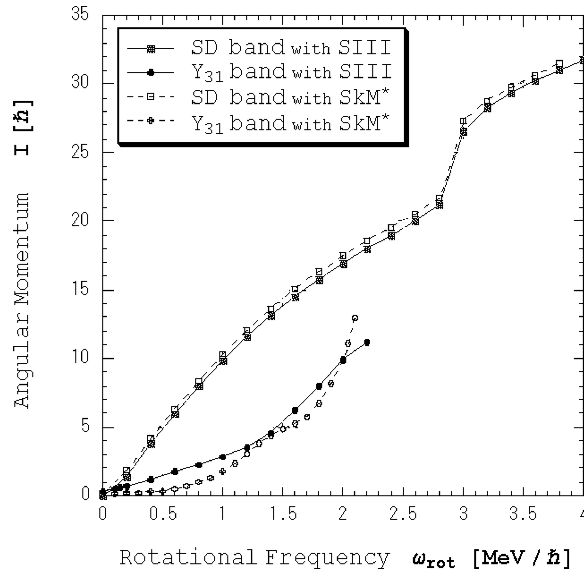
Fig. 2. Angular momentum I plotted as a function of rotational frequency ω_{rot} for the SD band and the Y_{31} band in ^{32}S. Results calculated with the SIII and SkM* forces are shown by solid and dashed lines, respectively.
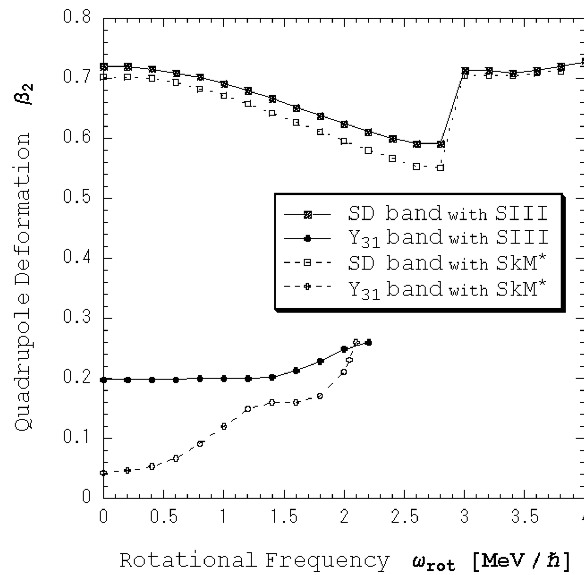
Fig. 3. Quadrupole deformation β_2 plotted as a function of rotational frequency ω_{rot} for the SD band and the Y_{31} band in ^{32}S. Results calculated with the SIII and SkM* forces are shown by solid and dashed lines, respectively.

$$\beta_2 \cos \gamma = \frac{4\pi}{5} \left\langle \sum_{i=1}^{A} r_i^2 Y_{20}(\theta_i, \phi_i) \right\rangle \left\langle \sum_{i=1}^{A} r_i^2 \right\rangle^{-1}, \tag{5}$$

$$\beta_2 \sin \gamma = -\frac{4\pi}{5} \left\langle \frac{1}{\sqrt{2}} \sum_{i=1}^{A} r_i^2 \left(Y_{22}(\theta_i, \phi_i) + Y_{22}^*(\theta_i, \phi_i) \right) \right\rangle \left\langle \sum_{i=1}^{A} r_i^2 \right\rangle^{-1}. \tag{6}$$

It is seen from Figs. 1–3 that the results of the calculations with the SIII and SkM* forces are quite similar: For both cases, the expected SD band becomes the yrast for $I \geqslant 14$, and it exhibits a singular behavior at about $I \simeq 24$. As we shall discuss in the next section, this is due to a band crossing associated with the rotation-aligned $[440]\frac{1}{2}$ level, and we call the yrast states above $I \simeq 24$ "hyperdeformed (HD)-like configuration" in order to distinguish them from the SD configuration. This configuration becomes unstable against fission for $I \geqslant 34$. In addition to the SD and HD-like configurations mentioned above, we found that the yrast states with $5 \leqslant I \leqslant 13$ possess an appreciable amount of non-axial octupole deformation of the Y_{31} type, so that we call, for convenience, this region of the yrast line "Y_{31} band", although, as discussed in Section 7, some caution is necessary in using this terminology.

Thus, the calculated yrast line can be roughly divided into the following four regions:

(1) $I \leqslant 4$, weakly prolate region,

(2) $5 \leqslant I \leqslant 13$, Y_{31} deformed region,

(3) $14 \leqslant I \leqslant 24$, SD region,

(4) $26 \leqslant I \leqslant 32$, HD-like region.

Below we first discuss the properties of the high-spin limit of the SD band, and later about the Y_{31} band. The lowest-spin region will be touched upon in Section 8 briefly.

4. High-spin limit of the SD band

As we saw in Figs. 1–3, the solutions of the cranked SHF equations corresponding to the yrast SD configuration are obtained from $I = 0$ to about $I = 22$.

Fig. 4 shows the potential energy function for the SD state at $I = 0$, evaluated by means of the constrained HF procedure [42] with the quadratic constraint on the mass-quadrupole moment. We see that the excitation energy of the SD state at $I = 0$ is about 12 MeV.

A particularly interesting point is the behavior of the SD band in the high-spin limit: It is clearly seen in Figs. 2 and 3 that a jump occurs both in the angular momentum I and the quadrupole deformation β_2 at $\omega_{rot} \simeq 2.9$ MeV/$\hbar$. At this point, I jumps from about 22 to 26, and β_2 suddenly increases from about 0.6 to 0.7. Such a discontinuity is well known [44] to occur in the description of the band crossing phenomena within a standard framework of the cranked mean-field approach. The point is more clearly seen in Fig. 5 as a singular behavior of the dynamical moment of inertia $\mathcal{J}^{(2)} = dI/d\omega_{rot}$ near the band crossing point. (Other properties of $\mathcal{J}^{(2)}$ will be discussed in the next section.)

Fig. 6 displays the shape evolution of the SD band as a function of angular momentum in the (β_2, γ) plane: With increasing angular momentum, small triaxial deformations
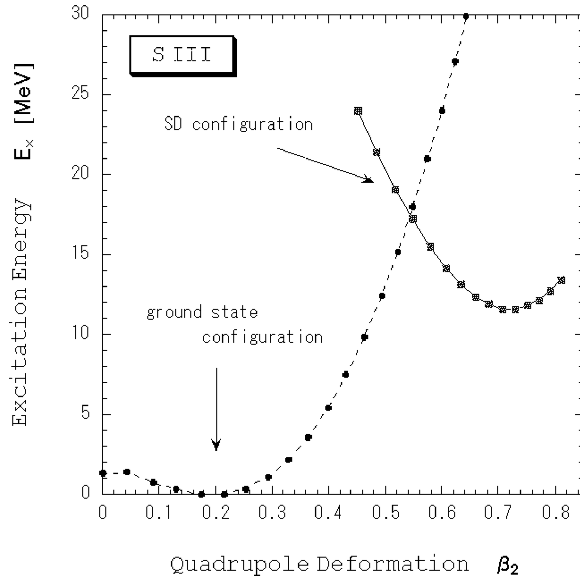
Fig. 4. Potential energy function at $I = 0$ for the SD configuration (solid line) relative to that for the ground state configuration (dashed line) in ^{32}S, calculated with the SIII force.
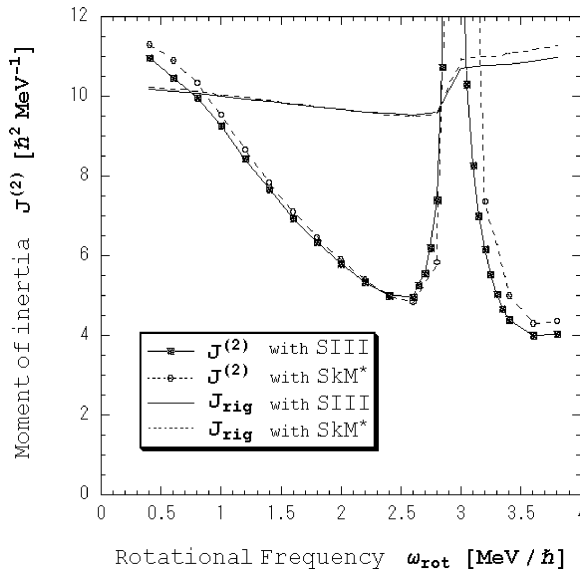
Fig. 5. Dynamical moment of inertia $\mathcal{J}^{(2)} = dI/d\omega_{\text{rot}}$ plotted as a function of ω_{rot} for the SD band in ^{32}S. Results calculated with the SIII and SkM* forces are shown by solid and dashed lines, respectively. For reference, the rigid moments of inertia $\mathcal{J}_{\text{rig}} = m \int \rho(\mathbf{r})(y^2 + z^2) \, d\mathbf{r}$ with the calculated density $\rho(\mathbf{r})$ are also indicated.
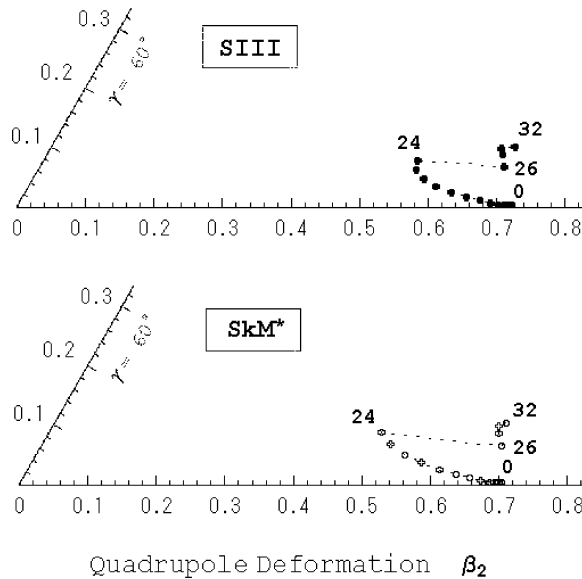
Fig. 6. Shape evolution as a function of angular momentum, plotted in the (β_2, γ) plane for the SD and HD-like configurations in ^{32}S. Results calculated with the SIII and SkM* forces are shown separately.

gradually set in and at $I \simeq 24$ the shape exhibits a striking "back-bending" toward larger prolate deformations. Evidently, this is due to the band crossing mentioned above. Such a singular behavior of the SD band can be noticed also in the previous cranked HF calculation with the BKN force [18]. In Fig. 6 we also plot the $I = 24$ and 26 states, which are missing in Figs. 1–3, by smoothly extrapolating the I–ω_{rot} and (β_2, γ)–I curves for the SD and the HD-like configurations, respectively (see Ref. [44] for the treatment of the band-crossing region).

The microscopic origin of this singular behavior may be understood when we examine the single-particle energy diagram in the rotating frame (routhians) presented in Fig. 7. We see that the rotation-aligned level associated with the $[440]\frac{1}{2}$ orbit comes down in energy with increasing ω_{rot} and crosses the Fermi level at $\omega_{\mathrm{rot}} \simeq 2.9$ MeV/$\hbar$ which corresponds to $I \simeq 24$. Thus, the yrast states above $I \simeq 24$ are characterized by the occupation of the $[440]\frac{1}{2}$ level by a single proton and a neutron. According to the deformed harmonic-oscillator model, $N = Z = 18$ is a magic number associated with the HD shell structure with axis ratio 3 : 1, in which the $[440]\frac{1}{2}$ level is occupied by two protons and two neutrons. In order to distinguish the yrast states with $I \geqslant 26$ from the SD states below $I \simeq 24$ and keeping in mind a connection to the HD configuration, we call them "the HD-like configuration" although the magnitude of the quadrupole deformation β_2 obtained in the SHF calculation is in fact comparable to that of the SD shape rather than the HD shape.

Let us note that if we regard the SD configuration as to correspond to the j–j-coupling shell model $4p$–$12h$ configuration $\pi[(f_{7/2})^2(sd)^{-6}] \otimes \nu[(f_{7/2})^2(sd)^{-6}]$ (relative to ^{40}Ca) in the spherical limit, the maximum angular momentum that can be generated by aligning
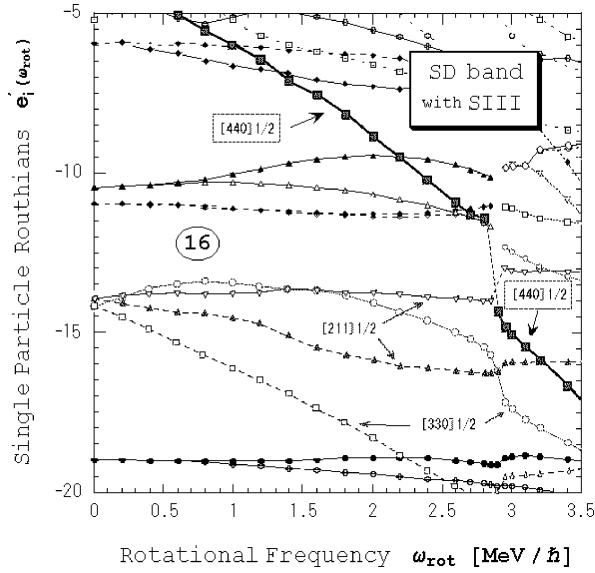
Fig. 7. Single-particle energy diagram (for neutrons) in the rotating frame for the SD band in ^{32}S, plotted as a function of $\omega_{\rm rot}$. The SIII force is used. Note that the structure of the yrast configuration drastically changes at $\omega_{\rm rot} \simeq 2.9$ MeV/$\hbar$, so that the diagram is discontinuous about this point, although levels characterized by the same asymptotic quantum numbers are linked by lines.

the single-particle angular momenta toward the direction of the rotation axis is $24\hbar$, and thus "the SD band termination" might be expected at this angular momentum. Interestingly, our calculation indicates that a crossover to the HD-like configuration takes place just at this region of the yrast line.

5. Comparison with the CHO model

The behavior at the high-spin limit of the SD band obtained in the SHF calculation possesses some similarities with that expected from the CHO model. This model has been frequently used [45–50] as a simplified model of rotating mean fields. With obvious notations, the single-particle Hamiltonian of this model is written as

$$h' = \sum_{k=1}^{3} \hbar\omega_k \left(c_k^\dagger c_k + \frac{1}{2} \right) - \omega_{\rm rot} l_1, \tag{7}$$

where

$$c_k^\dagger = \sqrt{\frac{m\omega_k}{2\hbar}} \left(x_k - \frac{i p_k}{m\omega_k} \right), \tag{8}$$

with (x_1, x_2, x_3) indicating (x, y, z), etc.

The orbital angular momentum operator l_1 consists of two parts:

$$l_1 = l_1^{(\Delta N=0)} + l_1^{(\Delta N=2)} \tag{9}$$

with

$$l_1^{(\Delta N=0)} = i\hbar \frac{\omega_2 + \omega_3}{2\sqrt{\omega_2 \omega_3}} (c_3^\dagger c_2 - c_2^\dagger c_3), \tag{10}$$

$$l_1^{(\Delta N=2)} = i\hbar \frac{\omega_3 - \omega_2}{2\sqrt{\omega_2 \omega_3}} (c_2^\dagger c_3^\dagger - c_3 c_2). \tag{11}$$

For a given value of $\omega_{\rm rot}$ or $I\hbar = \langle \sum_{i=1}^A (l_1)_i \rangle$, one can determine the oscillator frequencies $(\omega_1, \omega_2, \omega_3)$ such that the selfconsistency condition between the density and the potential,

$$\omega_1^2 \left\langle \sum_{i=1}^A (x_1^2)_i \right\rangle = \omega_2^2 \left\langle \sum_{i=1}^A (x_2^2)_i \right\rangle = \omega_3^2 \left\langle \sum_{i=1}^A (x_3^2)_i \right\rangle, \tag{12}$$

is fulfilled under a volume conservation condition [50]. Here, the brackets denote expectation values with respect to Slater determinantal states composed of single-particle eigenmodes of h'.

Let us denote the total number of quanta in each of the three directions $(k = 1, 2, 3)$ at $\omega_{\rm rot} = 0$ as

$$\Sigma_k = \left\langle \sum_{i=1}^A \left(c_k^\dagger c_k + \frac{1}{2} \right)_i \right\rangle, \tag{13}$$

and let us continuously follow the configuration specified by the set of values $(\Sigma_1, \Sigma_2, \Sigma_3)$ which are defined at $\omega_{\rm rot} \neq 0$ as the number of quanta associated with the normal modes of the CHO Hamiltonian h'. In terms of Σ_k, the selfconsistency condition at $\omega_{\rm rot} = 0$ is written as

$$\omega_1 \Sigma_1 = \omega_2 \Sigma_2 = \omega_3 \Sigma_3. \tag{14}$$

If the $\Delta N = 2$ part of the angular momentum operator l_1 is neglected, it is well known that there exists a maximum angular momentum $I_c = \Sigma_3 - \Sigma_2$ for a given configuration $(\Sigma_1, \Sigma_2, \Sigma_3)$, where the shape is oblate and the symmetry axis coincides with the rotation axis [45]. This shape evolution is caused by the effect of the $\Delta N = 0$ part of the cranking term, which tends to align the angular momentum of individual particles toward the rotation axis of the system (rotation alignment effect due to the Coriolis force). In the case of the doubly closed shell configuration for the SD magic number $N = Z = 16$ (including the spin-degeneracy factor 2), corresponding to the SD band in ^{32}S, $(\Sigma_1, \Sigma_2, \Sigma_3) = (24, 24, 48)$ taking into account protons and neutrons. We would thus expect the "SD band termination" at the maximum angular momentum $I_c = \Sigma_3 - \Sigma_2 = 24$. This number coincides with that evaluated in the previous section in relation to the j–j-coupling shell-model configurations.

On the other hand, the $\Delta N = 2$ part stretches the system toward larger deformations, and actual shape evolutions as functions of angular momentum are determined by the competition and balance between these two effects. Fully taking into account both effects
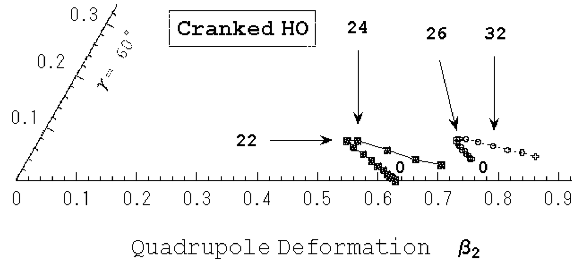
Fig. 8. Shape evolutions as functions of angular momentum in the (β_2, γ) plane, plotted with filled and open symbols, respectively, for the SD configuration $(\Sigma_1, \Sigma_2, \Sigma_3) = (24, 24, 48)$ and the HD-like configuration $(22, 24, 54)$ in the CHO model.

of the cranking term, Troudet and Arvieu [49,50] found that there is a critical value α_c of Σ_3/Σ_2,

$$\alpha_c = \frac{\sqrt{27} + \sqrt{2}}{\sqrt{27} - \sqrt{2}} \simeq 1.75, \tag{15}$$

such that the configuration $(\Sigma_1, \Sigma_2, \Sigma_3)$ does not (does) reach the oblate limit if Σ_3/Σ_2 is greater (less) than α_c. This is because, for large deformations, the stretching effect of the $\Delta N = 2$ term dominates at high spin over the alignment effect of the $\Delta N = 0$ term. In the case of ^{32}S, the SD configuration have $\Sigma_3/\Sigma_2 = \omega_2/\omega_3 = 2 > \alpha_c$ at $I = 0$. Therefore, the "oblate limit" mentioned above will not be reached and the shape at the "band termination" point will be triaxial.

Fig. 8 shows the shape evolution in the (β_2, γ) plane, calculated for the SD configuration of ^{32}S in the CHO model. Here, the result of calculation for the configuration $(22, 24, 54)$ is also presented, as an example of the HD-like configurations. We see that, although the triaxiality slowly sets in with increasing angular momentum, the shape of the SD states remains rather far from the oblate limit and exhibits a striking "back-bending" at about $I_c = 24$ toward larger prolate deformations for $I \geqslant I_c$. Apparently, the behavior near the critical angular momentum I_c for the SD band is quite similar to that of the SHF solutions presented in the previous section. On the other hand, it should be recalled in comparing Fig. 8 with Fig. 6 that the highest spin region of $I = 26 \sim 32$ on the yrast line corresponds to the HD-like configuration in the SHF solution: While the continuation of the SD configuration $(24, 24, 48)$ to the $I > 24$ region as well as that of the HD-like configuration $(22, 24, 54)$ to the $I < 26$ region are presented for the CHO model, only the yrast states were obtained and plotted in the SHF calculation.

Fig. 9 shows the angular momentum and the dynamical moment of inertia $\mathcal{J}^{(2)}$ as functions of the rotational frequency. We see that $\mathcal{J}^{(2)}$ gradually decreases until the critical point. It is interesting to compare this property with that of $\mathcal{J}^{(2)}$ for the SD band in the SHF calculation (Fig. 5). Apparently, they are quite similar. This suggests that the gradual decrease with increasing ω_{rot} of the dynamical moment of inertia for the SD band is rooted in the existence of the critical angular momentum I_c associated with the quantum SD shell structure. We feel that a more detailed investigation of the SD states near the "band
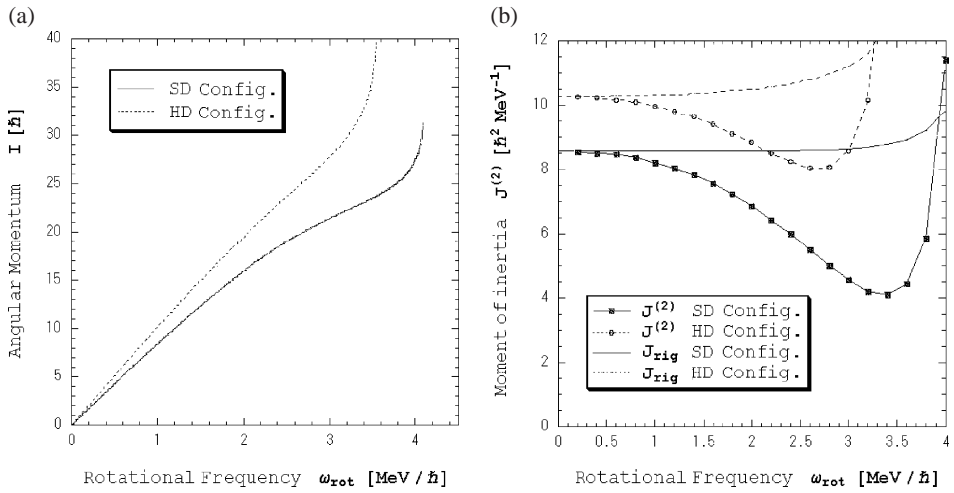
Fig. 9. (a) Plot of angular momentum vs. rotational frequency in the CHO model. Solid line is used for the SD configuration $(\Sigma_1, \Sigma_2, \Sigma_3) = (24, 24, 48)$, while dashed line for the HD-like configuration $(22, 24, 54)$. (b) Same as (a), but for dynamical moment of inertia $\mathcal{J}^{(2)} = dI/d\omega_{rot}$. For reference, rigid moments of inertia $\mathcal{J}_{rig} = m\langle\sum_{i=1}^{A}(y^2 + z^2)_i\rangle$ for these configurations are also indicated.

termination" point is a very important and challenging subject for a deeper understanding of the rotational motion of the nucleus as a finite Fermion system,

6. Effects of time-odd components

In this section we shortly discuss about the rotation-induced, time-odd components in the mean field. The moment of inertia of the SD band is expected to be a good physical quantity for identifying the effects of the time-odd components, since the pairing correlation plays only a minor role there. Concerning the effect of various time-odd components on the moment of inertia, we refer to Ref. [51] for a semiclassical description, to Ref. [52] for a rotating nuclear matter, and to Ref. [53] for SD bands around ^{152}Dy.

Table 1 shows individual contributions from various kinds of time-odd terms. It is interesting to note that the contributions from terms containing the spin-density $\rho(r)$, nearly cancel each other and, accordingly, the contribution from the current-density terms, denoted by $B_3 + B_4$, dominates in the sum. Such a remarkable cancellation of the spin-density terms was not seen in the case of ^{152}Dy [53], and may be specific to ^{32}S under consideration.

In Fig. 10 we compare the results of calculation with and without the time-odd components. It is seen that the time-odd components increase the angular momentum for a given value of ω_{rot}. Accordingly, the dynamical moment of inertia $\mathcal{J}^{(2)} = dI/d\omega_{rot}$ also increases. This trend is understood from the consideration of the local Galilean invariance of the Skyrme force [51,53] (for a more general analysis not restricted to the Skyrme force, see Refs. [45,52]): If the time-odd components is neglected, the local Galilean invariance

Table 1
Contributions from various terms in the time-odd energy density,

$$H_{\text{odd}}(\boldsymbol{r}) = -B_3 \boldsymbol{j}^2 - B_4\left(\boldsymbol{j}_n^2 + \boldsymbol{j}_p^2\right) + B_9(\boldsymbol{j}\cdot\nabla\times\boldsymbol{\rho} + \boldsymbol{j}_n\cdot\nabla\times\boldsymbol{\rho}_n + \boldsymbol{j}_p\cdot\nabla\times\boldsymbol{\rho}_p)$$

$$+ B_{10}\boldsymbol{\rho}^2 + B_{11}\left(\boldsymbol{\rho}_n^2 + \boldsymbol{\rho}_p^2\right) + B_{12}\rho^\alpha\boldsymbol{\rho}^2 + B_{13}\rho^\alpha\left(\boldsymbol{\rho}_n^2 + \boldsymbol{\rho}_p^2\right),$$

to the energy (in MeV), calculated at $\omega_{\text{rot}} = 1.0$ MeV/$\hbar$ for the SIII and SkM* forces. Here, $(\boldsymbol{j}_n, \boldsymbol{j}_p)$ and $(\boldsymbol{\rho}_n, \boldsymbol{\rho}_p)$ denote the nucleon currents and the spin densities (for neutrons and protons), respectively, and $\boldsymbol{j} = \boldsymbol{j}_n + \boldsymbol{j}_p$ and $\boldsymbol{\rho} = \boldsymbol{\rho}_n + \boldsymbol{\rho}_p$ (see Ref. [34] for their explicit expressions). In the columns designated by coefficients B_i, values after the spatial integration are listed, while the total value $\int d\boldsymbol{r}\, H_{\text{odd}}(\boldsymbol{r})$ and the sum of contributions from the current terms (the first two terms in the r.h.s. of the above equation) are shown in the columns denoted by "total" and "$B_3 + B_4$", respectively. For reference, the effective mass m^* in nuclear matter for each force is also listed.

	B_3	B_4	B_9	B_{10}	B_{11}	B_{12}	B_{13}	total	$B_3 + B_4$	m^*/m
SIII	−1.94	0.79	−0.17	−0.77	0.86	0.37	−0.18	−1.04	−1.15	0.76
SkM*	−1.83	0.90	−0.38	−0.44	2.45	0.00	−1.65	−0.95	−0.93	0.79
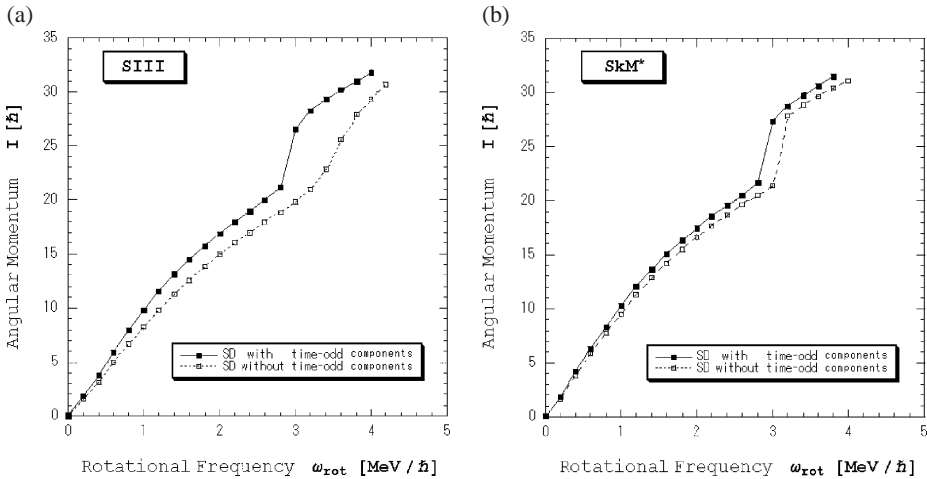
Fig. 10. (a) Angular momentum I plotted as a function of ω_{rot} for the SD band in ^{32}S. Solid line with filled squares (dashed line with open squares) indicates the result with (without) the time-odd components. The SIII force is used. (b) Same as (a), but with the SkM* force.

is violated and we obtain the moment of inertia associated with the effective mass m^*. By including the time-odd components, however, the local Galilean invariance is restored and we get the moment of inertia associated with the nucleon mass m. The calculated result presented in Fig. 10 is consistent with this expectation, but a more quantitative analysis is not necessarily easy, because, as seen in Fig. 5, the calculated moment of inertia significantly deviates from the rigid-body value due to the shell effect.

7. Y_{31} deformation

As mentioned in Section 3, we found that the yrast states in the region $5 \leqslant I \leqslant 13$ possess a significant amount of non-axial octupole deformations of the Y_{31} type. It should be emphasized that such an exotic deformation is absent at $I = 0$ but emerges at high spin. It has become possible to get this kind of solution by using the new cranked SHF code allowing for the simultaneous breaking of both axial and reflection symmetries.

As in [39], we define the octupole deformation parameters α_{3m} as

$$\alpha_{3m} = \frac{4\pi}{3AR^3} \left\langle \sum_{i=1}^{A} \left(r^3 X_{3m} \right)_i \right\rangle \quad (m = -3, \dots, 3) \tag{16}$$

with $R = 1.2 A^{1/3}$ fm. Here X_{3m} is a real basis of the spherical harmonics,

$$X_{30} = Y_{30}, \qquad X_{3|m|} = \frac{1}{\sqrt{2}} \left(Y_{3-|m|} + Y_{3-|m|}^* \right),$$

$$X_{3-|m|} = \frac{-i}{\sqrt{2}} \left(Y_{3|m|} - Y_{3|m|}^* \right), \tag{17}$$

where the quantization axis is chosen as the largest and smallest principal inertia axes for prolate and oblate solutions, respectively. The yrast solutions in the region $5 \leqslant I \leqslant 13$ have $\alpha_{31} \neq 0$ but $\alpha_{3m} = 0$ for $m \neq 1$. (See Ref. [54] for a general discussion on this kind of deformation and its consequence on rotational spectra.) Fig. 11 shows the calculated values of the Y_{31} deformation as a function of ω_{rot}. We see that the α_{31} value quickly rises when ω_{rot} exceeds 1 MeV/$\hbar$.
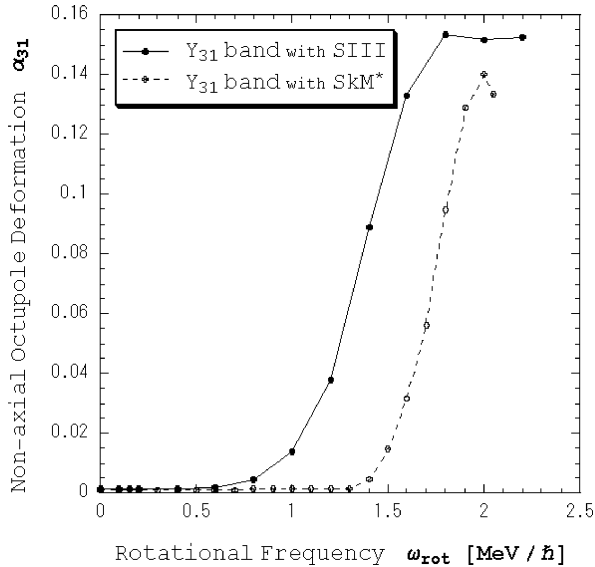
Fig. 11. Non-axial octupole deformation α_{31} plotted as a function of ω_{rot} for the Y_{31} band in ^{32}S. Results calculated with the SIII and SkM* forces are shown by solid and dashed lines, respectively.
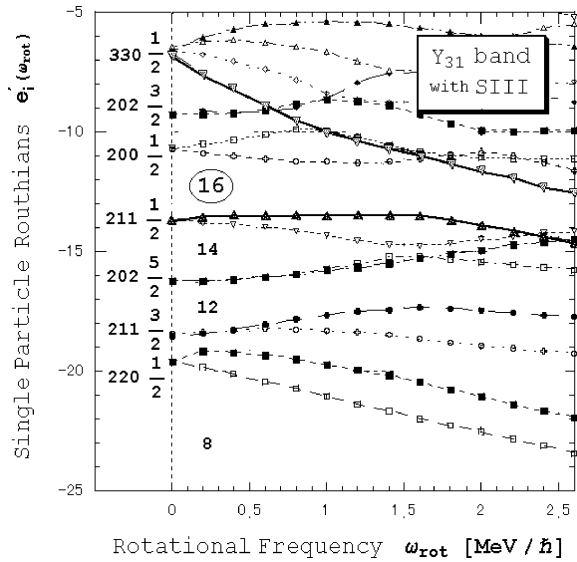
Fig. 12. Single-particle energy diagram (for neutrons) in the rotating frame for the Y_{31} band in ^{32}S, plotted as a function of ω_{rot}. The SIII force is used.
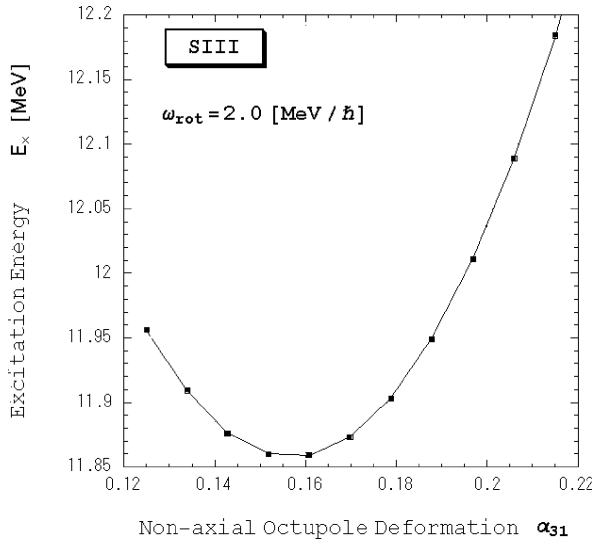
Fig. 13. Potential energy function for the Y_{31} band in ^{32}S at $\omega_{rot} = 2.0$ MeV/$\hbar$, calculated by means of the constrained HF procedure with the SIII force. Note the scale of the ordinate.

The microscopic origin of the growth of the non-axial octupole deformation α_{31} may be understood when we examine the single-particle energy diagram in the rotating frame (routhians) presented in Fig. 12. We note that a strong coupling and a quasi-level crossing between the rotation-aligned $[330]\frac{1}{2}$ orbit and the $[211]\frac{1}{2}$ orbit take place near the Fermi surface in the region $1.0 \leqslant \omega_{rot} \leqslant 2.2$ MeV/$\hbar$. The matrix element of

the $r^3 Y_{31}$ operator between the two single-particle states is large, since they satisfy the selection rule for the asymptotic quantum numbers ($\Delta \Lambda = 1$, $\Delta n_z = 2$). This strong coupling is responsible for the α_{31} deformation appearing in this region of the yrast line.

Fig. 13 shows the potential energy function with respect to the α_{31} direction, calculated by means of the constrained HF procedure. Note the scale of the ordinate. Although we obtain a clear minimum at a finite value of α_{31}, the potential is rather shallow in this direction, so that the amplitude of the quantum-mechanical zero-point vibrational motion might be larger than the equilibrium deformation. If this is the case, a treatment of dynamics going beyond the mean-field approximation is required in order to investigate the consequence of the α_{31} deformation on the quantum spectra in the yrast region under consideration. This is beyond the scope of the present paper.

It may be desirable to extend the potential energy curve in Fig. 13 to the $\alpha_{31} = 0$ limit. It turned out, however, difficult to do so, because many level-crossings take place with decreasing α_{31}. (If we extrapolate to this limit assuming parabolic dependence on α_{31}, we obtain about 2 MeV as a very crude estimate of the energy gain due to the α_{31} deformation.) For the same reason, it is also difficult to follow the continuation of the Y_{31} band to the higher spin region as soon as it departs from the yrast line.

8. Some remarks on experimental data

Although rich experimental data are available for excited states of ^{32}S, the high-spin yrast region in which we are interested is rather poorly known at the present time. Accordingly, we discuss experimental references only briefly.

For low-spin states with $I \leqslant 7$, detailed spectroscopic data are available up to excitation energy 11.76 MeV [19,20]. These excited states are shown to be well described by the spherical shell model calculations [19,20]. In these works, some negative-parity states were interpreted as octupole–quadrupole phonon multiplets. As a matter of fact, we need to go beyond the simple mean field theory in order to discuss such spectroscopic data in the low-spin region.

Highly excited states have been studied by various nuclear reactions as well as ^{16}O–^{16}O scattering. Investigating the ^{16}O(^{20}Ne, α)^{32}S(α)^{28}Si (g.s.) reaction, Morita et al. [55] suggested possible band structures of the quasi-molecular configuration of ^{16}O + ^{16}O and of some parity-doublet-like structures with angular momenta 5^-, 6^+, (7^-), (8^+) at the 12–15 MeV region. Recently, Curtis et al. [56] investigated the region with $I = 10$–16 and the excitation energy 32–38 MeV by means of the ^{12}C(^{24}Mg, ^{16}O^{16}O)^{4}He reaction, and suggested an existence of highly deformed states in this region. It is tempting to compare these experimental data with our theoretical calculations. The experimentally explored regions are, however, about 10 MeV above the theoretical yrast line. Therefore, a more detailed spectroscopic study is needed in order to associate these data with the yrast structure.

9. Conclusions

We have investigated the high-spin yrast structure of ^{32}S by means of the cranked SHF method in the 3D Cartesian-mesh representation without imposing restrictions on spatial symmetries, and suggested that

(1) a crossover from the SD to the HD-like configurations takes place on the yrast line at angular momentum $I \simeq 24$, which corresponds to the "band termination" point in the CHO model, and

(2) non-axial octupole deformations of the Y_{31} type play an important role in the yrast states in the range $5 \leqslant I \leqslant 13$.

In conclusion, we would like to stress again that the calculated yrast line for $I = 14$–20 lies about 10 MeV below the observed molecular resonance region associated with the ^{16}O–^{16}O configurations. Thus, a yrast γ-spectroscopy with higher resolving power is strongly desired in order to explore the high-spin region of the yrast line of ^{32}S.

Acknowledgements

References

[1] P.J. Nolan, P.J. Twin, Ann. Rev. Nucl. Part. Sci. 38 (1988) 533.
[2] S. Åberg, H. Flocard, W. Nazarewicz, Ann. Rev. Nucl. Part. Sci. 40 (1990) 439.
[3] R.V.F. Janssens, T.L. Khoo, Ann. Rev. Nucl. Part. Sci. 41 (1991) 321.
[4] C. Baktash, B. Haas, W. Nazaerewicz, Ann. Rev. Nucl. Part. Sci. 45 (1995) 485.
[5] C. Baktash, Prog. Part. Nucl. Phys. 38 (1997) 291.
[6] J. Dobaczewski, in: C. Baktash (Ed.), Proc. Int. Conf. on Nuclear Structure '98, Gatlinburg, TN, August 10–15, 1998, p. 315; nucl-th/9811043.
[7] R.K. Sheline, I. Ragnarsson, S.G. Nilsson, Phys. Lett. B 41 (1972) 115.
[8] G. Leander, S.E. Larsson, Nucl. Phys. A 239 (1975) 93.
[9] I. Ragnarsson, S.G. Nilsson, R.K. Sheline, Phys. Rep. 45 (1978) 1.
[10] T. Bengtsson, M.E. Faber, G. Leander, P. Möller, M. Ploszajczak, I. Ragnarsson, S. Åberg, Phys. Scr. 24 (1981) 200.
[11] Y. Abe, Y. Kondo, T. Matsuse, Prog. Theor. Phys. Suppl. 68 (1980) 303.
[12] W. Greiner, J.Y. Park, W. Scheid, Nuclear Molecule, World Scientific, Singapore, 1995.
[13] W. Nazarewicz, J. Dobaczewski, Phys. Rev. Lett. 68 (1992) 154.
[14] M. Freer, R.R. Betts, A.H. Wuosmaa, Nucl. Phys. A 587 (1995) 36.
[15] M. Freer, A.C. Merchant, J. Phys. G 23 (1997) 261, and references therein.
[16] Y. Fujiwara, H. Horiuchi, K. Ikeda, M. Kamimura, K. Katō, Y. Suzuki, E. Uegaki, Prog. Theor. Phys. Suppl. 68 (1980) 29.

[17] M. Girod, B. Grammaticos, Phys. Rev. C 27 (1983) 2317.
[18] H. Flocard, P.H. Heenen, S.J. Krieger, M.S. Weiss, Prog. Theor. Phys. 72 (1984) 1000.
[19] J. Brenneison et al., Z. Phys. A 357 (1997) 157, Z. Phys. A 357 (1997) 377.
[20] A. Kangasmäki et al., Phys. Rev. C 58 (1998) 699.
[21] P.G. Zint, U. Mosel, Phys. Lett. B 58 (1975) 269.
[22] W. Bauhoff, H. Schultheis, R. Schultheis, Phys. Rev. C 22 (1980) 861.
[23] H. Schultheis, R. Schultheis, Phys. Rev. C 25 (1982) 2126.
[24] J. Zhang, W.D.M. Rae, A.C. Merchant, Nucl. Phys. A 575 (1994) 61.
[25] J. Cseh, G. Lévai, A. Ventura, L. Zuffi, Phys. Rev. C 58 (1998) 2144.
[26] M. Beiner, H. Flocard, Nguyen van Giai, P. Quentin, Nucl. Phys. A 238 (1975) 29.
[27] J. Bartel, P. Quentin, M. Brack, C. Guet, H.-B. Håkansson, Nucl. Phys. A 386 (1982) 79.
[28] K.T.R. Davies, H. Flocard, S.J. Krieger, M.S. Weiss, Nucl. Phys. A 342 (1980) 111.
[29] P. Bonche, H. Flocard, P.H. Heenen, S.J. Krieger, M.S. Weiss, Nucl. Phys. A 443 (1985) 39.
[30] N. Tajima, S. Takahara, N. Onishi, Nucl. Phys. A 603 (1996) 23.
[31] P. Bonche, S. Koonin, J.W. Negele, Phys. Rev. C 13 (1976) 1226.
[32] S. Takahara, N. Tajima, N. Onishi, Nucl. Phys. A 642 (1998) 461.
[33] H. Flocard, P.H. Heenen, S.J. Krieger, M.S. Weiss, Nucl. Phys. A 391 (1982) 285.
[34] P. Bonche, H. Flocard, P.H. Heenen, Nucl. Phys. A 467 (1987) 115.
[35] M. Yamagami, K. Matsuyanagi, in: C. Baktash (Ed.), Proc. Int. Conf. on Nuclear Structure '98, Gatlinburg, TN, August 10–15, 1998, p. 327; nucl-th/9809038.
[36] H. Molique, J. Dobaczewski, J. Dudek, Preprint nucl-th/9907103.
[37] E. Chabanat, P. Bonche, P. Haensel, J. Meyer, F. Schaeffer, Nucl. Phys. A 635 (1998) 231.
[38] S. Takami, K. Yabana, K. Ikeda, Prog. Theor. Phys. 96 (1996) 407.
[39] S. Takami, K. Yabana, M. Matsuo, Phys. Lett. B 431 (1998) 242.
[40] M. Matsuo, S. Takami, K. Yabana, in: C. Baktash (Ed.), Proc. Int. Conf. on Nuclear Structure '98, Gatlinburg, TN, August 10–15, 1998, p. 345; Preprint YITP-98-69.
[41] M. Yamagami, Master Thesis, Kyoto University, Kyoto, 1997.
[42] H. Flocard, P. Quentin, A.K. Kerman, D. Vautherin, Nucl. Phys. A 203 (1973) 433.
[43] P.-G. Reinhard, D.J. Dean, W. Nazarewicz, J. Dobaczewski, J.A. Maruhn, M.R. Strayer, Phys. Rev. C 60 (1999) 014316.
[44] I. Hamamoto, in: D.A. Bromley (Ed.), Treatise on Heavy-Ion Science, Vol. 3, Plenum, New York, 1985, p. 313.
[45] A. Bohr, B.R. Mottelson, Nuclear Structure, Vol. 2, Benjamin, Reading, MA, 1975.
[46] J.G. Valatin, Proc. R. Soc. London A 238 (1956) 132.
[47] G. Ripka, J.P. Blaizot, N. Kassis, in: Heavy Ions, High Spin States and Nuclear Structure, Vol. 1, IAEA, Vienna, 1975, p. 445.
[48] V.G. Zelevinski, Sov. J. Nucl. Phys. 22 (1975) 565.
[49] T. Troudet, R. Arvieu, Z. Phys. A 291 (1979) 183.
[50] T. Troudet, R. Arvieu, Ann. Phys. 134 (1981) 1.
[51] K. Bencheikh, P. Quentin, J. Bartel, Nucl. Phys. A 571 (1994) 518.
[52] S. Frauendorf, K. Neergård, Z. Phys. A 354 (1996) 381.
[53] J. Dobaczewski, J. Dudek, Phys. Rev. C 52 (1995) 1827, Phys. Rev. C 55 (1997) 3177(E).
[54] S. Frauendorf, to be published in Rev. Mod. Phys.
[55] K. Morita et al., Phys. Rev. Lett. 55 (1985) 185.
[56] N. Curtis et al., Phys. Rev. C 53 (1996) 1804.

Adiabatic Selfconsistent Collective Coordinate Method for Large Amplitude Collective Motion in Nuclei with Pairing Correlations

Masayuki Matsuo,[*] Takashi Nakatsukasa[*] and Kenichi Matsuyanagi[**]

Yukawa Institute for Theoretical Physics, Kyoto University, Kyoto 606-8502 Japan
[*]*RI Beam Science Laboratory, RIKEN, Wako 351-0198, Japan*
[**]*Department of Physics, Kyoto University, Kyoto 606-8502, Japan*

An adiabatic approximation to the selfconsistent collective coordinate method is formulated in order to describe large amplitude collective motions in nuclei with pairing correlations on the basis of the time-dependent Hartree-Fock-Bogoliubov equations of motion. The basic equations are presented in a local harmonic form which can be solved in a manner similar to that of the quasiparticle RPA equations. The formalism guarantees the conservation of nucleon number expectation values. An extension to the multi-dimensional case is also discussed.

§1. Introduction

Large amplitude collective motion (LACM), such as fission, shape transitions, anharmonic vibrations and low energy heavy ion reactions, are often encountered in studies of nuclear structure and dynamics. To go beyond the phenomenological models assuming some macroscopic or collective degrees of freedom motivated by the experimental facts and intuition, many attempts have been made to construct theories that are able to describe the LACM on the microscopic basis of the nuclear many-body Hamiltonian. In particular, theories based on the time-dependent Hartree-Fock (TDHF) approximation have been investigated extensively.[1]-[16] The TDHF is a general framework for describing low-energy nuclear dynamics accompanying evolution of the nuclear selfconsistent mean field.[17],[18] A LACM corresponds to a specific solution of the TDHF equation of motion. Since such a solution forms only a subset of the all TDHF states (Slater determinants), it is often called a collective path, a collective subspace, or a collective submanifold. The collective coordinates are then a set of a small number of variables that parameterize the collective subspace, and the collective Hamiltonian is a function governing the time evolution of the collective coordinates. One of the main purposes of the LACM theories is to provide a scheme to determine the collective subspace and the collective Hamiltonian on the basis of the microscopic many-body Hamiltonian. Although studies of LACM theories form a vast field of research with many recent developments in different directions, realistic applications to nuclear structure problems are rather limited. In this paper, we would like to propose a new practical method to calculate

---

[*] Present address: Graduate School of Science and Technology, Niigata University, Niigata 950-2181, Japan.

the collective subspace.

The adiabatic approximation has been often utilized for formulating the theory of the collective subspace. Indeed, some class of LACM, such as nuclear fission, can be regarded as slow motion, thus justifying the adiabatic approximation. The adiabatic TDHF (ATDHF) theory [1)-3)] is one of the best known adiabatic theories and has been applied in some cases to realistic descriptions of heavy ion reactions. [3)] The ATDHF theory, however, had the problem of the non-uniqueness of the solution. [4),5)] Efforts to settle the non-uniqueness problem were made from different viewpoints. Reference 6) emphasizes the importance of the canonical variable condition and the analyticity as a function of a collective coordinate for finding a unique solution. The proposed procedure relying on the Taylor expansion method has not been applied to realistic calculations. Another work [7)] points out that the collective subspace can be uniquely determined by using the next order equation of the ATDHF theory. It has been found also that the adiabatic collective path of LACM becomes the valley line of the potential function in the multi-dimensional space associated with the TDHF states. [7)-9)] Further, the adiabatic collective path can be defined by equations for a local harmonic mode at each point of the collective path. These developments are summarized in a consistent way in the formalism of Ref. 8). Note, however, that the adiabatic theory of Ref. 8) relys on a multi-dimensional classical phase space representation of the TDHF determinantal states. [17),18)] A realistic application of this theory has not been made, except in the case of a light nucleus. [19)] Furthermore, a problem of particle number conservation arises when applied to superconducting nuclei (i.e. nuclei with pairing correlations). [10)]

Theories without the adiabatic approximation have also been developed within the TDHF framework. The early works in this direction are called local harmonic approximations. [12),13)] Later, a set of general equations that can determine the collective subspace and the collective Hamiltonian were found and formulated in a consistent form known as the selfconsistent collective coordinate method (SCC or SCCM). [14)] The theory is purely based on the TDHF with no further approximation. The method also provides a concrete and practical scheme to solve the basic equations using a power series expansion with respect to the boson-like variables defined as a linear combination of the collective coordinates and momenta. The pairing correlation in superconducting nuclei is easily incorporated within the SCCM by adopting the time-dependent Hartree-Fock-Bogoliubov (TDHFB) equation in place of the TDHF, and the conservation law for the particle number is consistently introduced in the basic framework of the SCCM. [15)] Thanks to these features, the SCCM has been applied to many realistic descriptions of anharmonic vibrations in medium and heavy nuclei. [16)] However, the expansion method may not be suitable for large amplitude motion of an adiabatic nature, for which change of the nuclear mean-field is so large that the power series expansion of the collective coordinates may not be justified.

In the present paper, we attempt to combine the merits of the two approaches mentioned above, the SCCM and the adiabatic theory, in order to formulate a theory that provides a consistent and practical method easily applicable to realistic descriptions of the adiabatic LACM in superconducting nuclei. We achieve this aim by

introducing an adiabatic approximation into the general framework of the SCCM. Here we treat superconducting nuclei since the pairing correlations play essential roles in many cases, like spontaneous fission, tunneling between superdeformed and normally deformed configurations, and coupling between coexisting states with different nuclear shapes (shape coexistence phenomena). Although the use of the superconducting mean field requires us to respect particle number conservation, the SCCM allows a simple and consistent treatment of the conservation law. We also avoid the non-uniqueness problem by utilizing principles similar to those of Refs. 7)–9). Furthermore, we show that the equations of the adiabatic SCCM thus formulated can be transformed into another set of equations that have a similar structure as the local harmonic approach in the adiabatic theories. [8] Therefore, the present formalism also inherits some aspects of the recent adiabatic theories such as Ref. 8).

In addition to the general formulation (§2), we present a practical scheme to solve the basic equations given in the local harmonic form for general classes of the many-body nuclear Hamiltonian (§3 and the Appendix). These equations are given in terms of the matrix elements of the many-body Hamiltonian written in terms of the quasiparticle operators, thus enabling us to develop a straightforward coding of a numerical program to solve the equations. In this way, we provide a concrete procedure to extract the collective subspace and the collective Hamiltonian. We also discuss a possible prescription to extend the formalism to cases of multi-dimensional collective motion (§4). Conclusions are outlined in §5.

§2. Basic equations

2.1. *The SCC method for superconducting nuclei*

In this subsection, we recapitulate the basic equations of the SCC method [14] in a manner suitable for treating superconducting nuclei.

We introduce the TDHFB approximation to describe LACM in superconducting many-fermion systems. Here the time-dependent many-body state vector $|\phi(t)\rangle$ is constrained to a generalized Slater determinant, which is chosen as a variational wave function. The time evolution of $|\phi(t)\rangle$ is then determined by the time-dependent variational principle

$$\delta \langle\phi(t)| \, i\frac{\partial}{\partial t} - \hat{H} \, |\phi(t)\rangle = 0, \qquad (2\cdot1)$$

where the variation is given by $\delta |\phi(t)\rangle = a_\alpha^\dagger a_\beta^\dagger |\phi(t)\rangle$ in terms of the quasiparticle operators $\{a_\alpha^\dagger, a_\alpha\}$, which satisfy the vacuum condition $a_\alpha |\phi(t)\rangle = 0$.

We assume that the LACM can be described in terms of the collective variables, i.e. the collective coordinate and momentum $\{q, p\}$ that are variables parameterizing the TDHFB state vector.[*] The whole space of the TDHFB state vectors can be parameterized by $M \times (M-1)$ variables (M being the number of the single particle states), as shown by the generalized Thouless theorem. [17], [18] The set of the TDHFB state vectors $|\phi(q,p)\rangle$ forms the collective subspace in which the LACM can be

---

[*] We focus our discussion on the case of a single collective coordinate. A multi-dimensional case is discussed in §4.

properly described. One of the main problems with which we are concerned is how to determine the collective subspace on the basis of the TDHFB equations of motion. At the same time, we need to determine the collective Hamiltonian $\mathcal{H}(q, p)$ that governs the equation of motion for the collective variables $\{q, p\}$. This is the general purpose of theories of LACM.

When we apply the LACM theories to nuclei in the superconducting phase, special attention has to be paid to particle number conservation. Since the TDHFB state vector is not an eigenstate of the particle number operator $\hat{N}$, one would like to formulate the LACM theory so that the particle number expectation value is conserved during the course of collective motion. This is a problem which is specific to the TDHFB, and does not exist for the TDHF for which the state vector is a number eigenstate.

It is well known [17] that the expectation value of a conserved observable remains constant during the time-evolution of $|\phi(t)\rangle$ governed by the TDHF(B) equations of motion. In the case of the pairing problem, the TDHFB state vector spontaneously violates the symmetry with respect to the gauge rotation $e^{-i\varphi\hat{N}}$, but rotational motion related to the gauge rotation (often called the "pairing rotation") emerges automatically to restore the gauge symmetry. Therefore, the LACM of superconducting nuclei, described by the TDHFB theory, necessarily accompany the pairing rotation, and we have to introduce [15] the collective coordinate, φ, the gauge angle, and the conjugate collective momenta, N, which represents the particle number. Thus, we are obliged to consider a collective subspace that is parameterized by the set of four collective variables $\{q, p, \varphi, N\}$.[*]

Let us now present the basic equations of the SCCM that determine the collective subspace $|\phi(q, p, \varphi, N)\rangle$ and the collective Hamiltonian $\mathcal{H}(q, p, \varphi, N)$. As discussed above, the variable φ is introduced to represent the gauge angle. This requirement is easily satisfied [15] if one uses the parameterization

$$|\phi(q, p, \varphi, N)\rangle = e^{-i\varphi\hat{N}} |\phi(q, p, N)\rangle, \tag{2·2}$$

where $\hat{N}$ is the number operator of particles. Here $|\phi(q, p, N)\rangle$ represents an intrinsic state that rotates in the gauge space.

The basic equations of the SCCM consist of a canonical variable condition and an invariance principle of the time-dependent Schrödinger equation (TDHFB equation in our case). The canonical variable condition is, in general, given by

$$\langle\phi(q, p, \varphi, N)| i\frac{\partial}{\partial q} |\phi(q, p, \varphi, N)\rangle = p + \frac{\partial S}{\partial q}, \tag{2·3a}$$

$$\langle\phi(q, p, \varphi, N)| \frac{\partial}{i\partial p} |\phi(q, p, \varphi, N)\rangle = -\frac{\partial S}{\partial p}, \tag{2·3b}$$

$$\langle\phi(q, p, \varphi, N)| i\frac{\partial}{\partial\varphi} |\phi(q, p, \varphi, N)\rangle = N + \frac{\partial S}{\partial\varphi}, \tag{2·3c}$$

$$\langle\phi(q, p, \varphi, N)| \frac{\partial}{i\partial N} |\phi(q, p, \varphi, N)\rangle = -\frac{\partial S}{\partial N}, \tag{2·3d}$$

_____

[*] For simplicity, here we assume a single kind of particles. Extension to systems with many kinds (e.g., protons and neutrons in nuclei) is straightforward.

for the collective subspace parameterized by two sets of coordinates (q, φ) and momenta (p, N). Although S is an arbitrary function of $\{q, p, \varphi, N\}$, we choose $S = 0$, which is appropriate for the adiabatic approximation.[6] Then the canonical variable condition can be rewritten as equations for the state $|\phi(q, p, N)\rangle$:

$$\langle \phi(q, p, N)| \, i \frac{\partial}{\partial q} \, |\phi(q, p, N)\rangle = p, \tag{2.4a}$$

$$\langle \phi(q, p, N)| \, \frac{\partial}{i \partial p} \, |\phi(q, p, N)\rangle = 0, \tag{2.4b}$$

$$\langle \phi(q, p, N)| \, \hat{N} \, |\phi(q, p, N)\rangle = N, \tag{2.4c}$$

$$\langle \phi(q, p, N)| \, \frac{\partial}{i \partial N} \, |\phi(q, p, N)\rangle = 0. \tag{2.4d}$$

The third equation requires that the collective variable N be identical to the expectation value of the number operator. In other words, the particle number expectation value does not depend on the collective variables (q, p) for the LACM under consideration. This is nothing but the condition of particle number conservation.

The collective Hamiltonian is defined as the value of the total energy in the collective subspace, given by

$$\mathcal{H} = \langle \phi(q, p, \varphi, N)| \, \hat{H} \, |\phi(q, p, \varphi, N)\rangle \tag{2.5a}$$

$$= \langle \phi(q, p, N)| \, \hat{H} \, |\phi(q, p, N)\rangle. \tag{2.5b}$$

Since the Hamiltonian $\hat{H}$ commutes with the number operator $\hat{N}$, the collective Hamiltonian does not depend on the gauge angle φ. Therefore, φ becomes cyclic, as we expect.

The invariance principle of the TDHFB equation plays a central role in determining the collective subspace, which requires that the TDHFB state vector $|\phi(q(t), p(t), \varphi(t), N(t))\rangle$ evolving in time within the collective subspace obey the full TDHFB equation, Eq. (2·1). This is equivalent to the condition that the collective subspace is an invariant subspace of the TDHFB equations of motion. Inserting Eq. (2·2) into the time-dependent variational principle, Eq. (2·1), we obtain

$$\delta \langle \phi(q, p, N)| \, \hat{H} - \frac{dq}{dt} \overset{\circ}{P} + \frac{dp}{dt} \overset{\circ}{Q} + \frac{dN}{dt} \overset{\circ}{\Theta} - \frac{d\varphi}{dt} \hat{N} \, |\phi(q, p, N)\rangle = 0, \tag{2.6}$$

where the infinitesimal generators defined by

$$\overset{\circ}{P} \, |\phi(q, p, N)\rangle = i \frac{\partial}{\partial q} \, |\phi(q, p, N)\rangle, \tag{2.7a}$$

$$\overset{\circ}{Q} \, |\phi(q, p, N)\rangle = \frac{1}{i} \frac{\partial}{\partial p} \, |\phi(q, p, N)\rangle, \tag{2.7b}$$

$$\overset{\circ}{\Theta} \, |\phi(q, p, N)\rangle = \frac{1}{i} \frac{\partial}{\partial N} \, |\phi(q, p, N)\rangle \tag{2.7c}$$

have been used. These operators are one-body operators which can be written as linear combinations of bilinear products $\{a_\alpha^\dagger a_\beta^\dagger, a_\beta a_\alpha, a_\alpha^\dagger a_\beta\}$ of the quasiparticle op-

erators defined with respect to $|\phi(q,p,N)\rangle$. Because of the canonical variable conditions, these infinitesimal generators satisfy the commutation relations

$$\langle\phi(q,p,N)|\,[\overset{\circ}{Q},\overset{\circ}{P}]\,|\phi(q,p,N)\rangle = i, \tag{2.8a}$$

$$\langle\phi(q,p,N)|\,[\overset{\circ}{\Theta},\hat{N}]\,|\phi(q,p,N)\rangle = i, \tag{2.8b}$$

and commutators of other combinations of $\overset{\circ}{Q},\overset{\circ}{P},\overset{\circ}{\Theta}$ and $\hat{N}$ give zero expectation value. By taking the variation as $\delta\,|\phi(q,p,N)\rangle = \{\overset{\circ}{P},\overset{\circ}{Q},\overset{\circ}{\Theta},\hat{N}\}\,|\phi(q,p,N)\rangle$, Eq. (2.6) produces the canonical equations of motion for the collective variables:

$$\frac{dq}{dt} = \frac{\partial\mathcal{H}}{\partial p} = i\,\langle\phi(q,p,N)|\,[\hat{H},\overset{\circ}{Q}]\,|\phi(q,p,N)\rangle\,, \tag{2.9a}$$

$$\frac{dp}{dt} = -\frac{\partial\mathcal{H}}{\partial q} = i\,\langle\phi(q,p,N)|\,[\hat{H},\overset{\circ}{P}]\,|\phi(q,p,N)\rangle\,, \tag{2.9b}$$

$$\frac{d\varphi}{dt} = \frac{\partial\mathcal{H}}{\partial N} = i\,\langle\phi(q,p,N)|\,[\hat{H},\overset{\circ}{\Theta}]\,|\phi(q,p,N)\rangle\,, \tag{2.9c}$$

$$\frac{dN}{dt} = -\frac{\partial\mathcal{H}}{\partial\varphi} = 0. \tag{2.9d}$$

Using Eq. (2.9), Eq. (2.6) reduces to an *equation of collective subspace*:

$$\delta\,\langle\phi(q,p,N)|\,\hat{H} - \frac{\partial\mathcal{H}}{\partial p}\overset{\circ}{P} - \frac{\partial\mathcal{H}}{\partial q}\overset{\circ}{Q} - \frac{\partial\mathcal{H}}{\partial N}\hat{N}\,|\phi(q,p,N)\rangle = 0. \tag{2.10}$$

If we take a variation $\delta_\perp$ that is orthogonal to the infinitesimal generators $\{\overset{\circ}{P},\overset{\circ}{Q},\overset{\circ}{\Theta},\hat{N}\}$, we can immediately show $\delta_\perp\,\langle\phi(q,p,N)|\,\hat{H}\,|\phi(q,p,N)\rangle = 0$, which implies that the energy expectation value is stationary in the collective subspace with respect to all the variations, except for those along directions tangent to the collective subspace. In other words, the collective mode is decoupled from the other modes of excitation.

We remark here that the above basic equations of the SCCM are invariant under point transformations of the collective coordinate

$$q \to q' = q'(q), \tag{2.11a}$$

$$p \to p' = p \times (dq'/dq)^{-1}. \tag{2.11b}$$

The basic principles, i.e. the canonical variable condition, Eq. (2.3), and the invariance principle of the TDHFB equation, Eq. (2.6), are not affected by the general canonical transformations of collective variables $\{q,p,\varphi,N\} \to \{q',p',\varphi',N'\}$. By taking the parameterization, Eq. (2.2), and the specific choice of $S = 0$ in Eq. (2.3), the allowed canonical transformations are restricted to the point transformations.[6]

2.2. *Adiabatic approximation*

Assuming that the LACM described by the collective variables $\{q,p\}$ is slow motion, we here introduce the adiabatic approximation to the SCCM. Namely, we expand the basic equations with respect to the collective momentum p, which is

appropriate for small values of momentum. Since the particle number variable N is a momentum variable in the present formulation, we also expand the basic equations with respect to $n = N - N_0$ when we consider a system with particle number N_0.

Let us first consider the expansion of the TDHFB state vector $|\phi(q, p, N)\rangle$ in the collective subspace. The origin of the expansion is the state $|\phi(q)\rangle \equiv |\phi(q, p, N)\rangle|_{p=0, N=N_0}$. We can assume that this is a time-even state, i.e., $\mathcal{T}|\phi(q)\rangle = |\phi(q)\rangle$ under the time-reversal operation $\mathcal{T}$. (Here we consider system of an even number of particles.) Thanks to the generalized Thouless theorem, the state vector $|\phi(q, p, N)\rangle$ can be expressed as

$$|\phi(q, p, N)\rangle = e^{i\hat{G}(q,p,n)}|\phi(q)\rangle \tag{2.12}$$

by using the unitary transformation $e^{i\hat{G}(q,p,n)}$. Here the Hermitian operator $\hat{G}$ is given by

$$\hat{G}(q,p,n) = \sum_{\alpha>\beta}\left(G_{\alpha\beta}(q,p,n)a_\alpha^\dagger a_\beta^\dagger + G_{\alpha\beta}^*(q,p,n)a_\beta a_\alpha\right) = \hat{G}(q,p,n)^\dagger. \tag{2.13}$$

Here and hereafter, the quasiparticle operators $\{a_\alpha^\dagger, a_\alpha\}$ are always defined locally at each value of q and satisfy the condition $a_\alpha|\phi(q)\rangle = 0$. We now expand the operator $\hat{G}(q,p,n)$ in powers of p and n and keep only the lowest order term. We have

$$\hat{G}(q,p,n) = p\hat{Q}(q) + n\hat{\Theta}(q), \tag{2.14a}$$

$$\hat{Q}(q) = \sum_{\alpha>\beta}\left(Q_{\alpha\beta}(q)a_\alpha^\dagger a_\beta^\dagger + Q_{\alpha\beta}^*(q)a_\beta a_\alpha\right) = \hat{Q}(q)^\dagger, \tag{2.14b}$$

$$\hat{\Theta}(q) = \sum_{\alpha>\beta}\left(\Theta_{\alpha\beta}(q)a_\alpha^\dagger a_\beta^\dagger + \Theta_{\alpha\beta}^*(q)a_\beta a_\alpha\right) = \hat{\Theta}(q)^\dagger. \tag{2.14c}$$

If we require that time-reversal of $|\phi(q, p, N)\rangle$ causes sign inversion of the collective momentum p, i.e. $\mathcal{T}|\phi(q, p, N)\rangle = |\phi(q, -p, N)\rangle$, the operators $\hat{Q}(q)$ and $\hat{\Theta}(q)$ must be time-even ($\mathcal{T}\hat{Q}(q)\mathcal{T}^{-1} = \hat{Q}(q)$) and time-odd ($\mathcal{T}\hat{\Theta}(q)\mathcal{T}^{-1} = -\hat{\Theta}(q)$), respectively. If we set $n = 0$ (i.e. $N = N_0$), the parameterization Eq. (2.12) together with Eq. (2.14) reduces to $|\phi(q, p)\rangle = e^{ip\hat{Q}(q)}|\phi(q)\rangle$, which has the same form as that introduced by Villars and is often used in the ATDHF theories.[1),3),7)]

The collective Hamiltonian is expanded as

$$\mathcal{H}(q, p, N) = V(q) + \frac{1}{2}B(q)p^2 + \lambda(q)n, \tag{2.15a}$$

$$V(q) = \mathcal{H}(q, p, N)|_{p=0, N=N_0} = \langle\phi(q)|\hat{H}|\phi(q)\rangle, \tag{2.15b}$$

$$B(q) = \frac{1}{2}\left.\frac{\partial^2\mathcal{H}(q, p, N)}{\partial p^2}\right|_{p=0, N=N_0}$$
$$= -\langle\phi(q)|[[\hat{H}, \hat{Q}(q)], \hat{Q}(q)]|\phi(q)\rangle, \tag{2.15c}$$

$$\lambda(q) = \left.\frac{\partial\mathcal{H}(q, p, N)}{\partial N}\right|_{p=0, N=N_0} = \langle\phi(q)|[\hat{H}, i\hat{\Theta}(q)]|\phi(q)\rangle, \tag{2.15d}$$

where we have kept terms up to second order in the collective momentum p, and up to the first order in n. The collective Hamiltonian for the system with $N = N_0$ particles ($n = 0$) is given by

$$\mathcal{H}(q, p, N_0) = V(q) + \frac{1}{2}B(q)p^2 \tag{2.16}$$

as the sum of the collective potential $V(q)$ and the collective kinetic energy (the second term).

We next expand the infinitesimal generators. It is convenient for this purpose to define the unitary transformations $\overset{\circ}{P}' = e^{-i\hat{G}}\overset{\circ}{P}e^{i\hat{G}}, \overset{\circ}{Q}' = e^{-i\hat{G}}\overset{\circ}{Q}e^{i\hat{G}}$ and $\overset{\circ}{\Theta}' = e^{-i\hat{G}}\overset{\circ}{\Theta}e^{i\hat{G}}$ of the infinitesimal generators $\overset{\circ}{P}, \overset{\circ}{Q}$ and $\overset{\circ}{\Theta}$. They are expanded as

$$\overset{\circ}{P}' = \hat{P}(q) + e^{-i\hat{G}}i\frac{\partial}{\partial q}e^{i\hat{G}} = \hat{P}(q) - p\frac{\partial \hat{Q}}{\partial q} - n\frac{\partial \hat{\Theta}}{\partial q} + \cdots, \tag{2.17}$$

$$\overset{\circ}{Q}' = e^{-i\hat{G}}\frac{\partial}{i\partial p}e^{i\hat{G}} = \hat{Q}(q) + \frac{i}{2}[\hat{Q}, p\hat{Q} + n\hat{\Theta}] + \cdots, \tag{2.18}$$

$$\overset{\circ}{\Theta}' = e^{-i\hat{G}}\frac{\partial}{i\partial N}e^{i\hat{G}} = \hat{\Theta}(q) + \frac{i}{2}[\hat{\Theta}, p\hat{Q} + n\hat{\Theta}] + \cdots, \tag{2.19}$$

with use of the general expansion formula

$$e^{-i\hat{G}}\partial e^{i\hat{G}} = i\partial\hat{G} + \frac{1}{2!}[i\partial\hat{G}, i\hat{G}] + \frac{1}{3!}[[i\partial\hat{G}, i\hat{G}], i\hat{G}] + \cdots. \tag{2.20}$$

The operator $\hat{P}(q)$ is the infinitesimal generator with respect to $|\phi(q)\rangle$ defined by

$$\hat{P}(q)|\phi(q)\rangle = i\frac{\partial}{\partial q}|\phi(q)\rangle. \tag{2.21}$$

Similarly, we introduce the unitary transformation of the number operator and expand it as

$$\overset{\circ}{N}' \equiv e^{-i\hat{G}}\hat{N}e^{i\hat{G}} = \hat{N} + i[\hat{N}, p\hat{Q} + n\hat{\Theta}] + \cdots. \tag{2.22}$$

Substituting these operators into the canonical variable condition, Eq. (2.4), we have

$$\langle\phi(q)|\overset{\circ}{P}'(q, p, N)|\phi(q)\rangle = p, \tag{2.23a}$$

$$\langle\phi(q)|\overset{\circ}{Q}'(q, p, N)|\phi(q)\rangle = 0, \tag{2.23b}$$

$$\langle\phi(q)|\overset{\circ}{\Theta}'(q, p, N)|\phi(q)\rangle = 0, \tag{2.23c}$$

$$\langle\phi(q)|\overset{\circ}{N}'(q, p, N)|\phi(q)\rangle = N. \tag{2.23d}$$

Now we expand these equations with respect to the momenta p and n, and obtain the following equations.

The zeroth order canonical variable conditions:

$$\langle\phi(q)|\hat{P}(q)|\phi(q)\rangle = \langle\phi(q)|i\frac{\partial}{\partial q}|\phi(q)\rangle = 0, \tag{2.24}$$

$$\langle\phi(q)|\hat{Q}(q)|\phi(q)\rangle = 0, \tag{2.25}$$

$$\langle\phi(q)|\hat{\Theta}(q)|\phi(q)\rangle = 0, \tag{2.26}$$

$$\langle\phi(q)|\hat{N}|\phi(q)\rangle = N_0. \tag{2.27}$$

Equations (2·25) and (2·26) are automatically fulfilled by the definition Eq. (2·14) of the operators $\hat{Q}(q)$ and $\hat{\Theta}(q)$. Equation (2·24) can be satisfied if the q-dependent phase of $|\phi(q)\rangle$ is properly chosen. Equation (2·27) is the constraint on $|\phi(q)\rangle$ for the conservation of the average particle number.

The first order canonical variable conditions:

$$\langle\phi(q)|\,\frac{\partial \hat{Q}(q)}{\partial q}\,|\phi(q)\rangle = -1, \tag{2·28}$$

$$\langle\phi(q)|\,[\hat{Q}(q), \hat{\Theta}(q)]\,|\phi(q)\rangle = 0, \tag{2·29}$$

$$\langle\phi(q)|\,[\hat{Q}(q), \hat{N}]\,|\phi(q)\rangle = 0. \tag{2·30}$$

One finds

$$\langle\phi(q)|\,[\hat{Q}(q), \hat{P}(q)]\,|\phi(q)\rangle = i, \tag{2·31}$$

which can be derived by differentiating Eq. (2·25) with respect to q and using Eq. (2·28). One can also derive from Eq. (2·27)

$$\langle\phi(q)|\,[\hat{P}(q), \hat{N}]\,|\phi(q)\rangle = 0. \tag{2·32}$$

These equations give constraints on the infinitesimal generators $\hat{Q}(q)$ and $\hat{P}(q)$ concerning the normalization, Eq. (2·31), and the orthogonality to the particle number operator, Eq. (2·32).

Next we expand the equation of collective subspace, Eq. (2·10), to obtain a complete set of the basic equations for the adiabatic approximation. After rewriting Eq. (2·10) as

$$\delta\,\langle\phi(q)|\,e^{-i\hat{G}}\hat{H}e^{i\hat{G}} - \frac{\partial\mathcal{H}}{\partial p}\overset{\circ}{P}' - \frac{\partial\mathcal{H}}{\partial q}\overset{\circ}{Q}' - \frac{\partial\mathcal{H}}{\partial N}\overset{\circ}{N}'\,|\phi(q)\rangle = 0, \tag{2·33}$$

we can expand each term with respect to p and n with use of the equations listed above.

The zeroth order equation of collective subspace:

$$\delta\,\langle\phi(q)|\,\hat{H} - \lambda(q)\hat{N} - \frac{\partial V}{\partial q}\hat{Q}(q)\,|\phi(q)\rangle = 0. \tag{2·34}$$

The first order equation of collective subspace:

$$\delta\,\langle\phi(q)|\,[\hat{H} - \lambda(q)\hat{N}, \hat{Q}(q)] - \frac{1}{i}B(q)\hat{P}(q)\,|\phi(q)\rangle = 0. \tag{2·35}$$

These equations are similar to the equations of path in Villars' ATDHF theory,[1] except that the present paper deals with the superconducting Hartree-Fock-Bogoliubov (HFB) state and that the Hamiltonian accompanies the q-dependent chemical potential term $-\lambda(q)\hat{N}$. As mentioned in §1, the ATDHF theory has the problem that the solution satisfying these two equations is not uniquely determined.[4,5] Although an additional validity condition was introduced to further constrain the solutions,[3,4] the procedure of Ref. 3) does not fully solve the problem since the method does not work around the HF minima.

The non-uniqueness problem has been investigated in recent studies of the adiabatic theories, and in our opinion they can be classified into two different approaches. The first one represented by Ref. 6) asserts that the solution is uniquely determined if an RPA boundary condition is specified at the HF minimum and if the analyticity of the collective path as a function of q is imposed together with the canonical variable condition. The solution, however, needs to be constructed in an analytic way or by means of a Taylor expansion method with respect to the collective coordinate q. We do not adopt this approach since we wish to construct a method applicable to systems exhibiting large excursions from the HFB minimum. We rather follow the other approach, represented by Refs. 7)–9). These theories require the additional condition that the equation of collective subspace (corresponding to the decoupling condition in Ref. 8)) should be satisfied up to the next order of the adiabatic expansion. In the present formulation, this second order condition is expressed as follows.

The second order equation of collective subspace:

$$\delta \langle \phi(q)| \frac{1}{2}[[\hat{H} - \lambda(q)\hat{N}, \hat{Q}(q)], \hat{Q}(q)] - B(q)\Delta\hat{Q}(q) |\phi(q)\rangle = 0, \qquad (2\cdot36)$$

where

$$\Delta\hat{Q}(q) = \frac{\partial \hat{Q}}{\partial q} + \Gamma(q)\hat{Q}(q), \qquad (2\cdot37)$$

$$\Gamma(q) = -\frac{1}{2B(q)}\frac{\partial B}{\partial q}. \qquad (2\cdot38)$$

This equation is equivalent in its mathematical form to the one given in Ref. 7) if the chemical potential term $-\lambda(q)\hat{N}$ is neglected. The last term $-B(q)\Delta\hat{Q}(q)$, often called a curvature term, was simply neglected in the original version of the local harmonic approximation. [12), 13)] In the next subsection, instead of neglecting this curvature term, we rewrite $\Delta\hat{Q}(q)$ and change Eq. (2·36) into a workable form.

It is worth noting here the invariance of the adiabatic equations with respect to the coordinate transformation. The collective momentum p undergoes a linear homogeneous transformation under the point transformation, Eq. (2·11). Therefore, different orders of the expansion with respect to the power of p are not mixed under the point transformation. The invariance property of the basic equations of SCCM is thus inherited by each equation of the adiabatic approximation listed above. One can also confirm this property by seeing that the quantities appearing in the equations transform as

$$\hat{Q}(q) \to \hat{Q}'(q') = \hat{Q}(q(q')) \left(\frac{dq'}{dq}\right), \qquad (2\cdot39a)$$

$$\hat{P}(q) \to \hat{P}'(q') = \hat{P}(q(q')) \left(\frac{dq'}{dq}\right)^{-1}, \qquad (2\cdot39b)$$

$$\frac{\partial V}{\partial q} \to \frac{\partial V'}{\partial q'} = \frac{\partial V}{\partial q} \left(\frac{dq'}{dq}\right)^{-1}, \qquad (2\cdot39c)$$

$$B \to B'(q') = B(q(q')) \left(\frac{dq'}{dq} \right)^2, \tag{2.39d}$$

$$\Delta \hat{Q}(q) \to \Delta \hat{Q}'(q') = \Delta \hat{Q}(q). \tag{2.39e}$$

§3. Local harmonic approximation to collective subspace

3.1. *Local harmonic equations*

In this section we present a concrete procedure to construct an approximate solution of the adiabatic SCC method. To this end, we first derive, from the adiabatic equations, another set of equations of collective subspace which can be solved in a manner similar to that for the RPA equation.

We first take the derivative of the zeroth order equation, Eq. (2·34), with respect to q. This leads to

$$\delta \langle \phi(q) | \left[\hat{H} - \lambda(q)\hat{N}, \frac{1}{i}\hat{P}(q) \right] - C(q)\hat{Q}(q)$$
$$- \frac{\partial V}{\partial q} \Delta \hat{Q}(q) - \frac{\partial \lambda}{\partial q} \hat{N} | \phi(q) \rangle = 0, \tag{3.1}$$

$$C(q) = \frac{\partial^2 V}{\partial q^2} - \Gamma(q) \frac{\partial V}{\partial q}, \tag{3.2}$$

where $\Delta \hat{Q}(q)$ and $\Gamma(q)$ are given by Eqs. (2·37) and (2·38), respectively. Using Eq. (2·36), we eliminate $\Delta \hat{Q}(q)$ and rewrite Eq. (3·1) as

$$\delta \langle \phi(q) | \left[\hat{H} - \lambda(q)\hat{N}, \frac{1}{i}\hat{P}(q) \right] - C(q)\hat{Q}(q)$$
$$- \frac{1}{2B(q)} \left[\left[\hat{H} - \lambda(q)\hat{N}, \frac{\partial V}{\partial q}\hat{Q}(q) \right], \hat{Q}(q) \right] - \frac{\partial \lambda}{\partial q} \hat{N} | \phi(q) \rangle = 0. \tag{3.3}$$

Furthermore, due to Eq. (2·34), we find

$$\frac{\partial V}{\partial q} \hat{Q} = (\hat{H} - \lambda \hat{N})_A, \tag{3.4}$$

where $(\hat{H} - \lambda \hat{N})_A$ represents the $a^\dagger a^\dagger$ and aa part of the operator $\hat{H} - \lambda \hat{N}$ containing two-quasiparticle creation and annihilation in the normal-ordered expression.

We thus replace Eqs. (2·34)–(2·36) by the equivalent set

$$\delta \langle \phi(q) | \hat{H}_M(q) | \phi(q) \rangle = 0, \tag{3.5}$$

$$\delta \langle \phi(q) | [\hat{H}_M(q), \hat{Q}(q)] - \frac{1}{i} B(q)\hat{P}(q) | \phi(q) \rangle = 0, \tag{3.6}$$

$$\delta \langle \phi(q) | \left[\hat{H}_M(q), \frac{1}{i}\hat{P}(q) \right] - C(q)\hat{Q}(q)$$
$$- \frac{1}{2B(q)} [[\hat{H}_M(q), (\hat{H} - \lambda(q)\hat{N})_A], \hat{Q}(q)] - \frac{\partial \lambda}{\partial q} \hat{N} | \phi(q) \rangle = 0. \tag{3.7}$$

In Eqs. (3·6) and (3·7), $\hat{H} - \lambda\hat{N}$ has been replaced by

$$\hat{H}_M(q) = \hat{H} - \lambda(q)\hat{N} - \frac{\partial V}{\partial q}\hat{Q}(q), \tag{3·8}$$

since the last term has no influence. The operator $\hat{H}_M(q)$ may be regarded as the Hamiltonian in the moving frame. The second and third terms can be identified with generalized cranking terms associated with the pairing rotation and the LACM, respectively.

Equations (3·6) and (3·7) are linear equations with respect to the one-body operators $\hat{Q}(q)$ and $\hat{P}(q)$. They have essentially the same structure as the standard RPA equations, except for the last two terms in Eq. (3·7). The quantity $C(q)$ is the local stiffness parameter defined as the second (covariant) derivative of the collective potential $V(q)$. The infinitesimal generators $\hat{Q}(q)$ and $\hat{P}(q)$ are thus closely related to the harmonic normal modes locally defined for $|\phi(q)\rangle$ and the moving frame Hamiltonian $\hat{H}_M(q)$. These equations may be called *local harmonic equations*.

It was shown in Ref. 7) that the zeroth, first and second order equations of AT-DHF give a valley line of a potential energy surface in a multi-dimensional configuration space associated with the TDHF states. Similarly, the local harmonic equations we have obtained, Eqs. (3·5)–(3·7), define the valley of the multi-dimensional potential energy surface. The solution of these equations will be uniquely determined if a suitable boundary condition is specified. These features are similar to the formulation of Ref. 8) where the valley equation of the potential energy surface is derived from the decoupling condition.

We remark again that the local harmonic equations in the present paper differ from those of Rowe-Bassermann [12] and Marumori [13] with respect to the third and fourth terms of Eq. (3·7), which arise from the curvature term (derivative of the generator) and the particle number constraint, respectively. It is important to keep the curvature term in order to maintain the relation between the collective subspace and the valley of the potential surface. We also note that the present formalism is invariant with respect to the point transformation of the collective coordinate, as is the formulation of Ref. 8).

3.2. *Matrix formulation of local harmonic equations*

Let us now give a procedure to find the operators $\hat{Q}(q)$ and $\hat{P}(q)$ that satisfy the local harmonic equations, (3·6) and (3·7), for a given state $|\phi(q)\rangle$. Since these are linear equations with respect to these operators, this can be done in a manner analogous to that for the standard RPA. To show this, we first express the operator $\hat{P}(q)$ and $\hat{N}$ in terms of the quasiparticle operators:

$$\hat{P}(q) = i\sum_{\alpha>\beta}\left(P_{\alpha\beta}(q)a_\alpha^\dagger a_\beta^\dagger - P_{\alpha\beta}^*(q)a_\beta a_\alpha\right) = \hat{P}(q)^\dagger, \tag{3·9}$$

$$\hat{N} = \sum_{\alpha>\beta}\left(N_{\alpha\beta}(q)a_\alpha^\dagger a_\beta^\dagger + N_{\alpha\beta}^*(q)a_\beta a_\alpha\right). \tag{3·10}$$

Note that the $a^\dagger a$ and c-number parts are neglected here since they do not change the state vector $|\phi(q)\rangle$, except for the phase. The Hamiltonian $\hat{H}$ can also be expressed

in terms of the same quasiparticle operators. Assuming that the matrix elements $Q_{\alpha\beta}$ and $P_{\alpha\beta}$ are real, the local harmonic equations can be written as the following matrix equations:

$$(\boldsymbol{A} - \boldsymbol{B})\boldsymbol{Q} - B(q)\boldsymbol{P} = 0, \tag{3·11a}$$

$$(\boldsymbol{A} + \boldsymbol{B})\boldsymbol{P} - C(q)\boldsymbol{Q} - \frac{1}{B(q)}\boldsymbol{D}\boldsymbol{Q} - \lambda'\boldsymbol{N} = 0, \tag{3·11b}$$

$$\boldsymbol{P}^T\boldsymbol{N} = 0, \tag{3·11c}$$

$$2\boldsymbol{Q}^T\boldsymbol{P} = 1, \tag{3·11d}$$

$$\lambda' = \frac{\partial\lambda}{\partial q}. \tag{3·11e}$$

Here all quantities are functions of q while $\boldsymbol{Q} = (\cdots, Q_{\alpha\beta}, \cdots)^T$, $\boldsymbol{P} = (\cdots, P_{\alpha\beta}, \cdots)^T$ and $\boldsymbol{N} = (\cdots, N_{\alpha\beta}, \cdots)^T$ form the vector representation of the matrix elements with $\alpha > \beta$. $\boldsymbol{A}$ and $\boldsymbol{B}$ are the matrices whose elements are given by

$$(\boldsymbol{A})_{\alpha\beta,\gamma\delta} = \delta_{\alpha\gamma}\delta_{\beta\delta}(e_\alpha + e_\beta) + v^{22}_{\alpha\beta,\gamma\delta}, \tag{3·12a}$$

$$(\boldsymbol{B})_{\alpha\beta,\gamma\delta} = v^{40}_{\alpha\beta\gamma\delta}, \tag{3·12b}$$

in terms of the matrix elements of the moving frame Hamiltonian,

$$\hat{H}_M(q) = \sum_\alpha e_\alpha a_\alpha^\dagger a_\alpha \tag{3·13a}$$

$$+\frac{1}{4}\sum_{\alpha\beta\gamma\delta} v^{22}_{\alpha\beta,\gamma\delta} a_\alpha^\dagger a_\beta^\dagger a_\delta a_\gamma \tag{3·13b}$$

$$+\frac{1}{4!}\sum_{\alpha\beta\gamma\delta}\left(v^{40}_{\alpha\beta\gamma\delta} a_\alpha^\dagger a_\beta^\dagger a_\gamma^\dagger a_\delta^\dagger + v^{04}_{\alpha\beta\gamma\delta} a_\delta a_\gamma a_\beta a_\alpha\right) \tag{3·13c}$$

$$+\frac{1}{3!}\sum_{\alpha\beta\gamma\delta}\left(v^{31}_{\alpha\beta\gamma,\delta} a_\alpha^\dagger a_\beta^\dagger a_\gamma^\dagger a_\delta + v^{13}_{\delta,\alpha\beta\gamma} a_\delta^\dagger a_\gamma a_\beta a_\alpha\right). \tag{3·13d}$$

Here, due to Eq. (2·34), the $a^\dagger a^\dagger$ and aa parts of $\hat{H}_M(q)$ vanish, and the $a^\dagger a$ part of $\hat{H}_M(q)$ is diagonalized. The matrix elements of the residual interactions in Eqs. (3·13b)–(3·13d) are antisymmetrized with respect to the quasiparticle indices. The matrices $\boldsymbol{A}$ and $\boldsymbol{B}$ have the same structures as those defined in the quasiparticle RPA formalism. [17] The matrix $\boldsymbol{D}$ is defined by

$$(\boldsymbol{D})_{\alpha\beta,\gamma\delta} = \frac{1}{2}\langle\phi(q)|\,[[[\hat{H}_M(q), (\hat{H} - \lambda(q)\hat{N})_A], a_\alpha^\dagger a_\beta^\dagger + a_\beta a_\alpha], a_\gamma a_\delta]\,|\phi(q)\rangle. \tag{3·14}$$

These matrix elements can be expressed also in terms of the Hamiltonian matrix elements as

$$(\boldsymbol{D})_{\alpha\beta,\gamma\delta} = (d^{22}_{\alpha\beta,\gamma\delta} - d^{40}_{\alpha\beta\gamma\delta} + d^{11}_{\alpha\gamma}\delta_{\beta\delta} - d^{11}_{\beta\gamma}\delta_{\alpha\delta} - d^{11}_{\alpha\delta}\delta_{\beta\gamma} + d^{11}_{\beta\delta}\delta_{\alpha\gamma})/2, \tag{3·15a}$$

$$d^{22}_{\alpha\beta,\gamma\delta} = \sum_\epsilon (v^{31}_{\alpha\beta\epsilon,\gamma}h_{\delta\epsilon} - v^{31}_{\alpha\beta\epsilon,\delta}h_{\gamma\epsilon} - v^{13}_{\alpha,\epsilon\gamma\delta}h_{\beta\epsilon} + v^{13}_{\beta,\epsilon\gamma\delta}h_{\alpha\epsilon}), \tag{3·15b}$$

$$d^{40}_{\alpha\beta\gamma\delta} = \sum_\epsilon (v^{31}_{\alpha\beta\gamma,\epsilon} h_{\epsilon\delta} - v^{31}_{\beta\gamma\delta,\epsilon} h_{\epsilon\alpha} + v^{31}_{\gamma\delta\alpha,\epsilon} h_{\epsilon\beta} - v^{31}_{\delta\alpha\beta,\epsilon} h_{\epsilon\gamma}), \tag{3.15c}$$

$$d^{11}_{\alpha\beta} = \sum_{\gamma>\delta} (v^{13}_{\alpha,\beta\gamma\delta} h_{\gamma\delta} - v^{31}_{\gamma\delta\alpha,\beta} h_{\gamma\delta}), \tag{3.15d}$$

where $h_{\alpha\beta}$ represents the matrix elements of $(\hat{H} - \lambda\hat{N})_A$ defined by

$$(\hat{H} - \lambda\hat{N})_A = \sum_{\alpha>\beta} h_{\alpha\beta}(a^\dagger_\alpha a^\dagger_\beta + a_\beta a_\alpha). \tag{3.16}$$

Note that $\boldsymbol{D}$ contains the matrix elements of the types v^{13} and v^{31}. These terms of the Hamiltonian do not contribute to the standard RPA equations.

The solution of the matrix equations is obtained as follows. From Eq. (3.11), we obtain

$$\boldsymbol{Q} = \lambda' B(q) \left((\boldsymbol{A} + \boldsymbol{B})(\boldsymbol{A} - \boldsymbol{B}) - \boldsymbol{D} - \Omega\right)^{-1} \boldsymbol{N}, \tag{3.17a}$$

$$\boldsymbol{P} = \lambda'(\boldsymbol{A} - \boldsymbol{B}) \left((\boldsymbol{A} + \boldsymbol{B})(\boldsymbol{A} - \boldsymbol{B}) - \boldsymbol{D} - \Omega\right)^{-1} \boldsymbol{N}, \tag{3.17b}$$

with

$$\Omega = B(q)C(q). \tag{3.18}$$

The condition that the collective mode is orthogonal to the number operator, Eq. (3.11c), gives the following equation:

$$S(\Omega) \equiv \boldsymbol{N}^T(\boldsymbol{A} - \boldsymbol{B}) \left((\boldsymbol{A} + \boldsymbol{B})(\boldsymbol{A} - \boldsymbol{B}) - \boldsymbol{D} - \Omega\right)^{-1} \boldsymbol{N} = 0. \tag{3.19}$$

The quantity $\Omega = B(q)C(q)$ represents the square of the frequency $\omega = \sqrt{BC}$ of the local harmonic mode, which is not necessarily positive. This equation can be regarded as a dispersion equation to determine $\Omega = \omega^2$ as a zero point of $S(\Omega)$. The normalization condition, Eq. (3.11d), then gives a constraint on the value of $\lambda'^2 B(q)$. The value of the mass parameter $B(q)$ is arbitrary, being related to the invariance under the point transformation Eq. (2.11). The choice of the coordinate q specifies the value of the mass parameter, $B(q)$. In practice, the coordinate is often scaled so as to make the mass parameter unity.

When the residual interactions are separable forces, such as the monopole pairing and the quadruple-quadrupole forces, the local harmonic equations reduce to a simpler form. The dispersion equation for the separable interaction does not require a matrix inversion as in Eq. (3.19). The details of these points are discussed in the Appendix.

Reference 10) discusses a problem of spurious (Nambu-Goldstone) modes for local harmonic approaches, and it is stated there that the RPA equation at non-equilibrium points must be extended in order to guarantee separation of the spurious modes. However, no practical way of solving the equation was given because the equation has parameters for which we do not have a method to calculate. In our present formulation, the RPA equation is indeed extended to assure the number conservation.

3.3. *Construction of collective subspace*

Let us finally give algorithms to construct the collective subspace $|\phi(q)\rangle$ as a function of the collective coordinate q. Note that the local harmonic equations, Eqs. (3·5)–(3·7), are regarded as local equations in the sense that the equations can be solved independently for different values of q. At the HFB ground state, $|\phi_0\rangle$, defined by the HFB equation

$$\delta \langle\phi_0| \hat{H} - \lambda_0 \hat{N} |\phi_0\rangle = 0, \tag{3·20}$$

we find $\partial V/\partial q = 0$. Therefore, $|\phi_0\rangle$ is always a state in the collective subspace because Eq. (3·5) is automatically satisfied. Equations (3·6) and (3·7) reduce to the standard RPA equations at $|\phi_0\rangle$ since the last two terms in Eq. (3·7) vanish. The operators $\hat{Q}$ and $\hat{P}$ are then determined as one of the normal modes of the RPA equation.

For non-equilibrium states, in general, Eq. (3·5) and the other two equations, (3·6) and (3·7), are coupled. We may solve the coupled equations in an iterative way. As discussed in §3.2, we can find the operators $\hat{Q}(q)^{(n)}$ and $\hat{P}(q)^{(n)}$ by solving Eqs. (3·6) and (3·7) for a given trial state $|\phi(q)\rangle^{(n)}$ (n denoting the iteration step). This defines the moving frame Hamiltonian $\hat{H}_M(q)^{(n+1)} = \hat{H} - \lambda(q)^{(n+1)}\hat{N} - \left(\frac{\partial V}{\partial q}\right)^{(n)} \hat{Q}(q)^{(n)}$, which can be used to construct a trial state $|\phi(q)\rangle^{(n+1)}$ for the next iteration. If the iteration converges, we obtain a state $|\phi(q)\rangle$ for which Eqs. (3·5)–(3·7) are simultaneously satisfied. Repeating the same procedure for different values of q, one finally obtains the collective subspace $|\phi(q)\rangle$ and the collective Hamiltonian as a function of q.

We remark here that the operator $\hat{P}(q)$ thus determined does not guarantee Eq. (2·21), although the other equations are satisfied. In this sense, the local harmonic solution is an approximate solution. The exact solution satisfying all the basic equations in §2.2 may not exist in realistic situations. Only when the system is "exactly decoupled" [8] does the above procedure give the exact solution.

It is possible to choose another algorithm which satisfies Eq. (2·21), at the expense of introducing errors into Eq. (3·5). Let $|\phi(q_0)\rangle$ be a solution that satisfies the basic equations at $q = q_0$. The infinitesimal generators $\hat{Q}(q_0)$ and $\hat{P}(q_0)$ are determined by solving Eqs. (3·6) and (3·7). Then we can generate the state $|\phi(q_0 + \delta q)\rangle$ for an infinitesimal shift of the collective coordinate as

$$|\phi(q_0 + \delta q)\rangle = e^{-i\delta q \hat{P}(q_0)} |\phi(q_0)\rangle. \tag{3·21}$$

Repeating this procedure, we can construct a collective subspace. This solution should coincide with that solved by the previous method if the system is exactly decoupled.

The two methods described above give different solutions in situations where the exact decoupling is not satisfied. In such cases, one can evaluate the quality of decoupling for the collective subspace or the validity of the local harmonic approximation by comparing the two solutions. We note also that the second method can be used to provide an initial guess, $|\phi(q)\rangle^{(0)}$, for the iteration of the first method.

§4. Extension to multi-dimensional collective subspace

In this section we extend the adiabatic SCC method to the case of a multi-dimensional collective subspace described by D collective coordinates and conjugate momenta, $\{q^i, p_i; i = 1, \cdots, D\}$.

One can easily derive the basic equations of the adiabatic SCC method in parallel to the derivation given in §2 by noting first that Eqs. (2·12) and (2·14) are now extended to

$$|\phi(q, p, N)\rangle = e^{i\hat{G}(q,p,n)} |\phi(q)\rangle, \tag{4·1}$$

$$\hat{G} = p_i \hat{Q}^i(q) + n\hat{\Theta}(q), \tag{4·2}$$

where the operator $\hat{Q}^i(q)$ now has D components with the coordinate label i. It is implied here and hereafter that any coordinate index (i in the above expression) appearing both as the superscript and subscript is summed over. The infinitesimal generator $\hat{P}_i(q)$ also has D components, each of which is related to the derivative $i\frac{\partial}{\partial q^i} |\phi(q)\rangle$. In the following, the coordinate dependence is often omitted. For instance, $B^{ij}(q)$ and $\hat{Q}^i(q)$ will be simply denoted by B^{ij} and $\hat{Q}^i$.

The adiabatic collective Hamiltonian is expressed as

$$\mathcal{H}(q, p, N) = V(q) + \frac{1}{2}B^{ij}(q)p_i p_j + \lambda(q)n. \tag{4·3}$$

The zeroth and the first order equations of the collective subspace are derived as

$$\delta \langle\phi(q)| \hat{H} - \lambda(q)\hat{N} - \frac{\partial V}{\partial q^i}\hat{Q}^i |\phi(q)\rangle = 0, \tag{4·4}$$

$$\delta \langle\phi(q)| [\hat{H} - \lambda(q)\hat{N}, \hat{Q}^i] - \frac{1}{i}B^{ij}\hat{P}_j |\phi(q)\rangle = 0, \tag{4·5}$$

while the second order equation becomes

$$\delta \langle\phi(q)| \frac{1}{2}[\hat{H} - \lambda(q)\hat{N}, \hat{Q}^i, \hat{Q}^j] + \frac{1}{6}\left[\frac{\partial V}{\partial q^k}\hat{Q}^k, \hat{Q}^i, \hat{Q}^j\right]$$
$$- \frac{1}{2}(B^{ik}\hat{Q}^j_{;k} + B^{jk}\hat{Q}^i_{;k}) |\phi(q)\rangle = 0 \tag{4·6}$$

with

$$\hat{Q}^i_{;j} = \frac{\partial \hat{Q}^i}{\partial q^j} + \Gamma^i_{kj}\hat{Q}^k, \tag{4·7}$$

$$\Gamma^i_{kj} = \frac{1}{2}B^{il}\left(\frac{\partial B_{lk}}{\partial q^j} + \frac{\partial B_{lj}}{\partial q^k} - \frac{\partial B_{kj}}{\partial q^l}\right), \tag{4·8}$$

where B_{ij} is the inverse matrix of B^{ij}, and the bracket including the three operators is defined by

$$[A, B, C] = \frac{1}{2}([[A, B], C] + [[A, C], B]). \tag{4·9}$$

Expanding the canonical variable condition with respect to p_i and n, the following equations are derived:

$$\langle\phi(q)|\,\hat{P}_i\,|\phi(q)\rangle = 0, \tag{4·10}$$

$$\langle\phi(q)|\,\hat{N}\,|\phi(q)\rangle = N_0, \tag{4·11}$$

and

$$\langle\phi(q)|\,[\hat{Q}^i, \hat{P}_j]\,|\phi(q)\rangle = i\delta_{ij}, \tag{4·12}$$

$$\langle\phi(q)|\,[\hat{Q}^i, \hat{N}]\,|\phi(q)\rangle = 0, \tag{4·13}$$

$$\langle\phi(q)|\,[\hat{P}_i, \hat{N}]\,|\phi(q)\rangle = 0. \tag{4·14}$$

These basic equations are invariant under the point transformation of the collective variables:

$$q^i \rightarrow q'^i = q'^i(q), \tag{4·15a}$$

$$p_i \rightarrow p'_i = p_j \times \left(\partial q^j/\partial q'^i\right). \tag{4·15b}$$

We have adopted the vector-tensor notation [20] to make clear the transformation properties under the point transformation. Quantities with a coordinate index as the subscript (superscript) have the transformation properties of the *covariant* (*contravariant*) vectors. For example,

$$\hat{Q}^i \rightarrow \hat{Q}'^i = \hat{Q}^j \times \left(\partial q'^i/\partial q^j\right), \tag{4·16}$$

$$\hat{P}_i \rightarrow \hat{P}'_i = \hat{P}_j \times \left(\partial q^j/\partial q'^i\right). \tag{4·17}$$

The mass tensor B^{ij} is the contravariant tensor of second rank. The operator $\hat{Q}^i_{;j}$ defined by Eq. (4·7) is the covariant derivative of $\hat{Q}^i$, and Γ^i_{kj} is the Christoffel symbol, where the mass tensor B_{ij} plays the role of metric tensor.

Let us now derive local harmonic equations of the collective subspace. Taking the q-derivative, the zeroth order equation (4·4) leads to

$$\delta\langle\phi(q)|\left[\hat{H} - \lambda(q)\hat{N}, \frac{1}{i}\hat{P}_i\right] - C_{ij}(q)\hat{Q}^j - \frac{\partial V}{\partial q^j}\hat{Q}^j_{;i} - \frac{\partial\lambda}{\partial q^i}\hat{N}\,|\phi(q)\rangle = 0, \tag{4·18}$$

$$C_{ij}(q) = \frac{\partial^2 V}{\partial q^i \partial q^j} - \Gamma^k_{ij}\frac{\partial V}{\partial q^k}. \tag{4·19}$$

As we have done for the $D = 1$ case, we would like to eliminate the covariant derivative $\hat{Q}^j_{;i}$ in Eq. (4·18) in order to give a feasible form of the local harmonic equation. This was done for the $D = 1$ case with the help of the second order equation of the collective subspace. The corresponding equations (4·6) give $D(D+1)/2$ constraints, while the number of unknown parameters, $\hat{Q}^j_{;i}$, is D^2. In fact, Eq. (4·6) is equivalent to

$$\delta\langle\phi(q)|\,\frac{1}{2}[[\hat{H} - \lambda(q)\hat{N}, \hat{Q}^j], \hat{Q}^i] + \frac{1}{6}\left[\left[\frac{\partial V}{\partial q^k}\hat{Q}^k, \hat{Q}^j\right], \hat{Q}^i\right] - (B^{ik}\hat{Q}^j_{;k} + \hat{R}^{ij})\,|\phi(q)\rangle = 0, \tag{4·20}$$

where $\hat{R}^{ij}$ are arbitrary one-body operators which are antisymmetric with respect to exchange of indices i and j. If we choose $\hat{R}^{ij} = 0$, we can eliminate the derivative term $\frac{\partial V}{\partial q^j} \hat{Q}^j_{;i}$. Then, Eq. (4·18) leads to

$$\delta \langle \phi(q)| \left[\hat{H} - \lambda(q)\hat{N}, \frac{1}{i}\hat{P}_i \right] - C_{ij}\hat{Q}^j$$
$$-\frac{1}{2}[[\hat{H} - \lambda(q)\hat{N}, (\hat{H} - \lambda(q)\hat{N})_A], B_{ij}\hat{Q}^j] - \frac{\partial \lambda}{\partial q^i}\hat{N} |\phi(q)\rangle = 0. \quad (4·21)$$

This equation is an analog of Eq. (3·7) and is linear in the infinitesimal generators $\hat{Q}^i$ and $\hat{P}_i$. We can numerically solve Eqs. (4·4), (4·5) and (4·21) in the same manner as discussed in §§3.2 and 3.3.

It should be remarked that the local harmonic equation Eq. (4·21) for $D > 1$ is derived from Eqs. (4·4) and (4·6), but with the additional condition $\hat{R}^{ij} = 0$ in Eq. (4·20). This condition is introduced to obtain the local harmonic equations parallel to the one-dimensional case.

§5. Conclusions

We have formulated the adiabatic approximation of the general framework of the selfconsistent collective coordinate method in order to describe large amplitude collective motion in superconducting nuclei. The formalism, based on the TDHFB equations of motion, guarantees the conservation of particle number in a transparent way. We have shown that the equations of collective subspace are reduced to local linear equations for the infinitesimal generators, which can be solved with use of the quasiparticle representation of the Hamiltonian matrix elements. This provides a concrete procedure to determine the states $e^{ip\hat{Q}(q)} |\phi(q)\rangle$ in the collective subspace and the collective Hamiltonian $\mathcal{H}(q, p) = V(q) + \frac{1}{2}B(q)p^2$ as functions of the collective coordinate q and momentum p. A possible extension to the case of multi-dimensional collective coordinates was also discussed.

We emphasize that the equations given in this paper are solvable by means of the matrix method similar to the standard RPA. We hope that the present adiabatic theory is useful to solve a number of open questions in realistic studies of large amplitude collective motion in nuclear systems.

Appendix A
——— *Solution for the Separable Interactions* ———

In this appendix, we give solutions of the local harmonic equations of collective subspace for the case in which the two-body interaction is given by separable forces. We assume that the Hamiltonian is given by

$$\hat{H} = \hat{h}_0 - \frac{\kappa}{2}\hat{F}^\dagger \hat{F}, \quad (A·1)$$

where $\hat{h}_0(=\hat{h}_0^\dagger)$ and $\hat{F}$ are one-body operators. Equivalently, one may write

$$\hat{H} = \hat{h}_0 - \frac{\kappa}{2}\hat{F}^{(+)}\hat{F}^{(+)} + \frac{\kappa}{2}\hat{F}^{(-)}\hat{F}^{(-)}, \tag{A·2}$$

$$\hat{F}^{(\pm)} \equiv (\hat{F} \pm \hat{F}^\dagger)/2 = \pm\hat{F}^{(\pm)\dagger}. \tag{A·3}$$

For separable forces, it is customary to neglect the Fock term of the forces. This approximation is easily and consistently implemented in the SCCM by assuming that the equation of motion for the time-dependent mean-field state $|\phi(t)\rangle$ is now given by the time-dependent Hartree-Bogoliubov equation without the Fock terms,

$$\delta \langle\phi(t)| \, i\frac{\partial}{\partial t} - \hat{h}(t) \, |\phi(t)\rangle = 0, \tag{A·4}$$

$$\hat{h}(t) = \hat{h}_0 - \kappa\hat{F}^{(+)} \langle\phi(t)| \, \hat{F}^{(+)} \, |\phi(t)\rangle + \kappa\hat{F}^{(-)} \langle\phi(t)| \, \hat{F}^{(-)} \, |\phi(t)\rangle . \tag{A·5}$$

The local harmonic equations (3·5)–(3·7) then become

$$\delta \langle\phi(q)| \, \hat{h}_M(q) \, |\phi(q)\rangle = 0, \tag{A·6}$$

$$\delta \langle\phi(q)| \, [\hat{h}_M(q), \hat{Q}(q)] - f_Q^{(-)}\hat{F}^{(-)} - \frac{1}{i}B(q)\hat{P}(q) \, |\phi(q)\rangle = 0, \tag{A·7}$$

$$\delta \langle\phi(q)| \left[\hat{h}_M(q), \frac{1}{i}B(q)\hat{P}(q)\right] - f_P^{(+)}\hat{F}^{(+)} - B(q)C(q)\hat{Q}(q) - f_R^{(+)}\hat{F}^{(+)}$$
$$-f_Q^{(-)}[\hat{F}^{(-)}, (\hat{h}(q) - \lambda(q)\hat{N})_A] - f_N\hat{N} \, |\phi(q)\rangle = 0, \tag{A·8}$$

where $\hat{h}_M(q)$ is the mean-field Hamiltonian in the moving frame defined by

$$\hat{h}_M(q) = \hat{h}(q) - \frac{\partial V}{\partial q}\hat{Q}(q) - \lambda(q)\hat{N}, \tag{A·9}$$

$$\hat{h}(q) = \hat{h}_0 - \kappa\hat{F}^{(+)} \langle\phi(q)| \, \hat{F}^{(+)} \, |\phi(q)\rangle , \tag{A·10}$$

and the definitions of the other symbols are

$$f_Q^{(-)} = -\kappa \langle\phi(q)| \, [\hat{F}^{(-)}, \hat{Q}(q)] \, |\phi(q)\rangle , \tag{A·11a}$$

$$f_P^{(+)} = \kappa \langle\phi(q)| \left[\hat{F}^{(+)}, \frac{1}{i}B(q)\hat{P}(q)\right] |\phi(q)\rangle , \tag{A·11b}$$

$$f_R^{(+)} = -\kappa \langle\phi(q)| \, [[\hat{F}^{(+)}, (\hat{h}(q) - \lambda(q)\hat{N})_A], \hat{Q}(q)] \, |\phi(q)\rangle /2, \tag{A·11c}$$

$$f_N = B(q)\frac{\partial\lambda}{\partial q}. \tag{A·11d}$$

We express all operators in the above equations in terms of the quasiparticle operators $\{a_\alpha^\dagger, a_\alpha\}$ defined for $\hat{h}_M(q)$ and $|\phi(q)\rangle$. For example, we have

$$\hat{h}_M(q) = \sum_\alpha e_\alpha a_\alpha^\dagger a_\alpha, \tag{A·12}$$

$$\hat{F}^{(+)} = \sum_{\alpha>\beta} F_{\alpha\beta}^{(+)}(a_\alpha^\dagger a_\beta^\dagger + a_\beta a_\alpha) + \sum_{\alpha\beta} F_{B,\alpha\beta}^{(+)}a_\alpha^\dagger a_\beta, \tag{A·13}$$

$$\hat{F}^{(-)} = \sum_{\alpha>\beta} F_{\alpha\beta}^{(-)}(a_\alpha^\dagger a_\beta^\dagger - a_\beta a_\alpha) + \sum_{\alpha\beta} F_{B,\alpha\beta}^{(-)}a_\alpha^\dagger a_\beta. \tag{A·14}$$

We have assumed here that all matrix elements are real. Equations (A·7) and (A·8) can then be reduced to linear equations for the matrix elements $Q_{\alpha\beta}$ and $P_{\alpha\beta}$ of the infinitesimal generators $\hat{Q}(q)$ and $\hat{P}(q)$. They are easily solved to give the expression

$$
\begin{aligned}
Q_{\alpha\beta} =\ & \frac{e_\alpha + e_\beta}{(e_\alpha + e_\beta)^2 - \Omega} F^{(-)}_{\alpha\beta} f^{(-)}_Q \\
& + \frac{1}{(e_\alpha + e_\beta)^2 - \Omega} \left(F^{(+)}_{\alpha\beta} f^{(+)}_{PR} + R^{(-)}_{\alpha\beta} f^{(-)}_Q + N_{\alpha\beta} f_N \right),
\end{aligned} \quad \text{(A·15)}
$$

$$
\begin{aligned}
BP_{\alpha\beta} =\ & \frac{e_\alpha + e_\beta}{(e_\alpha + e_\beta)^2 - \Omega} \left(F^{(+)}_{\alpha\beta} f^{(+)}_{PR} + R^{(-)}_{\alpha\beta} f^{(-)}_Q + N_{\alpha\beta} f_N \right) \\
& + \frac{\Omega}{(e_\alpha + e_\beta)^2 - \Omega} F^{(-)}_{\alpha\beta} f^{(-)}_Q,
\end{aligned} \quad \text{(A·16)}
$$

$$
f^{(+)}_{PR} =\ f^{(+)}_P + f^{(+)}_R, \quad \text{(A·17)}
$$

where we have introduced the one-body operator

$$
\hat{R}(q)^{(\pm)} \equiv [\hat{F}^{(\pm)}_B(q), (\hat{h}(q) - \lambda(q)\hat{N})_A] = \sum_{\alpha>\beta} R^{(\pm)}_{\alpha\beta} (a^\dagger_\alpha a^\dagger_\beta \mp a_\beta a_\alpha), \quad \text{(A·18)}
$$

with $\hat{F}^{(\pm)}_B(q)$ being the last terms of $\hat{F}^{(\pm)}$ in Eqs. (A·13) and (A·14).

Inserting this expression for the definition of $f^{(+)}_{PR}$ and $f^{(-)}_Q$, we obtain equations for the unknown quantities $f^{(+)}_{PR}$, $f^{(-)}_Q$ and f_N. Similarly, the condition of orthogonality to the number operator Eq. (3·11c) gives another equation for $f^{(+)}_{PR}$, $f^{(-)}_Q$ and f_N. These equations can be written in a 3×3 matrix form:

$$
\left(\ S_{xx'}(\Omega) \ \right) \begin{pmatrix} f^{(+)}_{PR} \\ f^{(-)}_Q \\ f_N \end{pmatrix} = 0, \quad \text{(A·19)}
$$

where

$$
S_{11} = 2S^{(1)}_{F(+)F(+)} + S^{(2)}_{R(+)F(+)} - \frac{1}{\kappa}, \quad \text{(A·20a)}
$$

$$
S_{12} = 2\Omega S^{(2)}_{F(+)F(-)} + 2S^{(1)}_{F(+)R(-)} + S^{(1)}_{R(+)F(-)} + S^{(2)}_{R(+)R(-)}, \quad \text{(A·20b)}
$$

$$
S_{13} = 2S^{(1)}_{F(+)N} + S^{(2)}_{R(+)N}, \quad \text{(A·20c)}
$$

$$
S_{21} = 2S^{(2)}_{F(-)F(+)}, \quad \text{(A·20d)}
$$

$$
S_{22} = 2S^{(1)}_{F(-)F(-)} + 2S^{(2)}_{F(-)R(-)} - \frac{1}{\kappa}, \quad \text{(A·20e)}
$$

$$
S_{23} = 2S^{(2)}_{F(-)N}, \quad \text{(A·20f)}
$$

$$
S_{31} = S^{(1)}_{NF(+)}, \quad \text{(A·20g)}
$$

$$
S_{32} = \Omega S^{(2)}_{NF(-)} + S^{(1)}_{NR(-)}, \quad \text{(A·20h)}
$$

$$
S_{33} = S^{(1)}_{NN}. \quad \text{(A·20i)}
$$

The functions $S_{XY}^{(1)}$ with the symbols X and Y denoting $(X, Y) = (F^{(+)}, F^{(+)})$, $(F^{(+)}, R^{(-)})$, $(F^{(+)}, N)$, $(R^{(+)}, F^{(-)})$, $(F^{(-)}, F^{(-)})$, (N, N), $(N, F^{(+)})$, $(N, R^{(-)})$ are given by

$$S_{XY}^{(1)} = \sum_{\alpha > \beta} \frac{e_\alpha + e_\beta}{(e_\alpha + e_\beta)^2 - \Omega} X_{\alpha\beta} Y_{\alpha\beta}, \tag{A·21}$$

while the functions $S_{XY}^{(2)}$ with $(X, Y) = (F^{(+)}, F^{(-)})$, $(R^{(+)}, F^{(+)})$, $(R^{(+)}, R^{(-)})$, $(R^{(+)}, N)$, $(F^{(-)}, F^{(+)})$, $(F^{(-)}, R^{(-)})$, $(F^{(-)}, N)$, $(N, F^{(-)})$ are given by

$$S_{XY}^{(2)} = \sum_{\alpha > \beta} \frac{1}{(e_\alpha + e_\beta)^2 - \Omega} X_{\alpha\beta} Y_{\alpha\beta}. \tag{A·22}$$

The value of Ω is determined by finding the zero point of the dispersion equation

$$\det\{S_{xx'}(\Omega)\} = 0. \tag{A·23}$$

Normalizations of $f_{PR}^{(+)}$, $f_Q^{(-)}$ and f_N are fixed by the condition Eq. (3·11d). It is straightforward to extend the above procedure to the case in which the two-body interaction is given by a sum of the separable forces.

References

1) F. Villars, Nucl. Phys. **A285** (1977), 269.
2) M. Baranger and M. Veneroni, Ann. of Phys. **114** (1978), 123.
3) K. Goeke and P.-G. Reinhard, Ann. of Phys. **112** (1978), 328.
   K. Goeke, F. Grümmer and P.-G. Reinhard, Ann. of Phys. **150** (1983), 504.
4) K. Goeke, P.-G. Reinhard and D. J. Rowe, Nucl. Phys. **A359** (1981), 408.
5) A. K. Mukherjee and M. K. Pal, Phys. Lett. **B100** (1981), 457.
6) A. Kuriyama and M. Yamamura, Prog. Theor. Phys. **70** (1983), 1675; **71** (1984), 122.
   M. Yamamura, A. Kuriyama and S. Iida, Prog. Theor. Phys. **71** (1984), 109.
   M. Yamamura and A. Kuriyama, Prog. Theor. Phys. Suppl. No. 93 (1987).
7) A. K. Mukherjee and M. K. Pal, Nucl. Phys. **A373** (1982), 289.
8) A. Klein, N. R. Walet and G. Do Dang, Ann. of Phys. **208** (1991), 90.
   For a recent review, see also G. Do Dang, A. Klein and N. R. Walet, preprint nucl-th/9911081.
9) D. J. Rowe, Nucl. Phys. **A391** (1982), 307.
10) T. Nakatsukasa, N. R. Walet and G. Do Dang, Phys. Rev. **C61** (2000), 014302.
11) T. Nakatsukasa and N. R. Walet, Phys. Rev. **C57** (1998), 1192; **C58** (1998), 3397.
12) D. J. Rowe and R. Bassermann, Can. J. Phys. **54** (1976), 1941.
13) T. Marumori, Prog. Theor. Phys. **57** (1977), 112.
14) T. Marumori, T. Maskawa, F. Sakata and A. Kuriyama, Prog. Theor. Phys. **64** (1980), 1294.
15) M. Matsuo, Prog. Theor. Phys. **76** (1986), 372.
16) M. Matsuo and K. Matsuyanagi, Prog. Theor. Phys. **74** (1985), 1227; **76** (1986), 93; **78** (1987), 591.
   K. Takada, K. Yamada and H. Tsukuma, Nucl. Phys. **A496** (1989), 224.
   K. Yamada, K. Takada and H. Tsukuma, Nucl. Phys. **A496** (1989), 239.
   K. Yamada and K. Takada, Nucl. Phys. **A503** (1989), 53.
   H. Aiba, Prog. Theor. Phys. **84** (1990), 908.
   M. Matsuo, in *New Trends in Nuclear Collective Dynamics*, ed. Y. Abe, H. Horiuchi and K. Matsuyanagi (Springer-Verlag, 1992), p. 219.
   K. Yamada, Prog. Theor. Phys. **85** (1991), 805; **89** (1993), 995.
17) P. Ring and P. Schuck, *The Nuclear Many-Body Problem* (Springer-Verlag, 1980).
18) J.-P. Blaizot and G. Ripka, *Quantum Theory of Finite Systems* (The MIT press, 1986).
19) N. R. Walet, G. Do Dang and A. Klein, Phys. Rev. **C43** (1991), 2254.
20) L. D. Landau and E. M. Lifshitz, *The Classical Theory of Fields* (Pergamon press, 1975).

Diabatic Mean-Field Description of Rotational Bands in Terms of the Selfconsistent Collective Coordinate Method

Yoshifumi R. Shimizu and Kenichi Matsuyanagi[*]

Department of Physics, Kyushu University, Fukuoka 812-8581, Japan
[*]Department of Physics, Graduate School of Science
Kyoto University, Kyoto 606-8502, Japan

Diabatic description of rotational bands provides a clear-cut picture for understanding the back-bending phenomena, where the internal structure of the yrast band changes dramatically as a function of angular momentum. A microscopic framework to obtain the diabatic bands within the mean-field approximation is presented by making use of the selfconsistent collective coordinate method. Applying the framework, both the ground state rotational bands and the Stockholm bands are studied systematically for the rare-earth deformed nuclei. An overall agreement has been achieved between the calculated and observed rotational spectra. It is also shown that the inclusion of the double-stretched quadrupole-pairing interaction is crucial to obtain an overall agreement for the even-odd mass differences and the rotational spectra simultaneously.

§1. Introduction

Back-bending of the yrast rotational bands is one of the most striking phenomena in the spectroscopic studies of rapidly rotating nuclei. [1,2] The first back-bending, which has been observed systematically in the rotational bands of the rare-earth nuclei, has been understood as a band-crossing between the ground state rotational band (g-band) and the lowest two-quasineutron excited band (s-band). A simple approach to describe the band-crossing is the cranked mean-field approximation, where the concept of independent particle motion in the rotating frame is fully employed. As long as the conventional (adiabatic) cranking model is used, however, the two bands mix at the same rotational frequency and, in the crossing region, loose their identities as individual rotational bands. It should be noted that the difficulty lies in the fact that the angular momenta of two bands are considerably different in the vicinity of the crossing frequency where the mixing takes place, especially in the case of sharp back-bendings, and such a mixing is largely unphysical. [3-5]

A key to solve this problem is to construct *diabatic rotational bands*, where the internal structure of the band does not change abruptly. [6-9] Once reliable diabatic bands are obtained it is rather straightforward to mix them if the number of independent bands are few as in the case of the first back-bending. Note, however, that it is highly non-trivial how to construct reliable diabatic bands in the mean-field approximation, because it is based on the variational principle and the mixing at the same rotational frequency is inevitable for states with the same quantum numbers (in the intrinsic frame). On the other hand, in the mean-field approximation, the effects of rotational motion on the internal structure of the g-band can be nicely taken into

account as selfconsistent changes of the deformation and the pairing gap parameters. Furthermore, rotation alignment effects of the quasiparticle angular momenta are described in a simple and clear way. Therefore, it is desired to develop a method to describe the rotational band diabatically within the mean-field approximation.

In this paper, we present a powerful method to obtain reliable diabatic rotational bands by making use of the selfconsistent collective coordinate (SCC) method. [10] The method is applied to the g- and s-bands and the results for nuclei in the rare-earth region are compared systematically with experimental data. In order to reproduce the rotational spectra, the choice of residual interaction is essential. We use the pairing-plus-quadrupole force type interaction. [11] However, it has been well-known that the moment of inertia is generally underestimated by about 20–30% if only the monopole-pairing interaction is included. [12] Therefore, we exploit the monopole and quadrupole type interaction in the pairing channel, and investigate the best form of the quadrupole-pairing part. This is done in §2. After fixing the suitable residual interaction, we present in §3 a formulation to describe the diabatic rotational bands and results of its application to nuclei in the rare-earth region. In practical applications it often happens that a complete set of the diabatic quasiparticle basis is necessary; for example, in order to go beyond the mean-field approximation. For this purpose, we present in §4 a practical method to construct the diabatic quasiparticle basis satisfying the orthonormality condition. Concluding remarks are given in §5.

§2. Quadrupole-pairing interaction suitable for deformed nuclei

In this section we try to fix the form of residual interactions, which is suitable to describe the properties of deformed rotating nuclei. It might be desirable to use effective interactions like Skyrme-type interactions, [13] but that is out of scope of the present investigation. We assume the separable-type schematic interactions instead, and try to fix their forms and strengths by a global fit of the basic properties; the even-odd mass difference and the moment of inertia.

2.1. *Residual interactions*

The residual interaction we use in the present work is of the following form:

$$V = -G_0 P_{00}^\dagger P_{00} - G_2 \sum_K P_{2K}^\dagger P_{2K} - \frac{1}{2} \sum_K \kappa_{2K} Q_{2K}^\dagger Q_{2K}, \qquad (2\cdot1)$$

where the first and the second terms are the monopole- and quadrupole-pairing interactions, while the third term is the quadrupole particle-hole type interaction. The pairing interactions are set up for neutrons and protons separately (the $T = 1$ and $T_z = \pm 1$ pairing) as usual, although it is not stated explicitly, and only the isoscalar part is considered for the quadrupole interaction. The quadrupole-pairing interaction is included for the purpose of better description of moment of inertia: It has been known for many years [12] that the cranking moments of inertia evaluated taking account of only the monopole-pairing interaction underestimate the experimental ones systematically in the rare-earth region, as long as the monopole-pairing strength is fixed to reproduce the even-odd mass differences. It should be

mentioned that the treatment of residual interactions in the pairing and the particle-hole channels are different: In the pairing channel the mean-field (pairing gap) is determined by the interaction selfconsistently, while that in the particle-hole channel (spatial deformation) is obtained by the Nilsson-Strutinsky method [14), 15)] and the interaction in this channel only describes the dynamical effects, i.e., the fluctuations around the equilibrium mean-field.

The basic quantity for deformed nuclei is the equilibrium deformation. For the present investigation, where the properties of deformed rotational nuclei are systematically studied, the Nilsson-Strutinsky method is most suitable to determine the equilibrium deformations, because there is no adjustable parameters. As emphasized by Kishimoto and Sakamoto, [17)] the particle-hole type quadrupole interaction for deformed nuclei should be of the double-stretched form: [17) - 19)]

$$Q_{2K} = \sum_{ij} q_{2K}(ij)\, c_i^\dagger c_j, \quad q_{2K}(ij) = \langle i|(r^2 Y_{2K})''|j\rangle, \tag{2.2}$$

where $c_i^\dagger$ is the nucleon creation operator in the Nilsson state $|i\rangle$. $(O)''$ means that the Cartesian coordinate in the operator O should be replaced such as $x_k \to x_k'' \equiv (\omega_k/\omega_0)x_k$ $(k = x, y, z)$, where ω_x, ω_y and ω_z are frequencies of the anisotropic oscillator potential and related to the deformation parameter (ϵ_2, γ); [15), 16)] here $\hbar\omega_0 \equiv \hbar(\omega_x\omega_y\omega_z)^{1/3} = 41.0/A^{1/3}$ MeV (A is the mass number). Then the selfconsistent condition gives, at the equilibrium shape, a vanishing mean value for the double-stretched quadrupole operator, $\langle Q_{2K}\rangle = 0$, and thus the meaning of residual interaction is apparent for the double-stretched interaction. Moreover, the force strengths are determined at the same time to be the so-called selfconsistent value,

$$\kappa_{2K} = \kappa_2^{\rm self} = \frac{4\pi}{3} \frac{\hbar\omega_0}{AR_0^2 b_0^2}, \quad \text{with} \quad b_0^2 = \frac{\hbar}{M\omega_0}, \quad R_0 = 1.2A^{1/3}\ \text{fm}, \tag{2.3}$$

by which the β- and γ-vibrational excitations are correctly described. Strictly speaking, the vanishing mean value of Q_{2K} holds only for the harmonic oscillator model. It is, however, easily confirmed that the mean value vanishes in a good approximation in the case of Nilsson potential. In fact the calculated ratio of mean values of the double-stretched and non-stretched quadrupole operator is typically within few percent, if the deformation parameter determined by the Strutinsky procedure is used.

Pairing correlations are important for the nuclear structure problem as well. The operators entering in the pairing type residual interactions are of the form

$$P_{00}^\dagger = \sum_{i>0} c_i^\dagger c_{\tilde i}^\dagger, \quad P_{2K}^\dagger = \sum_{ij>0} p_{2K}(ij)\, c_i^\dagger c_{\tilde j}^\dagger, \tag{2.4}$$

where $\tilde j$ denotes the time-reversal conjugate of the Nilsson state j. In contrast to the residual interactions in the particle-hole channel, there is no such selfconsitency condition known in the pairing channel. Therefore, we use the Hartree-Bogoliubov (HB) procedure (exchange terms are neglected) for the pairing interactions, only the monopole part of which leads to the ordinary BCS treatment. Note that the

generalized Bogoliubov transformation is necessary in order to treat the quadrupole-pairing interaction, since the pairing potential becomes state-dependent and contains non-diagonal elements:

$$\Delta_{ij} = \Delta_{00}\,\delta_{ij} + \sum_K \Delta_{2K}\,p_{2K}(ij), \tag{2.5}$$

where $\Delta_{00} = G_0\,\langle P_{00}\rangle$ and $\Delta_{2K} = G_2\,\langle P_{2K}\rangle$, the expectation values being taken with respect to the resultant HB state.

For the application of these residual interactions we are mainly concerned with deformed nuclei in the rare-earth region, where the neutron and proton numbers are considerably different. In such a case, the "iso-stretching" of multipole operators,[20],[21] $Q_\tau \to (2N_\tau/A)^{2/3}\,Q_\tau$ for $\tau = \nu, \pi$ (N_τ denotes the neutron or proton number and A the mass number), is necessary in accordance with the difference of the oscillator frequencies, $\omega_0^\tau = (2N_\tau/A)^{1/3}\omega_0$, or of the oscillator length, $(b_0^\tau)^2 = (2N_\tau/A)^{-1/3}b_0^2$. We employ this modification for the quadrupole interaction in the particle-hole channel.

2.2. *Treatment of pairing interactions*

As for the quadrupole-pairing part, there are at least three variants that have been used in the literature.[22]-[31] Namely, they are non-stretched, single-stretched and double-stretched quadrupole-pairing interactions, where the pairing form factor in the operator in Eq. (2.4) is defined as

$$p_{2K}(ij) = \langle i|r^2 Y_{2K}|j\rangle,\ \ \langle i|(r^2 Y_{2K})'|j\rangle,\ \ \langle i|(r^2 Y_{2K})''|j\rangle, \tag{2.6}$$

respectively. The single-stretching of operators is analogously performed by the replacement, $x_k \to x_k' \equiv \sqrt{\omega_k/\omega_0}\,x_k$ ($k = x, y, z$). Note that there are matrix elements between the Nilsson states with $\Delta N_{\mathrm{osc}} = \pm 2$ in Eq. (2.6). We have neglected them in the generalized Bogoliubov transformation in accordance with the treatment of the Nilsson potential, which is arranged to have vanishing matrix elements of $\Delta N_{\mathrm{osc}} = \pm 2$.[*]

Being consistent with the Nilsson-Strutinsky method, we use the smoothed pairing gap method[14] in which the monopole-pairing force strength is determined for a given set of single-particle energies by

$$\frac{2}{G_0} = \widetilde{g}_{\mathrm{F}} \log\left(\Lambda/\widetilde{\Delta} + \sqrt{(\Lambda/\widetilde{\Delta})^2 + 1}\right), \tag{2.7}$$

where $\widetilde{g}_{\mathrm{F}}$ is the Strutinsky smoothed single-particle level density at the Fermi surface, Λ is the cutoff energy of pairing model space, for which we use $\Lambda = 1.2\hbar\omega_0$, and $\widetilde{\Delta}$ is the smoothed pairing gap. We introduce a parameter d (MeV) to control the strength of the monopole-pairing force by

$$\widetilde{\Delta} = \frac{d}{\sqrt{A}}, \tag{2.8}$$

---

[*] The hexadecapole deformation leads extra $\Delta N_{\mathrm{osc}} = \pm 2, \pm 4$ coupling terms, but they are neglected in our calculations.

through Eq. (2·7), where the same smoothed pairing gap is used for both neutrons and protons, for simplicity. As for the quadrupole-pairing force strength, we take the following form,

$$G_2 = G_0 \frac{g_2}{R_0^4}, \quad \text{with} \quad R_0 = 1.2 A^{1/3} \text{ fm.} \tag{2·9}$$

Thus, we have two parameters d (MeV) and g_2 for the residual interactions in the pairing channel.

It is worthwhile mentioning that Eq. (2·7) gives the form,

$$G_0^\tau \approx \frac{c}{A} \left(\frac{2N_\tau}{A} \right)^{-1/3}, \quad \text{with} \quad c = \frac{82.0 \, (2/3)^{2/3}}{\log \left(2\Lambda/\widetilde{\Delta} \right)}, \tag{2·10}$$

for the semiclassical treatment of the isotropic harmonic oscillator model,[32), 33)] where $\widetilde{g}_F^\tau \approx (3N_\tau)^{2/3}/(\hbar\omega_0^\tau)$, and it is a good approximation for the Nilsson potential. The quantity $\log \left(2\Lambda/\widetilde{\Delta} \right)$ depends very slowly on the mass number and can be replaced by a representative value for a restricted region of mass table. Taking $\Lambda = \hbar\omega_0$, $d = 13$ and $A = 170$, one obtains $c \approx 23$, which gives the monopole-pairing force strength often used for nuclei in the rare-earth region.

2.3. *Determination of parameters d and g_2*

Now let us determine the form of the quadrupole-pairing interaction. Namely, we would like to answer the question of which form factor in Eq. (2·6) is best, and of what are the values of the parameters, d and g_2, introduced in the previous subsection. For this purpose, we adopt the following criteria; the moments of inertia $\mathcal{J}_0$ of the Harris formula[34)] and the even-odd mass differences (the third order formula[32)]) for even-even nuclei should be simultaneously reproduced as good as possible. Since the neutron contribution is more important for the moment of inertia, we have used the even-odd mass difference for neutrons, $E_\nu^{(\text{e-o})}$. Then it turns out that the proton even-odd mass difference is also reasonably well reproduced as long as the same smoothed pairing gap is used for neutrons and protons. Thus, the two parameters d (MeV) and g_2 are searched so as to minimize the root-mean-square deviations of these quantities divided by their average values,

$$X_{\text{rms}}(x) = \left[\frac{1}{N_{\text{data}}} \sum_{i=1}^{N_{\text{data}}} \left(x_i^{(\text{exp})} - x_i^{(\text{cal})} \right)^2 \right]^{1/2} \Big/ \left[\frac{1}{N_{\text{data}}} \sum_{i=1}^{N_{\text{data}}} x_i^{(\text{exp})} \right] \tag{2·11}$$

for $x = \mathcal{J}_0$ and $E_\nu^{(\text{e-o})}$. Nuclei used in the search are chosen from even-even rare-earth nuclei in Table I, thus $N_{\text{data}} = 83$ (58) for $x = E_\nu^{(\text{e-o})}$ ($\mathcal{J}_0$).

Table I. Nuclei included for the search of the pairing interaction parameters, d and g_2.

	$_{64}$Gd	$_{66}$Dy	$_{68}$Er	$_{70}$Yb	$_{72}$Hf	$_{74}$W
N for $E_\nu^{(\text{e-o})}$	76–100	78–102	80–104	80–108	84–110	86–114
N for $\mathcal{J}_0$	86–96	86–100	86–102	86–108	90–110	92–114

Note that the neutron even-odd mass difference has been calculated in the same way as the experimental data by taking the third order difference of calculated binding energies for even and odd N nuclei, where the blocking HB calculation has been done for odd-mass nuclei. In the Nilsson-Strutinsky method the grid of deformation parameters $-0.08 \leq \epsilon_2 \leq 0.40$ and $-0.08 \leq \epsilon_4 \leq 0.12$ with an interval of 0.04 are used. The ls and ll parameters of the Nilsson potential are taken from Ref. 35). We have assumed the axial symmetry in the calculation of this subsection since only the ground state properties are examined. Experimental binding energies are taken from the 1993 Atomic Mass Evaluation. [36] As for the experimental moment of inertia, the Harris parameters, $\mathcal{J}_0$ and $\mathcal{J}_1$, are calculated from the observed excitation energies of the 2^+ and 4^+ states belonging to the ground state band, experimental data being taken from Ref. 37) and the ENSDF database. [38] If the value of $\mathcal{J}_0$ calculated in this way becomes negative or $\mathcal{J}_1$ greater than 1000 $\hbar^4/\mathrm{MeV}^3$ (this happens for near spherical nuclei), then $\mathcal{J}_0$ is evaluated by only using the 2^+ energy, i.e., by $3/E_{2^+}$. The Thouless-Valtion moment of inertia, [39] which includes the effect of the $K = 1$ component of the residual quadrupole-pairing interaction, is employed as the calculated moment of inertia. Here, again, the matrix elements between states with $\Delta N_{\mathrm{osc}} = \pm 2$ are neglected for simplicity in the same way as in the step of diagonalization of the mean-field Hamiltonian. The contributions of them are rather small for the calculation of moment of inertia, since the $\Delta N_{\mathrm{osc}} = \pm 2$ matrix elements of the angular momentum operator are smaller than the $\Delta N_{\mathrm{osc}} = 0$ ones by a factor $\approx \epsilon_2$ and the energy denominators are larger. We have checked that those effects are less than 5 % for the Thouless-Valatin moment of inertia in well deformed nuclei.

In Fig. 1 we show root-mean-square deviations of the result of calculation for neutron even-odd mass differences and moments of inertia. We have found that the behavior of these two quantities, $X_{\mathrm{rms}}(E_\nu^{(\mathrm{e\text{-}o})})$ and $X_{\mathrm{rms}}(\mathcal{J}_0)$, as functions of g_2 with fixed d are opposite, and so the mean value

$$\overline{X}_{\mathrm{rms}} = \frac{1}{2} \left(X_{\mathrm{rms}}(E_\nu^{(\mathrm{e\text{-}o})}) + X_{\mathrm{rms}}(\mathcal{J}_0) \right) \tag{2.12}$$

become almost constant, especially for the case of the non-stretched quadrupole-pairing. Therefore, we also display the results for the maximum among the two,

$$X_{\mathrm{rms}}^{\mathrm{M}} = \max\left\{ X_{\mathrm{rms}}(E_\nu^{(\mathrm{e\text{-}o})}), X_{\mathrm{rms}}(\mathcal{J}_0) \right\}. \tag{2.13}$$

As is clear from Fig. 1, the best fit is obtained for the double-stretched quadrupole-pairing interaction with $d = 14$ (MeV) and $g_2 = 30$. It should be mentioned that the value of g_2 is close to the one $g_2 = 28\pi/3$ in Ref. 22), where it is derived from the multipole decomposition of the δ-interaction and this argument is equally applicable if the double-stretched coordinate is used in the interaction. It is interesting to notice that if the non-stretched or the single-stretched quadrupole-pairing interaction is used, then one cannot make either $\overline{X}_{\mathrm{rms}}$ or $X_{\mathrm{rms}}^{\mathrm{M}}$ smaller than 0.2. $\overline{X}_{\mathrm{rms}}$ in the non-stretched case is rather flat as a function of g_2 and the minimum occurs at $d = 12$ (MeV) and $g_2 = 0$ (no quadrupole-pairing). $X_{\mathrm{rms}}^{\mathrm{M}}$ in the non-stretched case takes the minimum at small quadrupole-pairing, $d = 12$ (MeV) and $g_2 = 2$. Both $\overline{X}_{\mathrm{rms}}$ and $X_{\mathrm{rms}}^{\mathrm{M}}$ are flat as a function of g_2 also in the single-stretched case,
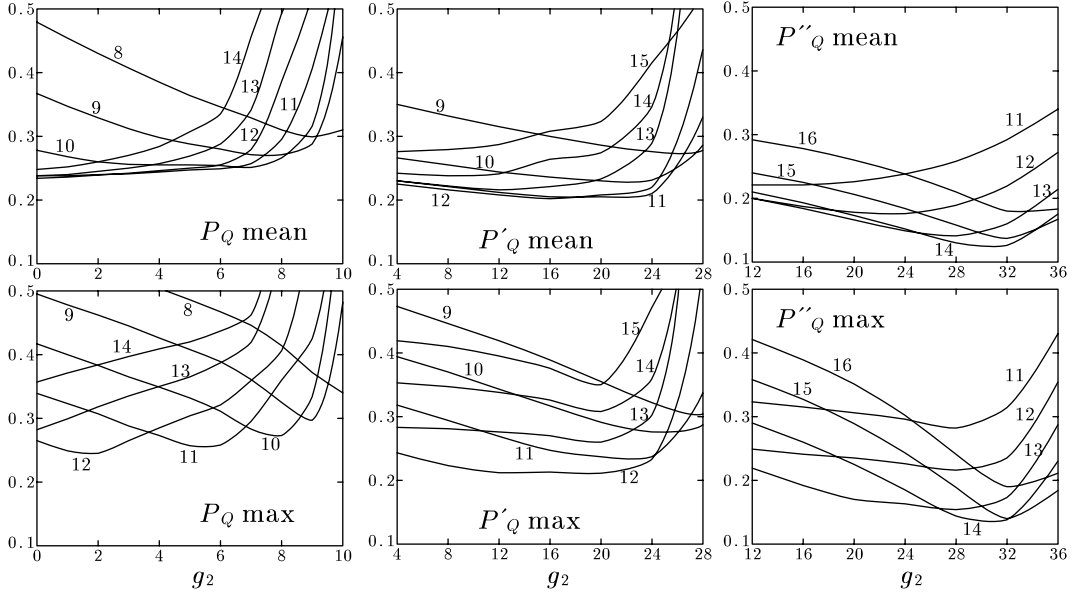
Fig. 1. Root-mean-square deviations of neutron even-odd mass differences and moments of inertia, calculated by using the non-stretched (left), single-stretched (middle), and double-stretched (right) residual quadrupole-pairing interactions. The upper panels show the results for $\overline{X}_{\mathrm{rms}}$ and the lower panels for $X_{\mathrm{rms}}^{\mathrm{M}}$, see Eqs. (2·12) and (2·13). They are calculated as functions of the two parameters d and g_2. Each curve is drawn with a fixed value of d (MeV), which is attached near the curve, as a function of g_2.

and take the minimum at $d = 12$ (MeV) and $g_2 = 16$. In contrast, the double-stretched interaction gives well developed minima for both $\overline{X}_{\mathrm{rms}}$ and $X_{\mathrm{rms}}^{\mathrm{M}}$. These results clearly show that one has to use the double-stretched quadrupole-pairing interaction. It should be mentioned that the importance of the double-stretched quadrupole-pairing interaction has been recently recognized in somewhat different contexts in Refs. 27)–30), and by a similar investigation in Ref. 31).

One may wonder why the non- and single-stretched interactions do not essentially improve the root-mean-square deviations. The quadrupole-pairing interaction affects $E_\nu^{(\text{e-o})}$ and $\mathcal{J}_0$ in two ways: One is the static (mean-field) effect through the change of static pairing potential (2·5), and the other is a dynamical effect (higher order than the mean-field approximation) and typically appears as the Migdal term in the Thouless-Valatin moment of inertia (c.f. Eqs. (3·73) and (3·74)). The former effect can be estimated by the averaged pairing gap,

$$\overline{\Delta} = \sum_i \Delta_{ii} \Big/ \sum_i 1 = \Delta_{00} + \sum_K \Delta_{2K} \sum_i p_{2K}(ii) \Big/ \sum_i 1, \qquad (2·14)$$

where the summation is taken over the Nilsson basis states i included in the pairing model space. Stronger quadrupole-pairing interaction results in larger $\overline{\Delta}$, which leads to the increase of even-odd mass difference on one hand and the reduction of moment of inertia on the other hand. The Migdal term coming from the $K = 1$ component of the quadrupole-pairing interaction makes the moment of inertia larger when the force
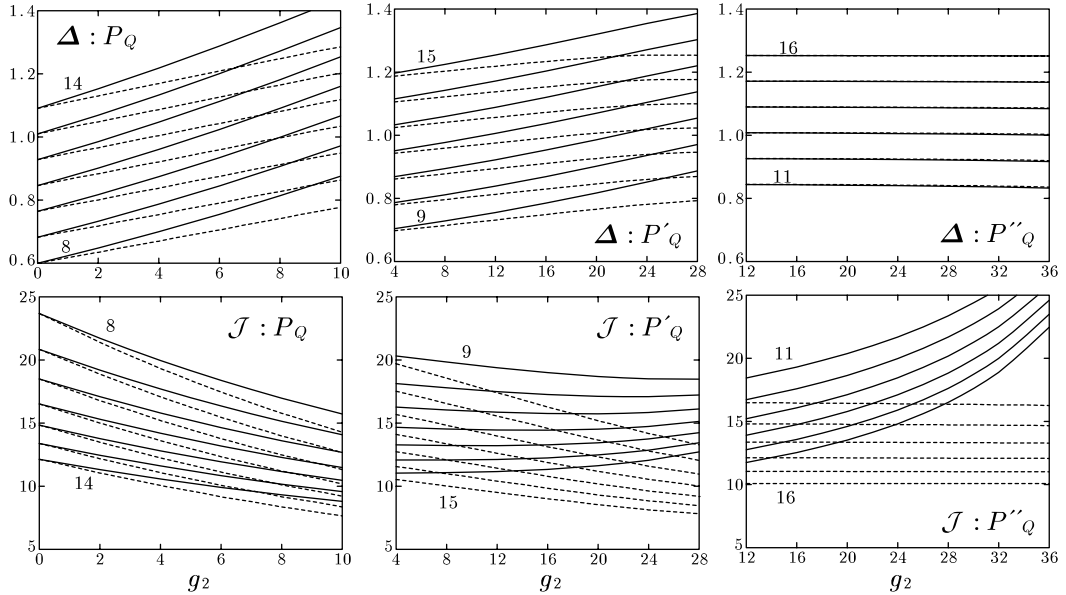
Fig. 2. Pairing gaps (upper panels) and moments of inertia (lower panels), calculated by using the non-stretched (left), single-stretched (middle), and double-stretched (right) residual quadrupole-pairing interactions. Average pairing gaps $\overline{\Delta}$ and monopole-pairing gaps Δ_{00} (MeV), see Eq. (2·14), are displayed by solid and dashed curves, respectively, in the upper panels, while Thouless-Valatin and Belyaev moments of inertia ($\hbar^2$/MeV) (c.f. Eq. (3·73)) are displayed as solid and dashed curves, respectively, in the lower panels. They are calculated as functions of the two parameters d and g_2. Each curve is drawn with a fixed value of d (MeV), which is attached near the curve and changed by step of 1 MeV, as a function of g_2. The calculation has been done for a typical deformed nucleus, ^{168}Yb, with deformation parameters (ϵ_2, ϵ_4) = (0.2570, 0.0162).

strength is increased. Therefore, the moment of inertia either increases or decreases as a function of force strength, depending on which effect is stronger. In Fig. 2, we show the energy gap and the moment of inertia for a typical rare-earth deformed nuclei ^{168}Yb as functions of the two parameters d and g_2 in parallel with Fig. 1. One can see that the average as well as monopole-pairing gaps increases rapidly as a function of the quadrupole-pairing strength if the non-stretched interaction is used. This static effect is so strong that the Thouless-Valatin moment of inertia decreases. In the case of the single-stretched case, similar trend is observed for the pairing gap, though it is not so dramatic as in the case of non-stretched interaction. The static effect almost cancels out the dynamical effect and then the Thouless-Valatin moment of inertia stays almost constant against g_2 in this case. On the other hand, if one uses the double-stretched interaction, the pairing gap stays almost constant as a function of g_2. This is because $\langle P_{2K} \rangle \approx 0$ holds in a very good approximation, which is in parallel with the fact that the quadrupole equilibrium shape satisfies the selfconsistent condition, $\langle Q_{2K} \rangle = 0$, for the double-stretched quadrupole operator. Thus the effect of the double-stretched quadrupole-pairing interaction plays a similar role as the particle-hole interaction channel; it acts as a residual interaction and does not contribute to the static mean-field.

2.4. *Results of calculation*

It has been found in the previous subsection that the double-stretched form of the quadrupole-pairing interaction with parameters $d = 14$ MeV and $g_2 = 30$ gives the best fitting for the even-odd mass differences and the moments of inertia in the rare-earth region. Resulting root-mean-square deviations are $X_{\mathrm{rms}}(E_\nu^{(\mathrm{e\text{-}o})}, \mathcal{J}_0) = (0.115, 0.136)$. If one uses $(d, g_2) = (13, 28)$ or $(12, 20)$, as examples, those quantities become $X_{\mathrm{rms}}(E_\nu^{(\mathrm{e\text{-}o})}, \mathcal{J}_0) = (0.154, 0.127)$ or $(0.235, 0.121)$, respectively. Therefore, making the two quantities smaller is complementary as discussed in §2.3.

We compare the results of calculation with experimental data in Fig. 3 as functions of neutron number. In this calculation the results of Sm ($Z = 62$), Os ($Z = 76$) and Pt ($Z = 78$) isotopes are also included, which are not taken into account in the fitting procedure. As is clear from the figure, both even-odd mass differences and moments of inertia are not well reproduced in heavy Os and Pt isotopes; especially even-odd mass differences are underestimated by about 20%, and moments of inertia overestimated by about up to 50% in Pt nuclei with $N \gtrsim 100$. In these nuclei, low-lying spectra suggest that they are γ-unstable, and therefore correlations in the γ degrees of freedom are expected to play an important role. Except for these nuclei, the overall agreements have been achieved, particularly for deformed nuclei with $N \approx$
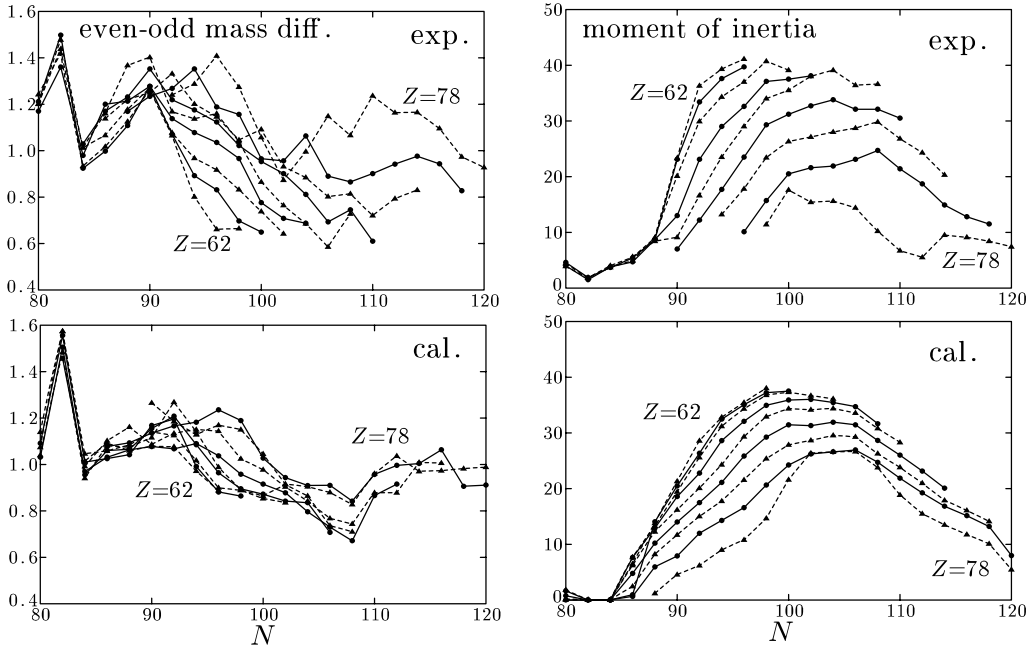
Fig. 3. Comparison of calculated even-odd mass differences (left panels, in MeV) and moments of inertia (right panels, in $\hbar^2/\mathrm{MeV}$) with experimental data for nuclei in the rare-earth region. Experimental data are displayed in the upper panels while the calculated ones in the lower panels. Isotopes with $Z = 62$–78 are connected by solid ($Z = 0 \bmod 4$) or dashed ($Z = 2 \bmod 4$) curves as functions of neutron number N. The double-stretched quadrupole-pairing interaction is used with parameters $d = 14$ MeV and $g_2 = 30$.
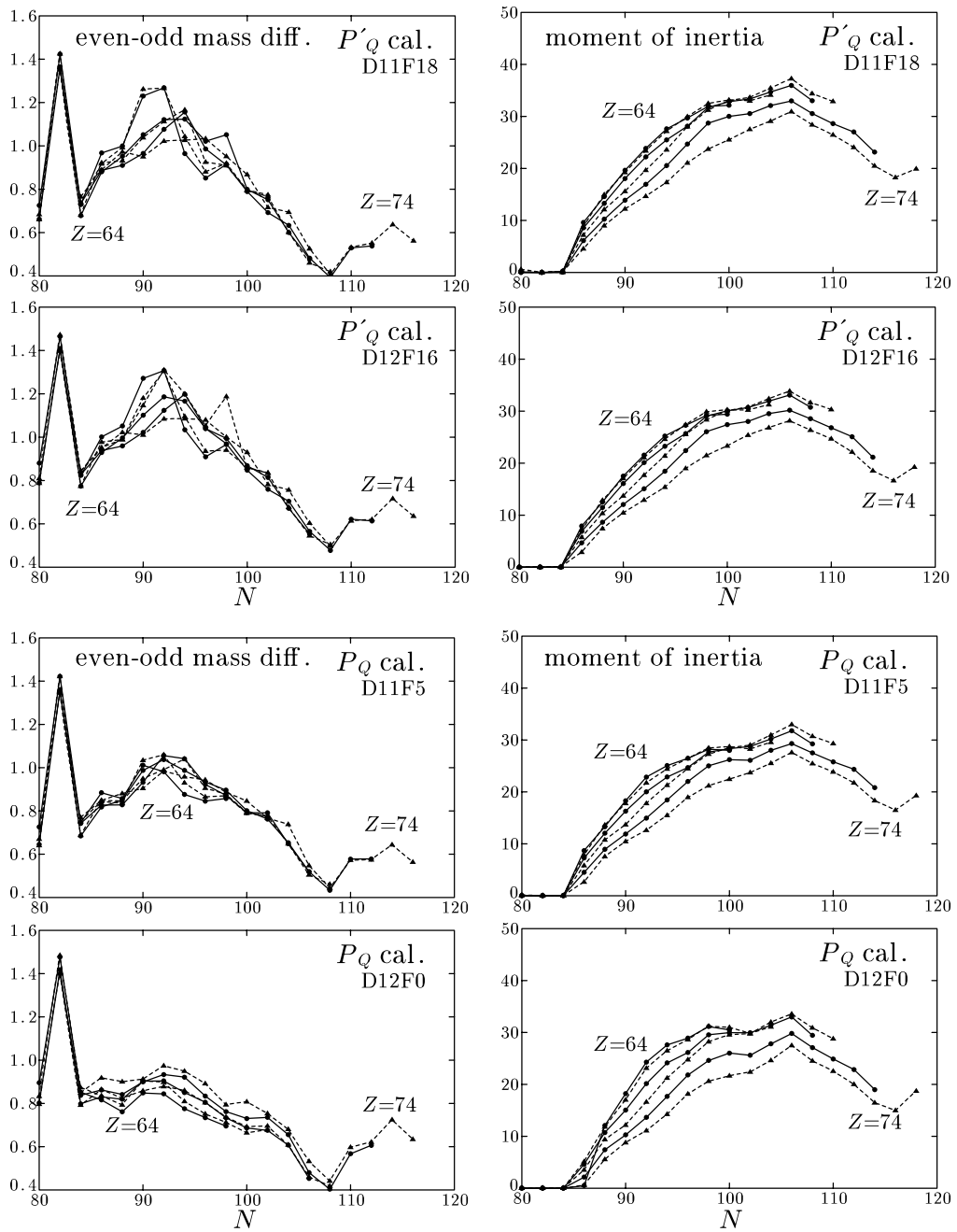
Fig. 4. Even-odd mass differences (left panels) and moments of inertia (right panels) for $Z =$ 64–74 isotopes, calculated by using the single- and non-stretched quadrupole-pairing interactions. The panels from top to bottom show the results of the single-stretched cases with parameters ($d = 11$ MeV, $g_2 = 18$) and ($d = 12$ MeV, $g_2 = 16$), and of the non-stretched cases with parameters ($d = 11$ MeV, $g_2 = 5$) and ($d = 12$ MeV, $g_2 = 0$), respectively.

90–100. It is, however, noted that some features seen in experimental data are not reproduced in the calculation: (1) The maximum at $N = 90$ and the minimum at $N = 106$ or 110 in the even-odd mass difference are shifted to $N = 92$ and $N = 108$, respectively. This is because details of the neutron single-particle level spacings in the present Nilsson potential are slightly inadequate. (2) The proton number dependences of both the even-odd mass difference and the moment of inertia are too weak: curves of both quantities bunch more strongly in the calculation. This trend is clearer in light Z nuclei, $Z \leq 68$, for example, Gd or Dy; the even-odd mass difference in these isotopes decreases more slowly as a function of neutron number in the calculation, which results in the slower increase of the moment of inertia. This problem suggests that some neutron-proton correlations might be necessary.

For comparison's sake, results obtained by using the quadrupole-pairing interactions of the single-stretched and the non-stretched types are displayed in Fig. 4. In the calculation of the single-stretched case, the values of the two parameters, $d = 11$ MeV and $g_2 = 18$, are employed, resulting $X_{\mathrm{rms}}(E_\nu^{(\mathrm{e-o})}, \mathcal{J}_0) = (0.240, 0.170)$, in one case, and the values $d = 12$ MeV and $g_2 = 16$, resulting $X_{\mathrm{rms}}(E_\nu^{(\mathrm{e-o})}, \mathcal{J}_0) = (0.192, 0.214)$, in another case. Comparing with the experimental data in Fig. 3, the decrease of even-odd mass difference with neutron number is too strong, while the increase of moment of inertia near $N \approx 90$ is too slow. In the calculation of non-stretched case, the values of the two parameters, $d = 11$ MeV and $g_2 = 5$ are employed, resulting $X_{\mathrm{rms}}(E_\nu^{(\mathrm{e-o})}, \mathcal{J}_0) = (0.257, 0.237)$, in one case, and the values $d = 12$ MeV and $g_2 = 0$, resulting $X_{\mathrm{rms}}(E_\nu^{(\mathrm{e-o})}, \mathcal{J}_0) = (0.265, 0.204)$, in another case. The average values of the even-odd mass difference are considerably smaller and those of the moment of inertia are 20–30% smaller compared to the experimental data. Note that the last case ($d = 12$ MeV and $g_2 = 0$) is nothing but the calculation without the quadrupole-pairing interaction. The trend of weak proton number dependence does not change for all three forms of the quadrupole-pairing interaction.

The merit of the Nilsson-Strutinsky method is that a global calculation is possible once the mean-field potential is given. We have then performed the calculation for nuclei in the actinide region with the same pairing interaction and parameters as in the rare-earth region, i.e., the double-stretched quadrupole-pairing with $d = 14$ MeV and $g_2 = 30$. The result is shown in Fig. 5. Nuclei in the light actinide region are spherical or weakly deformed with possible octupole deformations. The experimental moments of inertia suggest that nucleus in this region begins to deform at $N \approx 134$, and gradually increases the deformation until a rather stable deformation is established at $N \gtrsim 140$. In the nuclei with $Z = 88$ and 90, the neutron number at which the deformation starts to grow is too large in the calculation, and the even-odd mass differences take considerably different behaviour from the experimental data. This disagreement possibly suggests the importance of octupole correlations. Except for these deficiencies, both even-odd mass differences and moments of inertia in heavy well-deformed nuclei are very well reproduced in the calculation. It should be emphasized that the parameters fixed in §2.3 for the rare-earth region are equally well applicable for the actinide region.
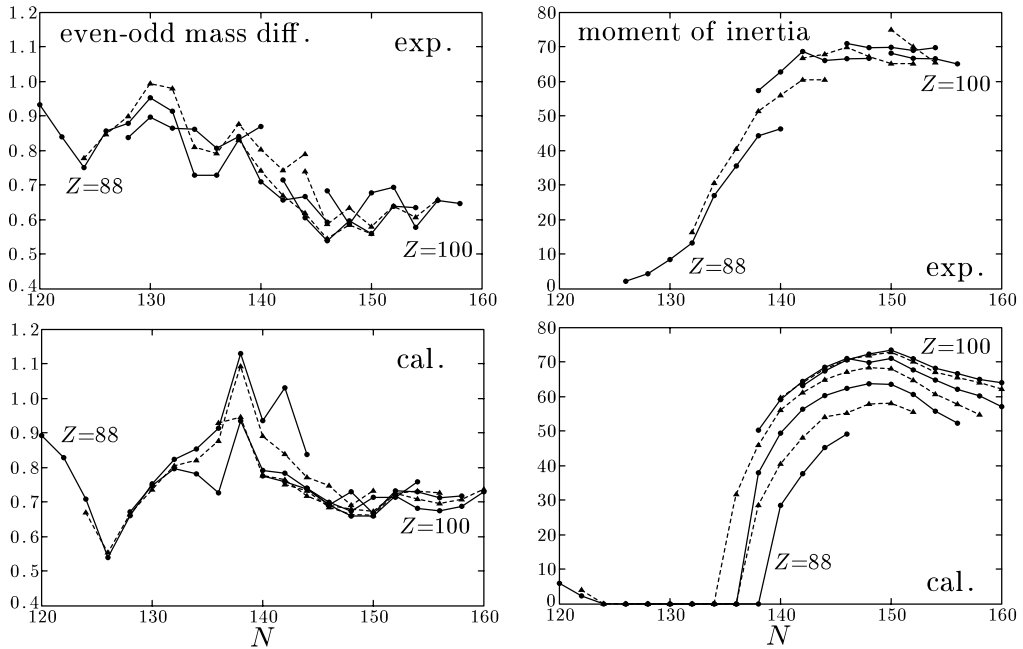
Fig. 5. Same as Fig. 3, but for nuclei in the actinide region. Isotopes with $Z = 88$–100 are connected by solid ($Z = 0$ mod 4) or dashed ($Z = 2$ mod 4) curves as functions of neutron number N.

§3. SCC method for constructing diabatic rotational bands

The SCC method [10] is a theory aiming at a microscopic description of large amplitude collective motions in nuclei. The rotational motion is one of the most typical large amplitude motions. Therefore it is natural to apply the SCC method to the nuclear collective rotation. In Ref. 40), this line has been put into practice for the first time in order to obtain the diabatic rotational bands, where the interband interaction associated with the quasiparticle alignments is eliminated. It has also been shown that the equation of path in the SCC method leads to the selfconsistent cranking model in the case of rotational motion. Corresponding to the uniform rotation about one of the principal axes of nuclear deformation, the one-dimensional rotation has been considered as in the usual cranking model. We keep this basic feature in the present work.

More complete formulation and its application to the ground state rotational bands (g-bands) in realistic nuclei have been done in Ref. 41), followed by further applications to the Stockholm bands (s-bands) [42] and improved calculations with including the quadrupole-pairing interaction. [43] In these works the basic equations of the SCC method have been solved in terms of the angular momentum expansion (I-expansion). Thus, the A and B parameters in the rotational energy expansion, $E(I) = A\,I(I+1) + B\,[I(I+1)]^2$, have been studied in detail. It is, however, well known that applicability of the I-expansion is limited to relatively low-spin regions. This limitation is especially severe in the case of the s-bands: One has to take the

starting angular momentum I_0 ($\approx 10\hbar$ [42]) and the expansion in terms of $(I - I_0)$ is not very stable. Because of this problem comparisons with experimental data have not been possible for the s-bands. [42] In the present study, the rotational frequency expansion is utilized instead, according to the original work. [40] Then the diabatic cranking model is naturally derived. Thus, after obtaining the diabatic quasiparticle states, we construct the s-band as the two-quasiparticle aligned band on the vacuum g-band at given rotation frequencies. This is precisely the method of the cranked shell model, [44] which has been established as a powerful method to understand the high-spin rotational bands accompanying quasiparticle excitations.

Another important difference of the present work from Refs. 41)‐43) is that the expansion method based on the normal modes of the random phase approximation (RPA) is used for solving the basic equations in these references. The method is very convenient to investigate detailed contents of the rotation-vibration couplings, e.g. how each normal mode contributes to the rotational A and/or B parameters, as has been discussed in Refs. 41) and 42). On the other hand, we are aiming at a systematic study of rotational spectra of both g- and s-bands in the rare-earth region. Then the use of the RPA response-function matrix is more efficient for such a purpose, because it is not necessary to solve the RPA equation for all the normal modes explicitly.

It has to be mentioned that the problem of nucleon number conservation, i.e., the pairing rotation, can be treated similarly. [45] Actually, if the SCC method is applied to the spatial rotational motion, the mean value of the nucleon number changes as the angular momentum or the rotational frequency increases. A proper treatment of the pairing rotations is required, i.e., the coupling of the spatial and pairing rotations should be included. [45] However, it has been found [41] that the effect of the coupling is negligibly small for the case of the rotational motion in well deformed nuclei. Therefore, we simply neglect the proper treatment of the nucleon number in the following.

Although it is not the purpose of this paper to review applications of the SCC method to other nuclear structure phenomena, we would here like to cite a brief review [46] and some papers, in which low-frequency quadrupole vibrations are analyzed on the basis of the SCC method: anharmonic gamma vibrations, [47]‐[49] shape phase transitions in Sm isotopes, [50]‐[52] anharmonicities of the two-phonon states in Ru and Se isotopes, [53] single-particle levels and configurations in the shape phase transition regions, [54] and a derivation of the Bohr-Mottelson type collective Hamiltonian and its application to transitional Sm isotopes. [55]

3.1. *Basic formulation*

The starting point of the SCC method is the following time-dependent Hartree-Bogoliubov (TDHB) mean-field state

$$|\phi(\theta, I_x)\rangle = W(\theta, I_x)|\phi_0\rangle, \tag{3.1}$$

which is parametrized by the time-dependent collective variables $\theta(t)$ and $I_x(t)$ through the unitary transformation $W(\theta, I_x)$ from the ground (non-rotating) state $|\phi_0\rangle$. In the case of rotational motion, I_x corresponds to the angular momentum

about the rotating axis x, which is a conserved quantity, and θ is the conjugate angle variable around the x-axis. In order to guarantee the rotational invariance, $W(\theta, I_x)$ has to be of the form

$$W(\theta, I_x) = e^{-i\theta J_x} e^{iG(I_x)}, \tag{3.2}$$

where J_x is the angular momentum operator about the x-axis, and $G(I_x)$ is a one-body Hermite operator by which the intrinsic state is specified:

$$|\phi(\theta, I_x)\rangle = e^{-i\theta J_x}|\phi_{\text{intr}}(I_x)\rangle, \quad |\phi_{\text{intr}}(I_x)\rangle = e^{iG(I_x)}|\phi_0\rangle. \tag{3.3}$$

The generators of the unitary transformation $W(\theta, I_x)$ are defined by $(\partial W/\partial q)W^{-1}$ for $q = \theta$ or I_x, and they have, from Eq. (3.2), the form

$$\frac{\partial W}{\partial I_x} W^{-1} = e^{-i\theta J_x} \frac{\partial e^{iG(I_x)}}{\partial I_x} e^{-iG(I_x)} e^{i\theta J_x} \equiv i\Theta(I_x), \tag{3.4}$$

$$i\frac{\partial W}{\partial \theta} W^{-1} = J_x. \tag{3.5}$$

One of the basic equations of the SCC method is the canonical variable conditions, [10] which declare that the introduced collective variables are canonical coordinate and momentum. In the present case they are given as

$$\langle \phi(\theta, I_x)|i\Theta(I_x)|\phi(\theta, I_x)\rangle = 0, \tag{3.6}$$

$$\langle \phi(\theta, I_x)|J_x|\phi(\theta, I_x)\rangle = I_x, \tag{3.7}$$

and from which the weak canonical variable condition is derived:

$$\langle \phi(\theta, I_x)| \, [J_x, i\Theta(I_x)] \, |\phi(\theta, I_x)\rangle = 1. \tag{3.8}$$

The other basic equations, the canonical equations of motion for the collective variables and the equation of path, are derived by the TDHB variational principle,[*]

$$\delta\langle \phi(\theta, I_x)|\left(H - i\frac{d}{dt}\right)|\phi(\theta, I_x)\rangle = 0, \tag{3.9}$$

or by using the generators, Eqs. (3.4) and (3.5),

$$\langle \phi(\theta, I_x)| \, [O, \, H - \dot{\theta}J_x + \dot{I}_x\Theta(I_x) \,] \, |\phi(\theta, I_x)\rangle = 0, \tag{3.10}$$

where O is an arbitrary one-body operator. Taking the generators as O and using the canonical variable conditions, Eqs. (3.6)–(3.8), one obtains the canonical equations of motion:

$$\dot{\theta} = \frac{\partial \mathcal{H}}{\partial I_x} = \omega_{\text{rot}}(I_x), \tag{3.11}$$

$$\dot{I}_x = -\frac{\partial \mathcal{H}}{\partial \theta} = 0, \tag{3.12}$$

---

[*] In this subsection $\hbar = 1$ unit is used.

with

$$\mathcal{H}(I_x) \equiv \langle\phi(\theta, I_x)|H|\phi(\theta, I_x)\rangle = \langle\phi_{\text{intr}}(I_x)|H|\phi_{\text{intr}}(I_x)\rangle, \tag{3.13}$$

where the rotational invariance of the Hamiltonian, $[H, J_x] = 0$, is used. Equation (3·12) is nothing else than the angular momentum conservation, and Eq. (3·11) tells us that the rotational frequency is constant, i.e., the uniform rotation. Making use of these equations of motion, the variational principle reduces to the equation of path

$$\delta\langle\phi_{\text{intr}}(I_x)|\, H - \omega_{\text{rot}}(I_x)J_x\, |\phi_{\text{intr}}(I_x)\rangle = 0, \tag{3.14}$$

namely it leads precisely to the cranking model. The remaining task is to solve this equation to obtain the operator $iG(I_x)$ under the canonical variable conditions, which are now rewritten as

$$\langle\phi_{\text{intr}}(I_x)|C(I_x)|\phi_{\text{intr}}(I_x)\rangle = 0, \quad C(I_x) \equiv \frac{\partial e^{iG(I_x)}}{\partial I_x}e^{-iG(I_x)}, \tag{3.15}$$

$$\langle\phi_{\text{intr}}(I_x)|J_x|\phi_{\text{intr}}(I_x)\rangle = I_x. \tag{3.16}$$

In Ref. 41), Eqs. (3·14)–(3·16) are solved by means of the power series expansion method with respect to I_x, which gives the functional form of the rotational frequency $\omega_{\text{rot}}(I_x)$. It is, however, well known that the convergence radius of the power series expansion with respect to ω_{rot} is much larger, so that the applicability of the method can be enlarged.[33] Thus, the independent variable is changed to be ω_{rot} instead of I_x in the equations above. In the following, we write the rotational frequency as ω in place of ω_{rot} for making the notation simpler. Now the basic equations can be rewritten as

$$\delta\langle\phi_{\text{intr}}(\omega)|H - \omega J_x|\phi_{\text{intr}}(\omega)\rangle = 0, \tag{3.17}$$

$$\langle\phi_{\text{intr}}(\omega)|C(\omega)|\phi_{\text{intr}}(\omega)\rangle = 0, \quad C(\omega) \equiv \frac{\partial e^{iG(\omega)}}{\partial\omega}e^{-iG(\omega)}, \tag{3.18}$$

$$\langle\phi_{\text{intr}}(\omega)|J_x|\phi_{\text{intr}}(\omega)\rangle = I_x(\omega). \tag{3.19}$$

Note that the last equation is not the constraint now, but it just gives the functional form of the angular momentum I_x in terms of ω. The first two equations, Eqs. (3·17) and (3·18), are enough to get $iG(\omega)$, which makes the calculation simpler. The equation of motion is transformed to the canonical relation

$$\frac{\partial\mathcal{H}'}{\partial\omega} = -I_x(\omega), \tag{3.20}$$

with the total Routhian in the rotating frame

$$\mathcal{H}'(\omega) \equiv \langle\phi_{\text{intr}}(\omega)|H - \omega J_x|\phi_{\text{intr}}(\omega)\rangle. \tag{3.21}$$

In order to show this, we note the following identity,

$$\frac{\partial\langle\phi_{\text{intr}}(\omega)|O|\phi_{\text{intr}}(\omega)\rangle}{\partial\omega} = \langle\phi_{\text{intr}}(\omega)|\,[O,\, C(\omega)]\,|\phi_{\text{intr}}(\omega)\rangle, \tag{3.22}$$

for an arbitrary ω-independent one-body operator O. Then,

$$\frac{\partial \mathcal{H}'}{\partial \omega} = \langle \phi_{\text{intr}}(\omega)| \, [H - \omega J_x, \, C(\omega)] \, |\phi_{\text{intr}}(\omega)\rangle - \langle \phi_{\text{intr}}(\omega)|J_x|\phi_{\text{intr}}(\omega)\rangle, \qquad (3\cdot23)$$

which lead to Eq. (3·20) because the first term on the right-hand side vanishes due to the variational equation (3·17).

The one-body operator $iG(\omega)$ generates the unitary transformation from the non-rotating (ground) state $|\phi_0\rangle$, see Eq. (3·3), and it is composed of the $a_i^\dagger a_j^\dagger$ and $a_j a_i$ terms, where $a_i^\dagger$ and a_i are the creation and annihilation operators of the quasiparticle state i with respect to the ground state $|\phi_0\rangle$ as a vacuum state. The solution of the basic equations is obtained in the form of power series expansion

$$iG(\omega) = \sum_{n=1}^{\infty} iG^{(n)}(\omega), \qquad (3\cdot24)$$

with

$$iG^{(n)}(\omega) = \omega^n \left\{ \sum_{i<j} g^{(n)}(ij) \, a_i^\dagger a_j^\dagger - \text{h.c.} \right\}. \qquad (3\cdot25)$$

It is convenient to introduce a notation for the transformed operator, which is also expanded in power series of ω,

$$\overset{\circ}{O}(\omega) \equiv e^{-iG(\omega)} \, O \, e^{iG(\omega)} \equiv \sum_{n=0}^{\infty} \overset{\circ}{O}^{(n)}(\omega), \qquad (3\cdot26)$$

for which the following formula are useful;

$$e^{-iG}Oe^{iG} = \sum_{n=0}^{\infty} \frac{1}{n!} \underbrace{[\cdots[}_{n \text{ times}} O, \, iG] \cdots iG], \qquad (3\cdot27)$$

and

$$\overset{\circ}{C}(\omega) = e^{-iG}\frac{\partial e^{iG}}{\partial \omega} = \sum_{n=0}^{\infty} \frac{1}{(n+1)!} \underbrace{\left[\cdots \left[\frac{\partial iG}{\partial \omega}, \, iG \right] \cdots iG \right]}_{n \text{ times}}. \qquad (3\cdot28)$$

Then the basic equations for solving $iG(\omega)$ in the n-th order in ω are

$$\langle \phi_0| \, [a_j a_i, \, \overset{\circ}{H}^{(n)} - \omega \overset{\circ}{J}_x^{(n-1)}] \, |\phi_0\rangle = 0, \qquad (3\cdot29)$$

$$\langle \phi_0|\overset{\circ}{C}^{(n)}|\phi_0\rangle = 0, \qquad (3\cdot30)$$

and the canonical relation is

$$\frac{\partial \mathcal{H}'^{(n+1)}}{\partial \omega} = -I_x^{(n)}, \quad \text{or} \quad (n+1)\mathcal{H}'^{(n+1)} = -\omega I_x^{(n)}, \qquad (3\cdot31)$$

where the total Routhian and the expectation value of the angular momentum are also expanded in power series,

$$\mathcal{H}'(\omega) = \sum_{n=0}^{\infty} \mathcal{H}'^{(n)}, \quad I_x(\omega) = \sum_{n=1}^{\infty} I_x^{(n)}. \qquad (3\cdot32)$$

The lowest order solution is easily determined: The $n = 0$ and 1 parts of Eq. (3·30) are satisfied trivially, while the $n = 1$ part of Eq. (3·29) is written as

$$\langle \phi_0 | \, [a_j a_i, \, [H, \, iG^{(1)}]] \, | \phi_0 \rangle = \omega \langle \phi_0 | \, [a_j a_i, \, J_x] \, | \phi_0 \rangle, \qquad (3·33)$$

or

$$[H, \, iG^{(1)}]_{\mathrm{RPA}} = \omega J_{x\mathrm{RPA}}, \qquad (3·34)$$

where the subscript $[\ ]_{\mathrm{RPA}}$ means that only the RPA order term is retained; e.g., $J_{x\mathrm{RPA}} = a_i^\dagger a_j^\dagger$ and $a_j a_i$ parts of J_x. This is the RPA equation,[39] with respect to the ground state $| \phi_0 \rangle$, for the angle operator $i\Theta_{\mathrm{RPA}}$ conjugate to the symmetry conserving mode $J_{x\mathrm{RPA}}$, and we obtain

$$iG^{(1)} = \omega \mathcal{J}_0 \, i\Theta_{\mathrm{RPA}}, \quad I_x^{(1)} = \omega \mathcal{J}_0, \qquad (3·35)$$

where $\mathcal{J}_0$ is the Thouless-Valatin moment of inertia. Note that the general solution of Eq. (3·33) contains a term $i\omega c_J J_{x\mathrm{RPA}}$ with c_J being an arbitrary real constant. We have chosen $c_J = 0$ as a physical boundary condition, because J_x operator generates the transformation from the intrinsic to the laboratory frame and should be eliminated from the unitary transformation generating the intrinsic state, see Eq. (3·3). Once the lowest order solution ($n = 1$) is obtained, higher order solutions ($n \geq 2$) can be uniquely determined by rewriting Eqs. (3·29) and (3·30) in the following forms;

$$\langle \phi_0 | \, [a_j a_i, \, [H, \, iG^{(n)}]] \, | \phi_0 \rangle = \langle \phi_0 | \, [a_j a_i, B^{(n)}] \, | \phi_0 \rangle, \qquad (3·36)$$

$$\langle \phi_0 | \, [iG^{(n)}, \, i\Theta_{\mathrm{RPA}}] \, | \phi_0 \rangle = \frac{1}{(n-1)\mathcal{J}_0} \langle \phi_0 | D^{(n)} | \phi_0 \rangle, \qquad (3·37)$$

with

$$B^{(n)} \equiv \overset{\circ}{H}{}^{(n)} - [H, \, iG^{(n)}] - \omega \overset{\circ}{J}_x{}^{(n-1)}, \qquad (3·38)$$

$$D^{(n)} \equiv \overset{\circ}{C}{}^{(n)} - \left[\frac{\partial iG^{(n)}}{\partial \omega}, \, iG^{(1)} \right] - \left[\frac{\partial iG^{(1)}}{\partial \omega}, \, iG^{(n)} \right]. \qquad (3·39)$$

Here $B^{(n)}$ and $D^{(n)}$ only contain $iG^{(m)}$ with $m \leq n - 1$, and $\partial iG^{(n)}/\partial \omega = n \, iG^{(n)}/\omega$ and Eq. (3·35) are used. Equation (3·36) has the same structure as Eq. (3·33) or (3·34) and is an inhomogeneous linear equation for the amplitude $g^{(n)}(ij)$, where the inhomogeneous term is determined by the lower order solutions (see §3.3 for details).

As in the case of the first order equation, if $iG^{(n)}$ is expanded in terms of the complete set of the RPA eigenmodes which is composed of the non-zero normal modes and the zero mode ($J_{x\mathrm{RPA}}, \, i\Theta_{\mathrm{RPA}}$), the general solution of $iG^{(n)}$ contains the term proportional to $J_{x\mathrm{RPA}}$, and it is determined by Eq. (3·37). Once the boundary condition for $iG^{(1)}$ is chosen as above, however, the term proportional to $J_{x\mathrm{RPA}}$ should vanish. In order to show this, one has to note that matrix elements of the Hamiltonian and of the angular momentum can be chosen to be real with respect to the quasiparticle basis ($a_i^\dagger, \, a_i$) in a suitable phase convention, e.g., that of Ref. 32).

Then the matrix elements of the RPA normal mode operators and the angle operator $i\Theta_{\mathrm{RPA}}$ are also real, and so are the matrix elements of $iG^{(1)}$. If $iG^{(n)}$ is expanded in terms of the RPA eigenmodes, the imaginary part of its matrix elements arises only from the term proportional to $J_{x\mathrm{RPA}}$ because $iG^{(n)}$ is anti-Hermite while $J_{x\mathrm{RPA}}$ is Hermite. If we assume that $iG^{(m)}$ with $m \leq n-1$ has no $J_{x\mathrm{RPA}}$ term so that its matrix elements are real, then the right-hand side of Eq. (3·37) vanishes, because $D^{(n)}$ is an anti-Hermite operator with real matrix elements composed of $iG^{(m)}$ with $m \leq n-1$. Therefore, $iG^{(n)}$ neither contains the $J_{x\mathrm{RPA}}$ term. Thus, the fact that the operator iG has no $J_{x\mathrm{RPA}}$ term is proved by induction. The situation is exactly the same for the case of gauge rotation; the N_{RPA} term (N is either the neutron or proton number operator) also does not appear in iG. The method to solve the above basic equations for our case of the separable interaction (2·1) will be discussed in detail in §3.3.

3.2.   *Diabatic quasiparticle states in the rotating frame*

In the previous subsection the rotational motion based on the ground state $|\phi_0\rangle$ is considered in terms of the SCC method. The same treatment can be done for one-quasiparticle states. The one-quasiparticle state is written in the most general form as

$$|\phi_{1\text{-q.p.}}(\omega)\rangle = e^{iG(\omega)} \sum_i f_i(\omega) a_i^\dagger |\phi_0\rangle, \qquad (3\cdot40)$$

where $iG(\omega)$ as well as the amplitudes $f_i(\omega)$ are determined by the TDHB variational principle. Generally $iG(\omega)$ for the one-quasiparticle state is not the same as that of the ground state rotational band because of the blocking effect. However, we neglect this effect and use the same $iG(\omega)$ in the present work following the idea of the independent quasiparticle motion in the rotating frame.[44] Then by taking the variation

$$\delta \left[\frac{\langle \phi_{1\text{-q.p.}}(\omega)|H - \omega J_x|\phi_{1\text{-q.p.}}(\omega)\rangle}{\langle \phi_{1\text{-q.p.}}(\omega)|\phi_{1\text{-q.p.}}(\omega)\rangle} \right] = 0 \qquad (3\cdot41)$$

with respect to the amplitudes f_i, one obtains an eigenvalue equation,

$$\sum_j \epsilon'_{ij}(\omega) f_{j\mu}(\omega) = f_{i\mu}(\omega) E'_\mu(\omega), \qquad (3\cdot42)$$

with

$$\epsilon'_{ij}(\omega) = \langle \phi_0 | a_i \left(\overset{\circ}{H}(\omega) - \omega \overset{\circ}{J}_x(\omega) \right) a_j^\dagger | \phi_0 \rangle. \qquad (3\cdot43)$$

Namely the excitation energy $E'_\mu(\omega)$ and the amplitudes $f_{i\mu}(\omega)$ of the rotating quasiparticle state μ are obtained by diagonalizing the cranked quasiparticle Hamiltonian defined by

$$\begin{aligned} \overset{\circ}{h}'(\omega) &\equiv \text{one-body part of } [e^{-iG(\omega)}(H - \omega J_x) e^{iG(\omega)}] \\ &= \sum_{ij} \epsilon'_{ij}(\omega) a_i^\dagger a_j, \end{aligned} \qquad (3\cdot44)$$

where, due to the equation of path, Eq. (3·17) or (3·29), $\overset{\circ}{h}{}'(\omega)$ has no $a^\dagger a^\dagger$ and aa terms. Introducing the quasiparticle operator in the rotating frame,

$$\alpha_\mu^\dagger(\omega) = e^{iG(\omega)} \sum_i f_{i\mu}(\omega) a_i^\dagger\, e^{-iG(\omega)}, \tag{3·45}$$

we can see that the one-quasiparticle state (3·40) is written as

$$|\phi_{1\text{-q.p.}}(\omega)\rangle = \alpha_\mu^\dagger(\omega)|\phi_{\text{intr}}(\omega)\rangle, \tag{3·46}$$

and

$$h'(\omega) \equiv \text{one-body part of } (H - \omega J_x)$$
$$= \sum_\mu E_\mu'(\omega)\, \alpha_\mu^\dagger(\omega)\alpha_\mu(\omega). \tag{3·47}$$

Namely, the quasiparticle states in the rotating frame are nothing but those given in the selfconsistent cranking model. Thus, if H contains residual interactions, the effects of change of the mean-field are automatically included in the quasiparticle Routhian operator (3·44) in contrast to the simple cranked shell model where the mean-field parameters are fixed at $\omega = 0$.

It is crucially important to notice that the cutoff of the power series expansion in evaluating Eq. (3·44) results in the diabatic quasiparticle states; i.e., the positive and negative quasiparticle solutions do not interact with each other as functions of the rotational frequency. This surprising fact has been found in Ref. 40) and utilized in subsequent various applications to the problem of high-spin spectroscopy; see e.g., Ref. 56). Thus, we use

$$[\overset{\circ}{h}{}'(\omega)]^{(n \leq n_{\max})} = \sum_{ij} \left(\sum_{n=0}^{n_{\max}} \omega^n \epsilon_{ij}'^{(n)} \right) a_i^\dagger a_j, \tag{3·48}$$

with

$$\epsilon_{ij}'^{(n)} \equiv \langle\phi_0| a_i \left(\overset{\circ}{H}{}^{(n)} - \omega \overset{\circ}{J}_x{}^{(n-1)} \right) a_j^\dagger |\phi_0\rangle / \omega^n, \tag{3·49}$$

as a diabatic quasiparticle Routhian operator. If we take $n_{\max} = 1$ and use the solution (3·35), the first order Routhian operator is explicitly written as

$$[\overset{\circ}{h}{}'(\omega)]^{(n \leq 1)} = h - \omega(J_x - J_{x\text{RPA}}), \tag{3·50}$$

with $h \equiv$ one-body part of H. This Hamiltonian was used to construct a diabatic quasiparticle basis in Ref. 57) to study the g-s band crossing problem. We will show in §3.4 that the inclusion of higher order terms improves the quasiparticle Routhian in comparison with experimental data.

In order to study properties of one-body observables in the rotating frame, for example, the aligned angular momenta of quasiparticles, an arbitrary one-body operator O has to be expressed in terms of the diabatic quasiparticle basis (3·45);

$$O = e^{iG(\omega)} \overset{\circ}{O}(\omega) e^{-iG(\omega)}$$

$$= \langle \phi_{\mathrm{intr}}(\omega)|O|\phi_{\mathrm{intr}}(\omega)\rangle + \sum_{\mu\nu} O_B(\mu\nu;\omega)\,\alpha_\mu^\dagger \alpha_\nu$$

$$+ \sum_{\mu<\nu} \Big(O_{A+}(\mu\nu;\omega)\,\alpha_\mu^\dagger \alpha_\nu^\dagger + O_{A-}(\mu\nu;\omega)\,\alpha_\nu \alpha_\mu \Big), \qquad (3\cdot51)$$

where the matrix elements are written as

$$O_B(\mu\nu;\omega) = \sum_{ij} f_{i\mu}^*(\omega) f_{j\nu}(\omega) \langle \phi_0|\, a_i \Big(\sum_{n=0}^{n_{\max}} \overset{\circ}{O}{}^{(n)}(\omega) \Big) a_j^\dagger \,|\phi_0\rangle, \qquad (3\cdot52)$$

$$O_{A+}(\mu\nu;\omega) = \sum_{ij} f_{i\mu}^*(\omega) f_{j\nu}^*(\omega) \langle \phi_0|\, \Big[a_j a_i,\, \Big(\sum_{n=0}^{n_{\max}} \overset{\circ}{O}{}^{(n)}(\omega) \Big) \Big] \,|\phi_0\rangle, \quad (3\cdot53)$$

$$O_{A-}(\mu\nu;\omega) = \sum_{ij} f_{i\mu}(\omega) f_{j\nu}(\omega) \langle \phi_0|\, \Big[\Big(\sum_{n=0}^{n_{\max}} \overset{\circ}{O}{}^{(n)}(\omega) \Big),\, a_i^\dagger a_j^\dagger \Big] \,|\phi_0\rangle. \quad (3\cdot54)$$

It is clear from this expression that there are two origins of the ω-dependence of the matrix elements; one is the effect of collective rotation, Eq. (3·26), which is treated in the power series expansion in ω and truncated up to $n_{\max}$, and the other comes from the diagonalization of the quasiparticle Routhian operator, Eq. (3·42). Our method to calculate the rotating quasiparticle states can be viewed as a two-step diagonalization; the first step is the unitary transformation $e^{iG(\omega)}$, which eliminates the dangerous terms, the $a^\dagger a^\dagger$ and aa terms, of the Routhian operator $\overset{\circ}{h}{}'$ up to the order $n_{\max}$ in ω leading to the diabatic basis, while the second step diagonalizes its one-body part, the $a^\dagger a$ terms. We shall discuss this two-step transformation in more detail in §4.1. In this way we can cleanly separate the effects of the collective rotational motion on the intrinsic states of the g-band and on the independent quasiparticle motion in the rotating frame. As long as the one-step diagonalization is performed as in the case of the usual cranking model, this separation cannot be achieved and the problem of the unphysical interband mixing is inevitable.

3.3.   *Solution of the equation of path by means of the RPA response function*

Now we present a concrete procedure to solve the equation of path, Eq. (3·17), for our Hamiltonian which is composed of the Nilsson single-particle potential and the multi-component separable interaction (2·1). Let us rewrite our total Hamiltonian in the following form:

$$H = h - \frac{1}{2} \sum_\rho \chi_\rho Q_\rho Q_\rho, \qquad (3\cdot55)$$

where Q_ρ are Hermite operators satisfying

$$Q_\rho = Q_\rho^\dagger, \quad \langle \phi_0|Q_\rho|\phi_0\rangle = 0, \qquad (3\cdot56)$$

and $|\phi_0\rangle$ is the HB ground state of H.[*] The mean-field Hamiltonian h includes the pairing potential and the number constraint term as well as the Nilsson Hamiltonians:

$$h = h_{\rm Nils} - \sum_\tau \sum_{L=0,2} \Delta_{L0\tau}\left(P_{L0}^{\tau\dagger} + P_{L0}^{\tau}\right) - \sum_\tau \lambda_\tau N_\tau, \qquad (3\cdot57)$$

where the nuclei under consideration are assumed to be axially symmetric at $\omega = 0$. Our Hamiltonian has a symmetry with respect to the 180°-rotation around the rotation-axis (x-axis), the quantum number of which is called *signature*, $r = e^{-i\alpha}$; therefore the operators Q_ρ are classified according to the signature quantum numbers, [7] $r = \pm 1$ or $\alpha = 0, 1$. Moreover, we can choose the phase convention [32] in such a way that the matrix elements of the Hamiltonians H and of the angular momentum J_x are real. Then the operators Q_ρ are further classified into two categories, i.e., real and imaginary operators, whose matrix elements are real and pure imaginary, respectively. Since expectation values of the signature $r = -1$ ($\alpha = 1$) operators and of the imaginary operators vanish in the cranking model, operators with signature $r = +1$ and real matrix elements only contribute to the equation of path for the collective rotation. This observation is important. As shown at the end of §3.1, the boundary condition (3·35) for the collective rotation leads that the transformation operator $iG(\omega)$ does not contain the $J_{x\rm RPA}$ part in all orders. Absence of the imaginary operators guarantees that the matrix elements of $iG(\omega)$ are real and Eq. (3·18) is automatically satisfied: We need not use this equation anymore.

Thus, the operators that are to be included in Eq. (3·55) in order to solve the basic equations for $iG(\omega)$ are

$$\{Q_\rho\} = P_{00+}^\tau,\ P_{20+}^{(+)\tau},\ P_{21+}^{(+)\tau},\ P_{22+}^{(+)\tau},\ Q_{20}^{(+)}, Q_{22}^{(+)}, \qquad (3\cdot58)$$

and correspondingly the strengths are

$$\{\chi_\rho\} = G_0^\tau/2,\ G_2^\tau/2,\ G_2^\tau/2,\ G_2^\tau/2,\ \kappa_{20},\ \kappa_{22}, \qquad (3\cdot59)$$

where $\tau = \nu, \pi$ distinguishes the neutron and proton operators. Here the following definitions are used; for the pairing operators,

$$P_{00+} = P_{00}^\dagger + P_{00}, \quad P_{00-} = i\left(P_{00}^\dagger - P_{00}\right),$$
$$P_{2K+}^{(\pm)} = P_{2K}^{(\pm)\dagger} + P_{2K}^{(\pm)}, \quad P_{2K-}^{(\pm)} = i\left(P_{2K}^{(\pm)\dagger} - P_{2K}^{(\pm)}\right), \qquad (3\cdot60)$$

and for signature coupled operators,

$$P_{2K}^{(\pm)} = \frac{1}{\sqrt{1+\delta_{K0}}}\left(:P_{2K}: \pm :P_{2-K}:\right), \quad (K \geq 0)$$
$$Q_{2K}^{(\pm)} = \frac{1}{\sqrt{1+\delta_{K0}}}\left(:Q_{2K}: \pm :Q_{2-K}:\right), \quad (K \geq 0) \qquad (3\cdot61)$$

---

[*] We employ the HB approximation, i.e., do not include the exchange terms of the separable interactions throughout this paper.

where the superscript $(\pm)$ denotes the signature $r = \pm 1$, and $:O: \equiv O - \langle\phi_0|O|\phi_0\rangle$. The quasiparticle creation and annihilation operators should also be classified according to the signature quantum number; $a_i^\dagger$ for $r = +i$ $(\alpha = -1/2)$ and $a_{\bar{i}}^\dagger$ for $r = -i$ $(\alpha = +1/2)$. Then the mean-field Hamiltonian h is expressed in terms of them as

$$h = \sum_{i>0} \left(E_i a_i^\dagger a_i + E_{\bar{i}} a_{\bar{i}}^\dagger a_{\bar{i}} \right), \tag{3.62}$$

where $\sum_{i>0}$ means that only half of the single-particle levels has to be summed corresponding to the signature classification, and the quasiparticle energy at $\omega = 0$ satisfies $E_i = E_{\bar{i}}$. In the same way, Q_ρ are written as

$$Q_\rho = \sum_{ij>0} q_\rho^A(ij)\,(a_i^\dagger a_{\bar{j}}^\dagger + a_{\bar{j}} a_i) + \sum_{ij>0} \left(q_\rho^B(ij)\,a_i^\dagger a_j + \bar{q}_\rho^B(ij)\,a_{\bar{i}}^\dagger a_{\bar{j}} \right), \tag{3.63}$$

where the matrix elements satisfy, at $\omega = 0$, $q_\rho^A(ji) = \pm q_\rho^A(ij)$ and $\bar{q}_\rho^B(ij) = \pm q_\rho^B(ij)$ for Q_ρ with the time-reversal property being $\pm$, if the phase convention of Ref. 32) is used.

Now let us consider the method to solve the equations for $iG(\omega)$. As is already discussed in §3.1, the solution is sought in the form of power series expansion in ω, where the n-th order term $iG^{(n)}$ is written as

$$iG^{(n)} = \omega^n \sum_{ij>0} g^{(n)}(ij)\,(a_i^\dagger a_{\bar{j}}^\dagger - a_{\bar{j}} a_i). \tag{3.64}$$

The n-th order equation (3.36) has the structure of an inhomogeneous linear equation for the amplitudes $g^{(n)}(ij)$,

$$\boldsymbol{K} \begin{pmatrix} g^{(n)} \\ -g^{(n)} \end{pmatrix} = \begin{pmatrix} b^{(n)} \\ -b^{(n)} \end{pmatrix}, \tag{3.65}$$

where $\boldsymbol{K}$ is the RPA energy matrix

$$\boldsymbol{K}(ij;kl) = \begin{pmatrix} A(ij;kl) & B(ij;kl) \\ B^*(ij;kl) & A^*(ij;kl) \end{pmatrix}$$
$$= \begin{pmatrix} \langle\phi_0|\,[a_{\bar{j}}a_i,\,[H,\,a_k^\dagger a_{\bar{l}}^\dagger]\,]\,|\phi_0\rangle & \langle\phi_0|\,[a_{\bar{j}}a_i,\,[H,\,a_{\bar{l}}a_k]\,]\,|\phi_0\rangle \\ \langle\phi_0|\,[a_i^\dagger a_{\bar{j}}^\dagger,\,[H,\,a_k^\dagger a_{\bar{l}}^\dagger]\,]\,|\phi_0\rangle & \langle\phi_0|\,[a_i^\dagger a_{\bar{j}}^\dagger,\,[H,\,a_{\bar{l}}a_k]\,]\,|\phi_0\rangle \end{pmatrix}, \tag{3.66}$$

and the amplitudes $b^{(n)}(ij)$ in the inhomogeneous term are defined by

$$a^\dagger a^\dagger \text{ and } aa\,\text{parts of } B^{(n)} = \omega^n \sum_{ij>0} b^{(n)}(ij)\,(a_i^\dagger a_{\bar{j}}^\dagger + a_{\bar{j}} a_i). \tag{3.67}$$

For the first order $n = 1$, $B^{(1)} = \omega J_{x\mathrm{RPA}}$ and Eq. (3.65) determines the RPA angle operator $i\Theta_{\mathrm{RPA}}$, as discussed in §3.1. Since the part of interaction composed of the imaginary operators, e.g. P_{00-}, P_{20-} and $Q_{21}^{(+)}$, etc., which are related to the symmetry recovering mode $J_{x\mathrm{RPA}}$ (and N_{RPA}) are not included, the RPA matrix $\boldsymbol{K}$

(with signature $r = +1$) has no zero-modes and can be inverted without any problem. However, the dimension of the RPA matrix is not small in realistic situations, and therefore we invoke the merit of separable interactions; by using the response-function matrix for the Q_ρ operators, the inversion of the RPA matrix is reduced to the inversion of the response-function matrix itself whose dimension is much smaller. Inserting the Hamiltonian (3·55) into Eq. (3·36), we obtain

$$(E_i + E_{\bar{j}}) g^{(n)}(ij) - \sum_\rho q_\rho^A(ij) \chi_\rho \mathcal{Q}_\rho^{(n)} = b^{(n)}(ij), \tag{3.68}$$

where

$$\mathcal{Q}_\rho^{(n)} \equiv \langle \phi_0 | [Q_\rho, iG^{(n)}] | \phi_0 \rangle / \omega^n = 2 \sum_{ij>0} q_\rho^A(ij) g^{(n)}(ij). \tag{3.69}$$

Then inhomogeneous linear equations for $\mathcal{Q}_\rho^{(n)}$ can be easily derived as

$$\sum_\sigma (\delta_{\rho\sigma} - R_{\rho\sigma} \chi_\sigma) \mathcal{Q}_\sigma^{(n)} = \mathcal{B}_\rho^{(n)}, \tag{3.70}$$

where

$$R_{\rho\sigma} \equiv 2 \sum_{ij>0} \frac{q_\rho^A(ij) q_\sigma^A(ij)}{E_i + E_{\bar{j}}}, \quad \mathcal{B}_\rho^{(n)} \equiv 2 \sum_{ij>0} \frac{b^{(n)}(ij) q_\rho^A(ij)}{E_i + E_{\bar{j}}}. \tag{3.71}$$

Note that $R_{\rho\sigma}$ are the response functions for operators Q_ρ and Q_σ at zero excitation energy, and nothing but the inverse energy weighted sum rule values (polarizability). Equation (3·70) is much more easily solved than Eq. (3·65) because of the huge reduction of dimension, and we obtain

$$g^{(n)}(ij) = \frac{1}{E_i + E_{\bar{j}}} \left\{ \sum_{\rho\sigma} q_\rho^A(ij) \chi_\rho [(1 - R\chi)^{-1}]_{\rho\sigma} \mathcal{B}_\sigma^{(n)} + b^{(n)}(ij) \right\}, \tag{3.72}$$

where the matrix notations are used for $R = (R_{\rho\sigma})$ and $\chi = (\delta_{\rho\sigma} \chi_\rho)$. Apparently the $n = 1$ solution gives the Thouless-Valtin moment of inertia,

$$\mathcal{J}_0 = \mathcal{J}_{\mathrm{TV}} = \mathcal{J}_{\mathrm{Bely}} + \mathcal{J}_{\mathrm{Mig}}, \quad \mathcal{J}_{\mathrm{Bely}} = 2 \sum_{ij>0} \frac{J_x^A(ij) J_x^A(ij)}{E_i + E_{\bar{j}}}, \tag{3.73}$$

and

$$\mathcal{J}_{\mathrm{Mig}} = \sum_{\rho\sigma} \mathcal{B}_\rho^J \chi_\rho [(1 - R\chi)^{-1}]_{\rho\sigma} \mathcal{B}_\sigma^J, \quad \text{with } \mathcal{B}_\rho^J \equiv 2 \sum_{ij>0} \frac{J_x^A(ij) q_\rho^A(ij)}{E_i + E_{\bar{j}}}, \tag{3.74}$$

where $J_x^A(ij)$ denote the $a^\dagger a^\dagger$ and aa parts of J_x, and the summation (ρ, σ) in Eq. (3·74) runs, at $\omega = 0$, only over $\rho, \sigma = P_{21+}^{(+)\tau}$, namely the $K = 1$ quadrupole-pairing component. Once the perturbative solution of $iG(\omega)$ is obtained, the quasi-particle energy can be calculated by diagonalizing

$$\overset{\circ}{h}'(\omega) = \sum_{ij>0} \left(\epsilon'_{ij}(\omega) a_i^\dagger a_j + \bar{\epsilon}'_{ij}(\omega) a_{\bar{i}}^\dagger a_{\bar{j}} \right), \tag{3.75}$$

and one obtains

$$h'(\omega) = \sum_{\mu>0} \Big(E'_{\mu}(\omega)\, \alpha^{\dagger}_{\mu}(\omega)\alpha_{\mu}(\omega) + E'_{\bar{\mu}}(\omega)\, \alpha^{\dagger}_{\bar{\mu}}(\omega)\alpha_{\bar{\mu}}(\omega) \Big), \qquad (3\cdot76)$$

where the first and second terms in these two equations correspond to the quasiparticle states with signature $r = +i$ ($\alpha = -1/2$) and $r = -i$ ($\alpha = +1/2$), respectively.

At the end of this subsection a few remarks are in order: First, although it is assumed that the starting state $|\phi_0\rangle$ is the ground state at $\omega = 0$, the formulation developed above can be equally well applied also when the finite frequency state at $\omega = \omega_0$ is used as a starting state; i.e., $|\phi_0\rangle$ is determined by $\delta\langle\phi_0|H - \omega_0 J_x|\phi_0\rangle$. In such a case, however, the power series expansion should be performed with respect to $(\omega - \omega_0)$. In fact, the method has been applied in Ref. 42) to describe the s-band by taking the starting state as the lowest two-quasineutron state at finite frequency, although the angular momentum expansion in $(I - I_0)$ is used in it. Second, as can be inferred from the form of the n-th order solution (3·72), the ω-expansion is based on the perturbation with respect to the quantity $\omega/(E_i + E_j)$ (or ω/ω_λ(RPA), if the equation is solved in terms of the RPA eigenmodes). Therefore, it is expected that the convergence of the ω-expansion becomes poor when the average value of the two-quasiparticle energies is reduced: It is the case for the situation of weak pairing, or when one takes the starting state at a finite frequency where highly alignable two-quasiparticle states have considerably smaller excitation energies. The difficulty in the calculation of s-band in Ref. 42) is possibly caused by this problem. Third, as mentioned already, the expectation value of the nucleon number is not conserved along the rotational band. This is because the number operator N_τ does not commute with $iG(\omega)$; namely, there exists a coupling between the spatial and the pairing rotations. In order to achieve rigorous conservation of nucleon numbers, one has to apply the SCC method also to the pairing rotational motion, [45] and combine it to the present formalism. In view of such a more general formulation, the energy in the rotating frame (3·21) calculated in the present method is actually the double Routhian $\mathcal{H}''(\omega, \lambda_\tau = \lambda_{0\tau})$, where $\lambda_{0\tau}$ is the chemical potential fixed to conserve the number at the ground state $\omega = 0$. The ω-dependence of the expectation value of number operator starts from the second order, and its coefficient is very small as will be shown in §3.4. Therefore the effect of number non-conservation along the rotational band is very small; this fact has been checked in Ref. 41) by explicitly including the coupling to the pairing rotation. Finally, this method utilizing the response-function matrix can be similarly applied to the case of the (η^*, η)-expansion of the SCC method for problems of collective vibration. In such a case, a full RPA response matrix (containing both real and imaginary operators) is necessary, and one has to choose one of the RPA eigenenergies, to which the solution is continued in the small amplitude limit, as the excitation energy of the response function.

3.4. *Application to the g- and s- bands in rare-earth nuclei*

We apply the formulation of the SCC method for the collective rotation developed in the previous subsections to even-even deformed nuclei in the rare-earth region. In this calculation, the same Nilsson potential (the ls and ll parameters

from Ref. 35)) is used as in §2, but the hexadecapole deformation is not included. As investigated in Ref. 41), the couplings of collective rotation to the pairing vibrations as well as the collective surface vibrations are important. Therefore the model space composed of three oscillator shells, $N_{\rm osc} = 4$–6 for neutrons and $N_{\rm osc} = 3$–5 for protons, are employed and all the $\Delta N_{\rm osc} = 0, \pm 2$ matrix elements of the quadrupole operators are included in the calculation. In order to describe the properties of deformed nuclei, the deformation parameter is one of the most important factors. The Nilsson-Strutinsky calculation in §2 gives slightly smaller values compared with the experimental data deduced from the measured $B(E2, 2_g^+ \to 0_g^+)$ values. Therefore, we take the experimental values for the ϵ_2 parameter from Ref. 58). There exist, however, some cases where no experimental data are available. Then we take the value obtained by extrapolation from available data according to the scaling of the result of our Nilsson-Strutinsky calculation in §2; for example, $\epsilon_2(^{154}{\rm Dy})$ used is $\epsilon_2(^{154}{\rm Dy})^{\rm cal} \times \epsilon_2(^{156}{\rm Dy})^{\rm exp}/\epsilon_2(^{156}{\rm Dy})^{\rm cal}$. The values adopted in the calculation are listed in Table II.

The residual interaction is of the form given in Eq. (2·1), where the double-stretched form factor is taken according to the discussion in §2. However, we cannot use the same best values obtained in §2 for the strengths of the pairing interactions, since the model space and the treatment of $\Delta N_{\rm osc} = \pm 2$ matrix elements of the

Table II. Summary of the calculated results and comparison with experimental data for nuclei in the rare-earth region, Gd ($Z = 64$) to W ($Z = 74$). The deformation parameters ϵ_2 are taken from Ref. 58); superscript * denotes cases where no data is available and extrapolation based on our calculation in §2 is employed. The Harris parameters $\mathcal{J}_0$ and $\mathcal{J}_1$ are given in units of $\hbar^2/{\rm MeV}$ and $\hbar^4/{\rm MeV}^3$, respectively. The energy gaps Δ are in units of MeV. The third order even-odd mass differences based on the mass table of Ref. 36) are used as experimental pairing gaps.

	N	ϵ_2	$\mathcal{J}_0^{\rm cal}$	$\mathcal{J}_1^{\rm cal}$	$\mathcal{J}_0^{\rm exp}$	$\mathcal{J}_1^{\rm exp}$	$\Delta_\nu^{\rm cal}$	$\Delta_\pi^{\rm cal}$	$\Delta_\nu^{\rm exp}$	$\Delta_\pi^{\rm exp}$
Gd	88	0.164	11.8	308	8.7	—	1.157	1.424	1.108	1.475
	90	0.251	25.6	341	23.1	333	1.270	1.169	1.277	1.133
	92	0.274	31.5	165	33.4	179	1.222	1.097	1.070	0.960
	94	0.282	34.2	118	37.6	111	1.152	1.060	0.892	0.878
	96	0.287	36.0	98	39.7	101	1.073	1.030	0.831	0.871
Dy	88	0.205*	17.4	134	9.0	—	1.187	1.261	1.177	1.472
	90	0.242	24.3	223	20.1	348	1.233	1.138	1.269	1.162
	92	0.261	29.4	178	29.9	184	1.196	1.073	1.077	1.033
	94	0.271	32.7	136	34.3	123	1.128	1.033	0.967	0.978
	96	0.270	34.3	120	37.0	93	1.050	1.013	0.917	0.930
	98	0.275	36.8	117	40.7	98	0.970	0.984	0.832	0.875
Er	88	0.162*	12.2	110	8.7	—	1.105	1.321	1.213	1.396
	90	0.204	18.6	112	13.0	281	1.153	1.188	1.277	1.244
	92	0.245	26.2	154	23.1	196	1.165	1.075	1.138	1.137
	94	0.258	30.3	130	29.0	133	1.105	1.031	1.078	1.091
	96	0.269	33.5	104	32.6	93	1.028	0.995	1.035	0.987
	98	0.272	35.8	108	37.1	105	0.951	0.971	0.966	0.877
	100	0.271	36.4	103	37.5	57	0.919	0.953	0.776	0.857
	102	0.268	35.4	76	38.1	59	0.907	0.938	0.708	0.797

(continued.)

Table II.

	N	ϵ_2	$\mathcal{J}_0^{\mathrm{cal}}$	$\mathcal{J}_1^{\mathrm{cal}}$	$\mathcal{J}_0^{\mathrm{exp}}$	$\mathcal{J}_1^{\mathrm{exp}}$	$\Delta_\nu^{\mathrm{cal}}$	$\Delta_\pi^{\mathrm{cal}}$	$\Delta_\nu^{\mathrm{exp}}$	$\Delta_\pi^{\mathrm{exp}}$
Yb	90	0.172^*	14.4	83	9.1	221	1.124	1.200	1.402	1.253
	92	0.197^*	18.9	119	16.6	204	1.136	1.128	1.168	1.180
	94	0.218^*	23.8	141	23.5	186	1.106	1.070	1.137	1.214
	96	0.245^*	30.1	119	29.0	131	1.024	1.012	1.159	1.111
	98	0.258	33.6	111	34.0	127	0.950	0.981	1.039	0.983
	100	0.262	34.9	108	35.5	83	0.915	0.959	0.865	0.908
	102	0.267	34.5	75	38.0	70	0.889	0.938	0.764	0.840
	104	0.259	33.4	70	39.1	64	0.862	0.926	0.685	0.848
	106	0.250	32.3	93	36.4	55	0.847	0.918	0.585	0.815
Hf	92	0.163^*	14.1	90	12.2	178	1.154	1.105	1.219	1.260
	94	0.181^*	17.8	129	17.7	196	1.148	1.057	1.175	1.285
	96	0.207^*	23.6	134	23.5	191	1.083	1.004	1.123	1.182
	98	0.218^*	27.0	122	29.3	194	1.032	0.976	1.022	1.062
	100	0.227	29.5	116	31.2	131	0.986	0.952	0.953	0.988
	102	0.235	30.6	94	32.7	110	0.935	0.932	0.901	0.915
	104	0.245	31.4	74	33.8	88	0.867	0.915	0.811	0.864
	106	0.227	29.2	99	32.1	65	0.867	0.903	0.693	0.824
	108	0.227	26.9	100	32.1	40	0.898	0.887	0.745	0.856
W	92	0.148^*	12.1	70	9.4	159	1.159	1.006	1.331	1.295
	94	0.161^*	14.6	100	13.2	182	1.169	0.968	1.201	1.142
	96	0.179^*	18.5	122	17.8	216	1.139	0.928	1.146	1.100
	98	0.196^*	22.6	118	23.4	255	1.082	0.899	1.046	1.053
	100	0.206^*	25.4	110	26.3	171	1.032	0.880	1.091	1.023
	102	0.211^*	26.7	99	27.1	134	0.985	0.865	0.931	1.027
	104	0.214^*	27.3	83	28.0	112	0.929	0.850	0.884	1.036
	106	0.212	26.8	95	28.7	86	0.890	0.833	0.802	0.943
	108	0.208	24.5	92	29.8	53	0.903	0.817	0.814	0.849
	110	0.197	21.5	77	26.8	55	0.927	0.805	0.720	0.868
	112	0.191	19.6	76	24.3	67	0.919	0.794	0.793	0.907

quadrupole operators are different. Here we use $G_0^\nu = 20/A$ MeV and $G_0^\pi = 24/A$ MeV for the monopole-pairing interaction, by which monopole-pairing gaps calculated with the use of the above model space roughly reproduce the experimental even-odd mass differences (see Eq. (2·10), and note that an extra difference of the constant "c" in it between neutrons and protons comes from the difference of the model space). As for the double-stretched quadrupole-pairing interaction, we take $g_2^\nu = g_2^\pi = 24$ (see Eq. (2·9)), by which overall agreements are achieved for the moments of inertia. The results are summarized in Table II. Here calculated energy gaps Δ are the monopole-pairing gaps, but they are very similar to the average pairing gaps (2·14) because the double-stretched quadrupole-pairing interaction is used. The isoscalar (double-stretched) quadrupole interaction does not contribute to the Thouless-Valatin moment of inertia $\mathcal{J}_0$, but affects the higher order Harris parameter $\mathcal{J}_1$. We do not fit the strengths for each nucleus, but use $\kappa_{2K} = 1.45\,\kappa_2^{\mathrm{self}}$ (see Eq. (2·3)), which gives, on an average, about 1 MeV for the excitation energy of γ-vibrations in the above model space. We believe that this choice is more suitable to understand the systematic behavior of the result of calculation for nuclei in the

rare-earth region.

One of the most important output quantities is the rotational energy parameters, i.e., the Harris parameters, in our formalism of the ω-expansion. Up to the third order,

$$I_x(\omega) = I + 1/2 = \mathcal{J}_0\,\omega + \mathcal{J}_1\,\omega^3, \qquad (3\cdot77)$$

where $I = 0, 2, 4, \cdots (\hbar)$ for the $K = 0$ ground state bands. [44] The results are summarized in Table II in comparison with experimental data, where the experimental Harris parameters $\mathcal{J}_0$ and $\mathcal{J}_1$ are extracted from the E_{2+} and E_{4+} of the ground state band as follows:

$$\mathcal{J}_0 = \frac{1.5\,\omega_2^3 - 3.5\,\omega_1^3}{\omega_1\omega_2^3 - \omega_1^3\omega_2}, \quad \mathcal{J}_1 = \frac{3.5\,\omega_1 - 1.5\,\omega_2}{\omega_1\omega_2^3 - \omega_1^3\omega_2}, \qquad (3\cdot78)$$

with

$$\omega_1 \equiv E_{2+}/2, \quad \omega_2 \equiv (E_{4+} - E_{2+})/2. \qquad (3\cdot79)$$

If the resultant parameter becomes negative or $\mathcal{J}_1$ gets greater than $1000\ \hbar^4/\mathrm{MeV}^3$, then only $\mathcal{J}_0 = 3/E_{2+}$ parameters are shown in Table II. It is seen from the table that two Harris parameters are nicely reproduced, especially their mass number dependence. In contrast to the $\mathcal{J}_0$ parameter, for which only the residual quadrupole pairing interaction affects, the $\mathcal{J}_1$ parameter are sensitive to all components of the residual interaction. In other words, $\mathcal{J}_1$ reflects the mode-mode couplings of the collective rotation to other elementary excitation modes. Therefore the SCC method with the present residual interaction is considered to be a powerful means to describe the "non-adiabaticity" of nuclear collective rotations. Details of coupling mechanism has been investigated in Ref. 41) by decomposing the contributions from various RPA eigenmodes: It has been found that the couplings to the pairing vibrations and collective surface vibrations are especially important. Although the main contributions come from the collective modes, many RPA eigenmodes have to be included to reach the correct results, see also Ref. 48) for this point. The method of the response-function matrix described in §3.3 is very useful to include all RPA eigenmodes.

Expectation values of other observable quantities are also expanded in power series of ω, and their coefficients give us important information about the response of nucleus against the collective rotation. In Table III we show examples for the nucleon number, monopole-pairing gaps, and mass quadrupole moments:

$$\langle\phi_{\mathrm{intr}}(\omega)|N_\tau|\phi_{\mathrm{intr}}(\omega)\rangle = (N_\tau)_0 + (N_\tau)_1\,\omega^2, \qquad (3\cdot80)$$

$$G_0^\tau\langle\phi_{\mathrm{intr}}(\omega)|P_{00}^\tau|\phi_{\mathrm{intr}}(\omega)\rangle = (\Delta_\tau)_0 + (\Delta_\tau)_1\,\omega^2, \qquad (3\cdot81)$$

$$\langle\phi_{\mathrm{intr}}(\omega)|Q_{2K}^{(+)}|\phi_{\mathrm{intr}}(\omega)\rangle = (Q_{2K}^{(+)})_0 + (Q_{2K}^{(+)})_1\,\omega^2. \quad (K = 0, 2) \qquad (3\cdot82)$$

They are time-reversal even quantities so that the series contains up to the second order within the third order calculations. It should be noticed that these ω-expanded quantities are associated with the properties of the diabatic ground state band, which becomes non-yrast after the g-s band-crossing. As remarked at the end of §3.3, $(N_\tau)_1 \neq 0$ means that the nucleon number is not conserved along the rotational

Table III. Results of the ω-expansion for some observables in Er ($Z = 68$) isotopes. $Q_{2K}^{(+)}$ ($K = 0, 2$) are expectation values of the mass quadrupole operators. The zero-th order values of Δ are shown in Table II, and those of $Q_{22}^{(+)}$ are zero (axially symmetric at $\omega = 0$). Units of each quantity are shown in the second raw.

	N	$(N)_1$ $\hbar^2/\mathrm{MeV}^2$	$(Z)_1$ $\hbar^2/\mathrm{MeV}^2$	$(\Delta_\nu)_1$ $\hbar^2/\mathrm{MeV}$	$(\Delta_\pi)_1$ $\hbar^2/\mathrm{MeV}$	$(Q_{20}^{(+)})_0$ b	$(Q_{20}^{(+)})_1$ b$\,\hbar^2/\mathrm{MeV}^2$	$(Q_{22}^{(+)})_1$ b$\,\hbar^2/\mathrm{MeV}^2$
Er	88	14.5	−4.2	−0.45	−1.81	2.84	6.14	4.58
	90	9.9	−5.4	−0.72	−1.80	3.74	4.67	4.78
	92	7.5	−6.3	−1.58	−1.83	4.71	4.52	5.72
	94	3.6	−4.3	−2.12	−1.50	5.13	2.45	4.43
	96	1.8	−3.1	−2.34	−1.33	5.50	1.31	3.70
	98	1.0	−3.0	−2.83	−1.32	5.71	1.10	2.74
	100	−2.6	−3.4	−2.83	−1.35	5.82	0.86	1.51
	102	−3.5	−3.6	−2.34	−1.38	5.87	0.79	1.08

band. However, its breakdown is rather small; even in the worst case of ^{156}Er in Table III the deviation is about 1.3 at $\omega = 0.3$ MeV, and it is less than 0.1 at $\omega = 0.1$ MeV in ^{166}Er. It is well known that the pairing gap decreases as a function of ω due to the Coriolis anti-pairing effect. It is sometimes phenomenologically parametrized as[59]

$$
\Delta(\omega) = \left\{
\begin{array}{ll}
\Delta_0 \Big(1 - \dfrac{1}{2} \Big(\dfrac{\omega}{\omega_\mathrm{c}} \Big)^2 \Big) & \omega \le \omega_\mathrm{c}, \\[3mm]
\dfrac{1}{2} \Delta_0 \Big(\dfrac{\omega_\mathrm{c}}{\omega} \Big)^2 & \omega > \omega_\mathrm{c}.
\end{array}
\right.
\tag{3.83}
$$

Thus, our ω-expansion method precisely gives the phenomenological parameter $\omega_\mathrm{c} = \sqrt{-\Delta_0/2\Delta_1}$ ($\Delta_1 < 0$) in Eq. (3.83) from microscopic calculations. As shown in Table III, $(\Delta_\nu)_1$ varies considerably along the isotopic chain. The $(Q_{2K})_1$ are related to the shape change at high-spin states, and tell us how soft the nucleus is against rapid rotation. Since nuclei studied in the present work are axially symmetric in their ground states, $(Q_{20})_1$ and $(Q_{22})_1$ serve as measures of softness in the β- and γ-directions, respectively. As seen in Table III the isotopes get harder in both directions as the neutron number increases; especially, the $N = 88$ and $N = 90$ isotopes are known to undergo a shape change from the prolate collective to the oblate non-collective rotation scheme at very high-spin states ("band termination"[60]), while heavier isotopes ($N \ge 96$) are known to be well deformed keeping prolate shape until the highest observed spins. These features have been well known from the calculations of the potential energy surface in the (ϵ_2, γ)-plane, and our results seem to agree with them qualitatively. In order to see the effect of the residual interactions, the result obtained by neglecting them, i.e., that of a simple higher order Coriolis coupling calculations, is shown in Table IV. Comparing it with Tables II and III, it is clear that the residual interactions play an important role in the ω-dependence of observables. For example, $\mathcal{J}_1$ Harris parameter becomes quite small by a factor of about 1/2–1/3 when the residual interactions are switched off. The effect on the second order coefficients of the quadrupole moment is more dramatic and leads to about an order of magnitude reduction in soft nuclei.

Now let us study the quasiparticle Routhians obtained by means of the SCC

method. It is mentioned in §3.2 that the two-step diagonalization with the truncation of the ω-expansion up to $n_{\max}$, c.f. Eq. (3·48), leads to diabatic quasiparticle states in the rotating frame, in which the negative and positive eigenstates do not interact with each other. We show in Figs. 6 and 7 calculated quasiparticle Routhians for neutrons and protons, respectively. It is confirmed that the diabatic quasiparticle states are obtained. As discussed in §3.2, the diagonalization of the quasiparticle Hamiltonian in the SCC method is completely equivalent to that of the selfconsistent cranking model, which is known to lead to the adiabatic levels, if the first step unitary transformation $e^{iG(\omega)}$ is treated non-perturbatively in full order. Then what is the mechanism that realizes the diabatic levels? We believe that the cutoff of the ω-expansion extracts the smoothly varying part of the quasiparticle Hamiltonian; namely, ignoring its higher order terms eliminates the cause of abrupt changes of the microscopic internal structure by quasiparticle alignments. An analogous mechanism

Table IV. Similar to Table III but the residual interactions are artificially switched off in the calculation. The results for the Harris parameters are also included.

	N	$\mathcal{J}_0$ $\hbar^2/\mathrm{MeV}$	$\mathcal{J}_1$ $\hbar^4/\mathrm{MeV}^3$	$(N)_1$ $\hbar^2/\mathrm{MeV}^2$	$(\Delta_\nu)_1$ $\hbar^2/\mathrm{MeV}$	$(Q_{20}^{(+)})_1$ $\mathrm{b}\,\hbar^2/\mathrm{MeV}^2$	$(Q_{22}^{(+)})_1$ $\mathrm{b}\,\hbar^2/\mathrm{MeV}^2$
Er	88	7.5	11	1.00	-0.18	0.32	0.13
	90	12.1	18	1.05	-0.25	0.38	0.15
	92	18.1	28	0.97	-0.39	0.42	0.18
	94	21.4	34	0.60	-0.48	0.33	0.18
	96	24.6	34	0.67	-0.54	0.27	0.18
	98	27.6	51	0.83	-0.67	0.29	0.17
	100	28.3	55	-1.01	-0.67	0.15	0.15
	102	27.5	36	-0.85	-0.57	0.16	0.15
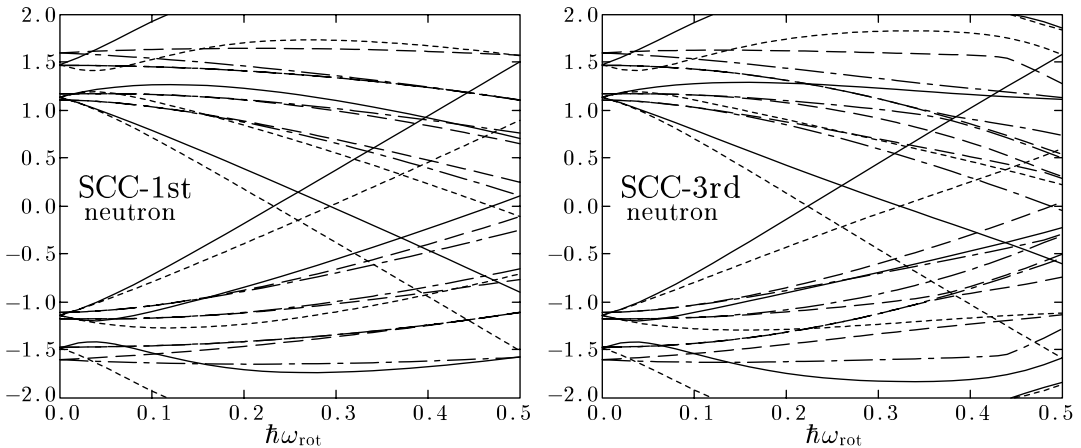
Fig. 6. Neutron quasiparticle Routhians plotted as functions of $\hbar\omega_{\mathrm{rot}}$ (MeV) suitable for ^{162}Er. They are obtained by diagonalizing the SCC quasiparticle Hamiltonian (3·48) up to the first order (left) and third order (right) of the ω-expansion. As in the case of the usual adiabatic quasiparticle energy diagram, the negative energy solutions, $-E'_\mu = E'_{\bar{\mu}}$ and $-E'_{\bar{\nu}} = E'_\nu$, are also drawn. The solid, dotted, dashed, and dash-dotted curves denote Routhians with $(\pi, r) = (+, +i)$, $(+, -i)$, $(-, +i)$, and $(-, -i)$, respectively.

has been known for many years in the Strutinsky smoothing procedure:[14]   The δ-function in the microscopic level density is replaced by the Gaussian smearing function times the sum of the Hermite polynomials (complete set), and the lower order cutoff of the sum (usually 6th order is taken) gives the smoothed level density. It should be noted, however, that the plateau condition guarantees that the order of cutoff does not affect the physical results in the case of the Strutinsky method. We have not yet succeeded in obtaining such a condition in the present case of the cutoff of the ω-expansion in the SCC method for the collective rotation. Therefore we have to decide the $n_{\max}$ value by comparison of the calculated results with experimental data. We mainly take $n_{\max} = 3$ in the following; determination of the optimal choice of $n_{\max}$ remains as a future problem.

In Figs. 6 and 7 the results obtained by truncating up to the first order ($n_{\max} = 1$)
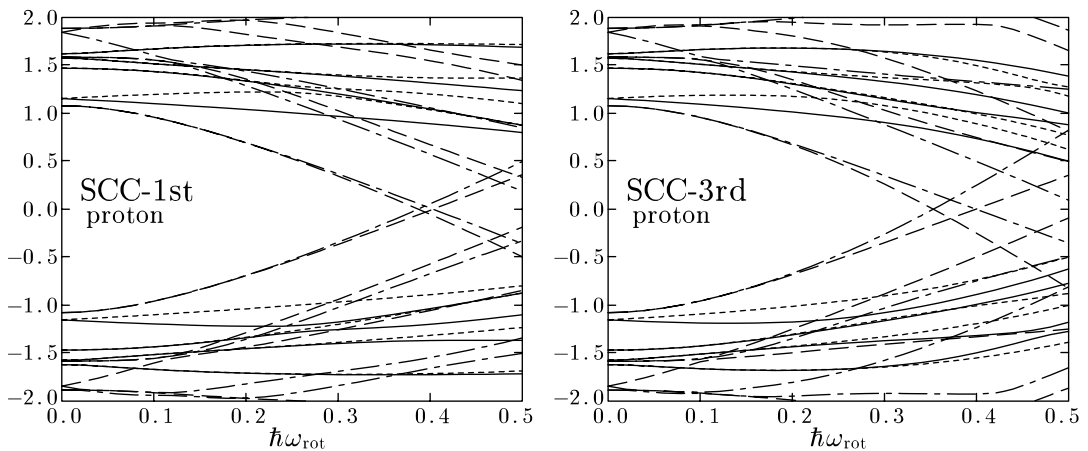
Fig. 7.   Same as Fig. 6 but for proton quasiparticles.
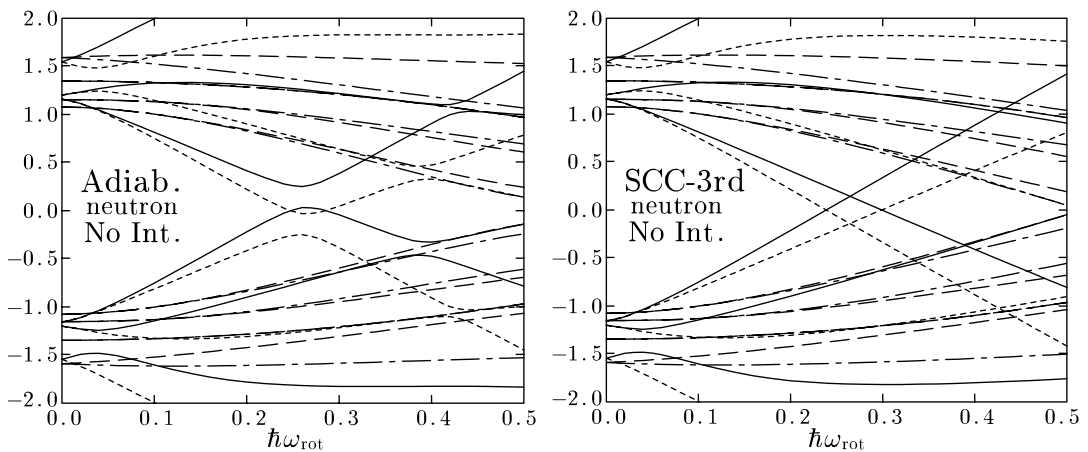
Fig. 8.   Same as Fig. 6 but obtained by the adiabatic cranking (left) and the third order SCC (right) with neglecting the residual interactions.

and the third order ($n_{\max} = 3$) are compared. It is clear that the higher order terms considerably modify the quasiparticle energy diagrams. Especially, the alignments of the lowest pair of quasiparticles are reduced for neutrons (low K states of the $i_{13/2}$-orbitals), while they are increased for protons (medium K states of the $h_{11/2}$-orbitals). Thus, the higher order effects depend strongly on the nature of orbitals. It should be stressed that the effects of the residual interaction, i.e., changes of the mean-field against the collective rotation, are contained in the quasiparticle diagrams presented in these figures. In this sense, they are different from the spectra of the cranked shell model, [44] where the mean-field is fixed at $\omega = 0$. In Fig. 8 are displayed the usual adiabatic quasineutron Routhians and the third order SCC Routhians, in both of which the residual interactions are neglected completely. Again, by comparing Fig. 8 with Fig. 6, it is seen that the effect of residual interactions considerably changes the quasiparticle states. In relation to the choice of $n_{\max}$, we compare in Fig. 9 the Routhians obtained by changing the cutoff order $n_{\max} = 1, 3, 5$. In this figure, the usual non-selfconsistent adiabatic Routhians are also displayed, and for comparison's sake, the residual interactions are completely neglected in all cases. Moreover, the rotational frequency is extended to unrealistically large values in order to see the asymptotic behavior of the Routhian. Comparing the adiabatic Routhians with those of the SCC method, positive and negative energy solutions cross irrespective of the strength of level-repulsion. Although the adiabatic levels
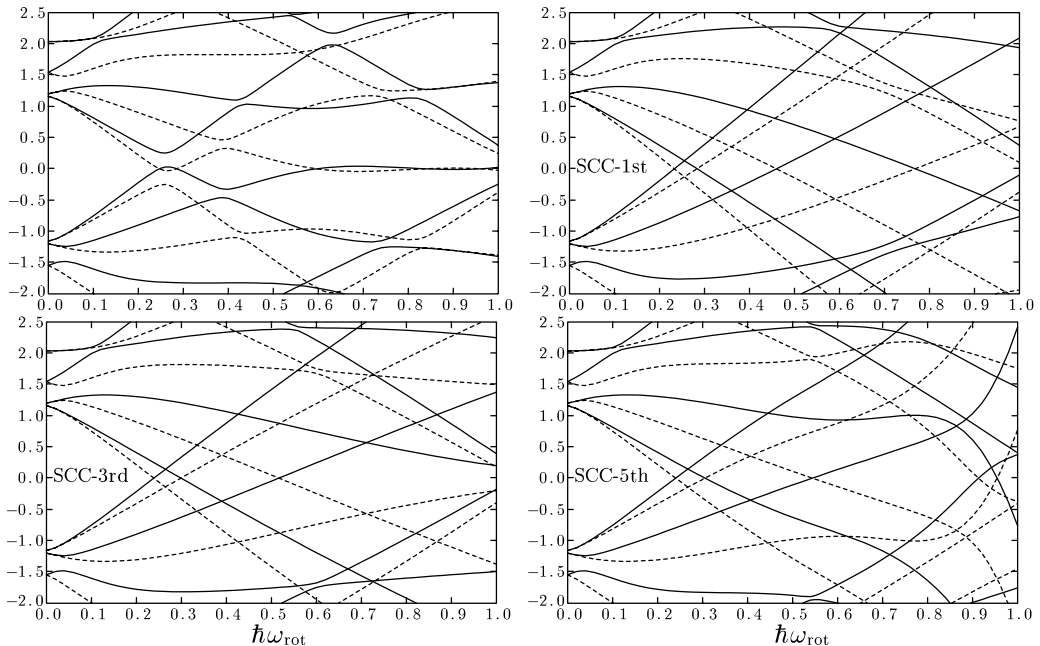
Fig. 9. Neutron quasiparticle Routhians for the $N_{\mathrm{osc}} = 6$ ($i_{13/2}$) orbits suitable for ^{162}Er. The left upper, right upper, left lower, and right lower panels denote the results of the adiabatic cranking, the SCC up to the first order, 3rd order, and 5th order, respectively. The solid and dotted curves denote Routhians with $r = +i$ ($\alpha = -1/2$) and $r = -i$ ($\alpha = +1/2$), respectively. The effect of residual interaction is completely neglected in this calculation.

change their characters abruptly at the crossing, if their average behavior is compared to the calculated ones, the third order results ($n_{\max} = 3$) agree best with the adiabatic levels. The first order results, for example, give the alignments (the slopes of Routhians) too large. On the other hand, the divergent behavior is clearly seen at about $\omega \geq 0.8$ MeV in the fifth order results. The inclusion of the effect of the residual interactions makes this convergence radius in ω even smaller.

Finally, we would like to discuss the results of application of the present formalism to the g- and s-bands, which are observed systematically and compose the yrast lines of even-even nuclei. Although we can compare the Routhians (3·21), or equivalently the rotational energy (3·13), it is known that the relation I_x versus ω gives a more stringent test. Therefore we compare the calculated I_x–ω relation with the experimental one in Fig. 10 for even-even nuclei in the rare-earth region, in which the band crossings are identified along the yrast sequences. In this calculation the $I_x(\omega)$ of the g-band is given by Eq. (3·77) with calculated values of the Harris parameters (see Table II). As for the $I_x(\omega)$ of the s-band, we calculate it on the simplest assumption of the independent quasiparticle motions in the rotating frame, which is the same as that of the cranked shell model:

$$|\phi_s(\omega)\rangle = \alpha_1^\dagger(\omega)\alpha_{\bar{1}}^\dagger(\omega)|\phi_{\mathrm{intr}}(\omega)\rangle, \quad |\phi_g(\omega)\rangle = |\phi_{\mathrm{intr}}(\omega)\rangle, \qquad (3\cdot84)$$

where $\alpha_1^\dagger(\omega)$ and $\alpha_{\bar{1}}^\dagger(\omega)$ are the lowest $r = +i$ and $r = -i$ quasineutron creation operators in the rotating frame. Then, the $I_x(\omega)$ of the s-band is the sum of $I_x(\omega)$ of the g-band and the aligned angular momenta of two quasineutrons, which are calculated according to Eqs. (3·51)–(3·54),

$$\left(I_x(\omega)\right)_{s\text{-band}} = I_x(\omega) + i_1(\omega) + i_{\bar{1}}(\omega), \quad \left(I_x(\omega)\right)_{g\text{-band}} = I_x(\omega), \qquad (3\cdot85)$$

or by using the canonical relation between the Routhian and the aligned angular momentum, the alignments i_μ and $i_{\bar{\mu}}$ can be calculated as usual:

$$i_\mu(\omega) = -\frac{\partial E'_\mu(\omega)}{\partial \omega}, \quad i_{\bar{\mu}}(\omega) = -\frac{\partial E'_{\bar{\mu}}(\omega)}{\partial \omega}. \qquad (3\cdot86)$$

Since our quasiparticle Routhians behave diabatically as functions of the rotational frequency, the resultant g- and s-bands are also non-interacting bands; we have to mix them at the same angular momentum to obtain the interacting bands corresponding to the observed bands. Such a band mixing calculation is straightforward in our formalism if the interband g-s interaction is provided. However, it is a very difficult task as long as the usual adiabatic cranking model is used. In the present stage we are not able to estimate the g-s interband interaction theoretically. Therefore, we do not attempt to perform such band-mixing calculations in the present paper (but see §4.2).

Looking into the results displayed in Fig. 10, one see that our diabatic formalism of collective rotation based on the SCC method is quite successful. The overall agreements are surprisingly good, considering the fact that we have only used a global parametrization of the strengths of the residual interaction:

$$G_0^\nu = 20/A, \quad G_0^\pi = 24/A \ \text{(MeV)}, \tag{3·87}$$

$$g_2^\nu = g_2^\pi = 24, \tag{3·88}$$

$$\kappa_{2K} = 1.45 \, \kappa_2^{\text{self}}, \tag{3·89}$$
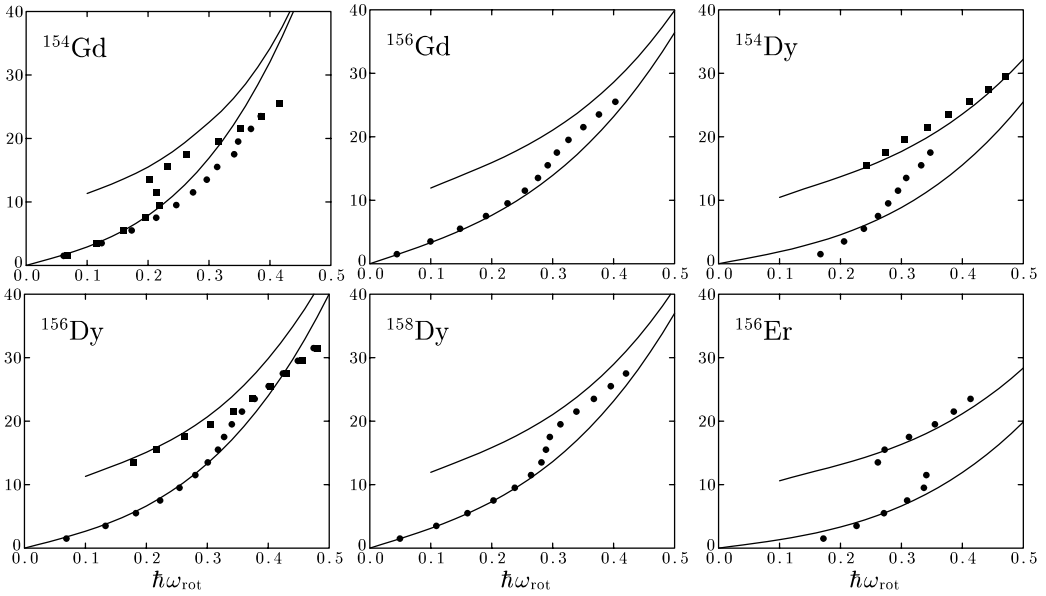

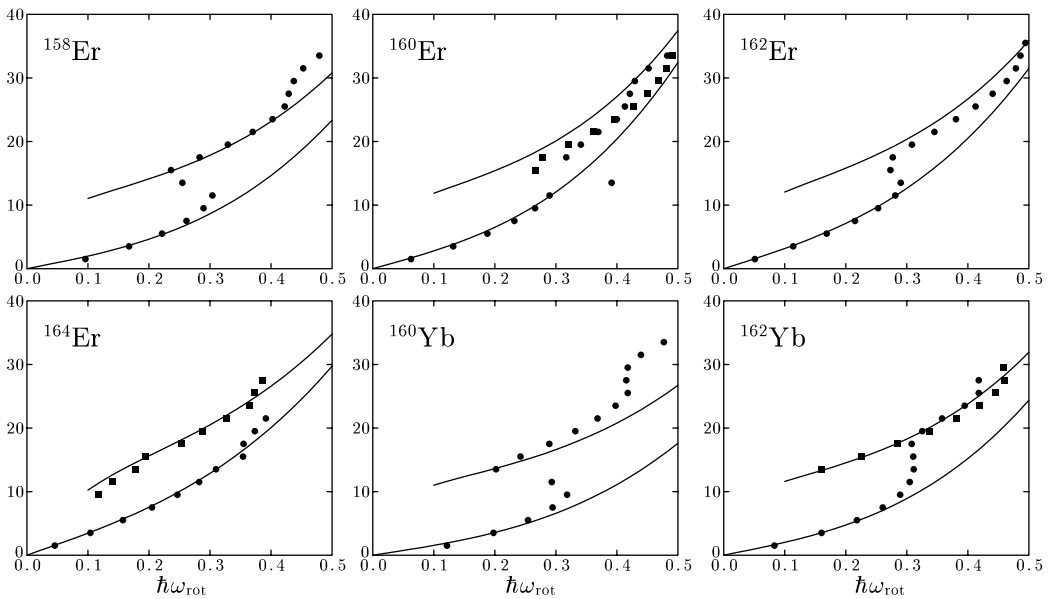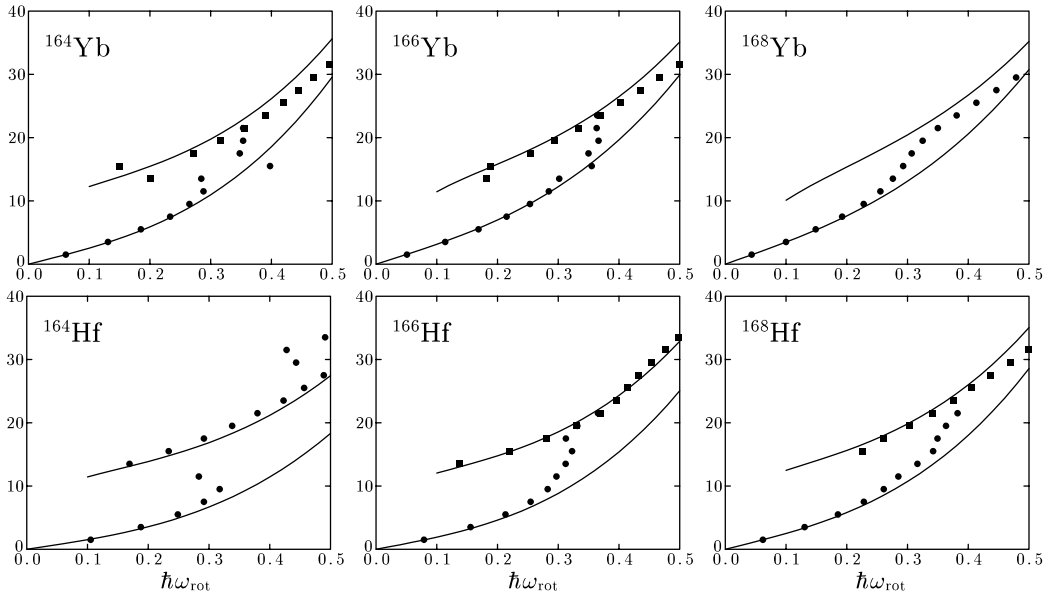Fig. 10. (continued.)

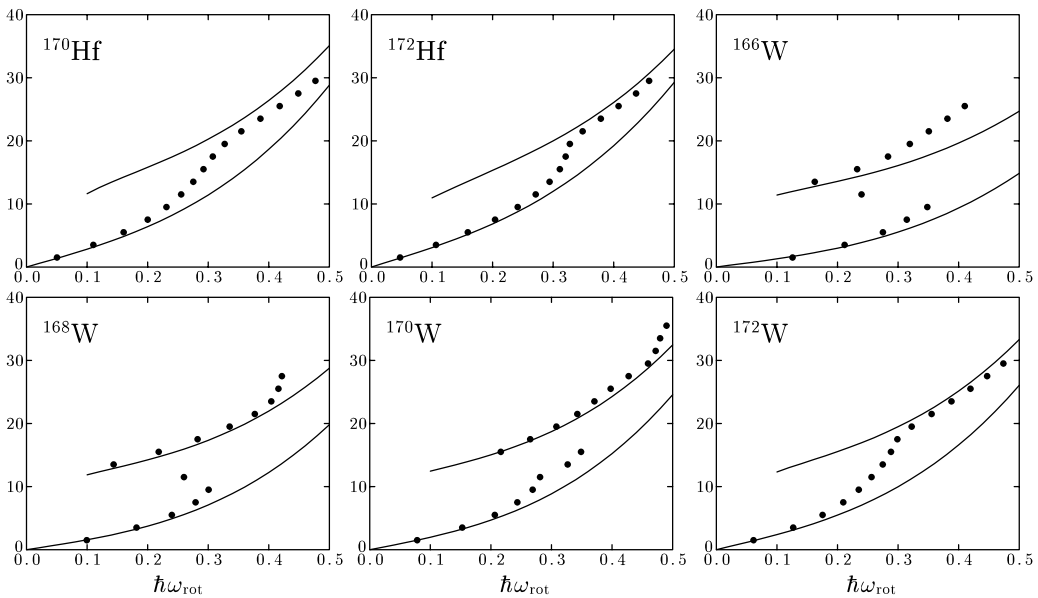Fig. 10. (continued.)

Fig. 10.   (continued.)

Fig. 10.   Comparison of the third order SCC method calculations for the diabatic *g*- and *s*-bands
with experimental data. The angular momenta $\langle J_x \rangle = I + 1/2$ ($\hbar$) are displayed versus the
rotational frequency $\hbar\omega_{rot}$ (MeV) for nuclei in the rare-earth region, Gd ($Z = 64$) to W ($Z = 74$)
isotopes. Filled circles denote experimental data smoothly extended from the ground state.
Data for excited bands are also included as filled squares when available, which are, in most
cases, identified as *s*-bands.

for the model space of three N_{osc}-shells (4–6 for neutrons and 3–5 for protons). The

agreements of the calculated g-bands come from the fact that the Harris parameters (Table II) are nicely reproduced in the calculation. Further agreements of the s-bands are not trivial, and tell us that we have obtained reliable diabatic quasiparticle spectra (Figs. 6 and 7). It is known that, if the I_x–ω relations of s-bands are parametrized in the form, $I_x = i + \mathcal{J}_0\,\omega + \mathcal{J}_1\,\omega^3$, the $\mathcal{J}_1$ Harris parameters of s-bands are systematically smaller than those of g-bands. This feature is quite well reproduced in the calculations, as is clearly seen in Fig. 10, and the reason is that the value of the aligned angular momentum of two quasineutrons decreases as a function of ω. The suitable decrease is obtainable only if the residual interactions are included and the diabatic quasiparticle Routhians are evaluated up to the third order.

§4. Diabatic quasiparticle basis and the interband interaction between the g- and s-bands

The formulation of the previous section gives a consistent perturbative solution, with respect to the rotational frequency, of the basic equations of the SCC method for collective rotation. However, it has a problem as a method to construct the diabatic quasiparticle basis: The wave functions of the diabatic levels are orthonormal only within the order of cutoff ($n_{\max}$) of the ω-expansion. In the previous section only the independent quasiparticle states, i.e., one-quasiparticle states or the g- and s-bands, are considered and this problem does not show up. The quasiparticle states have another important role that they are used as a basis of complete set for a more sophisticated many body technique beyond the mean-field approximation; for example, the study of collective vibrations at high spin in terms of the RPA method in the rotating frame. [7),56),61)-64)] In such an application it is crucial that the diabatic quasiparticle basis satisfies the orthonormal property. We present in this section a possible method to construct the diabatic basis satisfying the orthonormality condition.

Another remaining problem which is not touched in the previous section is how to theoretically evaluate the interband interaction between the ground state band and the two-quasineutron aligned band. Since we do not have a satisfactory answer yet to this problem, we only present a scope for possible solutions at the end of this section.

4.1. *Construction of diabatic quasiparticle basis in the SCC method*

Although the basic idea is general, we restrict ourselves to the case of collective rotation and use the good signature representation with real phase convention, introduced in §3.3, for the matrix elements of the Hamiltonian H and of the angular momentum J_x. First let us recall that the diabatic quasiparticle basis in the rotating frame is obtained by the two-step unitary transformation (3·45). The first transformation by $e^{iG(\omega)}$ can be represented as follows [10)]

$$e^{iG(\omega)}a_i^\dagger e^{-iG(\omega)} = \sum_{j>0}\Big[\cos\sqrt{gg^{\mathrm{T}}}\Big]_{ij}a_j^\dagger - \sum_{j>0}\Big[g\,\frac{\sin\sqrt{g^{\mathrm{T}}g}}{\sqrt{g^{\mathrm{T}}g}}\Big]_{ij}a_{\bar{j}}, \qquad (4\cdot1)$$

$$e^{iG(\omega)}a_i^\dagger e^{-iG(\omega)} = \sum_{j>0}\Big[\cos\sqrt{g^{\mathrm{T}}g}\,\Big]_{ij}a_{\bar{j}}^\dagger + \sum_{j>0}\Big[g^{\mathrm{T}}\frac{\sin\sqrt{gg^{\mathrm{T}}}}{\sqrt{gg^{\mathrm{T}}}}\Big]_{ij}a_j, \qquad (4\cdot2)$$

with real matrix elements $g_{ij}(\omega) = \sum_{n\geq1}\omega^n g^{(n)}(ij)$, see Eq. (3·64), where g^{T} denotes the transpose of g. Thus, by using an obvious matrix notation, the transformation to the rotating quasiparticle operator from the $\omega = 0$ quasiparticle operator is given as

$$\begin{pmatrix} \alpha \\ \bar{\alpha}^\dagger \end{pmatrix} = \begin{pmatrix} f^{\mathrm{T}} & 0 \\ 0 & \bar{f}^{\mathrm{T}} \end{pmatrix} \begin{pmatrix} \cos\sqrt{gg^{\mathrm{T}}} & -g\dfrac{\sin\sqrt{g^{\mathrm{T}}g}}{\sqrt{g^{\mathrm{T}}g}} \\ g^{\mathrm{T}}\dfrac{\sin\sqrt{gg^{\mathrm{T}}}}{\sqrt{gg^{\mathrm{T}}}} & \cos\sqrt{g^{\mathrm{T}}g} \end{pmatrix} \begin{pmatrix} a \\ a^\dagger \end{pmatrix} \qquad (4\cdot3)$$

$$\equiv \mathcal{F}^{\mathrm{T}}(\omega)\,\mathcal{G}^{\mathrm{T}}(\omega)\begin{pmatrix} a \\ a^\dagger \end{pmatrix}, \qquad (4\cdot4)$$

where the real matrix elements $f_{i\mu}(\omega)$ and $\bar{f}_{i\mu}(\omega)$ are the amplitudes that diagonalize the quasiparticle Hamiltonian in the rotating frame, see Eq. (3·42), for signature $r = +i$ and $-i$, respectively. The cutoff of the ω-expansion means that the generator $iG(\omega)$, i.e. the matrix g, is solved up to the $n = n_{\max}$ order,

$$g(\omega) = [g(\omega)]^{(n\leq n_{\max})} = \sum_{n=1}^{n_{\max}}\omega^n g^{(n)}, \qquad (4\cdot5)$$

and at the same time the transformation matrix $\mathcal{G}(\omega)$ itself is treated perturbatively

$$\mathcal{G}(\omega) = \begin{pmatrix} 1 - \omega^2 g^{(1)}g^{(1)\mathrm{T}} + \cdots & \omega g^{(1)} + \cdots \\ -\omega g^{(1)\mathrm{T}} + \cdots & 1 - \omega^2 g^{(1)\mathrm{T}}g^{(1)} + \cdots \end{pmatrix}, \qquad (4\cdot6)$$

while the other one, $\mathcal{F}(\omega)$, is treated non-perturbatively by the diagonalization procedure. The origin of difficulty arising when the diabatic basis is utilized as a complete set lies in this treatment of $\mathcal{G}(\omega)$, because the orthogonality of the matrix $\mathcal{G}(\omega)$ is broken in higher-orders.

Now the solution to this problem is apparent: The generator matrix $g(\omega)$ is solved perturbatively like in Eq. (4·5), but the transformation matrix $\mathcal{G}(\omega)$ has to be treated non-perturbatively as in Eq. (4·3). In order to realize this treatment we introduce new orthogonal matrices, D and $\bar{D}$, which diagonalize gg^{T} and $g^{\mathrm{T}}g$ within the signature $r = +i$ and $-i$ states, respectively,

$$\sum_{j>0}(gg^{\mathrm{T}})_{ij}D_{jk} = D_{ik}\theta_k^2, \quad \sum_{j>0}(g^{\mathrm{T}}g)_{ij}\bar{D}_{jk} = \bar{D}_{ik}\theta_k^2, \qquad (4\cdot7)$$

where we have used the fact that the matrices gg^{T} and $g^{\mathrm{T}}g$ have common eigenvalues, which are non-negative, and then we have

$$\mathcal{G}(\omega) = \begin{pmatrix} D(\cos\theta)D^{\mathrm{T}} & g\bar{D}(\sin\theta/\theta)\bar{D}^{\mathrm{T}} \\ -g^{\mathrm{T}}D(\sin\theta/\theta)D^{\mathrm{T}} & \bar{D}(\cos\theta)\bar{D}^{\mathrm{T}} \end{pmatrix}. \qquad (4\cdot8)$$

Here $(\cos\theta)$ and $(\sin\theta/\theta)$ denote diagonal matrices, whose matrix elements are $\delta_{ij}\cos\theta_i$ and $\delta_{ij}\sin\theta_i/\theta_i$, respectively. The physical meaning is that the orthogonal matrices D and $\bar{D}$ are transformation matrices from the quasiparticle operators $(a_i^\dagger, a_i)$ and $(a_{\bar{i}}^\dagger, a_{\bar{i}})$ at $\omega = 0$ to their canonical bases, which diagonalize the density matrices ρ and $\bar{\rho}$ with respect to the rotational HB state $|\phi_{\mathrm{intr}}(\omega)\rangle$, respectively;

$$\rho_{ij} \equiv \langle\phi_{\mathrm{intr}}(\omega)|a_i^\dagger a_j|\phi_{\mathrm{intr}}(\omega)\rangle = \left[\cos\sqrt{gg^{\mathrm{T}}}\right]_{ij},$$

$$\bar{\rho}_{ij} \equiv \langle\phi_{\mathrm{intr}}(\omega)|a_{\bar{i}}^\dagger a_{\bar{j}}|\phi_{\mathrm{intr}}(\omega)\rangle = \left[\cos\sqrt{g^{\mathrm{T}}g}\right]_{ij}. \tag{4.9}$$

Thus the method to construct the rotating quasiparticle basis is summarized as follows. First, solve the basic equation of the SCC method and obtain the generator matrix $g(\omega)$ up to the $n_{\max}$ order as in Eq. (4.5). At the same time, diagonalize the quasiparticle Hamiltonian and obtain the eigenstates as in Eq. (3.42) for both signatures $r = \pm i$. Second, diagonalize the density matrices (4.9), or equivalently Eq. (4.7), and obtain the orthogonal matrices D and $\bar{D}$ of the canonical bases. Finally, by using these matrices D and $\bar{D}$ calculate the transformation matrix $\mathcal{G}(\omega)$ as in Eq. (4.8), and then the basis transformation is determined by Eq. (4.4).

It is instructive to consider a concrete case of the cranked shell model; i.e., the effect of residual interactions or the selfconsistency of mean-field is neglected at $\omega > 0$. The quasiparticle basis is obtained by diagonalizing the generalized Hamiltonian matrix:

$$\begin{pmatrix} h_{\mathrm{Nils}} - \omega j_x & -\Delta \\ -\Delta & -(h_{\mathrm{Nils}} + \omega j_x) \end{pmatrix} \begin{pmatrix} U & \bar{V} \\ V & \bar{U} \end{pmatrix} = \begin{pmatrix} U & \bar{V} \\ V & \bar{U} \end{pmatrix} \begin{pmatrix} E' & 0 \\ 0 & -\bar{E}' \end{pmatrix},$$
$$\tag{4.10}$$

where h_{Nils} and j_x denote matrices with respect to the Nilsson (or the harmonic oscillator) basis at $\omega = 0$, and (U, V) and $(\bar{U}, \bar{V})$ are coefficients of the generalized Bogoliubov transformations from the Nilsson nucleon operators $(c_i^\dagger, c_i)$ and $(c_{\bar{i}}^\dagger, c_{\bar{i}})$ (in the good signature representation),

$$\alpha_\mu^\dagger = \sum_{i>0}(U_{i\mu}c_i^\dagger + V_{i\mu}c_{\bar{i}}), \quad \alpha_{\bar{\mu}}^\dagger = \sum_{i>0}(\bar{U}_{i\mu}c_{\bar{i}}^\dagger + \bar{V}_{i\mu}c_i), \tag{4.11}$$

or in the matrix notation

$$\begin{pmatrix} c \\ c^\dagger \end{pmatrix} = \mathcal{U}\begin{pmatrix} \alpha \\ \alpha^\dagger \end{pmatrix}, \quad \mathcal{U} \equiv \begin{pmatrix} U & \bar{V} \\ V & \bar{U} \end{pmatrix}. \tag{4.12}$$

In contrast, the transformation $\mathcal{U}$ is decomposed into three steps in our construction method of the diabatic quasiparticle basis; (i) the Bogoliubov transformation $\mathcal{U}_0$ between the nucleon $(c, \bar{c}^\dagger)$ and the quasiparticle $(a, \bar{a}^\dagger)$ at $\omega = 0$,

$$\begin{pmatrix} c \\ \bar{c}^\dagger \end{pmatrix} = \mathcal{U}_0\begin{pmatrix} a \\ \bar{a}^\dagger \end{pmatrix}, \quad \mathcal{U}_0 \equiv \begin{pmatrix} u & v \\ -v^{\mathrm{T}} & u \end{pmatrix}, \tag{4.13}$$

where u and v are the matrices of transformation at $\omega = 0$ (they are diagonal, e.g. $u_{ij} = u_i\delta_{ij}$, if only the monopole-pairing interaction is included), (ii) the transformation matrix $\mathcal{G}(\omega)$ in Eq. (4.4), generated by $e^{iG(\omega)}$, and (iii) the diagonalization

step of the rotating quasiparticle Hamiltonian $\mathcal{F}(\omega)$ in Eq. (4·4), see also Eq. (3·42), namely

$$\mathcal{U}(\omega)^{\mathrm{SCC}} = \mathcal{U}_0\,\mathcal{G}(\omega)\mathcal{F}(\omega). \tag{4·14}$$

Here both $\mathcal{G}(\omega)$ and $\mathcal{F}(\omega)$ depend on the order of cutoff n_{max} in solving the generator $iG(\omega)$ by the ω-expansion method, but they themselves have to be calculated non-perturbatively, especially for $\mathcal{G}$ by Eq. (4·8) with (4·7). As noted at the end of §3.3, we can apply the SCC method starting from the finite frequency ω_0. In such a case $\mathcal{U}_0$ is the transformation at $\omega = \omega_0$, and $\mathcal{G}$ and $\mathcal{F}$ are obtained by expansions in terms of $(\omega - \omega_0)$; thus,

$$\mathcal{U}(\omega)^{\mathrm{SCC}} = \mathcal{U}_0(\omega_0)\,\mathcal{G}(\omega - \omega_0)\mathcal{F}(\omega - \omega_0) \quad \text{if started at } \omega = \omega_0. \tag{4·15}$$

It should be stressed that the transformation (4·14) only approximately diagonalize the Hamiltonian in Eq. (4·10) within the n_{max} order in the sense of ω-expansion. Namely, some parts of the Hamiltonian corresponding to the terms higher order than n_{max} are neglected, and this is exactly the reason why we can obtain the diabatic basis, whose negative and positive solutions are non-interacting.

In the case where the effect of residual interactions is neglected, i.e. corresponding to the higher order cranking, we can easily solve the basic equations of the SCC method. It is useful to present the solution for practical purposes; for example for the construction of the diabatic quasiparticle basis for the cranked shell model calculations. The solutions for $g^{(n)}$ up to the third order are given as follows:

$$g^{(1)}(ij) = \frac{1}{E_i + E_{\bar{j}}} J_x^A(ij), \tag{4·16}$$

$$g^{(2)}(ij) = \frac{1}{E_i + E_{\bar{j}}} (J_x^B g^{(1)} + g^{(1)} \bar{J}_x^B)_{ij}, \tag{4·17}$$

$$g^{(3)}(ij) = \frac{1}{E_i + E_{\bar{j}}} \Big[(J_x^B g^{(2)} + g^{(2)} \bar{J}_x^B) \\
+ \frac{1}{3}(J_x^A g^{(1)\mathrm{T}} g^{(1)} + 2 g^{(1)} J_x^{A\mathrm{T}} g^{(1)} + g^{(1)} g^{(1)\mathrm{T}} J_x^A) \Big]_{ij}, \tag{4·18}$$

and the solutions for the rotating quasiparticle Hamiltonian (3·48)–(3·49):

$$\epsilon'^{(0)}_{ij} = \delta_{ij} E_i, \quad \bar{\epsilon}'^{(0)}_{ij} = \delta_{ij} E_{\bar{i}}, \tag{4·19}$$

$$\epsilon'^{(1)}_{ij} = -J_x^B(ij), \quad \bar{\epsilon}'^{(1)}_{ij} = -\bar{J}_x^B(ij), \tag{4·20}$$

$$\epsilon'^{(2)}_{ij} = \frac{1}{2}(J_x^A g^{(1)\mathrm{T}} + g^{(1)} J_x^{A\mathrm{T}})_{ij}, \quad \bar{\epsilon}'^{(2)}_{ij} = \frac{1}{2}(J_x^{A\mathrm{T}} g^{(1)} + g^{(1)\mathrm{T}} J_x^A)_{ij}, \tag{4·21}$$

$$\epsilon'^{(3)}_{ij} = \frac{1}{2}(J_x^A g^{(2)\mathrm{T}} + g^{(2)} J_x^{A\mathrm{T}})_{ij}, \quad \bar{\epsilon}'^{(3)}_{ij} = \frac{1}{2}(J_x^{A\mathrm{T}} g^{(2)} + g^{(2)\mathrm{T}} J_x^A)_{ij}, \tag{4·22}$$

where the quasiparticle energies at the starting frequency are given in Eq. (3·62), and the matrix elements of J_x at the starting frequency are given as in Eq. (3·63) with Q_ρ replaced by J_x. If the starting frequency is $\omega = 0$, then $E_{\bar{i}} = E_i$, and the matrix elements of J_x satisfy the relations, $J_x^{A\mathrm{T}} = -J_x^A$, $\bar{J}_x^B = -J_x^B$, and

$J_x^{BT} = J_x^B$. The transformation $\mathcal{G}(\omega)$ is calculated from Eqs. (4·16)–(4·18), and $\mathcal{F}(\omega)$ from Eqs. (4·19)–(4·22). It should be mentioned that the selfconsistent mean-field calculation is in principle possible in combination with the diabatic basis prescription presented above.

4.2. *Estimate of the g-s interaction*

Once the diabatic g- and s-bands states (3·84) are obtained as functions of ω, one can immediately construct them as functions of angular momentum I, because the I_x–ω relation has no singularity, as shown in Fig. 10, and can easily be inverted:

$$|\phi_g(I)\rangle = |\phi_g(\omega_g(I))\rangle, \quad |\phi_s(I)\rangle = |\phi_s(\omega_s(I))\rangle, \qquad (4·23)$$

where $\omega_g(I)$ and $\omega_s(I)$ are the inverted relations of (3·85) with $I_x = I + 1/2$. Physically, one has to consider the coupling problem between them at a fixed spin value I. It is, however, a difficult problem because one has to calculate, for example, a matrix element like $\langle \phi_s(I)|H|\phi_g(I)\rangle$, which is an overlap between two different HB states; they are not orthogonal to each other due to the difference of the frequencies $\omega_g(I)$ and $\omega_s(I)$. Although such a calculation is possible by using the Onishi formula for the overlap of general HB states,[39] it would damage the simple picture of quasiparticle motions in the rotating frame, and is out of scope of the present investigation.

Here we assume that the wave functions vary smoothly along the diabatic rotational bands as functions of spin I or frequency ω, so that the interband interaction between the g- and s-bands can be evaluated at the common frequency by

$$v_{g\text{-}s}(I) = \langle \phi_s(\omega_{gs}(I))|H|\phi_g(\omega_{gs}(I))\rangle, \qquad (4·24)$$

where ω_{gs} is defined by an average of ω_s and ω_g,

$$\omega_{gs}(I) \equiv \frac{\omega_g(I) + \omega_s(I)}{2}. \qquad (4·25)$$

We note that this quantity corresponds, in a good approximation, to the crossing frequency $\omega_c^{g\text{-}s}$ at the crossing angular momentum $I_c^{g\text{-}s}$,

$$\omega_{gs}(I_c^{g\text{-}s}) \approx \omega_c^{g\text{-}s}, \qquad (4·26)$$

where $\omega_c^{g\text{-}s}$ is defined as a frequency at which the lowest diabatic two-quasiparticle energy vanishes, $E_1'(\omega) + E_{\bar{1}}'(\omega) = 0$. Using the fact that $|\phi_s(\omega)\rangle$ is the two-quasiparticle excited state on $|\phi_g(\omega)\rangle$ (see Eq. (3·84)), the interaction can be rewritten as

$$v_{g\text{-}s}(I) = \omega_{gs}(I)\langle \phi_s(\omega_{gs}(I))|J_x|\phi_g(\omega_{gs}(I))\rangle, \qquad (4·27)$$

because of the variational principle (3·17). Applying the idea of ω-expansion and taking up to the lowest order, we have, at the crossing angular momentum $I_c^{g\text{-}s}$,

$$v_{g\text{-}s}(I_c^{g\text{-}s}) \approx \omega_c^{g\text{-}s} \sum_{ij>0} f_{i1}(\omega_c^{g\text{-}s})\bar{f}_{j1}(\omega_c^{g\text{-}s})J_x^A(ij), \qquad (4·28)$$
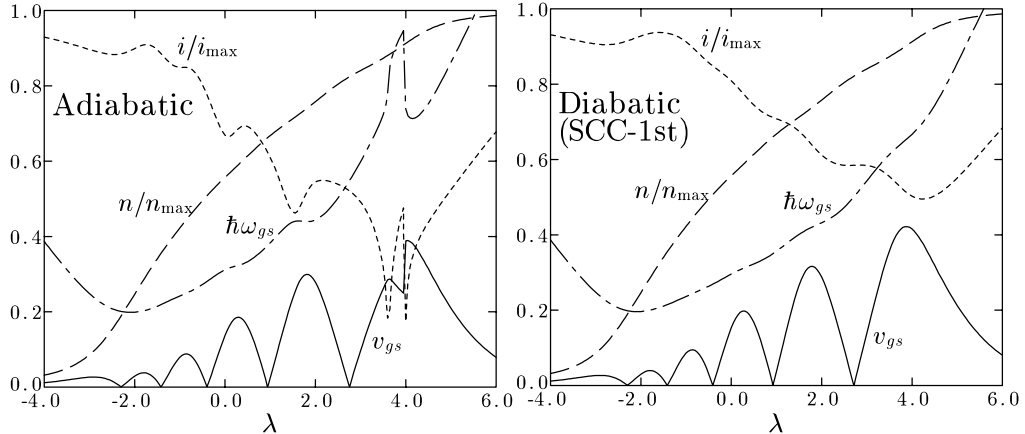
Fig. 11. The g-s interband interaction (solid), the crossing frequency $\hbar\omega_{gs}$ (dash-dotted) in MeV, the alignment i (dotted), and the expectation value of number operator n (dashed), plotted as functions of the chemical potential λ in MeV, for the $i_{13/2}$ single-j shell model without residual interactions. The result of the usual adiabatic cranked shell model is displayed in the left panel, while that of the diabatic SCC 1st order calculation in the right panel. Here the alignment i and the number n is scaled by their maximum values, $i_{max} = 12\hbar$ and $n_{max} = 14$. The energy unit is chosen such that the splitting of the $i_{13/2}$-shell roughly reproduces that of a typical well deformed rare-earth nucleus; i.e. $\kappa = 2.5$ MeV in Eq. (4·29), and the constant $\Delta = 1.0$ MeV is used.

where $f_{i1}(\omega)$ and $\bar{f}_{j1}(\omega)$ are the amplitudes of the diabatic quasiparticle diagonalization (3·42) for the lowest $r = \pm i$ quasineutrons, and should be calculated nonperturbatively with respect to ω.

In Fig. 11 (right panel), we show the result evaluated by using Eq. (4·28) for a simple single-j shell model ($i_{13/2}$) with a constant monopole-pairing gap and no residual interactions, in which the single-particle energies are given by

$$e_i = \kappa \frac{3m_i^2 - j(j+1)}{j(j+1)}, \quad (m_i = 1/2, \cdots, j) \tag{4·29}$$

with a parameter κ describing the nuclear deformation. In this figure other quantities, the alignment of the lowest two-quasiparticle state, the number expectation value, and the crossing frequency are also shown as functions of the chemical potential. These quantities can also be evaluated in terms of the usual adiabatic cranking model, and they are also displayed in the left panel. Note that in the adiabatic cranking model the crossing frequency is defined as a frequency at which the adiabatic two-quasiparticle energy $E_1^{\prime(ad)}(\omega) + E_{\bar{1}}^{\prime(ad)}(\omega)$ becomes the minimum, and the interband interaction is identified as the half of its minimum value. [44] As is well known, [65] the g-s interaction oscillates as a function of the chemical potential, and both the absolute values and the oscillating behavior of the result of calculation roughly agree with the experimental findings. Comparing two calculations, the interband interaction (4·28) seems to give a possible microscopic estimate based on the diabatic description of the g- and s-bands. We would like to stress, however,

that its derivation is not very sound. It is an important future problem to derive the coupling matrix element on a more sound ground.

§5.   Concluding remarks

In this paper, we have formulated the SCC method for the nuclear collective rotation. By using the rotational frequency expansion rather than the angular momentum expansion, we have applied it to the description of the g- and s-bands successfully. The systematic calculation gives surprisingly good agreements with experimental data for both rotational bands. It has been demonstrated that the resultant quasiparticle states develop diabatically as functions of the rotational frequency; i.e. the negative and positive energy levels do not interact with each other. Although the formulation is mathematically equivalent to the selfconsistent cranking model, the cutoff of the ω-expansion results in the diabatic levels and its mechanism is also discussed. The perturbative ω-expansion is, however, inadequate to use the resultant quasiparticle basis states as a complete set. We have then presented a method to construct the diabatic quasiparticle basis set, which rigorously satisfies the orthonormality condition and can be safely used for the next step calculation, e.g. the RPA formalism for collective vibrations at high-spin.

In order to obtain a good overall description of the rotational band for nuclei in the rare-earth region, we have investigated the best possible form of residual quadrupole-pairing interactions. It is found that the double-stretched form factor is essential for reproducing the even-odd mass difference and the moment of inertia simultaneously.

Since the calculated g- and s-bands in our formulation are diabatic rotational bands, the interband interaction between them should be taken into account for their complete descriptions. As in any other mean-field model, however, the wave function obtained in our formalism is a wave packet with respect to the angular momentum variable. Therefore, it is not apparent how to evaluate the interband interaction from microscopic point of view. We have presented a possible estimate of the interaction, which leads to a value similar to that estimated by the level repulsion in the adiabatic cranking model. Further investigations are still necessary to give a definite conclusion to this problem.

Acknowledgments

References

1) I. Hamamoto, *Treatise on Heavy-Ion Science*, ed. D. A. Bromly (Prenum Press, 1985), vol. 3, p. 313.

2) Z. Szymansky, *Fast Nuclear Rotation* (Clarendon Press, 1983).
3) I. Hamamoto, Nucl. Phys. **A271** (1976), 15.
4) E. R. Marshalek and A. L. Goodman, Nucl. Phys. **A294** (1978), 92.
5) R. Bengtsson and S. Frauendorf, Nucl. Phys. **A314** (1979), 27.
6) S. Frauendorf, in *Nuclear Physics*, ed. C. H. Dasso, R. A. Broglia and A. Winther (North-Holland, 1982), p. 111.
7) Y. R. Shimizu and K. Matsuyanagi, Prog. Theor. Phys. **70** (1983), 144; **72** (1984), 799.
8) T. Bengtsson, Nucl. Phys. **A496** (1989), 56.
9) M. Matsuo, T. Døssing, E. Vigezzi, R. A. Broglia and K. Yoshida, Nucl. Phys. **A617** (1997), 1.
10) T. Marumori, T. Maskawa, F. Sakata and A. Kuriyama, Prog. Theor. Phys. **64** (1980), 1294.
11) D. R. Bes and R. A. Sorensen, *Advances in Nuclear Physics* (Prenum Press, 1969), vol. 2, p. 129.
12) S. G. Nilsson and O. Prior, K. Dan. Vidensk. Selsk. Mat.-Fys. Medd. **32** (1961), no. 16.
13) D. Vautherin and D. M. Brink, Phys. Rev. **C3** (1972), 626.
14) M. Brack, J. Damgaard, A. S. Jensen, H. C. Pauli, V. M. Strutinsky and C. Y. Wong, Rev. Mod. Phys. **44** (1972), 320.
15) I. Ragnarsson, S. G. Nilsson and R. K. Sheline, Phys. Rep. **45** (1978), 1.
16) S. G. Nilsson and I. Ragnarsson, *Shapes and Shells in Nuclear Structure* (Cambridge University Press, 1995).
17) H. Sakamoto and T. Kishimoto, Nucl. Phys. **A501** (1989), 205, 242.
18) T. Kishimoto et al., Phys. Rev. Lett. **35** (1975), 552.
T. Kishimoto, *Proc. 1980 RCNP Int. Symp. Highly Exited States in Nuclear Reactions, Osaka*, p. 145.
19) E. R. Marshalek, Phys. Rev. **29** (1984), 640.
20) M. Baranger and K. Kumar, Nucl. Phys. **A110** (1968), 490.
21) H. Sakamoto, Nucl. Phys. **A557** (1993), 583c.
22) I. Hamamoto, Nucl. Phys. **A232** (1974), 445.
23) M. Wakai and A. Faessler, Nucl. Phys. **A295** (1978), 86.
24) M. Diebel, Nucl. Phys. **A419** (1984), 353.
25) J. D. Garrett et al., Phys. Lett. **B118** (1982), 297.
26) H. Sakamoto and T. Kishimoto, Phys. Lett. **B245** (1990), 321.
27) T. Kubo, H. Sakamoto, T. Kammuri and T. Kishimoto, Phys. Rev. **C54** (1996), 2331.
28) W. Satuła and R. Wyss, Phys. Rev. **C50** (1994), 2888.
29) R. Wyss and W. Satuła, Phys. Lett. **B351** (1995), 393.
30) W. Satuła and R. Wyss, Physica Scripta **T56** (1995), 159.
31) F. R. Xu, R. Wyss and P. M. Walker, Phys. Rev. **C60** (1999), 051301(R).
32) A. Bohr and B. R. Mottelson, *Nuclear Structure* (W. A. Benjamin Inc., 1969), vol. I.
33) A. Bohr and B. R. Mottelson, *Nuclear Structure* (W. A. Benjamin Inc., 1975), vol. II.
34) S. M. Harris, Phys. Rev. **138** (1965), B509.
35) T. Bengtsson and I. Ragnarsson, Nucl. Phys. **A436** (1985) 14.
36) G. Audi and A. H. Wapstra, Nucl. Phys. **A565** (1993), 1.
37) M. Sakai, Atomic and Nuclear Data Tables **31** (1984), 399.
38) Evaluated Nuclear Structure Data File, http://isotopes.lbl.gov/isotopes/vuensdf.html.
39) P. Ring and P. Schuck, *The Nuclear Many-Body Problem* (Springer-Verlag, 1980).
40) Y. R. Shimizu and K. Matsuyanagi, Prog. Theor. Phys. **74** (1985), 1346.
41) J. Terasaki, T. Marumori and F. Sakata, Prog. Theor. Phys. **85** (1991), 1235.
42) J. Terasaki, Prog. Theor. Phys. **88** (1992), 529.
43) J. Terasaki, Prog. Theor. Phys. **92** (1994), 535.
44) R. Bengtsson and S. Frauendorf, Nucl. Phys. **A327** (1979), 139.
45) M. Matsuo, Prog. Theor. Phys. **76** (1986), 372.
46) M. Matsuo, Springer Proceedings in Physics, *New Trends in Nuclear Collective Dynamics*, ed. Y. Abe, H. Horiuchi and K. Matsuyanagi (Springer-Verlag, 1992), vol. 58, p. 219.
47) M. Matsuo, Prog. Theor. Phys. **72** (1984), 666.
48) M. Matsuo and K. Matsuyanagi, Prog. Theor. Phys. **74** (1985), 1227; **76** (1986), 93; **78** (1987), 591.
49) M. Matsuo, Y. R. Shimizu and K. Matsuyanagi, *Proceedings o The Niels Bohr Centennial*

Conf. on Nuclear Structure, ed. R. Broglia, G. Hagemann and B. Herskind (North-Holland, 1985), p. 161.
50) K. Takada, K. Yamada and H. Tsukuma, Nucl. Phys. **A496** (1989), 224.
51) K. Yamada, K. Takada and H. Tsukuma, Nucl. Phys. **A496** (1989), 239.
52) K. Yamada and K. Takada, Nucl. Phys. **A503** (1989), 53.
53) H. Aiba, Prog. Theor. Phys. **83** (1990), 358; **84** (1990), 908.
54) K. Yamada, Prog. Theor. Phys. **85** (1991), 805.
55) K. Yamada, Prog. Theor. Phys. **89** (1993), 995.
56) M. Matsuzaki, Y. R. Shimizu and K. Matsuyanagi, Prog. Theor. Phys. **79** (1988), 836.
57) Y. Tanaka and S. Suekane, Prog. Theor. Phys. **66** (1981), 1639.
58) K. E. G. Löbner, M. Vetter and V. Hönig, Nculear Data Tables **A7** (1970), 495.
59) R. Wyss, W. Satuła, W. Nazarewicz and A. Johnson, Nucl. Phys. **A511** (1990), 324.
60) A. V. Afanasjev, D. B. Fossan, G. J. Lane and I. Ragnarsson, Phys. Rep. **322** (1999), 1.
61) E. R. Marshalek, Nucl. Phys. **A275** (1977), 416; **A331** (1979), 429.
62) D. Janssen and I. N. Mikhailov, Nucl. Phys. **A318** (1979), 390.
63) J. I. Egido, H. J. Mang and P. Ring, Nucl. Phys. **A339** (1980), 390.
64) V. G. Zelevinsky, Nucl. Phys. **A344** (1980), 109.
65) R. Bengtsson, I. Hamamoto and B. Mottelson, Phys. Lett. **73B** (1978), 259.

Symmetry-unrestricted Skyrme–Hartree–Fock–Bogoliubov calculations for exotic shapes in $N = Z$ nuclei from ^{64}Ge to ^{84}Mo

M. Yamagami [a], K. Matsuyanagi [a,*], M. Matsuo [b]

[a] *Department of Physics, Graduate School of Science, Kyoto University, Kyoto 606-8502, Japan*
[b] *Graduate School of Science and Technology, Niigata University, Niigata 950-2101, Japan*

Abstract

By performing fully 3D symmetry-unrestricted Skyrme–Hartree–Fock–Bogoliubov calculations, we discuss shape coexistence and possibility of exotic deformations simultaneously breaking the reflection and axial symmetries in proton-rich $N = Z$ nuclei: ^{64}Ge, ^{68}Se, ^{72}Kr, ^{76}Sr, ^{80}Zr and ^{84}Mo. Results of calculation indicate that the oblate ground state of ^{68}Se is extremely soft against the Y_{33} triangular deformation, and that the low-lying spherical minimum coexisting with the prolate ground state in ^{80}Zr is extremely soft against the Y_{32} tetrahedral deformation. © 2001 Elsevier Science B.V. All rights reserved.

1. Introduction

The Hartree–Fock–Bogoliubov (HFB) method with the Skyrme interactions is one of the standard approaches in nuclear structure research [1,2]. In the last two decades it has become possible to solve the HFB equations directly in the coordinate mesh space [3,4]. In recent years, in order to investigate the structure of drip-line nuclei, the need for such coordinate-space HFB calculations has been greatly increased and intensive analyses have been made for neutron radii and skins in spherical neutron-rich nuclei [5–11]: since the easier HF plus BCS method breaks down when treating the pairing correlation in weakly bound systems due to a leakage of nucleons into the continuum, we need to calculate

---

* Corresponding author.
E-mail address: ken@ruby.scphys.kyoto-u.ac.jp (K. Matsuyanagi).

the mean-field (particle–hole) correlations and the pairing (particle–particle) correlations selfconsistently in order to preserve confinement of the nuclear density while allowing the pairing excitations to positive-energy resonant states [3] (see, e.g., [12] and references therein for mean-field approaches other than the Skyrme–HFB method).

Recently, Terasaki, Heenen, Flocard and Bonche [13,14] have removed the restriction of spherical symmetry in solving the coordinate-space Skyrme–HFB equations in order to investigate the possibility to get three-dimensional (3D) deformed solutions in neutron rich nuclei. In their works, a Skyrme interaction is used to describe the Hartree–Fock (HF) Hamiltonian while a density-dependent zero-range interaction is used for the pairing channel. The mean-field HF equations are solved by the imaginary-time evolution method [15] in a 3D cubic mesh space while the HFB equations are solved in terms of the two-basis method developed earlier in [16,17]. The discretization in 3D mesh space has the advantage over methods relying on an expansion in the harmonic-oscillator basis that nuclei with exotic deformations can be treated at the same level of accuracy [18–20]. In these works, however, reflection symmetries with respect to three planes are imposed for the nuclear density so that only one spatial octant is needed to solve the HFB equations.

The major purpose of this paper is to extend their method by removing the symmetry restrictions mentioned above and investigate the possibility of exotic shapes simultaneously breaking the axial and reflection symmetries in the mean field. For this purpose, we have constructed a new computer code that carries out Skyrme–HFB calculations in the 3D cartesian-mesh space without imposing any restrictions on the spatial symmetry. Recently, on the basis of the Skyrme HF plus BCS calculations with no restriction on the nuclear shape, Takami, Yabana and Matsuo [21,22] suggested that the oblate ground state of ^{68}Se is extremely soft against the Y_{33} triangular deformation, and that the low-lying "spherical" minimum coexisting with the prolate ground state in ^{80}Zr has the Y_{32} tetrahedral shape. As the first application of a fully 3D, symmetry-unrestricted Skyrme HFB method with the use of the density-dependent zero-range pairing interaction [13,14,17,23–30], we investigate in this paper shape coexistence and possibility of nonaxial octupole deformations in proton rich $N = Z$ nuclei in the $A = 64$–84 region and examine the above predictions. These nuclei are especially interesting objects to study, since proton and neutron deformed shell effects act coherently and rich possibilities arise for coexistence and competition of different shapes (see [31] for earlier references). In recent years, active experimental studies of these nuclei are going on by means of combinations of radioactive nuclear beams and new gamma-ray and charged-particle detector systems (see [32–35] for reviews). It should be noted here that, although extensive theoretical calculations and rich experimental evidences have been accumulated for axially symmetric octupole (Y_{30}) deformations, as reviewed in [36,37], only a few calculations using Woods–Saxon–Strutinsky methods are available [38–41] except for light nuclei, and no firm experimental evidence exists up to now concerning the nonaxial octupole (Y_{31}, Y_{32}, Y_{33}) deformations in the mean fields. For light nuclei, nonaxial octupole deformations have been discussed [42–46] in connection with alpha-cluster structures [47]; for instance, a triangular structure of ^{12}C [42,44] and a tetrahedral shape for ^{16}O [45,46].

Our motive for developing the coordinate-space Skyrme–HFB method is not only to investigate the possibilities of emergence of new types of symmetry breakdown in the ground states of proton-rich and neutron-rich nuclei, but also to investigate, in the future, low-lying modes of excitation of such unstable nuclei by means of the RPA and the Selfconsistent Collective Coordinate (SCC) method [48] on the basis of the HFB basis thus obtained. We intend to proceed in parallel with other calculations with the use of more phenomenological shell model potentials and separable interactions. The Skyrme–HFB method is suited for this aim, as it provides a local mean-field potential so that such a comparative study is easy.

In Section 2, a brief account of the method of the coordinate-space Skyrme–HFB calculation is given. In Section 3, results of numerical calculation are presented and discussed. In Section 4, a conclusion is given.

2. Skyrme–HFB calculation

2.1. Two basis method

For convenience, we here recapitulate the two basis method [13,14,16,17] adopted as the algorithm of our computer code. In this method, the imaginary-time evolution method is combined with a diagonalization of the HFB Hamiltonian matrix to construct the canonical basis.

We first determine the single-particle wave functions ϕ_i satisfying the HF equations

$$h\big[\rho(\mathbf{r})\big]\phi_i(\mathbf{r}) = \varepsilon_i \phi_i(\mathbf{r}) \tag{1}$$

by means of the imaginary-time evolution method [15]. Here h, ε_i and $\rho(\mathbf{r})$ denote the mean-field Hamiltonian, the single-particle energies and the total nuclear density, respectively. (The isospin index τ is omitted for simplicity.) We next diagonalize the HFB Hamiltonian matrix [1]

$$\begin{pmatrix} h-\lambda & \Delta \\ -\Delta^* & -h^*+\lambda \end{pmatrix} \begin{pmatrix} U_k \\ V_k \end{pmatrix} = E_k \begin{pmatrix} U_k \\ V_k \end{pmatrix} \tag{2}$$

to get the one-body density matrix ρ and the pairing tensor κ:

$$\rho = V^* V^{\mathrm{T}}, \qquad \kappa = V^* U^{\mathrm{T}}. \tag{3}$$

We then diagonalize the density matrix ρ and obtain the occupation coefficients n_α and the unitary transformation W which relates the HF wave functions ϕ_i to the canonical basis wave functions φ_α:

$$\rho_{kl} = \sum_\alpha n_\alpha W_{k\alpha} W^{\dagger}_{\alpha l}, \tag{4}$$

$$\varphi_\alpha(\mathbf{r}) = \sum_j W_{j\alpha} \phi_j(\mathbf{r}). \tag{5}$$

In the canonical basis φ_α, the HFB density matrix in the coordinate space is diagonal:

$$\rho(\boldsymbol{r}, \boldsymbol{r}') = \sum_{\alpha} n_{\alpha} \varphi_{\alpha}(\boldsymbol{r}) \varphi_{\alpha}(\boldsymbol{r}')^*. \tag{6}$$

These steps are repeated until the convergence is achieved.

The single-particle wave functions and densities are represented on a full 3D cartesian-mesh space within a spherical container. In the present calculation, the radius of the spherical container and mesh spacing are set to $R_{\mathrm{mesh}} = 10.0$ fm and $h = 1.0$ fm, respectively. Tajima et al. [49,50] have carefully examined possible errors due to the use of the mesh size $h = 1.0$ fm and they found that, since discretization errors are essentially independent of the nuclear shape, deformation energies obtained with this mesh size are quite accurate (see also [51]). Actually, we have constructed the new Skyrme–HFB code by extending the cranked Skyrme–HF code [52] written previously and applied to the investigation of the yrast structure of ^{32}S, so that the cranking term can be included. In this paper, however, we examine only the cases of zero angular momentum.

2.2. The Skyrme plus density-dependent pairing interactions

We use the SIII parameter set [53] of the Skyrme interaction for the mean-field (particle–hole) channel, which has been successful in describing systematically the ground-state quadrupole deformations in proton and neutron rich Kr, Sr, Zr and Mo isotopes [19] and in a wide area of nuclear chart [49]. For the pairing (particle–particle) channel, we use the density-dependent zero-range interaction [13,14,17,23–30], which has been successful in describing, for instance, the odd–even staggering effects in charge radii:

$$V_{\mathrm{pair}}(\boldsymbol{r}_1, \boldsymbol{r}_2) = \frac{V_0}{2}(1 - \widehat{P}_{\sigma})\left(1 - \frac{\rho(\boldsymbol{r}_1)}{\rho_c}\right)\delta(\boldsymbol{r}_1 - \boldsymbol{r}_2) \tag{7}$$

with the notation of [17], where the strength V_0 and the density ρ_c are parameters and $\widehat{P}_{\sigma}$ denotes the spin exchange operator. For these parameters, we use the standard values [14,17]: $V_0 = -1000.0$ MeV fm^3, $\rho_c = 0.16$ fm^{-3}. The pairing interaction is smoothly cut off at 5 MeV above the Fermi energy in the same way as in [19]. For a more general form of the density-dependent pairing interaction, we refer to [54,55].

To check the dependence on the Skyrme-interaction parameter sets, we make calculations with the SkM* [56] and SLy4 [57] sets for an example of ^{68}Se. We refer to a recent work by Reinhard et al. [58] for a detailed and systematic study of shape coexistence phenomena in relation to the properties of various versions of the Skyrme interaction. We shall also check the dependence on the pairing strength V_0 adopted.

2.3. Constrained HFB calculation

In order to investigate the deformation properties away from the HFB equilibrium points, we perform constrained HFB calculations with the use of the quadratic constraints for the mass-quadrupole (octupole) moments [59] to obtain the energy surfaces as functions of the quadrupole (octupole) deformations. Because no spatial symmetry is imposed on the 3D mesh space, the center of mass and the directions of the principal axes of the nucleus can move freely without affecting the total energy. To evaluate the physical quantities like

deformation parameters, it is crucially important to fulfill the constraints to keep the center of mass,

$$\left\langle \sum_{i=1}^{A} x_i \right\rangle = \left\langle \sum_{i=1}^{A} y_i \right\rangle = \left\langle \sum_{i=1}^{A} z_i \right\rangle = 0, \tag{8}$$

and the directions of the principal axes,

$$\left\langle \sum_{i=1}^{A} (xy)_i \right\rangle = \left\langle \sum_{i=1}^{A} (yz)_i \right\rangle = \left\langle \sum_{i=1}^{A} (zx)_i \right\rangle = 0. \tag{9}$$

These requirements are taken care of by means of the quadrupole constraints on these conditions as in our previous study [52].

2.4. Deformation parameters

As measures of the deformation, we calculate the mass-multipole moments,

$$\alpha_{lm} = \frac{4\pi}{3AR^l} \int r^l X_{lm}(\Omega) \rho(\mathbf{r}) \, d\mathbf{r} \quad (m = -l, \ldots, l) \tag{10}$$

where $\rho(\mathbf{r}) = \sum_\alpha v_\alpha^2 |\varphi_\alpha(\mathbf{r})|^2$, $R = 1.2A^{1/3}$ fm and X_{lm} are real bases of the spherical harmonics:

$$X_{l0} = Y_{l0}, \tag{11}$$

$$X_{l|m|} = \frac{1}{\sqrt{2}} \left(Y_{l-|m|} + Y_{l-|m|}^* \right), \tag{12}$$

$$X_{l-|m|} = \frac{-i}{\sqrt{2}} \left(Y_{l|m|} - Y_{l|m|}^* \right). \tag{13}$$

Here the quantization axis is chosen as the largest (smallest) principal axis for prolate (oblate) solutions. We then define the quadrupole deformation parameter β_2, the triaxial deformation parameter γ, and the octupole deformation parameters β_3 and β_{3m} by

$$\alpha_{20} = \beta_2 \cos\gamma, \qquad \alpha_{22} = \beta_2 \sin\gamma, \tag{14}$$

$$\beta_3 = \left(\sum_{m=-3}^{3} \alpha_{3m}^2 \right)^{1/2}, \qquad \beta_{3m} = \left(\alpha_{3m}^2 + \alpha_{3-m}^2 \right)^{1/2} \quad (m = 0, 1, 2, 3). \tag{15}$$

For convenience, we also use the familiar notation $-\beta_2$ for oblate shapes with $(\beta_2, \gamma = 60°)$.

3. Results and discussion

3.1. Quadrupole deformations

The solutions of the Skyrme–HFB equations obtained in the numerical calculations for ^{64}Ge, ^{68}Se, ^{72}Kr, ^{76}Sr, ^{80}Zr and ^{84}Mo are summarized in Table 1. The calculated ground-state shape changes from triaxial (^{64}Ge), oblate (^{68}Se, ^{72}Kr), large prolate (^{76}Sr, ^{80}Zr), to

Table 1
Solutions of the HFB equations for proton-rich $N = Z$ nuclei in the $A = 64$–84 region

	Oblate	Spherical	Prolate
^{64}Ge			g.s.
			$\beta, \gamma = 0.27, 25°$ (triaxial)
			$\beta_3 = 0.0$
			$\Delta_p = 1.25,\ \Delta_n = 1.12$
^{68}Se	g.s.		0.52
	$\beta, \gamma = 0.28, 60°$		$\beta, \gamma = 0.26, 0°$
	$\beta_3 = \beta_{33} \approx 0.08$		$\beta_3 = 0.0$
	$\Delta_p = 1.28,\ \Delta_n = 1.13$		$\Delta_p = 1.29,\ \Delta_n = 1.15$
^{72}Kr	g.s.		0.92
	$\beta, \gamma = 0.32, 60°$		$\beta, \gamma = 0.40, 0°$
	$\beta_3 = 0.0$		$\beta_3 = 0.0$
	$\Delta_p = 1.03,\ \Delta_n = 1.23$		$\Delta_p = 1.25,\ \Delta_n = 0.92$
^{76}Sr	1.79		g.s.
	$\beta, \gamma = 0.30, 60°$		$\beta, \gamma = 0.51, 0°$
	$\beta_3 = \beta_{33} \approx 0.0$		$\beta_3 = 0.0$
	$\Delta_p = 1.47,\ \Delta_n = 1.43$		$\Delta_p = 0.67,\ \Delta_n = 0.50$
^{80}Zr	0.86	1.01	g.s.
	$\beta, \gamma = 0.20, 60°$	$\beta, \gamma = 0.0, 0°$	$\beta, \gamma = 0.51, 0°$
	$\beta_3 = 0.0$	$\beta_3 = \beta_{32} \approx 0.15$	$\beta_3 = 0.0$
	$\Delta_p = 1.02,\ \Delta_n = 0.82$	$\Delta_p = 0.68,\ \Delta_n = 0.39$	$\Delta_p = 0.79,\ \Delta_n = 0.78$
^{84}Mo	0.20	g.s.	1.52
	$\beta, \gamma = 0.16, 60°$	$\beta, \gamma = 0.0, 0°$	$\beta, \gamma = 0.66, 0°$
	$\beta_3 = 0.0$	$\beta_3 = \beta_{30} \approx 0.0$	$\beta_3 = 0.0$
	$\Delta_p = 1.46,\ \Delta_n = 1.42$	$\Delta_p = 0.74,\ \Delta_n = 0.72$	$\Delta_p = 0.0,\ \Delta_n = 0.0$

For each nucleus, numbers in the first line indicate excitation energies measured from the ground state. The symbol $\approx$ indicates that the potential-energy curve is extremely shallow about the equilibrium value. Pairing gaps Δ_p and Δ_n are here defined as averages of diagonal elements $\Delta_{i\bar{i}}$ over 5 MeV interval around the Fermi surface, and their values (in MeV) at the equilibrium deformations are listed.

spherical shape (^{84}Mo) with increasing N ($= Z$). For ^{68}Se, ^{72}Kr, ^{76}Sr, ^{80}Zr and ^{84}Mo, we obtain two or three local minima close in energy, indicating shape coexistence. These gross features are consistent with available experimental data [60–66] and previous theoretical calculations [19,21,22,49,67–77].

The potential-energy curves obtained by the constrained HFB calculations are displayed in Fig. 1 as functions of the quadrupole deformation parameter β_2 and in Fig. 2 as functions of the triaxial deformation parameter γ. Below we remark on some specific points.

As seen in Fig. 2, the calculated potential-energy curve for ^{64}Ge is rather shallow with respect to the γ degree of freedom so that this nucleus may be regarded as "γ-soft." This result is consistent with the experimental indication [60] and also with the shell model calculation by the Monte Carlo diagonalization method [75].
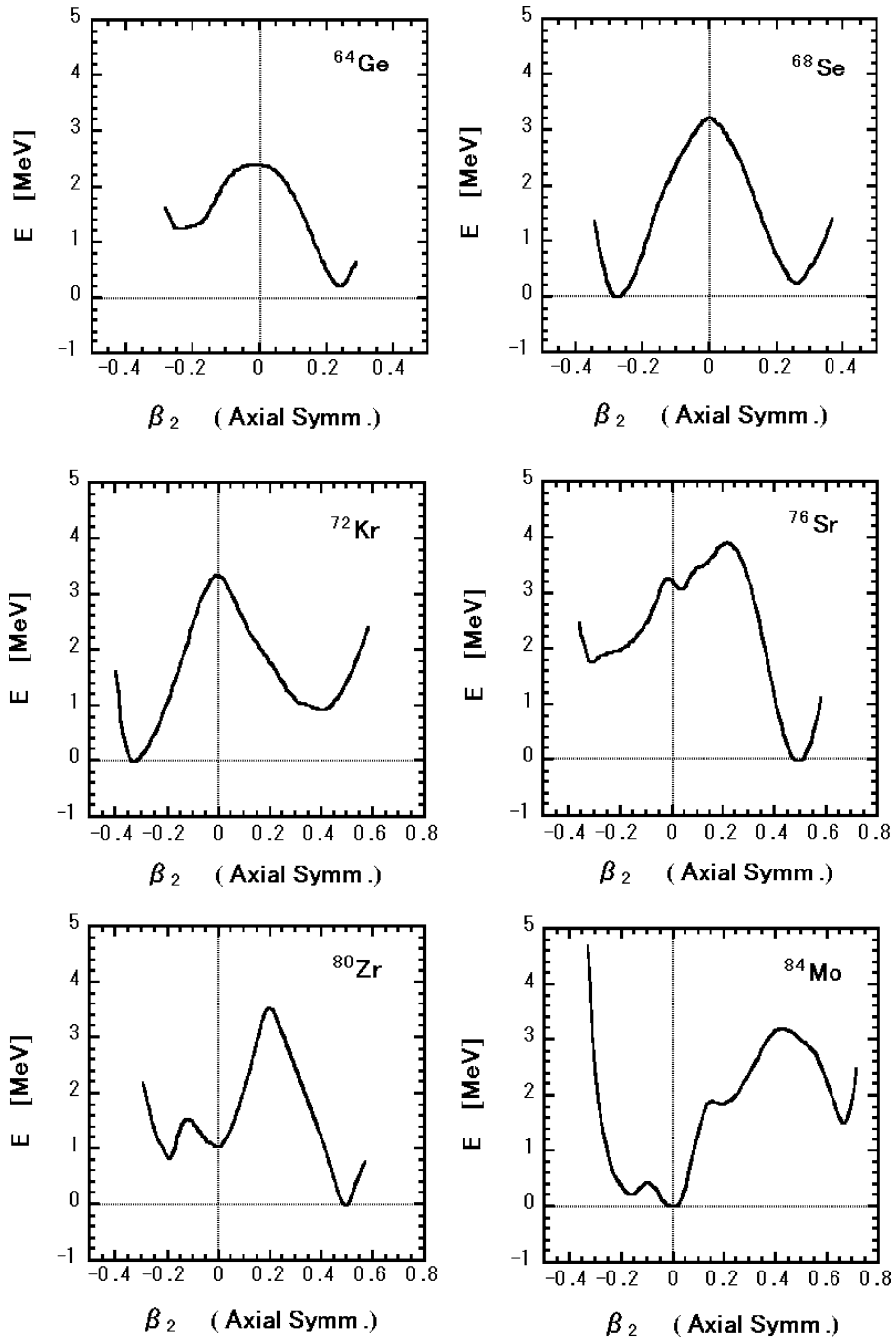
Fig. 1. Potential-energy curves calculated by the constrained Skyrme–HFB method for ^{64}Ge, ^{68}Se, ^{72}Kr, ^{76}Sr, ^{80}Zr and ^{84}Mo are drawn as functions of the quadrupole deformation parameter β_2. The SIII interaction is used for the particle–hole channel, while the density-dependent pairing interaction with $V_0 = -1000.0$ MeV fm^3 and $\rho_c = 0.16$ fm^{-3} is used for the particle–particle channel.
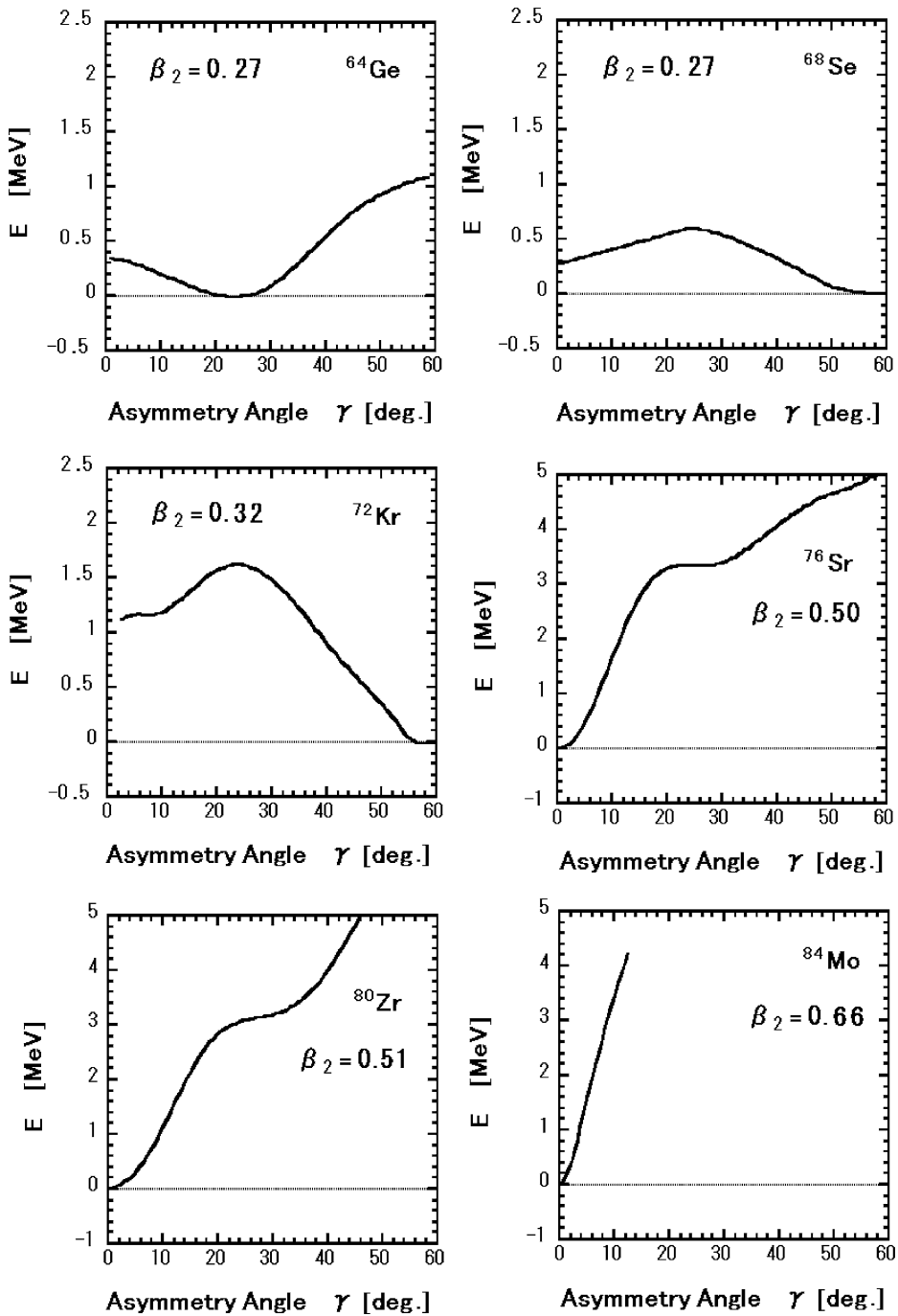
Fig. 2. Potential-energy curves calculated at fixed β_2 by the constrained Skyrme–HFB method for ^{64}Ge, ^{68}Se, ^{72}Kr, ^{76}Sr, ^{80}Zr and ^{84}Mo are drawn as functions of the triaxial deformation parameter γ. The effective interactions used are the same as in Fig. 1.

Quite recently, an excited prolate band coexisting with the ground-state oblate band has been found in ^{68}Se [63]. Their quadrupole deformations are estimated as $\beta_2 \approx 0.27$ and $\beta_2 \approx -0.27$, respectively. Although the prolate excited band-head 0^+ state has not yet been observed, its excitation energy is estimated to be about 0.6 MeV. Our calculated energy difference between the prolate and the oblate HFB solutions, 0.52 MeV, is in good agreement with this experimental data. The barrier between the prolate and the oblate minima is about 3 MeV in the plot with respect to β_2 in Fig. 1, but it is only about 0.3 MeV in the plot with respect to the triaxial deformation parameter γ in Fig. 2. It might be considered that, if the barrier is so low, the two bands built on the prolate and the oblate solutions interact strongly so that the shape coexistence picture is too much perturbed in contradiction with the experiment [63]. In our view, however, description of dynamics by going beyond the static mean-field approximation is necessary in order to discuss the interaction between the oblate and the prolate structures. In any case, understanding this shape coexistence dynamics is an interesting subject for future.

The second minimum with $\beta_2 \approx 0.66$ seen in the potential-energy curve for ^{84}Mo in Fig. 1 may be regarded as a superdeformed solution, since it is related to the $Z = N = 42$ deformed shell gap [68] formed by occupying the down-sloping [431]1/2 levels from the upper major shell by two protons and two neutrons. This second minimum was also obtained in [21]. It offers an interesting possibility that a superdeformed rotational band might be observed at such a low excitation energy as about 1.5 MeV. From a viewpoint of deformed shell structure, the ground-state solutions for ^{76}Sr and ^{80}Zr have characteristics different from the second minimum in ^{84}Mo and may be distinguished from the superdeformation, although they have large prolate deformations of $\beta_2 \approx 0.5$.

3.2. Nonaxial octupole deformations

As a result of the Skyrme–HFB calculations for proton-rich $N = Z$ nuclei from ^{64}Ge to ^{84}Mo (summarized in Table 1), we have found equilibrium shapes with finite nonaxial octupole deformations for ^{68}Se and ^{80}Zr. The density distribution at the HFB local minimum for ^{68}Se with the triangular deformation superposed on the oblate shape and that for ^{80}Zr with the tetrahedral deformation are illustrated in Fig. 3.
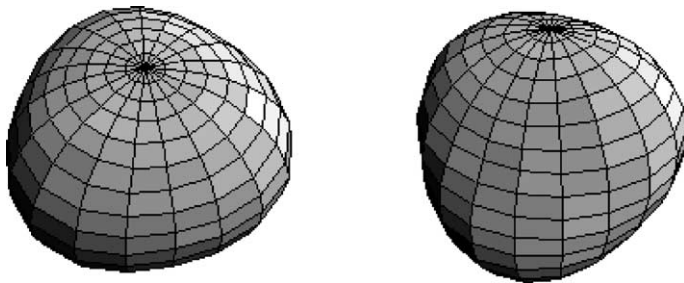

Fig. 3. Density contour surfaces at the half central density of the Skyrme–HFB solution with the oblate plus triangular shape ($\beta_2 = -0.28$, $\beta_{33} = 0.08$) for ^{68}Se (left-hand side) and that with the tetrahedral shape ($\beta_2 = 0.00$, $\beta_{32} = 0.15$) for ^{80}Zr (right-hand side), listed in Table 1.
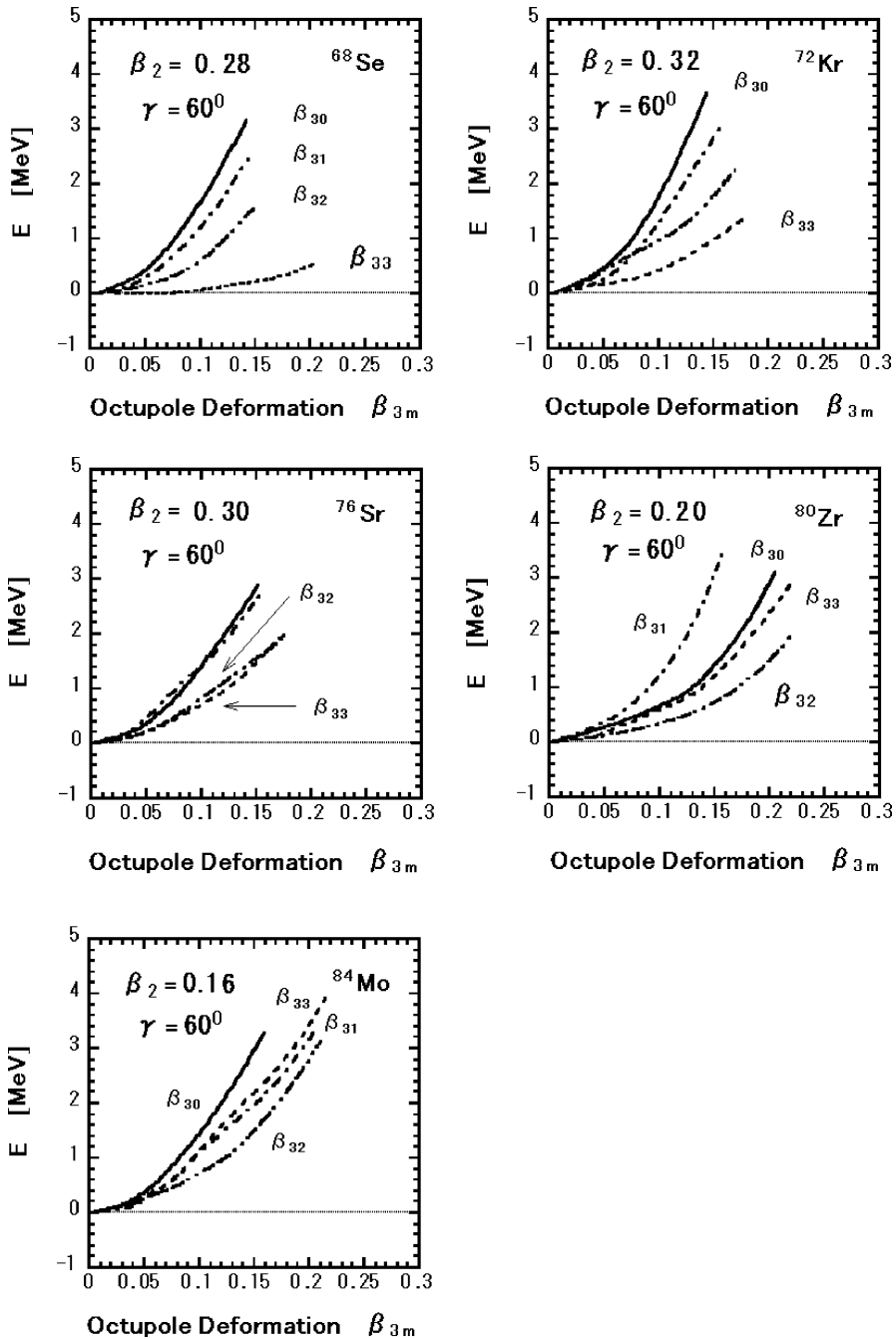
Fig. 4. Potential-energy curves calculated by the constrained Skyrme–HFB method are drawn as functions of the octupole deformation parameters β_{3m} ($m = 0, 1, 2, 3$) about the oblate minima (seen in Fig. 1) of the quadrupole deformation energies. One of the β_{3m} ($m = 0, 1, 2, 3$) is varied while the other β_{3m}'s are fixed to zero. The effective interactions used are the same as in Fig. 1.

In addition to the two cases mentioned above, Takami et al. [21] and Matsuo et al. [22] obtained, in their Skyrme–HF plus BCS calculations, finite equilibrium values of octupole deformations superposed on an oblate shape in ^{76}Sr and also on a near spherical shape in ^{84}Mo. According to their calculations, the potential-energy curves are very soft with respect to the octupole deformation degrees of freedom especially in the four cases mentioned above. In order to see the properties of the potential-energy curve in the neighborhood of the HFB equilibrium points and to make a better comparison with the results of Refs. [21,22], we have carried out constrained HFB calculations with respect to the β_{3m} ($m = 0, 1, 2, 3$) degrees of freedom about the local minima (seen in Fig. 1) of the quadrupole deformation energies.

Figs. 4, 5 and 6 show the potential-energy curves with respect to the octupole deformation parameters β_{3m} about the oblate, the spherical and the prolate (or triaxial) minima of the quadrupole deformation-energy curves, respectively. These curves are obtained by the constrained HFB calculations with the octupole operators $r^3 X_{3|m|}$ as constraints. We see that the oblate shape of ^{68}Se is extremely soft against the triangular (β_{33}) deformation and that the spherical shape of ^{80}Zr is extremely soft against the tetrahedral (β_{32}) deformation, in agreement with those of the Skyrme–HF plus BCS calculations of Refs. [21,22]. The oblate shape of ^{76}Sr is fairly soft with respect to the β_{32} and β_{33} deformations and the spherical ground state of ^{84}Mo is barely stable against all β_{3m} degrees of freedom, especially against β_{30}. In [22] an oblate solution with a finite equilibrium value of β_{32} is obtained for ^{76}Sr, while a similar solution for ^{76}Sr but with a finite equilibrium value of β_{33} and also a nearly spherical solution for ^{84}Mo with a finite equilibrium value of β_{30} is reported in [21]. Although such details differ depending on the treatment of the pairing correlations, the basic features, i.e., the softness to both β_{32} and β_{33} of the oblate shape of ^{76}Sr and the softness to β_{30} of the spherical shape of ^{84}Mo are in common between the present HFB calculations and those of [21,22]. Generally speaking, Figs. 4–6 indicate that the oblate shapes are softer for octupole deformations β_{3m} with higher values of m, while the prolate shapes favor lower values of m.
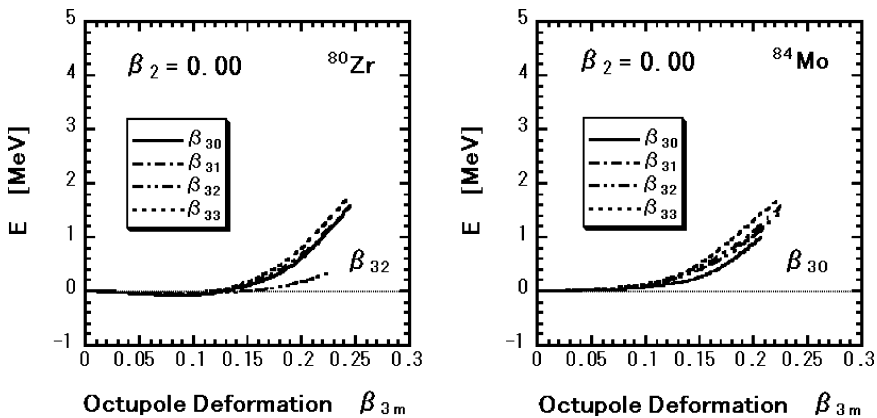

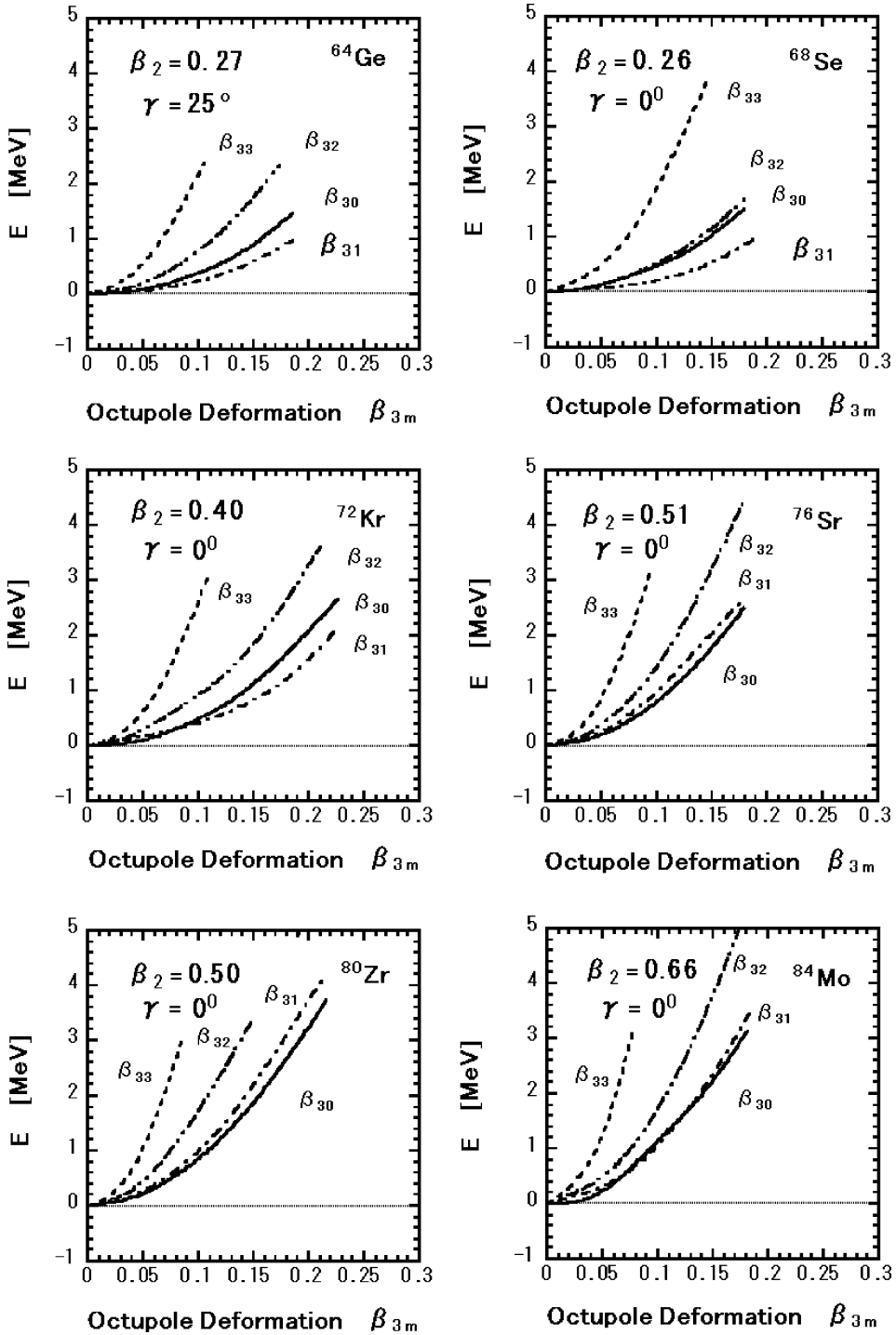Fig. 5. Same as Fig. 4 but about the spherical minima.

Fig. 6. Same as Fig. 4 but about the prolate minima (the triaxial minimum in the case of ^{64}Ge).

Below we focus our attention on the triangular deformation in ^{68}Se and the tetrahedral shape in ^{80}Zr and discuss about the microscopic origins of them.

3.2.1. Triangular deformation in ^{68}Se

Generally speaking, octupole correlations are associated with strong couplings between the shell-model orbits with $\Delta l = \Delta j = 3$ [36,37]. In the $A = 64$–84 region under consideration, they are $1g_{9/2}$ and $2p_{3/2}$. In order to understand why the oblate shape in ^{68}Se is unstable (or extremely soft) against the triangular deformation, however, we need to examine the interplay of the quadrupole and octupole deformation effects. Namely, as explained below, the emergence of the triangular deformation is strongly correlated with the magnitude of the oblate deformation.

When ^{68}Se ($N = Z = 34$) is oblately deformed, the high Ω levels $[404]\frac{9}{2}$ and $[413]\frac{7}{2}$ stemming from the $1g_{9/2}$ orbit go down in energy and approach the Fermi surfaces for $N = Z = 34$ and strong Y_{33} couplings with $[301]\frac{3}{2}$ and $[310]\frac{1}{2}$ levels (associated with the $2p_{3/2}$ orbit) take place. These Y_{33} coupling effects are seen as repulsions between these levels in Fig. 7 which displays the neutron single-particle energies as functions of the triangular deformation parameter β_{33}. Here, the single-particle energies mean eigenvalues of the HF Hamiltonian with the density $\rho(\boldsymbol{r})$ determined by the HFB equations, and the asymptotic Nilsson quantum numbers are used only for convenience of labeling these levels: they are, of course, not good quantum numbers.

In this figure, results of calculation with use of the SkM* and SLy4 interactions are also shown for comparison. We note that the Y_{33} coupling effects are slightly weaker in the case of the SkM* and SLy4 interactions in comparison with the case of the SIII interaction. This is because the spacings between the levels coupled by the Y_{33} operator are the smallest for the SIII interaction: the spacings at the oblate equilibrium deformations between the [404]9/2 and [301]3/2 levels are about 2.8, 3.4 and 3.6 MeV, and those between the [413]7/2 and [310]1/2 levels are about 3.8, 4.1 and 4.2 MeV for the SIII, SkM* and SLy4 interactions, respectively. Thus, as shown in Fig. 8, the potential-energy curve with respect to the triangular β_{33} deformation is softest for the case of the SIII interaction, although they are soft also for the cases of the SkM* and SLy4 interactions. Note that, in making this comparison, we have chosen the pairing-interaction strength V_0 such that the resulting pairing gaps Δ take about the same values for calculations with different Skyrme interactions (in order to make the effects of the pairing correlations approximately the same for all cases), as shown in the right-hand part of Fig. 8.

The importance of the triangular Y_{33} deformation superposed on the oblate shape was previously pointed out by Frisk, Hamamoto and May [78] in terms of a two-level model as well as the modified oscillator model which simulates the one-particle spectra in an infinite-well potential. Our result of the Skyrme–HFB calculation provides a realistic example which is consistent with their arguments.

3.2.2. Tetrahedral deformation in ^{80}Zr

As shown by Hamamoto, Mottelson, Xie and Zhang [79], the tetrahedral symmetry associated with the Y_{32} deformation brings about a bunching of the single-particle levels
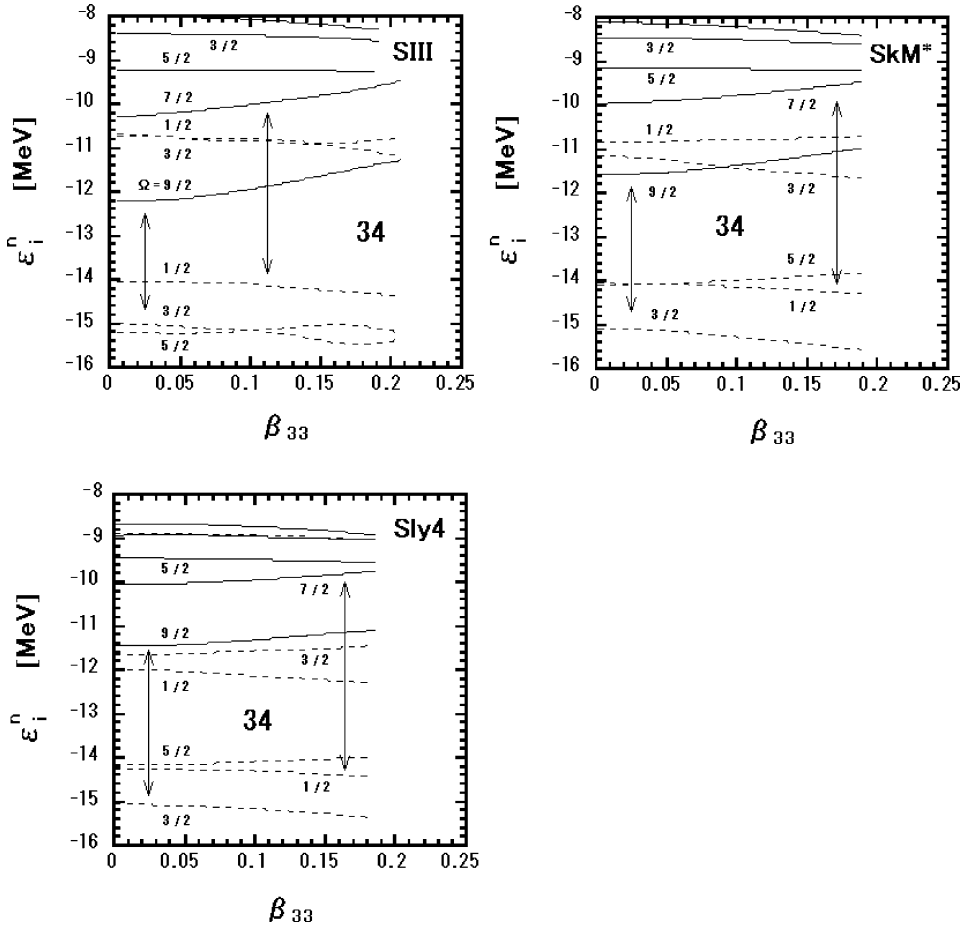
Fig. 7. Neutron single-particle energies for ^{68}Se plotted as functions of the octupole deformation parameter β_{33} about the oblate shape. Here, the single-particle energies mean eigenvalues of the HF Hamiltonian with the density $\rho(\boldsymbol{r})$ determined by the HFB equations. Results for the SIII, SkM* and SLy4 parameter sets are compared. Equilibrium quadrupole deformations obtained for each Skyrme interaction are $\beta_2 = -0.28, -0.25$ and -0.24 for SIII, SkM* and SLy4, respectively. Solid (broken) lines indicate levels which have positive (negative) parity in the limit $\beta_{33} = 0$. The projection of the angular momentum on the symmetry axis, Ω, is a good quantum number only at $\beta_{33} = 0$. The arrows indicate the $\Delta\Omega = 3$ coupling associated with the triangular Y_{33} deformation as discussed in the text. The single-particle spectrum for protons is almost the same as for neutrons.

and create a remarkable shell structure: the $N = Z = 40$ is one of the magic numbers for such tetrahedral shapes. Such a shell effect is common to various finite fermion systems, and in fact the tetrahedral deformation has been predicted, for instance, for sodium clusters consisting of 40 atoms by the density functional Kohn–Sham calculation [80,81], in which there is no spin–orbit coupling. The instability of the spherical shape of ^{80}Zr against the Y_{32} deformation, as exhibited in Fig. 5, is evidently connected to the magic number $N = Z = 40$ for the tetrahedral shape.
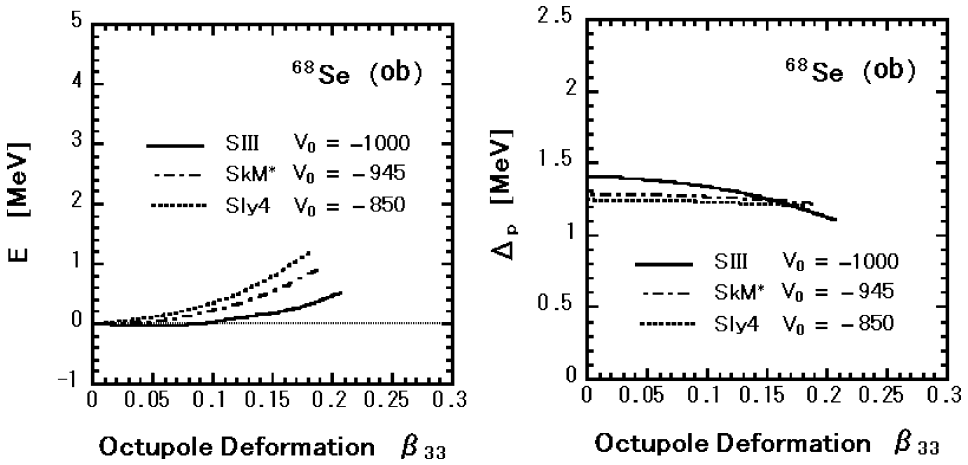
Fig. 8. Comparison of the HFB potential-energy curves for ^{68}Se about the oblate shape as functions of the triangular deformation parameter β_{33}, calculated for different versions of the Skyrme interaction (left-hand side). The pairing-interaction strengths V_0 are chosen such that the average pairing gaps become approximately equal for all Skyrme interactions (as displayed in the right-hand side). The calculated deformation parameter β_2 are -0.28, -0.25 and -0.24 for the SIII, SkM* and SLy4 interactions, respectively.

Fig. 9 shows the single-particle energy diagrams as function of octupole deformation parameter β_{3m} ($m = 0, 1, 2, 3$). As expected, we can see for the case of $m = 2$ a remarkable bunching of single-particle levels and an increase of the shell gap at $N = 40$ with increasing β_{32}, while the other octupole deformations ($m = 0, 1, 3$) do not exhibit such a feature. Looking into details, one notices a fine splitting of the $1g_{9/2}$ level into three levels which correspond to irreducible representations of the double tetrahedral (spinor-T_d) group [41,45]; a twofold-degenerate level and two fourfold-degenerate levels.

Thus, the tetrahedral shell gap at $N = Z = 40$ emerges even under the presence of the strong spin–orbit coupling. It should also be noted that the tetrahedral minimum is obtained in the calculation selfconsistently including the pairing correlations.

3.3. Pairing gaps

In this subsection, we first examine dependence of the pairing gaps on deformations, and then discuss dependence of the nonaxial octupole deformations on the pairing strength. The result of calculation for the pairing gaps at equilibrium deformations in each nucleus is listed in Table 1. As the pairing gaps in the HFB theory depend on single-particle levels, the numbers listed in this table are averages of the diagonal elements in the HF basis, $\Delta_{i\bar{i}}$, over 5 MeV interval in the vicinity of the Fermi surfaces.

In the literature, slightly different quantities like averages of the diagonal matrix elements in the canonical basis, $\Delta_{\alpha\bar{\alpha}}$, weighted by the coefficients of the Bogoliubov transformation, $u_\alpha v_\alpha$ [82–84] or v_α^2 [3], are used for similar purposes. Fig. 10 compares these quantities for the case of triangular deformations superposed on the oblate shape in ^{68}Se. We see that the two average quantities, $\langle \Delta_{i\bar{i}} \rangle$ and $\langle \Delta_{\alpha\bar{\alpha}} u_\alpha v_\alpha \rangle$, are approximately
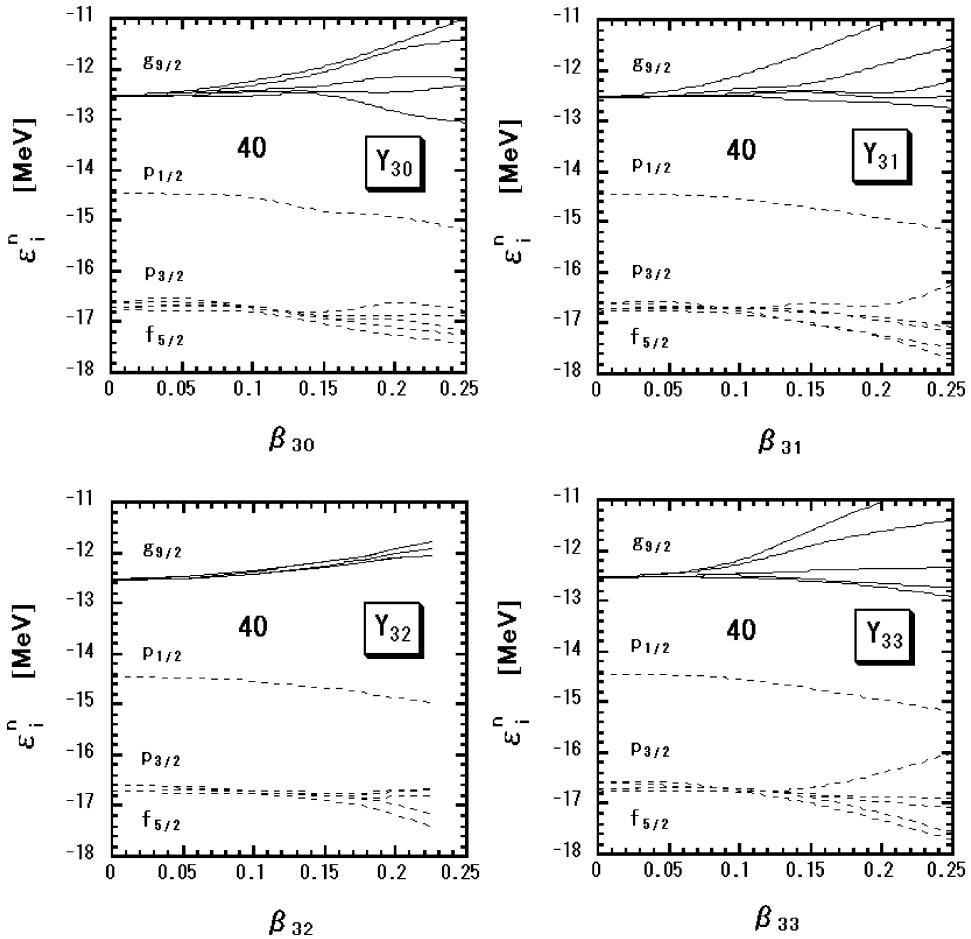
Fig. 9. Neutron single-particle energies for ^{80}Zr plotted as functions of the octupole deformation parameters β_{3m} ($m = 0, 1, 2, 3$) about the spherical shape. Here, the single-particle energies mean eigenvalues of the HF Hamiltonian with the density $\rho(r)$ determined by the HFB equations. The SIII interaction is used. Solid (broken) lines indicate levels which have positive (negative) parity in the limit $\beta_{32} = 0$. The single-particle spectrum for protons is almost the same as for neutrons.

equal. We also confirm that the averages do not significantly depend on the averaging interval.

Figs. 11, 12 and 13 display the variation of the pairing gaps with the quadrupole deformation parameter β_2, the triaxial deformation parameter γ, and the octupole deformation parameters β_{3m} ($m = 0, 1, 2, 3$), respectively. We observe that gross features of deformation dependence of the pairing gap correlate with the corresponding potential-energy curves displayed in Figs. 1, 2 and 4–6. Such correlations are rather easy to be understood from the behavior of the single-particle level density near the Fermi surface, i.e., from the well-known (spherical or deformed) shell effects that the level density near the Fermi surface becomes relatively low in the vicinities of the local minima of the potential-
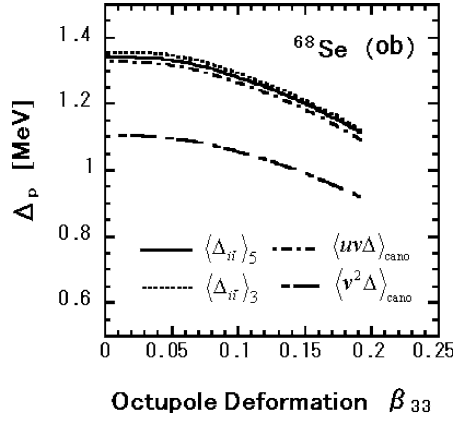
Fig. 10. Comparison of differently defined average pairing gaps for ^{68}Se, plotted as functions of the triangular deformation parameter β_{33} superposed on the oblate shape. Here, $\langle \Delta_{i\bar{i}} \rangle_{\Delta E} = \sum_i f_i f_{\bar{i}} g_i g_{\bar{i}} \Delta_{i\bar{i}} \big/ \sum_i f_i f_{\bar{i}} g_i g_{\bar{i}}$, $\langle uv\Delta \rangle_{\text{cano}} = \sum_\alpha u_\alpha v_\alpha \langle \varphi_\alpha | \Delta | \varphi_\alpha \rangle \big/ \sum_\alpha u_\alpha v_\alpha$ [82–84] and $\langle v^2 \Delta \rangle_{\text{cano}} = \sum_\alpha v_\alpha^2 \langle \varphi_\alpha | \Delta | \varphi_\alpha \rangle \big/ \sum_\alpha v_\alpha^2$ [7], where $f_i = (1 + \exp[(\varepsilon_i - \lambda_{\text{F}} - \Delta E/2)/\mu])^{-1/4}$, $g_i = (1 + \exp[(\varepsilon_i - \lambda_{\text{F}} + \Delta E/2)/\mu])^{-1/4}$ with $\Delta E = 3$ or 5 MeV.
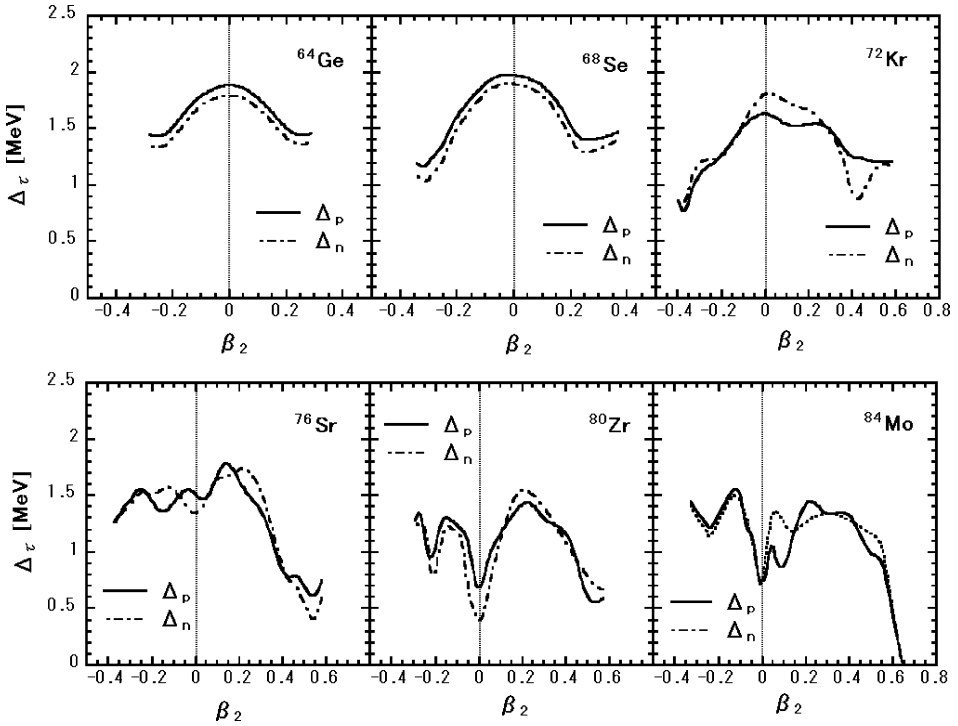
Fig. 11. Variations of the pairing gaps Δ_τ ($\tau = $ p, n) calculated by the constrained Skyrme–HFB method as functions of the quadrupole deformation parameter β_2 for ^{64}Ge, ^{68}Se, ^{72}Kr, ^{76}Sr, ^{80}Zr and ^{84}Mo. The effective interactions used are the same as in Fig. 1.
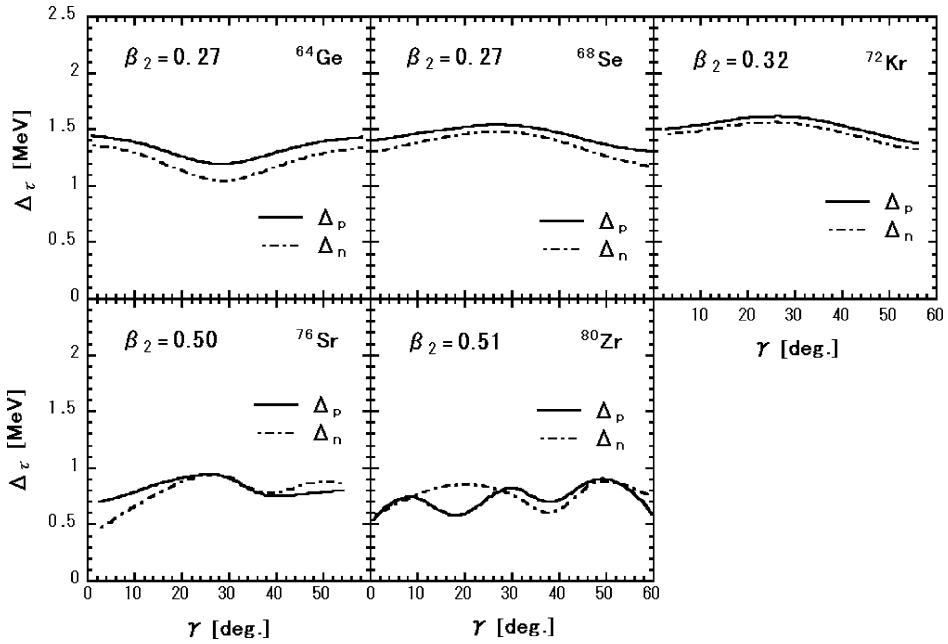
Fig. 12. Variations of the pairing gaps Δ_τ ($\tau =$ p, n) calculated by the constrained Skyrme–HFB method as functions of the triaxial deformation parameter γ at fixed β_2 for ^{64}Ge, ^{68}Se, ^{72}Kr, ^{76}Sr and ^{80}Zr. The effective interactions used are the same as in Fig. 1.

energy curve [85]. Thus, the pairing correlation becomes weaker and the paring gap decreases near the local minima. On the other hand, the level density becomes relatively high and the pairing gap increases near the local maxima of the potential-energy curve.

Because of significant shape changes in the sequence of isotopes (isotones) in the $A = 64-84$ region, it is not always easy to extract the magnitudes of pairing correlations from experimental odd–even staggerings of binding energies and to assess the appropriateness of the pairing-interaction strength $V_0 = -1000$ MeV fm^3 used in our HFB calculations. Quite recently, however, Satuła, Dobaczewski and Nazarewicz [86] have proposed a method for separating out the pairing correlation effects from the deformed mean-field (single-particle energy) effects on the odd–even staggerings, and evaluated average pairing gaps; these are in the range $1.0-1.6$ MeV for the mass region under consideration [87]. We note that these values agree rather well with the well-known global trend $\overline{\Delta} = 12/\sqrt{A}$ MeV [88], which are in the range $1.3-1.5$ MeV for $A = 64-84$. Our calculated values of the pairing gaps, listed in Table 1 and drawn in Figs. 11–13, mostly lie in this range of values, so that we may say that the adopted strength for V_0 is reasonable.

Another possible source of ambiguity in evaluating the pairing gaps is the proton–neutron isoscalar pairings which are expected to play an important role in the $N = Z$ nuclei (see, for example, [89,90] and references therein). We have assumed that such isoscalar pairings are absent in the states under consideration. Although this assumption should be examined, there are some experimental indications [90,91] that this may be a fairly good
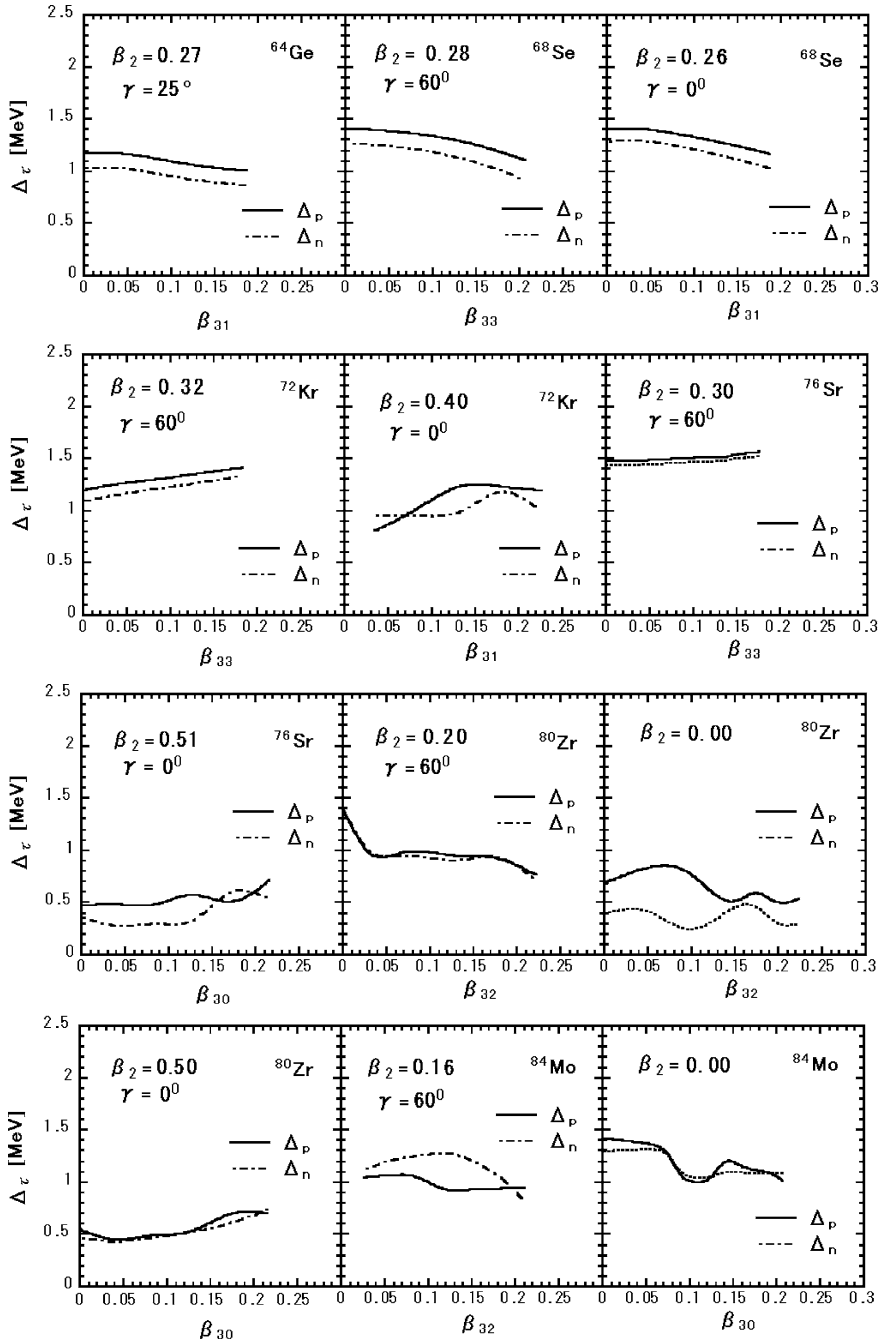
Fig. 13. Variations of the pairing gaps Δ_τ ($\tau = $ p, n) calculated by the constrained Skyrme–HFB method as functions of the octupole deformation parameter β_{3m} ($m = 0, 1, 2, 3$) about the local minima (seen in Fig. 1) of the quadrupole deformation energies for ^{64}Ge, ^{68}Se, ^{72}Kr, ^{76}Sr, ^{80}Zr and ^{84}Mo. The effective interactions used are the same as in Fig. 1.
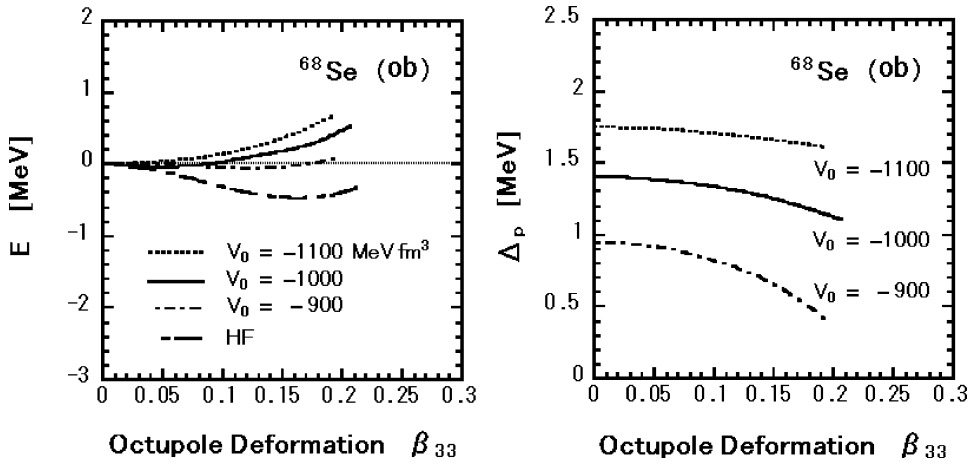
Fig. 14. Comparison of the potential-energy curves (left-hand side) and average pairing gaps for protons (right-hand side) calculated by the constrained Skyrme–HFB method as functions of the triangular deformation parameter β_{33} about the oblate shape for ^{68}Se with use of different strengths V_0 of the density-dependent pairing interaction (and with the same SIII interaction).

approximation. It is clear that we need a more systematic and detailed investigations, both theoretical calculations and experimental explorations, for a better understanding of the pairing correlations in the proton-rich $N = Z$ nuclei in the $A = 64−84$ region.

In order to examine the sensitivity of the calculated results to the strength V_0 of the pairing interaction, we have made a calculation of the potential-energy curve about the oblate shape in ^{68}Se as a function of the triangular octupole deformation parameter β_{33} for $V_0 = −900, −1000$ and $−1100$ MeV fm^3. The result is shown in Fig. 14. As expected, the potential-energy curve becomes shallower with increasing (absolute value of) V_0. Thus, the local minimum at $\beta_{33} \approx 0.10$ disappears with 10% increase of the (absolute) value of V_0. In any case, the potential is so shallow that we cannot associate a definite physical significance with the equilibrium values of β_{33}. We can still draw from these calculations an important conclusion that the oblate ground state of ^{68}Se is extremely soft with respect to the triangular octupole deformation.

3.4. Discussion

Actually, we need a more detailed investigation on the physical implication of the extremely soft potentials like those with respect to the triangular deformation in ^{68}Se and for the tetrahedral shape degree of freedom in ^{80}Zr. As is well known in the case of the axially symmetric Y_{30} octupole deformation [92–96], a definite minimum develops at finite value of β_{30} after the parity projection when the mean-field potential is very soft with respect to β_{30}. For the case of nonaxial octupole deformations, a similar effect of the parity projection has been demonstrated by Takami, Yabana and Ikeda [42] for light nuclei. It remains to be examined whether or not the situation is similar for the nonaxial octupole deformations in medium-mass nuclei under consideration.

More generally speaking, investigations of modes of excitation and of excitation spectra associated with the instabilities toward the nonaxial octupole shape deformations is one of the major challenges for future. The present paper should be regarded as providing a HFB mean-field basis for a study of dynamics by means of methods like the quasiparticle RPA and the SCC method [48].

4. Conclusion

We have constructed a new computer code that carries out Skyrme–HFB calculations in the 3-dimensional cartesian-mesh space without imposing any restriction on the spatial symmetry, and investigated shape coexistence and nonaxial octupole deformations in proton-rich $N = Z$ nuclei, ^{64}Ge, ^{68}Se, ^{72}Kr, ^{76}Sr, ^{80}Zr and ^{84}Mo. The ground-state shape changes from triaxial (^{64}Ge), oblate (^{68}Se, ^{72}Kr), large prolate (^{76}Sr, ^{80}Zr), to spherical (^{84}Mo) as $N (= Z)$ increases, in agreement with the available experimental data and the previous theoretical calculations. The extreme softness toward the Y_{33} triangular deformation of the oblate ground state of ^{68}Se and that toward Y_{32} tetrahedral deformation of the excited spherical minimum of ^{80}Zr, pointed out by Takami et al. [21,22] on the basis of the Skyrme–HF plus BCS calculations, have been confirmed by the fully selfconsistent Skyrme–HFB calculations with the use of the density-dependent zero-range pairing interaction.

The symmetry-unrestricted Skyrme–HFB computer code constructed in this work provides a selfconsistent mean-field basis for future investigation of collective modes of excitation in neutron-rich nuclei with neutron skins as well as in proton-rich nuclei.

References

[1] P. Ring, P. Schuck, The Nuclear Many-Body Problem, Springer-Verlag, Berlin, 1980.
[2] S. Åberg, H. Flocard, W. Nazarewicz, Annu. Rev. Nucl. Part. Sci. 40 (1990) 439.
[3] J. Dobaczewski, H. Flocard, J. Treiner, Nucl. Phys. A 422 (1984) 103.
[4] A. Bulgac, Preprint FT-194-1980, Bucharest, 1980, nucl-th/9907088.
[5] R. Smolańczuk, J. Dobaczewski, Phys. Rev. C 48 (1993) R2166.
[6] J. Dobaczewski, W. Nazarewicz, T.R. Werner, Z. Phys. A 354 (1996) 27.

[7] J. Dobaczewski, W. Nazarewicz, T.R. Werner, J.F. Berger, C.R. Chinn, J. Dechargé, Phys. Rev. C 53 (1996) 2809.

[8] S. Mizutori, J. Dobaczewski, G.A. Lalazissis, W. Nazarewicz, P.-G. Reinhard, Phys. Rev. C 61 (2000) 044326.

[9] P.-G. Reinhard, M. Bender, K. Rutz, J.A. Maruhn, Z. Phys. A 358 (1997) 277.

[10] N. Tajima, in: H. Horiuchi, M. Kamimura, H. Toki, F. Fujiwara, M. Matsuo, Y. Sakuragi (Eds.), Proc. Int. Symp. on Innovative Computational Methods in Nuclear Many-Body Problems, Osaka, Japan, November 10–15, 1997, World Scientific, Singapore, 1998, p. 343.

[11] N. Tajima, in: Proc. Int. Symp. on Models and Theories of the Nuclear Mass, Wako, Japan, July 19–23, 1999, RIKEN Review 26 (2000) 87.

[12] J. Meng, Nucl. Phys. A 635 (1998) 3.

[13] J. Terasaki, P.-H. Heenen, H. Flocard, P. Bonche, Nucl. Phys. A 600 (1996) 371.

[14] J. Terasaki, H. Flocard, P.-H. Heenen, P. Bonche, Nucl. Phys. A 621 (1997) 706.

[15] K.T.R. Davies, H. Flocard, S.J. Krieger, M.S. Weiss, Nucl. Phys. A 342 (1980) 111.

[16] B. Gall, P. Bonche, J. Dobaczewski, H. Flocard, P.-H. Heenen, Z. Phys. A 348 (1994) 183.

[17] J. Terasaki, P.-H. Heenen, P. Bonche, J. Dobaczewski, H. Flocard, Nucl. Phys. A 593 (1995) 1.

[18] H. Flocard, P.H. Heenen, S.J. Krieger, M.S. Weiss, Nucl. Phys. A 391 (1982) 285.

[19] P. Bonche, H. Flocard, P.-H. Heenen, S.J. Krieger, M.S. Weiss, Nucl. Phys. A 443 (1985) 39.

[20] P. Bonche, H. Flocard, P.H. Heenen, Nucl. Phys. A 467 (1987) 115.

[21] S. Takami, K. Yabana, M. Matsuo, Phys. Lett. B 431 (1998) 242.

[22] M. Matsuo, S. Takami, Y. Yabana, in: C. Baktash (Ed.), Proc. Int. Conf. on Nuclear Structure '98, Gatlinburg, TN, August 10–15, 1998, AIP Conference Proceedings, Vol. 481, American Institute of Physics, New York, 1999, p. 345.

[23] R.R. Chasman, Phys. Rev. C 14 (1976) 1935.

[24] G.F. Bertsch, H. Esbensen, Ann. Phys. 209 (1991) 327.

[25] V.E. Starodubsky, M.V. Zverov, Phys. Lett. B 276 (1992) 269.

[26] N. Tajima, P. Bonche, H. Flocard, P.-H. Heenen, M.S. Weiss, Nucl. Phys. A 551 (1993) 434.

[27] D. Zawischa, U. Regge, R. Stapel, Phys. Lett. B 185 (1987) 299.

[28] U. Regge, D. Zawischa, Phys. Rev. Lett. 61 (1988) 149.

[29] S.A. Fayans, S.V. Tolokonnikov, E.L. Trykov, D. Zawischa, Phys. Lett. B 338 (1994) 1.

[30] I.N. Borzov, S.A. Fayans, E. Krömer, D. Zawischa, Z. Phys. A 355 (1996) 117.

[31] J. Eberth, R.A. Meyer, K. Sisteich (Eds.), Nuclear Structure of the Zr Region, Springer, Berlin, 1988.

[32] J. Simpson, Nucl. Phys. A 654 (1999) 178c.

[33] W. Nazarewicz, Nucl. Phys. A 654 (1999) 195c.

[34] A.C. Mueller, Nucl. Phys. A 654 (1999) 215c.

[35] I. Tanihata, Nucl. Phys. A 654 (1999) 235c.

[36] I. Ahmad, P.A. Butler, Annu. Rev. Nucl. Part. Sci. 43 (1993) 71.

[37] P.A. Butler, W. Nazarewicz, Rev. Mod. Phys. 68 (1996) 349.

[38] J. Skalski, Phys. Rev. C 43 (1991) 140.

[39] R.R. Chasman, Phys. Lett. B 266 (1991) 243.

[40] X. Li, J. Dudek, P. Romain, Phys. Lett. B 271 (1991) 281.

[41] X. Li, J. Dudek, Phys. Rev. C 49 (1994) R1250.

[42] S. Takami, K. Yabana, K. Ikeda, Prog. Theor. Phys. 96 (1996) 407.

[43] G. Leander, S.E. Larsson, Nucl. Phys. A 239 (1975) 93.

[44] J. Eichler, A. Faessler, Nucl. Phys. A 157 (1970) 166.

[45] N. Onishi, R.K. Sheline, Nucl. Phys. A 165 (1971) 180.

[46] J.P. Elliott, J.A. Evans, E.E. Maqueda, Nucl. Phys. A 437 (1985) 208.

[47] Y. Fujiwara, H. Horiuchi, K. Ikeda, M. Kamimura, K. Katō, Y. Suzuki, E. Uegaki, Suppl. Prog. Theor. Phys. 68 (1980) 29.

[48] T. Marumori, T. Maskawa, F. Sakata, A. Kuriyama, Prog. Theor. Phys. 64 (1980) 1294.

[49] N. Tajima, S. Takahara, N. Onishi, Nucl. Phys. A 603 (1996) 23.
[50] S. Takahara, N. Tajima, N. Onishi, Nucl. Phys. A 642 (1998) 461.
[51] P. Hoodbhoy, J.W. Negele, Nucl. Phys. A 288 (1977) 23.
[52] M. Yamagami, K. Matsuyanagi, Nucl. Phys. A 672 (2000) 123.
[53] M. Beiner, H. Flocard, N. Van Giai, P. Quentin, Nucl. Phys. A 238 (1975) 29.
[54] S.A. Fayans, D. Zawischa, Phys. Lett. B 383 (1996) 19.
[55] S.A. Fayans, S.V. Tolokonnikov, E.L. Trykov, D. Zawischa, Nucl. Phys. A 676 (2000) 49.
[56] J. Bartel, P. Quentin, M. Brack, C. Guet, H.-B. Håkansson, Nucl. Phys. A 386 (1982) 79.
[57] E. Chabanat, P. Bonche, P. Haensel, J. Meyer, R. Schaeffer, Nucl. Phys. A 627 (1997) 710, Nucl. Phys. A 635 (1998) 231.
[58] P.-G. Reinhard, D.J. Dean, W. Nazarewicz, J. Dobaczewski, J.A. Maruhn, M.R. Strayer, Phys. Rev. C 60 (1999) 014316.
[59] H. Flocard, P. Quentin, A.K. Kerman, D. Vautherin, Nucl. Phys. A 203 (1973) 433.
[60] P.J. Ennis, C.J. Lister, W. Gelletly, H.G. Price, B.J. Varley, P.A. Butler, T. Hoare, S. Ćwiok, W. Nazarewicz, Nucl. Phys. A 535 (1991) 392.
[61] C.J. Lister, P.J. Ennis, A.A. Chishti, B.J. Barley, W. Gellely, H.G. Price, A.N. James, Phys. Rev. C 42 (1990) R1191.
[62] S. Skoda, B. Fiedler, F. Becker, J. Eberth, S. Freund, T. Steinhardt, O. Stuch, O. Thelen, H.G. Thomas, L. Käubler, J. Reif, H. Schnare, R. Schwengner, T. Servene, G. Winter, V. Fischer, A. Jungclaus, D. Kast, K.P. Lieb, C. Teich, C. Ender, T. Härtlein, F. Köck, D. Schwalm, P. Baumann, Phys. Rev. C 58 (1998) R5.
[63] S.M. Fischer, D.P. Balamuth, P.A. Hausladen, C.J. Lister, M.P. Carpenter, D. Seweryniak, J. Schwartz, Phys. Rev. Lett. 84 (2000) 4064.
[64] G. de Angelis, C. Fahlander, A. Gadea, E. Farnea, W. Gelletly, A. Aprahamian, D. Bazzacco, F. Becker, P.G. Bizzeti, A. Bizzeti-Sona, F. Brandolini, D. de Acuna, M. De Poli, J. Eberth, D. Foltescu, S.M. Lenzi, S. Lunardi, T. Martinez, D.R. Napoli, P. Pavan, C.M. Petrache, C. Rossi Alvarez, D. Rudolph, B. Rubio, W. Satula, S. Skoda, P. Spolaore, H.G. Thomas, C.A. Ur, R. Wyss, Phys. Lett. B 415 (1997) 217.
[65] C.J. Lister, M. Campbell, A.A. Chishti, W. Gelletly, L. Goettig, R. Moscrop, B.J. Varley, A.N. James, T. Morrison, H.G. Price, J. Simpson, K. Connell, O. Skeppstedt, Phys. Rev. Lett. 59 (1987) 1270.
[66] D. Bucurescu, C. Rossi Alvarez, C.A. Ur, N. Marginean, P. Spolaore, D. Bazzacco, S. Lunardi, D.R. Napoli, M. Ionescu-Bujor, A. Iordachescu, C.M. Petrache, G. de Angelis, A. Gadea, D. Foltescu, F. Brandolini, G. Falconi, E. Farnea, S.M. Lenzi, N.H. Medina, Zs. Podalyak, M. De Poli, M.N. Rao, R. Venturelli, Phys. Rev. C 56 (1997) 2497.
[67] K. Hyde, J. Moreau, M. Waroquier, Phys. Rev. C 29 (1984) 1859.
[68] W. Nazarewicz, J. Dudek, R. Bengtsson, T. Bengtsson, I. Ragnarsson, Nucl. Phys. A 435 (1985) 397.
[69] J. Dudek, W. Nazarewicz, N. Rowley, Phys. Rev. C 35 (1987) 1489.
[70] J.P. Maharana, Y.K. Gambhir, J.A. Sheikh, P. Ring, Phys. Rev. C 46 (1992) R1163.
[71] E. Kirchuk, P. Federman, S. Pittel, Phys. Rev. C 47 (1993) 567.
[72] G.A. Lalazissis, M.M. Sharma, Nucl. Phys. A 586 (1995) 201.
[73] A. Petrovici, K.W. Schmid, A. Faessler, Nucl. Phys. A 605 (1996) 290.
[74] A. Petrovici, K.W. Schmid, A. Faessler, Nucl. Phys. A 665 (2000) 333.
[75] M. Honma, T. Mizusaki, T. Otsuka, Phys. Rev. Lett. 77 (1996) 3315.
[76] I. Hamamoto, X.Z. Zhang, Z. Phys. A 353 (1995) 145.
[77] P. Sarriguren, E. Moya de Guerra, A. Escuderos, Nucl. Phys. A 658 (1999) 13.
[78] F. Frisk, I. Hamamoto, F.R. May, Phys. Scr. 50 (1994) 628.
[79] I. Hamamoto, B. Mottelson, H. Xie, X.Z. Zhang, Z. Phys. D 21 (1991) 163.
[80] S.M. Reimann, M. Koskinen, H. Häkkinen, P.E. Lindelof, M. Manninen, Phys. Rev. B 56 (1997) 12147.

[81] J. Kolehmainen, M. Koskinen, H. Häkkinen, M. Manninen, Czech. J. Phys. 48 (1998) 679.
[82] S. Takahara, N. Onishi, N. Tajima, Phys. Lett. B 331 (1994) 261.
[83] M. Bender, K. Rutz, P.-G. Reinhard, J.A. Maruhn, nucl-th/0005028.
[84] T. Duguet, P. Bonche, P.-H. Heenen, nucl-th/0005040.
[85] M. Brack, J. Damgaad, A.S. Jensen, H.C. Pauli, V.M. Strutinsky, C.Y. Wong, Rev. Mod. Phys. 44 (1972) 320.
[86] W. Satuła, J. Dobaczewski, W. Nazarewicz, Phys. Rev. Lett. 81 (1998) 3599.
[87] J. Dobaczewski, P. Magierski, W. Nazarewicz, W. Satula, Z. Szymański, Phys. Rev. C 63 (2001) 024308.
[88] A. Bohr, B.R. Mottelson, Single-Particle Motion, Nuclear Structure, Vol. I, Benjamin, 1969.
[89] W. Satuła, D.J. Dean, J. Gary, S. Mizutori, W. Nazarewicz, Phys. Lett. B 407 (1997) 103.
[90] A.O. Macchiavelli, P. Fallon, R.M. Clark, M. Cromaz, M.A. Deleplanque, R.M. Diamond, G.J. Lane, I.Y. Lee, F.S. Stephens, C.E. Svensson, K. Vetter, D. Ward, Phys. Rev. C 61 (2000) 041303(R).
[91] P. Vogel, Nucl. Phys. A 662 (2000) 148.
[92] H. Noto, Y. Abe, J. Hiura, H. Tanaka, Prog. Theor. Phys. 55 (1976) 1432.
[93] S. Marcos, H. Flocard, P.-H. Heenen, Nucl. Phys. A 410 (1983) 125.
[94] P. Bonche, S.J. Krieger, M.S. Weiss, J. Dobaczewski, H. Flocard, P.-H. Heenen, Phys. Rev. Lett. 66 (1991) 876.
[95] J. Meyer, P. Bonche, M.S. Weiss, J. Dobaczewski, H. Flocard, P.-H. Heenen, Nucl. Phys. A 588 (1995) 597.
[96] J.L. Egido, L.M. Robledo, Nucl. Phys. A 524 (1991) 65.

Periodic-orbit bifurcations and superdeformed shell structure

A. G. Magner,[1,2] S. N. Fedotkin,[2] K. Arita,[3] K. Matsuyanagi,[4] and M. Brack[5]

[1]*Research Center for Nuclear Physics, Osaka University, Osaka 567-0047, Japan*

[2]*Institute for Nuclear Research, 03680 Prospekt Nauki 47, Kiev-28, Ukraine*

[3]*Department of Physics, Nagoya Institute of Technology, Nagoya 466-8555, Japan*

[4]*Department of Physics, Graduate School of Science, Kyoto University, Kyoto 606-8502, Japan*

[5]*Institute for Theoretical Physics, University of Regensburg, D-93040 Regensburg, Germany*

We have derived a semiclassical trace formula for the level density of the three-dimensional spheroidal cavity. To overcome the divergences occurring at bifurcations and in the spherical limit, the trace integrals over the action-angle variables were performed using an improved stationary phase method. The resulting semiclassical level density oscillations and shell-correction energies are in good agreement with quantum-mechanical results. We find that the bifurcations of some dominant short periodic orbits lead to an enhancement of the shell structure for ''superdeformed'' shapes related to those known from atomic nuclei.

I. INTRODUCTION

The periodic-orbit theory (POT) [1–7] is a nice tool for studying the correspondence between classical and quantum mechanics and, in particular, the interplay of deterministic chaos and quantum-mechanical behavior. But also for systems with integrable or mixed classical dynamics, the POT leads to a deeper understanding of the origin of shell structure in finite fermion systems from such different areas as nuclear [5,8–10], metallic cluster [11,12], or mesoscopic semiconductor physics [13,14]. Bifurcations of periodic orbits may have significant effects, e.g., in connection with the so-called ''superdeformations'' of atomic nuclei [5,6,9,15], and were recently shown to affect the quantum oscillations observed in the magneto-conductance of a mesoscopic device [14].

In the semiclassical trace formulas that connect the quantum-mechanical density of states with a sum over the periodic orbits of the classical system [1–3], divergences arise at critical points where bifurcations of periodic orbits occur or where symmetry breaking (or restoring) transitions take place. At these points the stationary-phase approximation, used in the semiclassical evaluation of the trace integrals, breaks down. Various ways of avoiding these divergences have been studied [2,4,16], some of them employing uniform approximations [17–20]. Here we employ an improved stationary-phase method (ISPM) for the evaluation of the trace integrals in the phase-space representation, based on the studies in Refs. [4,18] which we have derived for the elliptic billiard [21]. It yields a semiclassical level density that is regular at all bifurcation points of the short diameter orbit (and its repetitions) and in the circular (disk) limit. Away from the critical points, our result reduces to the extended Gutzwiller trace formula [3,5–7] and is identical to that of Berry and Tabor [4] for the leading-order families of periodic orbits.

The main purpose of the present Rapid Communication is to report on the extension of our semiclassical approach to the three-dimensional (3D) spheroidal cavity [22], which may be taken as a simple model for a large deformed nucleus [5,8] or a (highly idealized) deformed metal cluster [11,12], and to specify the role of orbit bifurcations in the shell structure responsible for the superdeformation. Although the spheroidal cavity is integrable (see, e.g., Ref. [23]), it exhibits all the difficulties mentioned above (i.e., bifurcations and symmetry breaking) and therefore gives rise to an exemplary case study of a nontrivial 3D system. We apply the ISPM for the bifurcating orbits and succeed in reproducing the superdeformed shell structure by the POT, hereby observing a considerable enhancement of the shell-structure amplitude near the bifurcation points.

II. THEORY

The level density $g(E)$ is obtained from the semiclassical Green function [1] by taking the imaginary part of its trace in $(\mathbf{I}, \boldsymbol{\Theta})$ action-angle variables [6,21],

$$g(E) = \sum_i \delta(E - \varepsilon_i) \simeq \text{Re} \sum_\alpha \int \frac{d\mathbf{I}' \, d\boldsymbol{\Theta}''}{(2\pi\hbar)^3} \delta(E - H)$$

$$\times \exp\left\{ \frac{i}{\hbar} [S_\alpha(\mathbf{I}', \mathbf{I}'', t_\alpha) + (\mathbf{I}'' - \mathbf{I}') \cdot \boldsymbol{\Theta}''] - i\frac{\pi}{2}\mu_\alpha \right\}.$$

$$(1)$$

Here $\{\varepsilon_i\}$ is the single-particle energy spectrum and $H = H(\mathbf{I})$ is the classical Hamiltonian. The sum is taken over all classical trajectories α specified by the initial actions $\mathbf{I}'$ and final angles $\boldsymbol{\Theta}''$. $S_\alpha(\mathbf{I}', \mathbf{I}'', t_\alpha) = -\int_{\mathbf{I}'}^{\mathbf{I}''} \mathbf{I} \cdot d\boldsymbol{\Theta}$ is the action integral and t_α the time for the motion along the trajectory α, and μ_α is the Maslov index related to the caustic and the turning points [21,22]. In the spheroidal variables $\{u, v, \varphi\}$, the action $\mathbf{I}$ has the components

$$I_u = \frac{pc}{\pi} \int_{-u_c}^{u_c} du \sqrt{\sigma_1 - \sin^2 u - \sigma_2/\cos^2 u},$$

$$I_v = \frac{pc}{\pi} \int_{v_c}^{v_t} dv \sqrt{\cosh^2 v - \sigma_1 - \sigma_2/\sinh^2 u},$$

$$(2)$$

63 065201-1

$$I_\varphi = pc\sqrt{\sigma_2}.$$

Hereby $p = (2mE)^{1/2}$ is the particle's momentum and $c = (b^2 - a^2)^{1/2}$ half the distance between the foci; b and a are the semiaxes (with $b > a$) of the spheroid with its volume fixed by $a^2 b = R^3$ and the axis ratio $\eta = b/a$ as deformation parameter; and $\pm u_c$ (or v_c) and v_t are the caustic and turning points, respectively. In Eq. (2) we use the dimensionless "action" variables σ_1, σ_2 [21] in which the torus of the classical motion is given by

$$\sigma_2^- = 0 \leq \sigma_2 \leq \frac{1}{\eta^2 - 1} = \sigma_2^+,$$

$$\sigma_1^- = \sigma_2 \leq \sigma_1 \leq \frac{\eta^2}{\eta^2 - 1} - \sigma_2(\eta^2 - 1) = \sigma_1^+.$$

In the ISPM, we expand the action S_α in Eq. (1) up to second-order terms around its stationary points and keep the preexponential factor at zero order, taking the integrations over the torus within the *finite* limits given by Eq. (3). For the oscillating ("shell-correction") part of the level density $\delta g(E) = g(E) - \tilde{g}(E)$, where $\tilde{g}(E)$ is its smooth part [7,24], we obtain

$$\delta g(E) \simeq \frac{1}{E_0} \text{Re} \sum_\beta A_\beta(E) \exp\left(ikL_\beta - i\frac{\pi}{2}\mu_\beta\right) w_\beta^\gamma, \quad (4)$$

where $k = p/\hbar$ is the wave number and $E_0 = \hbar^2/2mR^2$ our energy unit. The amplitudes A_β will be specified below. The sum over β includes all two-parameter families of three-dimensional (3D) periodic orbits and elliptic and hyperbolic 2D orbits lying in a plane containing the symmetry axis (all with degeneracy parameter $\mathcal{K} = 2$), the one-parameter families of (2D) equatorial orbits lying in the central plane perpendicular to the symmetry axis (with $\mathcal{K} = 1$), and the (1D) isolated long diameter (with $\mathcal{K} = 0$). In Eq. (4), L_β is the length of the orbit β at the stationary point (σ_1^*, σ_2^*) which for the 3D orbits lies inside the physical region of the torus (3), and is analytically continued outside this region. The $\sigma_2 = 0$ boundary of Eq. (3) is occupied by the 2D orbits with $\mathcal{K} = 2$. The stationary points are determined by the roots of the periodicity conditions $\omega_u/\omega_v = n_u/n_v$ and $\omega_u/\omega_\varphi = n_u/n_\varphi$; hereby $\omega_\kappa = \partial H/\partial I_\kappa$ are the frequencies and n_κ are coprime integers which specify the periodic orbits $\beta = M(n_v, n_\varphi, n_u)$, where M is the repetition number. The factor $w_\beta^\gamma = \exp(-\gamma^2 L_\beta^2/4R^2)$ in Eq. (4) is the result of a convolution of the level density with a Gaussian function over a range γ in the variable kR. This ensures the convergence of the POT sum (4) by suppressing the longer orbits which are not relevant for the coarse-grained gross-shell structure [6,7].

For Strutinsky's shell-correction energy δU [3,7,24], we obtain (with time reversal symmetry and a spin factor 2)

$$\delta U = 2\sum_{i=1}^{N/2} \varepsilon_i - 2\int_0^{\tilde{E}_F} E\tilde{g}(E)dE$$

$$\simeq 8R^2 E_F \text{Re} \sum_\beta \frac{A_\beta(E_F)}{L_\beta^2} \exp\left(ik_F L_\beta - i\frac{\pi}{2}\mu_\beta\right). \quad (5)$$

The Fermi energies E_F (and with it k_F) and $\tilde{E}_F$ are determined by the particle number conservation $N = 2\int_0^{E_F} g(E)dE = 2\int_0^{\tilde{E}_F} \tilde{g}(E)dE$. Due to the factor L_β^{-2}, the PO sum in Eq. (5) may converge faster for the shortest orbits than the level density (4) for small γ. Any enhancement of the amplitudes A_β of the most degenerate short periodic orbits (e.g., due to bifurcations or to symmetry restoring, as discussed below) therefore leads to an enhancement of the shell structure and hence to an increased stability of the system.

We present here only the amplitudes of the leading contributions to Eqs. (4) and (5). For further details (including, e.g., explicit expressions for the Maslov indices μ_α), we refer to a forthcoming, more extensive publication [22].

For the amplitudes A_β of the most degenerate ($\mathcal{K} = 2$) families of periodic 3D and 2D orbits, we obtain

$$A_\beta^{(\mathcal{K}=2)} = \frac{icL_\beta[\partial I_u/\partial\sigma_1]_{\sigma_n^*}}{\pi(4MRn_v)^2\sqrt{K_\beta\sigma_2^*}} \prod_{n=1}^{2} \text{erf}(x_n^-, x_n^+). \quad (6)$$

The quantity $K_\beta = K_\beta^{(1)} K_\beta^{(2)}$ is related to the main curvatures $K_\beta^{(n)}$ of the energy surface $E = H(\sigma_1, \sigma_2)$ in the "action" plane (σ_1, σ_2), given by

$$K_\beta^{(n)} = \left[\frac{\partial^2 I_v}{\partial\sigma_n^2} + \frac{\omega_u}{\omega_v}\frac{\partial^2 I_u}{\partial\sigma_n^2} + \frac{\omega_\varphi}{\omega_v}\frac{\partial^2 I_\varphi}{\partial\sigma_n^2}\right]_{\sigma_n^*}, \quad (n=1,2). \quad (7)$$

In Eq. (6), the arguments of the two-dimensional error function $\text{erf}(x,y) = 2\int_x^y dz e^{-z^2}/\sqrt{\pi}$ are given by the turning points in the action plane

$$x_n^\pm = \sqrt{-i\pi M n_v K_\beta^{(n)}/\hbar}(\sigma_n^\pm - \sigma_n^*) \quad (n=1,2); \quad (8)$$

see Eq. (3) for the boundaries $\sigma_n^\pm$. All quantities in Eq. (6) can be expressed analytically in terms of elliptic integrals. For the 3D orbits, our result (6) is in agreement with that obtained by exact Poisson summation over the EBK spectrum (cf. Refs. [4,7]).

For the contribution of the $\mathcal{K} = 1$ families of equatorial orbits to Eq. (4), we obtain the amplitudes

$$A_\beta^{(\mathcal{K}=1)} = \sqrt{\frac{i\sin^3\phi_\beta}{\pi M n_v kR\,\eta F_\beta}} \prod_{n=1}^{3} \text{erf}(x_n^-, x_n^+), \quad (9)$$

where $\phi_\beta = \pi n_\varphi/n_v$, F_β is their stability factor [1,2,6], $\sigma_1^* = \sigma_2^* = \cos^2\phi_\beta/(\eta^2 - 1)$, and

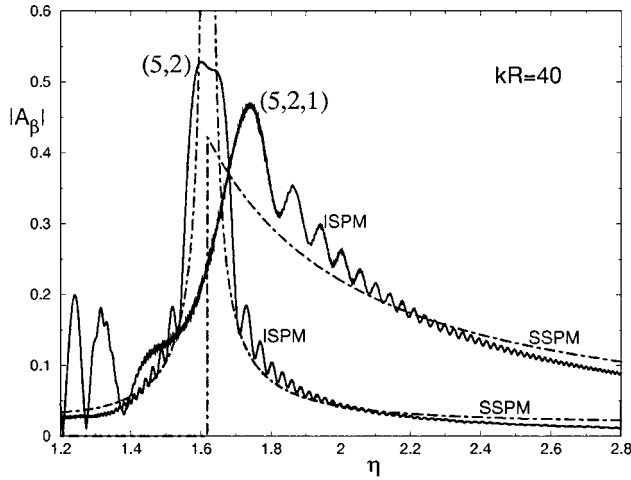$$x_3^+ = kc\sqrt{\frac{-i\pi\hbar F_\beta}{64 M n_v(\sigma_2^* + 1)K_\beta^{(1)}}}, \quad x_3^- = 0. \quad (10)$$

FIG. 1. Moduli of amplitudes $|A_\beta|$ vs η for the equatorial "star" orbit (5,2) ($\mathcal{K}=1$) and the 3D orbit (5,2,1) ($\mathcal{K}=2$) bifurcating from it at $\eta=1.618\ldots$. Solid lines: using the ISPM according to Eqs. (9) and (6), respectively; dash-dotted lines: using the standard stationary-phase approach.

The contribution of the isolated long diameter orbit, which may be expressed in terms of incomplete Airy integrals [21,22], is not important for deformations of the order $\eta \sim 1.2-2$.

III. DISCUSSION OF RESULTS

In Fig. 1 we show $|A_\beta|$ versus deformation η (at $kR=40$) for a pair of orbits involved in a typical bifurcation scenario. At the critical point $\eta=1.618\ldots$ the equatorial "star" orbit (5,2) undergoes a bifurcation at which the 3D orbit (5,2,1) is born; the latter does not exist below $\eta=1.618\ldots$.

In the standard stationary-phase approach (SSPM; dash-dotted lines), the amplitude of the (5,2) orbit diverges at $\eta=1.618\ldots$, whereas that of the bifurcated orbit (5,2,1) is finite but discontinuous. As seen in Fig. 1, the ISPM (solid lines) leads to a finite amplitude $A_{(5,2)}^{(\mathcal{K}=1)}$ for the (5,2) orbit. This is because the factor F_β in the denominator of Eq. (9), which goes to zero at the bifurcation, is cancelled by the same factor in the numerator of x_3^+ (10) via the third error function in Eq. (9). A similar result was found for the short diameter orbit 2(2,1) in the elliptic billiard [21]. Furthermore, the ISPM softens the discontinuity for the (5,2,1) orbit, leading to a maximum amplitude slightly above the critical deformation.

The relative enhancement of these amplitudes A_β near the bifurcation point can also be understood qualitatively from the following argument. At the bifurcation of the equatorial (5,2) orbit, its degeneracy parameter $\mathcal{K}=1$ locally increases to 2, because it is there degenerate with the orbit family (5,2,1) that has $\mathcal{K}=2$ at all deformations $\eta \geq 1.618\ldots$. This is similar to a symmetry restoring transition. An increase of the symmetry parameter $\mathcal{K}$ by one unit leads to one more exact integration compared to the SSPM, and thus the amplitudes (6) and (9) acquire an enhancement factor $\sqrt{kL_\beta} \propto \sqrt{pR/\hbar}$ (cf. Refs. [3,7]).
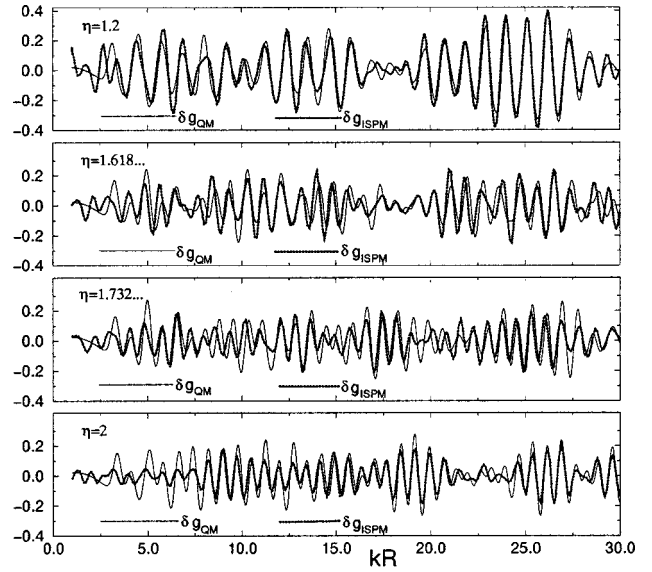

FIG. 2. Level density $\delta g(E)$ (4) (unit E_0^{-1}) vs kR for different critical deformations η. The Gaussian averaging parameter is $\gamma = 0.3$. Thin solid lines: quantum-mechanical results; thick dotted lines: semiclassical results using the ISPM.

A similar enhancement of the double triangle 2(3,1) and the 3D orbit (6,2,1) is found near their bifurcation point $\eta = \sqrt{3} = 1.732\ldots$. However, the curvature $K_\beta^{(1)}$ (7) for orbits like $M(3t,t,1)$ ($t=2,3,\ldots$) is identically zero and hence the SSPM is divergent for all deformations $\eta \geq 1$, in contrast to the situation with orbits like (5,2,1) with finite $K_\beta^{(1)}$. Here we have to take into account the next nonzero third-order terms in the expansion of S_α, although the $(3t,t,1)$ ISPM amplitude (6) is finite and continuous everywhere. The amplitude can then be expressed in terms of incomplete Airy and Gairy integrals with finite limits [22]. For the equatorial orbits $t(3,1)$, like for the double triangles 2(3,1), one has a zero curvature $K_\beta^{(1)}$ only at the bifurcation point $\eta = \sqrt{3}$. Here $F_\beta/K_\beta^{(1)} \to 0$, and a similar mechanism of cancellation of singularities for other orbits takes place through Eqs. (8)–(10). But the relative enhancement of the ISPM amplitudes (6,9) of such orbits at the bifurcations is of order kL_β because of a change of the degeneracy parameter $\mathcal{K}$ by *two* units (see Ref. [22] for details). In this sense we avoid here a double singularity related to a double restoring of symmetry.

In Figs. 2 and 3, we present semiclassical level densities $\delta g(E)$ (4) versus kR and shell-correction energies δU (5) versus $N^{1/3}$ for various critical deformations (thick dotted lines), and compare them to the corresponding quantum-mechanical results (thin solid lines). We observe a very good agreement of the gross-shell structure at all deformations. The most significant contributions to these results near the critical deformations are coming from bifurcating orbits with lengths smaller than about $10R$, in line with the convergence arguments for the POT sums (4) and (5) mentioned above. For the bifurcation at $\eta = 1.618\ldots$, the orbits (5,2,1) and (5,2) give contributions comparable with other 2D orbits. For $\eta = \sqrt{3}$, the bifurcating orbits (6,2,1) and (6,2) are also important.
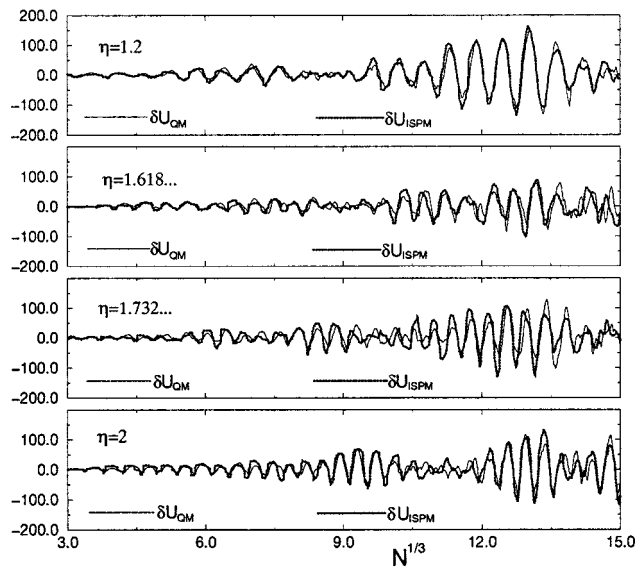
FIG. 3. Shell-correction energy δU (5) (unit E_0) vs cube root of particle number $N^{1/3}$ (same notation and same deformations as in Fig. 2).

The role of the bifurcating orbits increases for larger deformations and is dominating at the superdeformation $\eta=2$. For this deformation, the most important orbits in the present spheroidal cavity model are the 3D orbits (5,2,1), (6,2,1), (7,2,1), and (8,2,1).

These results are in agreement with both heights and positions of the peaks in the length spectra obtained in Ref. [15] from the Fourier transforms of the quantum level densities $g(kR)$ at the same deformations.

IV. SUMMARY AND CONCLUSIONS

We have obtained an analytical trace formula for the 3D spheroidal cavity model, which is continuous through all critical deformations where bifurcations of periodic orbits occur. We find an enhancement of the amplitudes $|A_\beta|$ at deformations $\eta \sim 1.6 - 2.0$ due to bifurcations of 3D orbits from the shortest 2D orbits. We believe that this is an important mechanism which contributes to the stability of superdeformed systems. Our semiclassical analysis may therefore lead to a deeper understanding of shell structure effects in superdeformed fermionic systems, not only in nuclei or metal clusters but also, e.g., in deformed semiconductor quantum dots whose conductance and magnetic susceptibilities are significantly modified by shell effects.

[1] M. Gutzwiller, J. Math. Phys. **12**, 343 (1971), and earlier references quoted therein; *Chaos in Classical and Quantum Mechanics* (Springer Verlag, New York, 1990).

[2] R. B. Balian and C. Bloch, Ann. Phys. (N.Y.) **69**, 76 (1972).

[3] V. M. Strutinsky, Nukleonica **20**, 679 (1975); V. M. Strutinsky and A. G. Magner, Sov. Phys. Part. & Nucl. **7**, 138 (1977).

[4] M. V. Berry and M. Tabor, Proc. R. Soc. London, Ser. A **349**, 101 (1976).

[5] V. M. Strutinsky, A. G. Magner, S. R. Ofengenden, and T. Døssing, Z. Phys. A **283**, 269 (1977).

[6] A. G. Magner, S. N. Fedotkin, F. A. Ivanyuk, P. Meier, M. Brack, S. M. Reimann, and H. Koizumi, Ann. Phys. (Leipzig) **6**, 555 (1997).

[7] M. Brack and R. K. Bhaduri, *Semiclassical Physics*, Frontiers in Physics Vol. 96 (Addison-Wesley, Reading, MA, 1997).

[8] H. Frisk, Nucl. Phys. A **511**, 309 (1990).

[9] K. Arita and K. Matsuyanagi, Nucl. Phys. A **592**, 9 (1995).

[10] M. Brack, S. M. Reimann, and M. Sieber, Phys. Rev. Lett. **79**, 1817 (1997); M. Brack, P. Meier, S. M. Reimann, and M. Sieber, in *Similarities and Differences between Atomic Nuclei and Clusters*, edited by Y. Abe *et al.* (AIP, New York, 1998), p. 17.

[11] H. Nishioka, K. Hansen, and B. R. Mottelson, Phys. Rev. B **42**, 9377 (1990).

[12] M. Brack, S. Creagh, P. Meier, S. Reimann, and M. Seidl, in *Large Clusters of Atoms and Molecules*, edited by T. P. Martin (Kluwer, Dordrecht, 1996), p. 1; M. Brack, J. Blaschke, S. C. Creagh, A. G. Magner, P. Meier, and S. M. Reimann, Z. Phys. D: At., Mol. Clusters **40**, 276 (1997).

[13] S. M. Reimann, M. Persson, P. E. Lindelof, and M. Brack, Z. Phys. B: Condens. Matter **101**, 377 (1996).

[14] J. Blaschke and M. Brack, Europhys. Lett. **50**, 294 (2000).

[15] K. Arita, A. Sugita, and K. Matsuyanagi, Prog. Theor. Phys. **100**, 1223 (1998).

[16] S. C. Creagh, Ann. Phys. (N.Y.) **248**, 60 (1997).

[17] S. Tomsovic, M. Grinberg, and D. Ullmo, Phys. Rev. Lett. **75**, 4346 (1995); D. Ullmo, M. Grinberg, and S. Tomsovic, Phys. Rev. E **54**, 136 (1996).

[18] M. Sieber, J. Phys. A **30**, 4563 (1997).

[19] M. Sieber, J. Phys. A **29**, 4715 (1996); H. Schomerus and M. Sieber, *ibid.* **30**, 4537 (1997); M. Sieber and H. Schomerus, *ibid.* **31**, 165 (1998).

[20] M. Brack, P. Meier, and K. Tanaka, J. Phys. A **32**, 331 (1999).

[21] A. G. Magner, S. N. Fedotkin, K. Arita, K. Matsuyanagi, T. Misu, T. Schachner, and M. Brack, Prog. Theor. Phys. **102**, 551 (1999).

[22] A. G. Magner, S. N. Fedotkin, K. Arita, K. Matsuyanagi, and M. Brack (unpublished).

[23] H. Nishioka, M. Ohta, and S. Okai, Mem. Konan Univ., Sci. Ser. **38(2)**, 1 (1991), and unpublished.

[24] V. M. Strutinsky, Nucl. Phys. A **122**, 1 (1968).

Wobbling motion in atomic nuclei with positive-γ shapes

Masayuki Matsuzaki*

Department of Physics, Fukuoka University of Education, Munakata, Fukuoka 811-4192, Japan

Yoshifumi R. Shimizu†

Department of Physics, Graduate School of Sciences, Kyushu University, Fukuoka 812-8581, Japan

Kenichi Matsuyanagi‡

Department of Physics, Graduate School of Science, Kyoto University, Kyoto 606-8502, Japan
(Received 1 January 2002; published 20 March 2002)

The three moments of inertia associated with the wobbling mode built on the superdeformed states in ^{163}Lu are investigated by means of the cranked shell model plus random phase approximation to the configuration with an aligned quasiparticle. The result indicates that it is crucial to take into account the direct contribution to the moments of inertia from the aligned quasiparticle so as to realize $\mathcal{J}_x > \mathcal{J}_y$ in positive-γ shapes. Quenching of the pairing gap cooperates with the alignment effect. The peculiarity of the recently observed ^{163}Lu data is discussed by calculating not only the electromagnetic properties but also the excitation spectra.

Rotation is one of the specific collective motions in finite many-body systems. Most of the nuclear rotational spectra can be understood as the outcome of one-dimensional (1D) rotations of axially symmetric nuclei. Two representative models—the moment of inertia of the irrotational fluid, $\mathcal{J}^{\mathrm{irr}}$, and that of the rigid rotor, $\mathcal{J}^{\mathrm{rig}}$, both specified by an appropriate axially symmetric deformation parameter β—could not reproduce the experimental ones given by $\mathcal{J}^{\mathrm{exp}}$; $\mathcal{J}^{\mathrm{irr}} < \mathcal{J}^{\mathrm{exp}} < \mathcal{J}^{\mathrm{rig}}$. From a microscopic viewpoint, the moment of inertia can be calculated as the response of the many-body system to an externally forced rotation—the cranking model [1]. This reproduces $\mathcal{J}^{\mathrm{exp}}$ well by taking into account the pairing correlation. Triaxial nuclei can rotate about their three principal axes and the three corresponding moments of inertia depend on their shapes in general. In spite of a lot of theoretical studies, their shape (in particular the triaxiality parameter γ) dependence has not been understood well because of the lack of decisive experimental data. Recently, some evidences of 3D rotations have been observed, such as the shears bands and the so-called chiral-twin bands [2]. In addition to these fully 3D motions, from the general argument of symmetry breaking, there must be a low-lying collective mode associated with the symmetry reduction from a 1D rotating axially symmetric mean field to a 3D rotating triaxial one. This is called the wobbling mode. Notice that the collective mode associated with the "phase transition" from an axially symmetric to a triaxial mean field in the nonrotating case is the well-known γ vibration. Therefore, the wobbling mode can be said to be produced by an interplay of triaxiality and rotation. The wobbling mode is described as a small amplitude fluctuation of the rotational axis away from the principal axis with the largest moment of inertia. Bohr and Mottelson first discussed this mode [3].

Mikhailov and Janssen [4] and Marshalek [5] described this mode in terms of the random phase approximation (RPA) in the rotating frame. In these works it was shown that at $\gamma = 0$ this mode turns into the odd-spin members of the γ vibrational band while at $\gamma = 60°$ or $-120°$ it becomes the precession mode built on the top of the high-K isomeric states [6]. Here we note that, according to the direction of the rotational axis relative to the three principal axes of the shape, γ runs from $-120°$ to $60°$.

Recently, electromagnetic (EM) properties of the second triaxial superdeformed (TSD2) band in ^{163}Lu were reported and it was concluded that the TSD2 is a wobbling band excited on the previously known yrast TSD1 band, on the basis of comparisons to a particle-rotor model (PRM) calculation [7,8]. In conventional PRM calculations an irrotational moment of inertia,

$$\mathcal{J}_k^{\mathrm{irr}} = \frac{4}{3}\mathcal{J}_0 \sin^2\left(\gamma + \frac{2}{3}\pi k\right), \tag{1}$$

where $k = 1 - 3$ denote the x, y, and z principal axes, is assumed. The magnitude $\mathcal{J}_0$ is treated as an adjustable parameter although it can be identified as $\mathcal{J}_0 = 3B_2\beta^2$, where B_2 is the inertia parameter in the Bohr Hamiltonian [9]. This reduces to $\mathcal{J}^{\mathrm{irr}}$ in the first paragraph by substituting $\gamma = 0$ and $k = 1$, and satisfies such a required property that collective rotations about the symmetry axes are forbidden. Since $\mathcal{J}_y^{\mathrm{irr}}$ is largest for $0 < \gamma < 60°$ and the main rotation occurs about the axis of the largest inertia, the PRM with $\mathcal{J}_k^{\mathrm{irr}}$ cannot describe the positive-γ rotation, that is, the rotation about the shortest axis (x axis). Then in Refs. [7,8] the so-called γ-reversed moment of inertia [10], $\mathcal{J}_k^{\mathrm{rev}}$, defined by inverting the sign of γ in Eq. (1), was adopted. Although this reproduced the measured EM properties well, this does not satisfy the required property mentioned above and its physical implications are not very clear. In this Rapid Communication, therefore, we study the moments of inertia associated with the wobbling motion excited on the positive-γ states by

———————
*Email address: matsuza@fukuoka-edu.ac.jp
†Email address: yrsh2scp@mbox.nc.kyushu-u.ac.jp
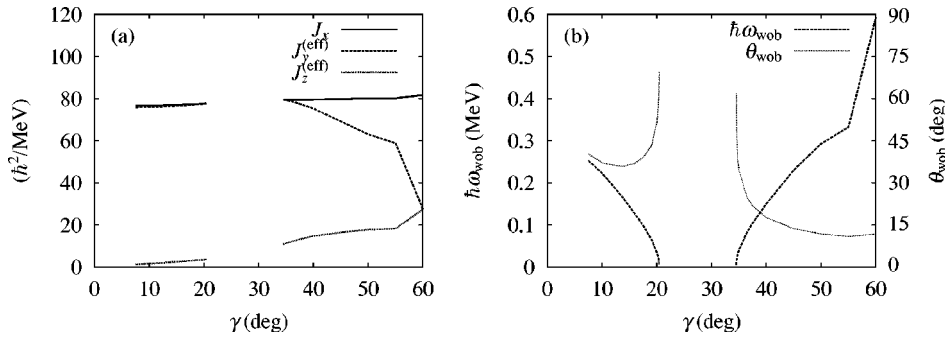‡Email address: ken@ruby.scphys.kyoto-u.ac.jp

FIG. 1. (a) Moments of inertia and (b) wobbling frequency (left scale) and wobbling angle (right) in the five quasiparticle state in ^{147}Gd calculated as functions of γ at $\hbar\omega_{\rm rot}=0.3$ MeV. The dip around $\gamma=55°$ stems from a weak fragmentation of collectivity. Note that the present method of calculation does not apply to $\gamma\approx 0$.

means of the cranked shell model plus RPA. This framework does not divide the system into a valence particle and a rotor, and therefore, can calculate the three moments of inertia of the whole system microscopically. We believe that this is the first step toward understanding the fully 3D nuclear rotations.

We have developed a computer code for the RPA to excitation modes built on configurations with arbitrary number of aligned quasiparticles (QPs). In this paper, we present the results for the 4–6 QP configurations in Gd isotopes and the 1 QP one in ^{163}Lu. In particular, this is the first RPA calculation for the rotating odd-A configurations, to our knowledge. Note that this approach is different from the conventional particle-vibration coupling calculations where the RPA itself is performed for the even-even "core" configurations. Since the details of the formulation have already been given in Refs. [11,12], here we describe only the outline. The QP states were obtained by diagonalizing the cranked triaxial Nilsson plus BCS Hamiltonian at each rotational frequency $\omega_{\rm rot}$ by adjusting chemical potentials to give correct average particle numbers. The doubly stretched $\mathbf{l}^2$ and $\mathbf{l}\cdot\mathbf{s}$ potentials were adopted, and their strengths were taken from Ref. [13]. The RPA calculation was performed by adopting the pairing plus doubly stretched Q-Q interaction. The existence of aligned QPs is taken into account by exchanging the definitions of the QP creation and annihilation operators in an appropriate manner. Actual calculations were done in five major shells ($N_n^{\rm (osc)}=3$–7 and $N_p^{\rm (osc)}=2$–6) by using the dispersion equation [5],

$$(\hbar\omega)^2=(\hbar\omega_{\rm rot})^2\frac{[\mathcal{J}_x-\mathcal{J}_y^{\rm (eff)}(\omega)][\mathcal{J}_x-\mathcal{J}_z^{\rm (eff)}(\omega)]}{\mathcal{J}_y^{\rm (eff)}(\omega)\mathcal{J}_z^{\rm (eff)}(\omega)}, \quad (2)$$

obtained by decoupling the Nambu-Goldstone mode analytically assuming $\gamma\neq 0$. This equation is independent of the strengths of the interaction. Not only the collective wobbling mode ($\omega=\omega_{\rm wob}$) but also many noncollective modes are obtained from this equation. The effective inertia $\mathcal{J}_{y,z}^{\rm (eff)}(\omega)$ $=J_{y,z}^{\rm (PA)}(\omega)/\Omega_{y,z}(\omega)$, defined in the principal-axis (PA) frame (their concrete expressions were given in Ref. [12]), depend on the eigenmode while the kinematical $\mathcal{J}_x=\langle J_x\rangle/\omega_{\rm rot}$, where the expectation value taken with respect to the whole system is common to all the modes. It should be noted that Eq. (2) coincides with the original expression for $\omega_{\rm wob}$ [3] if $\mathcal{J}_x$ and $\mathcal{J}_{y,z}^{\rm (eff)}(\omega)$ are replaced with constant moments of inertia.

In the following, we present some numerical results. Here the parameters ϵ_2 (alternative to β), γ, Δ_n, and Δ_p were chosen so as to reproduce the available experimental data, and kept constant as functions of $\omega_{\rm rot}$. We have confirmed that qualitative features of the result are robust and the details of the parameter dependence will be given in a separate publication [14]. It is nontrivial to obtain the wobbling solution in the RPA for positive-γ nuclei and the QP alignment is indispensable for its appearance. In order to show this, we first discuss a theoretical calculation for a precession mode that might be built on top of the $I^\pi=49/2^+$ isomeric state in ^{147}Gd, where the whole angular momentum is built up by the alignment of the five QPs, $[(\pi h_{11/2})^2(\nu h_{9/2},f_{7/2})^2]_{18^+}$ in ^{146}Gd plus $[\nu i_{13/2}]_{13/2^+}$, so that a $\gamma=60°$ shape (axially symmetric about the x axis) is realized. This state is obtained by cranking with $\hbar\omega_{\rm rot}=0.3$ MeV. We chose $\epsilon_2=0.19$ and Δ_n $=\Delta_p=0.6$ MeV, and reproduced the observed static quadrupole moment and the g factor [15,16]. In order to see the behavior of the three moments of inertia, we calculated the wobbling mode by changing the parameter γ from 60°. The result is presented in Fig. 1(a). Although at a first glance their γ dependence resembles that of the rigid rotor,

$$\mathcal{J}_k^{\rm rig}=\frac{16\pi}{15}B_2\left(1-\sqrt{\frac{5}{4\pi}}\beta\cos\left(\gamma+\frac{2}{3}\pi k\right)\right), \quad (3)$$

the physical content of $\mathcal{J}_x$ changes with γ; the fraction of the collective contribution decreases as γ increases and reaches 0 at $\gamma=60°$. Accordingly, it can be conjectured that the γ dependence of the "rotor" contribution is approximately irrotational and the QP contribution is superimposed on top of the former by aligning its angular momentum to the x axis. Our previous calculation [12,17] for a negative-γ nucleus, ^{182}Os, also supports this and consequently it is thought that the wobbling mode can appear relatively easily in superfluid negative-γ nuclei. To see if this conjecture is meaningful, starting from ^{146}Gd we add the $i_{13/2}$ quasineutrons sequentially. The result shows that $\mathcal{J}_x$ increases as the number of aligned QPs increases. Since the increase in $\mathcal{J}_{y,z}^{\rm (eff)}$ is rather moderate, the increase in $\mathcal{J}_x$ leads to that of the wobbling frequency $\omega_{\rm wob}$. Thus, the change from $\mathcal{J}_x<\mathcal{J}_y$ in $\mathcal{J}_k^{\rm irr}$ to $\mathcal{J}_x>\mathcal{J}_y$ in $\mathcal{J}_k^{\rm rev}$ may be related qualitatively to the increase in $\mathcal{J}_x$ stemming from the alignment that is not accounted for in the PRM, considering the fact that the alignment of particle states leads to $\gamma>0$.
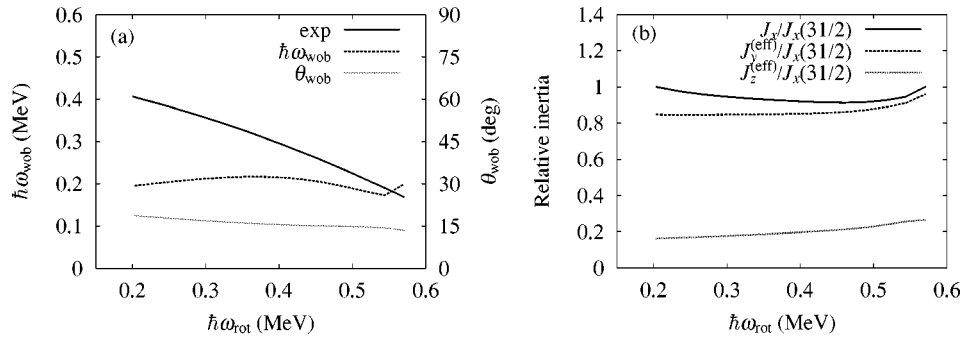
FIG. 2. (a) Wobbling frequency (left scale) and wobbling angle (right) and (b) moments of inertia in the TSD2 band in ^{163}Lu as functions of $\hbar\omega_{\rm rot}$. Here the latter were given by normalized to $\mathcal{J}_x(31/2) = 99.2\hbar^2/\text{MeV}$. The proton BC crossing occurs at $\hbar\omega_{\rm rot} \gtrsim 0.55$ MeV in the calculation. Experimental values were calculated from the energy levels in Refs. [7,8].

At $\gamma \sim 30°$, where $\mathcal{J}_y$ reaches its maximum as in the irrotational model, we could not obtain a wobbling solution. In Fig. 1(b), $\hbar\omega_{\rm wob}$ and the wobbling angle

$$\theta_{\rm wob} = \tan^{-1} \frac{\sqrt{|J_y^{\rm (PA)}(\omega_{\rm wob})|^2 + |J_z^{\rm (PA)}(\omega_{\rm wob})|^2}}{\langle J_x \rangle} \quad (4)$$

are graphed. This shows that $\omega_{\rm wob}$ becomes imaginary and $\theta_{\rm wob}$ blows up in this region. Comparing Figs. 1(a) and 1(b), it may be inferred that the wobbling motion excitation on a mean field rotating about the x axis becomes unstable at $\gamma \sim 30°$ due to $\mathcal{J}_x < \mathcal{J}_y^{\rm (eff)}$, and that a tilted-axis rotation would be realized. Putting this unstable region in between, the solution in the larger-γ side is like a precession of an axially symmetric body about the x axis, whereas that in the smaller-γ side is like a γ vibration around an axially symmetric shape about the z axis.

Now we turn to the TSD bands in ^{163}Lu. We chose $\epsilon_2 = 0.43$, $\gamma = 20°$, and $\Delta_n = \Delta_p = 0.3$ MeV, and obtained transition quadrupole moments $Q_t = 10.9-11.3$ e b for $\hbar\omega_{\rm rot} = 0.20-0.57$ MeV in accordance with the data, $Q_t = 10.7 \pm 0.7$ e b [18]. We have obtained for the first time (aside from the theoretical simulation above) the wobbling solution in the RPA for positive-γ nuclei. Here it should be stressed that the inclusion of the five major shells and the alignment effect of the proton $i_{13/2}$ quasiparticle is essential for obtaining this result. In Fig. 2(a) the measured excitation energy of the TSD2 band relative to that of the TSD1 and the calculated $\hbar\omega_{\rm wob}$ are shown. The most peculiar point in the experimental data is that $\omega_{\rm wob}$ decreases as a function of $\omega_{\rm rot}$. If $\omega_{\rm rot}$-independent moments of inertia such as the irrotational ones are adopted, $\omega_{\rm wob}$ increases linearly with $\omega_{\rm rot}$, see the comment below Eq. (2). The wobbling frequency is sensitive to the difference among the three moments of inertia, and the ratios $\mathcal{J}_y^{\rm (eff)}/\mathcal{J}_x$ and $\mathcal{J}_z^{\rm (eff)}/\mathcal{J}_x$ actually determine $\omega_{\rm wob}$. For example, the γ-reversed moments of inertia give $\mathcal{J}_y^{\rm rev}/\mathcal{J}_x^{\rm rev} = 0.43$ and $\mathcal{J}_z^{\rm rev}/\mathcal{J}_x^{\rm rev} = 0.12$ for $\gamma = 20°$ leading to $\omega_{\rm wob} \simeq 3\omega_{\rm rot}$, which is quite different from the experimental data. In contrast, as shown in Fig. 2(b), the three moments of inertia calculated microscopically depend on $\omega_{\rm rot}$ even when the shape parameters are fixed, and the resultant $\omega_{\rm wob}$ can either increase or decrease in general. In the present case of ^{163}Lu in Fig. 2, $\mathcal{J}_x - \mathcal{J}_y^{\rm (eff)}$ mainly determines the $\omega_{\rm rot}$ depen-

dence. Its decrease is a consequence of that of $\mathcal{J}_x$; the partial contribution to $\mathcal{J}_x$ from the proton $i_{13/2}$, $i_x/\omega_{\rm rot}$, decreases as $\omega_{\rm rot}$ increases since this orbital is already fully aligned and therefore the aligned angular momentum i_x is approximately constant. Thus, our result for $\omega_{\rm wob}$ stays almost constant against $\omega_{\rm rot}$, and even decreases slightly at higher frequencies approaching the experimentally observed one. This clearly shows that microscopic calculation of the three moments of inertia is crucial to understand the $\omega_{\rm rot}$ dependence of $\omega_{\rm wob}$ in ^{163}Lu. Let us compare this result with that for ^{147}Gd above. In ^{147}Gd, $\mathcal{J}_y^{\rm (eff)}/\mathcal{J}_x \simeq 1$, $\mathcal{J}_z^{\rm (eff)} \sim 0$, and $|Q_1^{(-)}/Q_2^{(-)}| \ll 1$ at $\gamma \lesssim 20°$. The last quantity measures the rotational K-mixing. This indicates that this solution is essentially similar to the γ vibration in an axially symmetric nucleus as mentioned above. In contrast, the result that $\mathcal{J}_y^{\rm (eff)}/\mathcal{J}_x = 0.90$, $\mathcal{J}_z^{\rm (eff)}/\mathcal{J}_x = 0.19$, and $|Q_1^{(-)}/Q_2^{(-)}| = 0.78$ for ^{163}Lu at $\hbar\omega_{\rm rot} = 0.3$ MeV, for example, indicates that this solution is more like a wobbling motion of a triaxial body. The wobbling angle shown in Fig. 2(a) is $19°-13°$ for the calculated range. It is evident that the present small-amplitude approximation holds better at high spins. We confirmed that this wobbling solution disappeared as γ decreased. Another feature distinct from the γ vibration is that the present solution exists even at $\Delta_n = \Delta_p = 0$, whereas it is well known that the pairing field is indispensable for the existence of low-lying shape vibrations. This is related to such a tendency that the moments of inertia approach the rigid ones, $\mathcal{J}_x > \mathcal{J}_y$ for $\gamma > 0$, as the pairing gap decreases even without aligned QPs.

A significant point of the data in Refs. [7,8] is that the interband EM transition rates connecting the states I (TSD2) to $I-1$ (TSD1) were precisely measured. In Fig. 3, we compare our numerical results with the measured ones in a form similar to those in Refs. [7,8]. Calculated values for I (TSD2) $\rightleftharpoons I+1$ (TSD1) are also included in order to show the staggering behavior characteristic to this kind of transitions [12]. Figure 3(a) presents the relative $B(E2)$. The data indicate huge collectivity of the interband $B(E2)$, such as 170 Weisskopf unit. Although the present RPA solution is extremely collective, $|c_{n={\rm wob}}| \simeq 0.9$ in the sum rule (Eq. (4.30) in Ref. [12]), in comparison to usual low-lying vibrations, the calculation accounts for $1/2-1/3$ of the measured strength. Figure
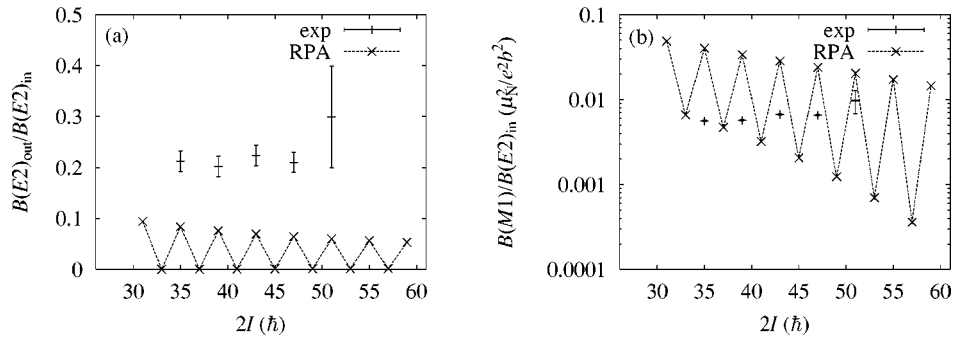
FIG. 3. Interband transition rates for I (TSD2) $\to I \pm 1$ (TSD1) transitions as functions of $2 \times$ spin I, (a) $E2$ and (b) $M1$. They are divided by the in-band $E2(I \to I-2)$ transition rates. Experimental values were taken from Ref. [8]. Noting that the states $I+1$ (TSD1) are slightly higher in energy than I (TSD2) at $I > 51/2$ and $B(T_\lambda; I \to I+1) \simeq B(T_\lambda; I+1 \to I)$ at high spins, we plotted those for $I \to I+1$ at the places with the abscissae $I+1$ in order to show clearly their characteristic staggering behavior.

3(b) graphs $B(M1)/B(E2)_{\text{in}}$. The smallness of $B(M1)$ also reflects collectivity, that is, the coherence with respect to the $E2$ operator, indirectly. Having confirmed the insensitivity to $g_s^{(\text{eff})}$, we adopted $0.6 g_s^{(\text{free})}$ conforming to Ref. [8] and calculated $B(M1)$. The result is similar to that of the PRM. We confirmed that the sign of the $E2/M1$ mixing ratios was correct.

To summarize, we have performed, for the first time, the RPA calculation in the rotating frame to the triaxial superdeformed odd-A nucleus ^{163}Lu and discussed the physical conditions for the appearance of the wobbling solution in the RPA. We have confirmed that the proton $i_{13/2}$ alignment is indispensable for the appearance of the wobbling mode in

this nucleus. The appearance of the wobbling mode requires $\mathcal{J}_x > \mathcal{J}_y^{(\text{eff})} (\neq \mathcal{J}_z^{(\text{eff})})$, but the moments of inertia of the even-even core exhibit irrotational-like γ dependence and, therefore, cannot fulfill this condition for positive-γ shapes. Consequently, the alignment effect that increases $\mathcal{J}_x$ is necessary. Quenching of the pairing correlation also cooperates with the alignment effect for making the γ dependence rigidlike.

[1] D.R. Inglis, Phys. Rev. **96**, 1059 (1954).
[2] S. Frauendorf, Rev. Mod. Phys. **73**, 463 (2001).
[3] A. Bohr and B. R. Mottelson, *Nuclear Structure* (Benjamin, New York, 1975), Vol. II.
[4] I.N. Mikhailov and D. Janssen, Phys. Lett. **72B**, 303 (1978).
[5] E.R. Marshalek, Nucl. Phys. **A331**, 429 (1979).
[6] C.G. Andersson, J. Krumlinde, G. Leander, and Z. Szymański, Nucl. Phys. **A361**, 147 (1981).
[7] S.W. Ødegård *et al.*, Phys. Rev. Lett. **86**, 5866 (2001).
[8] I. Hamamoto *et al.*, Acta Phys. Pol. B **32**, 2545 (2001).
[9] A. Bohr, Mat. Fys. Medd. K. Dan. Vidensk. Selsk. **26**, (1952).
[10] I. Hamamoto and B. Mottelson, Phys. Lett. **132B**, 7 (1983).
[11] Y.R. Shimizu and K. Matsuyanagi, Prog. Theor. Phys. **72**, 799 (1984).

[12] Y.R. Shimizu and M. Matsuzaki, Nucl. Phys. **A588**, 559 (1995).
[13] T. Bengtsson and I. Ragnarsson, Nucl. Phys. **A436**, 14 (1985).
[14] M. Matsuzaki, Y. R. Shimizu, and K. Matsuyanagi (unpublished).
[15] O. Häusser, P. Taras, W. Trautmann, D. Ward, T.K. Alexander, H.R. Andrews, B. Haas, and D. Horn, Phys. Rev. Lett. **42**, 1451 (1979).
[16] O. Häusser, H.-E. Mahnke, J.F. Sharpey-Schafer, M.L. Swanson, P. Taras, D. Ward, H.R. Andrews, and T.K. Alexander, Phys. Rev. Lett. **44**, 132 (1980).
[17] M. Matsuzaki, Nucl. Phys. **A509**, 269 (1990).
[18] W. Schmitz *et al.*, Phys. Lett. B **303**, 230 (1993).